Ultracold Molecules and Atom Pairs in Optical Lattice Potentials

Dissertation

by

Klaus Winkler

submitted to
the Faculty of Mathematics, Computer Science and Physics
of the University of Innsbruck
in partial fulfillment of the requirements for the degree of doctor of science

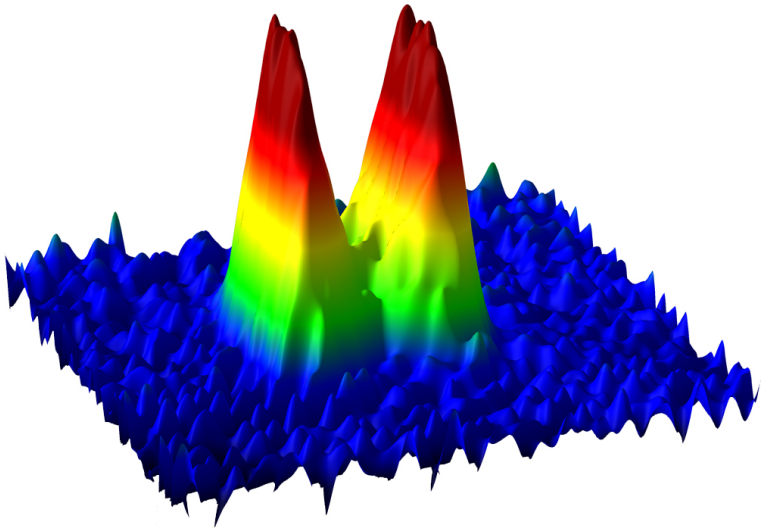

Advisors:
a. Univ.-Prof. Dr. Johannes Hecker Denschlag
Univ.-Prof. Dr. Rudolf Grimm
Institute of Experimental Physics

Innsbruck, July 2007

Abstract

In this thesis I report on experiments with ultracold molecules and atom pairs in optical lattice potentials. We combine the capabilities of the optical lattices with two powerful "tools" used in atom physics: magnetic Feshbach resonances and two-color Raman transitions. We demonstrate a high degree of control of ultracold lattice gases on the quantum level by both realizing a coherent optical transfer between two molecular states, and by exploring a so far undiscovered "exotic" bound state, which is caused by the repulsive interaction between the atoms.
The starting point of the presented experiments is a pure quantum lattice gas of ultracold molecules. This molecular lattice gas is produced by first loading a Bose-Einstein condensate of ^{87}Rubidium atoms into a three-dimensional optical lattice. We can then efficiently convert the atoms in doubly occupied lattice sites into molecules by magneto-association across a Feshbach resonance. With this method the conversion is performed in a very controlled way and we create the molecules with almost unity efficiency in a well-defined quantum state.
In the first part of this thesis I report on the demonstration of a coherent optical transfer of a pure ensemble of ultracold molecules to a deeper bound molecular state via stimulated Raman adiabatic passage (STIRAP). The key idea of this method is to keep the molecules in a dark superposition state during the transfer. This state is decoupled from the light and thus losses due to spontaneous light scattering are suppressed. We are able to test interferometrically the coherence of this molecular quantum superposition state. These results represent an important step towards Bose-Einstein condensation of molecules in the vibrational ground state.
In the second part of this work I report on the discovery of a novel kind of bound object, consisting of two atoms which repel each other. We create the repulsively bound atom pairs by dissociating the molecules in the individual lattice sites with the help of a magnetic Feshbach resonance. This new type of bound object remains stable because the large repulsive interaction between the atoms cannot be converted into kinetic energy in the structured environment of an optical lattice where the phase space for the unbound constituents is strongly restricted. The lack of dissipation in optical lattices allows the pairs to be long-lived, and to undergo coherent dynamics on long timescales. Signatures of the pairs are also recognized in the characteristic momentum distribution and through spectroscopic measurements. We are able to consistently describe our results with the Bose-Hubbard model. This is of importance since this model is also the theoretical basis for many other strongly correlated condensed matter systems and quantum information.

Contents

Introduction

The ongoing success of ultracold gases is largely based on the very high degree of experimental control over the atoms. The internal and external degrees of freedom of the atoms can be manipulated on the quantum level using light fields, radio frequency and magnetic fields. The atoms can be prepared in a single quantum state and can be trapped, so that they are well isolated from the outside world. This leads to long coherence times and allows for studying the coherent dynamics of the atomic ensemble in a pure environment.
A seminal step in the field of the ultracold gases was the realization of Bose-Einstein condensation (BEC) of dilute atomic gases [ANDERSON *et al.* (1995); DAVIS *et al.* (1995); BRADLEY *et al.* (1995)]. This step has enabled numerous fascinating experiments in which fundamental quantum mechanics was studied in a macroscopic and accessible system (for an overview see [ANGLIN AND KETTERLE (2002)]). The main focus of the early atomic BEC experiments was thereby to investigate condensate properties of matter waves in the mean field regime, as described theoretically by the Bogoliubov mean field theory for weakly interacting quantum gases (for a review see [DALFOVO *et al.* (1999)]).
In recent years, the use of so-called "optical lattices" opened new exciting possibilities beyond mean field. The behavior of coherent quantum matter in these periodic light potentials has become a very active research field. The optical lattices are formed by standing waves of laser light fields. Neutral atoms can be trapped in the intensity maxima (or minima) of these standing waves due to the optical dipole force (see e.g. [GRIMM *et al.* (2000)]). The periodic potential of the light field leads to similar band structure of the energy spectrum as known from solid state physics. In contrast to "classical" solid state physics we are able to control the parameters of the lattice and so exactly to control the dynamics of the atoms in the lattice. Additionally, the lack of dissipation in optical lattices allows the atoms undergo coherent dynamics on long timescales (see e.g. [JAKSCH AND ZOLLER (2005)]). A strongly interacting lattice gas of ultracold bosonic atoms can be described by the Bose-Hubbard model [FISHER *et al.* (1989); JAKSCH *et al.* (1998)]. An important prediction of the Bose-Hubbard model is the Mott insulator-superfluid quantum phase transition. This quantum phase transition was first observed experimentally by GREINER *et al.* (2002). The Mott-insulator state is characterized by an exact number of atoms localized at individual lattice sites, with no phase coherence across the lattice.
In our work we investigated quantum states in a three dimensional optical lattice with exactly two atoms per lattice site. In the pure environment of the optical lattice we have been able to exactly control and manipulate the external and internal degrees of freedom of the sample of paired atoms. For that purpose we have used two powerful tools of atom physics as "control knobs", magnetic Feshbach resonances and stimulated Raman transitions.
The use of magnetic Feshbach resonances allows both tuning the interaction between the

atoms [INOUYE *et al.* (1998)] and molecule formation by magneto-association [DONLEY *et al.* (2002)]. These possibilities gave rise to a variety of new experiments and breakthroughs in the last years as, e.g., the preparation of pure molecular quantum gases out of bosonic atoms [HERBIG *et al.* (2003); XU *et al.* (2003); DÜRR *et al.* (2004A)], the experimental creation of molecular Bose-Einstein condensates out of fermionic atoms [JOCHIM *et al.* (2003); GREINER *et al.* (2003); ZWIERLEIN *et al.* (2003)] and investigations of the crossover to a strongly interacting fermionic superfluid [CHIN *et al.* (2004); REGAL *et al.* (2004); ZWIERLEIN *et al.* (2004)].
Stimulated Raman transitions represent another important tool for the manipulation of ultracold gases. Important applications are, e.g., Raman cooling [DAVIDSON *et al.* (1994)], atom interferometry [WEITZ *et al.* (1994)] and photo-association of molecules in a BEC [WYNAR (2000)]. Interesting phenomena connected to Raman light fields are coherent dark states. Since their discovery [ARIMONDO AND ORRIOLS (1976)], dark states have found numerous applications. Prominent examples are electromagnetically induced transparency [BOLLER *et al.* (1991)] and lasing without inversion [SCULLY *et al.* (1989)], slow light [HAU *et al.* (1999)] and ultra-sensitive magneto-meters [STÄHLER *et al.* (2002)]. A particular application is the coherent transfer of population between two long-lived states by a stimulated Raman adiabatic passage (STIRAP) (for a review see [BERGMANN *et al.* (1998)]).
In our experiments we combined the exciting possibilities of strongly interacting particles in an optical lattice with the possibilities given by magnetic Feshbach ramping and stimulated Raman transitions. This allowed us to demonstrate a coherent switching between two molecular quantum states via a stimulated Raman adiabatic passage [WINKLER *et al.* (2007)]. The exquisite control over the molecules in a specific ro-vibrational state in the lattice opens the way to a number of new interesting studies in, for instance, few body collision physics [CHIN *et al.* (2005); STAANUM *et al.* (2006); ZAHZAM *et al.* (2006)], chemistry in the ultracold regime, high resolution spectroscopy, as well as quantum computation [DEMILLE (2002)] and the creation of a molecular BEC in the molecular ground state [JAKSCH *et al.* (2002)].
Moreover, we have been able to explore a so far undiscovered "exotic" bound state, which is caused by the repulsive interaction between the paired atoms [WINKLER *et al.* (2006)]. We prepared this bound state by dissociating the molecules in the single sites of the optical lattice with the help of the magnetic Feshbach resonance. This new type of bound object remains stable because, in the structured, dissipation free environment of an optical lattice, the large repulsive interaction between the atoms cannot be converted into kinetic energy. There is no analogue in traditional condensed matter systems of such repulsively bound pairs, owing to the presence of strong decay channels. Our results exemplified the strong correspondence between the optical lattice physics of ultracold bosonic atoms and the Bose-Hubbard model, a link that is vital for future applications of these systems to the study of strongly correlated condensed matter and to quantum information.

This thesis is organized as follows:

• The first chapter deals with the production of a pure, ultracold molecular sample in an optical 3D lattice. This molecular sample was the starting point of two experiments which represent the main part of this work.
• In the second chapter I discuss the realization of an efficient and highly selective transfer scheme, where an ensemble of $^{87}Rb_2$ Feshbach molecules in an optical lattice is coherently converted to a deeper bound molecular state via stimulated Raman adiabatic passage (STIRAP).
• In the third chapter I review an experiment where we used the Feshbach molecules in an optical lattice to create and analyze a quantum state consisting solely of pairs of atoms in the optical lattice. Consistent with a theoretical analysis, we observed a long lifetime of these repulsively bound pairs, even under conditions when they collide with one another. We also recognized clear signatures of the pairs in the characteristic momentum distribution and through spectroscopic measurements.

Publications

The following articles have been published in the framework of this PhD thesis. The full articles are attached in the appendix.

- *Coherent optical transfer of Feshbach molecules to a lower vibrational state.*
  K. Winkler, F. Lang, G. Thalhammer, P.v.d. Straten, R. Grimm, and J. Hecker Denschlag.
  Phys. Rev. Lett. **98**, 043201, 2007.

- *Repulsively bound atom pairs in an optical lattice.*
  K. Winkler, G. Thalhammer, F. Lang, R. Grimm, J. Hecker Denschlag, A. J. Daley, A. Kantian, H. P. Büchler, and P. Zoller.
  Nature **441**, 853, 2006.

- *Long distance transport of ultracold atoms using a 1D optical lattice.*
  S. Schmid, G. Thalhammer, K. Winkler, F. Lang, and J. Hecker Denschlag.
  New Journal of Physics **8**, 159, 2006

- *Long-lived Feshbach molecules in a three-dimensional optical lattice.*
  G. Thalhammer, K. Winkler, F. Lang, S. Schmid, R. Grimm, and J. Hecker Denschlag.
  Phys. Rev. Lett. **96**, 050402, 2006.

- *Atom-molecule dark states in a Bose-Einstein condensate.*
  K. Winkler, G. Thalhammer, M. Theis, H. Ritsch, R. Grimm, and J. Hecker Denschlag.
  Phys. Rev. Lett. **95**, 063202, 2005.

- *Inducing an optical Feshbach resonance via stimulated Raman coupling.*
  G. Thalhammer, M. Theis, K. Winkler, R. Grimm, and J. Hecker Denschlag.
  Physical Review A **71**, 033403, 2005.

- *Tuning the scattering length with an optically induced Feshbach resonance*.
  M. Theis, G. Thalhammer, K. Winkler, M. Hellwig, G. Ruff, R. Grimm and J. Hecker Denschlag.
  Phys. Rev. Lett. **93**, 123001, 2004.

1 Experimental Procedures

The starting point of all the experiments described in my thesis is a pure sample of an ultracold cloud of ^{87}Rubidium molecules in an three dimensional optical lattice. In this chapter I will give a short overview about the experimental steps needed to obtain these ultracold molecules. The single steps can be summarized as follows:

- Pre-cooling and trapping of ^{87}Rubidium atoms in a magneto optical trap (MOT)
- Magnetic transport of the cold atomic cloud into a glass-cell
- Bose-Einstein condensation
- Loading of the Bose-Einstein condensate (BEC) into a 3D optical lattice
- Molecule production by sweeping across a Feshbach resonance
- Purification by removing all remaining unbound atoms

To obtain a pure molecular sample there are several technical requirements to be met. We need a special experimental apparatus working at ultrahigh vacuum conditions because at all stages of the experiment the atoms and molecules have to be protected from collisions with background gas. We started to construct this apparatus in 2001 [THEIS (2005); WINKLER (2002)]. Thereby we followed the design of the Bloch/Esslinger/Hänsch-group at the LMU in Munich to separate the magneto-optical trap (MOT) chamber from the place where the Bose-Einstein condensate is created (see Fig. 1.1) [GREINER *et al.* (2001)]. The big advantage of this design is an exceptionally good optical access from all six orthogonal directions at the glass cell (see Fig. 1.1) where all our experiments are carried out.
We need additionally a complex laser- and magnetic field system for cooling, trapping and manipulating the atoms and molecules. A computer system controls exactly the time sequences of the different processes.
The technical details of the experimental setup will not be discussed here since they are already described in previous theses in our group. A detailed description of the vacuum apparatus and the magnetic transport can be found in the doctoral thesis of Matthias Theis [THEIS (2005)] and in my diploma thesis [WINKLER (2002)]. The laser system and the computer control system is reviewed in the thesis of Gregor Thalhammer [THALHAMMER (2007)].

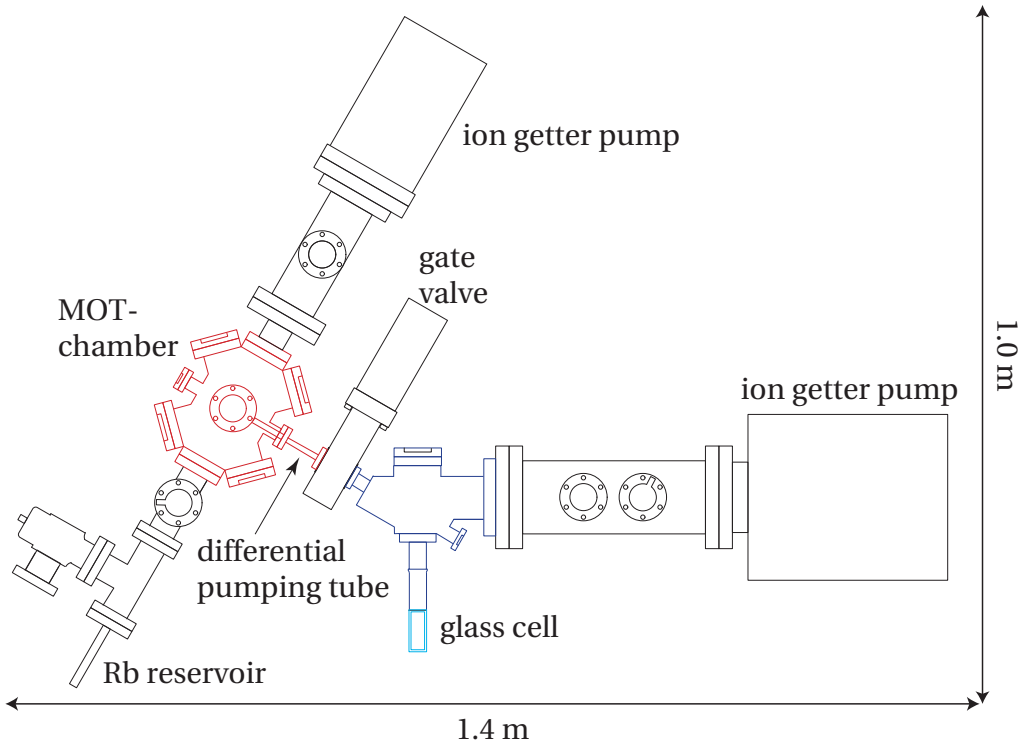

Figure 1.1:
Overview of the vacuum system: the left part is the MOT chamber, which is separated by a differential pumping tube from the XUHV section with the glas cell. The pre-cooled atoms in the MOT chamber are magnetically transported into the glass cell where the BEC is produced in a magnetic trap and all the experiments are carried out.

1.1 Preparation and transport of the cold atomic cloud

In a first step about 3×10^9 ^{87}Rubidium atoms are loaded within 6 s into a magneto-optical trap (MOT) directly from the background gas and are then cooled further to about 50 µK in a molasses cooling phase. The background gas pressure in the MOT chamber is about 5×10^{-8} mbar. After optically pumping into the $|F = 1, m_F = -1\rangle$ electronic ground state we load the atom cloud into a magnetic quadrupole trap with a gradient of 130 G/cm in the (strong) vertical direction. Within 1.4 s the atoms are then moved via a magnetic transfer line over a distance of 48 cm including a 120° corner into a glass cell (for details see [WINKLER (2002); THEIS (2005)]). The glass cell is at a pressure below 10^{-11} mbar. For our magnetic transport (similar to that described in [GREINER *et al.* (2001)]) 13 pairs of quadrupole coils are used (see Fig. 1.2). Each of the transfer coils has an inner diameter of 23.6 mm, an outer diameter of 65 mm, and a height of 5.7 mm and consist of 34 windings. They are arranged in two layers above and below the vacuum chamber with a separation of 50 mm. Peak currents of 75 A are necessary to maintain a vertical gradient of 130 G/cm during transfer. In the glass cell we load the cloud into a Quadrupole-Ioffe con-

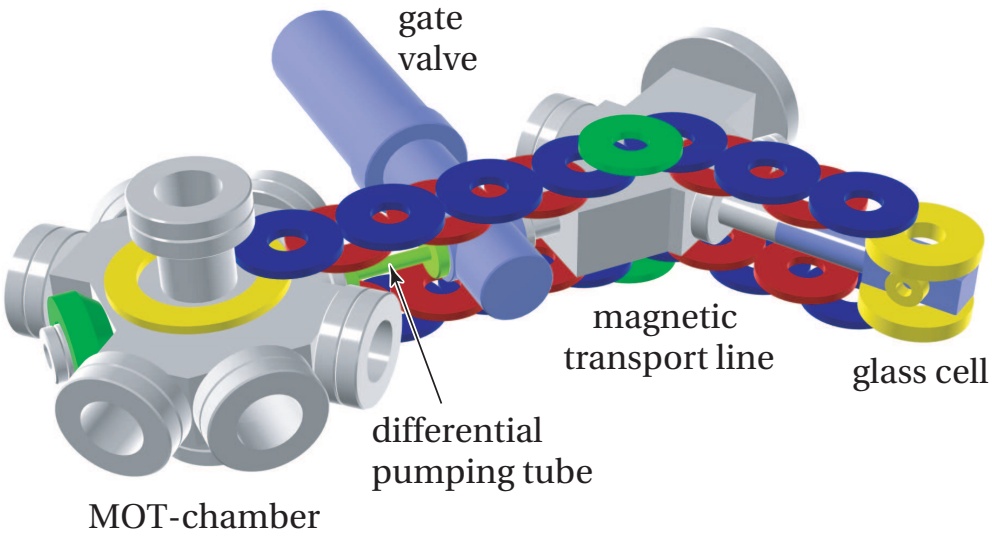

Figure 1.2:
Part of the vacuum apparatus and magnetic transfer line. The drawing shows how the 13 pairs of transfer coils (red, blue and green), the MOT coil (yellow, left-hand side), the push coil (green, left-hand side) and the QUIC trap are arranged around the vacuum chambers.

figuration (QUIC) trap [ESSLINGER *et al.* (1998)], ending up with typically 4×10^8 atoms at a temperature of about 250 µK. All three coils of the QUIC trap are operated at a current of 40 A, dissipating 350 W. This results in trap frequencies of $\omega_{\text{radial}}/2\pi = 150$ Hz and $\omega_{\text{axial}}/2\pi = 15$ Hz at a magnetic bias field of 2 G.

1.2 Bose-Einstein condensation

To achieve Bose-Einstein condensation we use forced radio-frequency (rf) evaporation for a period of 14 s (see Fig. 1.3). About 1 s before reaching Bose-Einstein condensation we reduce the current through the QUIC trap from 40 A to 30 A to avoid that the trap frequency is a multiple of the 50 Hz power line frequency. We experimentally observed that this procedure reduces the oscillation of the BEC in the trap considerably.
The Bose Einstein Condensate (BEC) used for our measurements consists typically of about 5×10^5 ^{87}Rb atoms in the spin state $|F = 1, m_F = -1\rangle$ [THALHAMMER *et al.* (2005)]. In principle it is possible for us to obtain BECs with up to 2×10^6 atoms. However it turned out that for experiments in optical lattices a smaller number of particles is favorable (see Sec. 1.3).

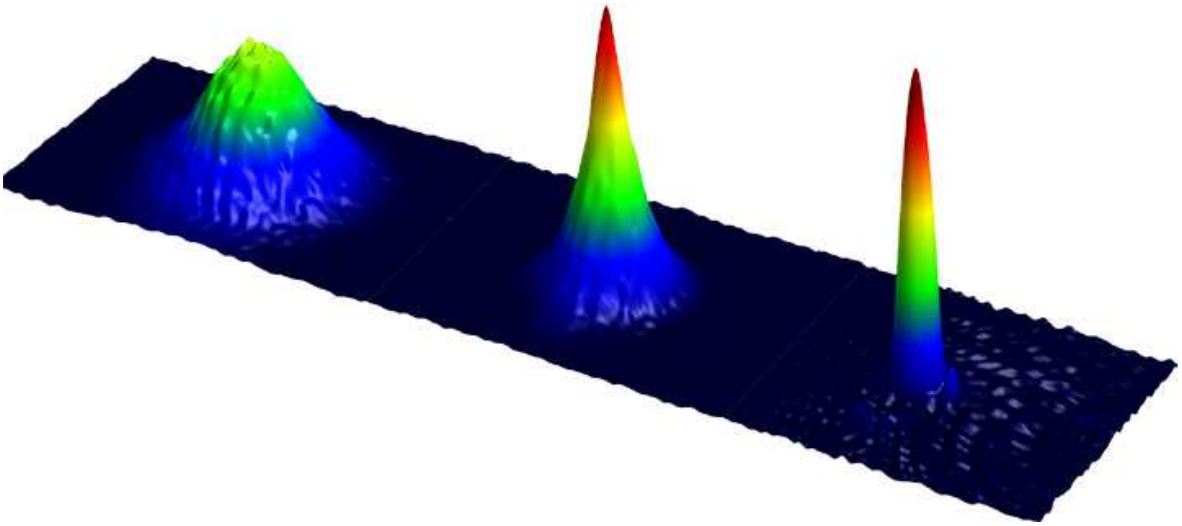

Figure 1.3:
Bose Einstein condensation: from left to right the temperature is decreased by changing the final value of the radio frequency used for the forced evaporation. Left: thermal cloud near BEC transition, center: a BEC is growing out of the thermal cloud, right: pure BEC of about 1×10^6 atoms. These "3d"-pictures are derived from absorption images (see Sec. 1.5). The peak height and the color represent the atomic density.

Transport of the Bose-Einstein condensate

After creating the BEC, the QUIC trap is converted into a Ioffe-type magnetic trap with trap frequencies $\omega_{x,y,z} = 2\pi \times (7, 19, 20)$ Hz by adjusting the currents through the quadrupole and Ioffe coils and by applying additional magnetic field gradients (see Fig. 1.4) [THALHAMMER (2007)]. This causes the BEC to move over a distance of 8 mm into the center of the QUIC quadrupole coils which are later used to generate the homogeneous magnetic field for Feshbach ramping (see Sec. 1.4). It is important that the BEC is exactly in the center of the quadrupole coils to minimize the magnetic field gradients of the homogeneous magnetic field.
To change the position of the BEC, the current in the quadrupole coils is reduced from 30 A to about 14.6 A while we leave the current in the Ioffe coil constant at 30 A. We use additional coils (coils 1,2 in Fig. 1.4) in anti-Helmholtz configuration for an exact horizontal positioning. Because of the strongly reduced trap frequencies of the moved trap, the BEC considerably sags down (about 2.5 mm). We use a levitation coil, which creates a vertical gradient, to compensate this sagging of the BEC. In the moved Ioffe-type magnetic trap we reach a peak density of the BEC of about 4×10^{13} cm^{-3}.

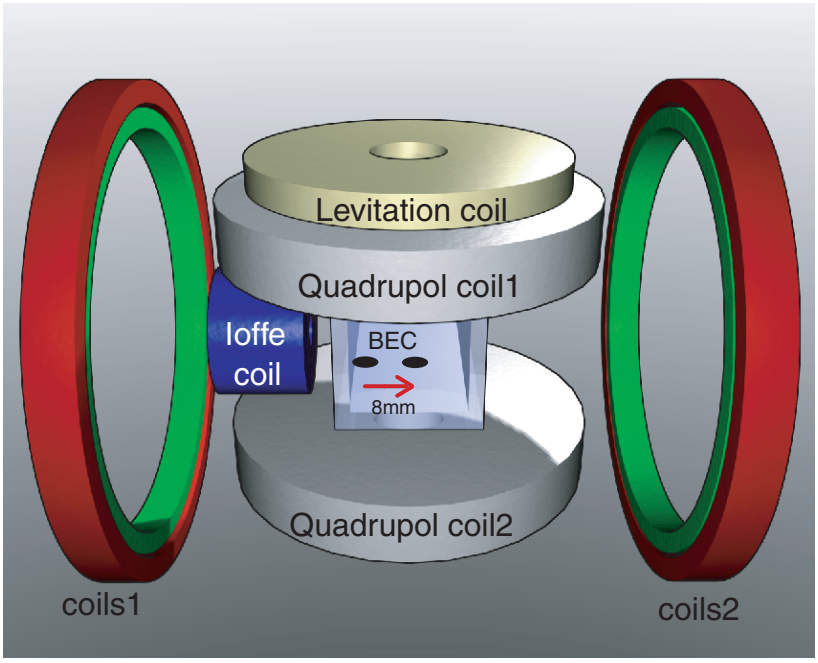

Figure 1.4:
The BEC is moved over a distance of 8 mm into the center of the QUIC quadrupole coils by adjusting the currents through the quadrupole and Ioffe coils and by applying additional magnetic field gradients (see text).

1.3 Optical lattice potential

We use an three dimensional optical lattice for the preparation of a pure ultracold molecular sample. The lattice serves several purposes. First, it isolates the molecules from each other and shields them from detrimental collisions. This allows to create a long-lived sample also with dimers of bosonic atoms. Second, due to the high trap frequencies in the single lattice sites, the matrix elements for atom-molecule coupling are strongly enhanced allowing an efficient atom-molecule conversion (see Sec. 1.4). Additionally, lattice sites occupied with exactly two atoms represent a perfectly controlled quantum system which can be rigorously treated theoretically (see Sec. 3.1). An optical lattice can be created by superimposing two counter-propagating laser beams which form a standing wave in one dimension. In the focus of beam the resulting periodic potential has the form

$$V(r,z) = V_0\, \mathrm{e}^{-2r^2/w_0^2} \sin^2(k_{\mathrm{lat}} z), \tag{1.1}$$

with $k_{\mathrm{lat}} = 2\pi/\lambda$ the wave number. λ is the wavelength of the lattice laser, V_0 is the potential depth of the optical lattice, w_0 the beam waist. z is the direction of the beam propagation, r is the radial direction. The potential depth V_0 is thereby four times larger than the depth of the dipole trap without retro-reflection, due to the constructive interference between the two counter propagating laser beams. V_0 can be calculated through

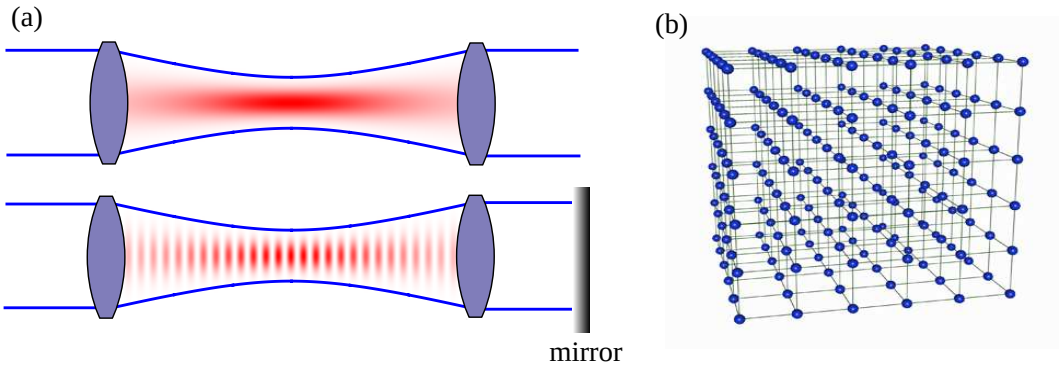

Figure 1.5:
(a) A gaussian laser beam forms a standing wave when it gets retro-reflected.
(b) Three superimposed orthogonal standing waves form in the intersection point a 3D lattice.

[GRIMM *et al.* (2000)]

$$V_0 \sim 4 \times \frac{3\pi c^2}{2w_0^3}\frac{\Gamma}{\Delta} I, \tag{1.2}$$

with c being the speed of light and Γ the line-width of the excited state (which is $2\pi \times$ 5.9 MHz for ^{87}Rb). Δ is the relative detuning to the center of the D_1 line at $\lambda_1 = 795$ nm and D_2 line at $\lambda_2 = 780$ nm. I is the light intensity. Note, that Eq. (1.2) is only valid for large detunings $\Delta >> \Gamma$.
The easiest way to implement counter-propagating laser beams is simply to retro-reflect a single laser beam (see Fig. 1.5).

3D optical lattice

To form a three dimensional lattice three standing waves can be superimposed orthogonally to each other. The resulting microtraps in the intersection point of the laser beams have a trap frequency of

$$\omega_{ho} = \sqrt{2V_0 k_{\text{lat}}^2/m} \tag{1.3}$$

in a harmonic approximation and spacing of $a = \lambda/2$ with m the atom mass.
The 3D lattice used for our experiments is cubic and consists of three retro-reflected intensity stabilized laser beams which propagate orthogonally to each other. They are derived from a frequency-stable single-mode Titanium:Sapphire laser ($\approx$ 500 kHz linewidth) with a wavelength of typically $\lambda = 830.44$ nm. For this wavelength, the laser is detuned by about 100 GHz from the closest transition to an excited molecular level, minimizing light induced losses as a precondition for long molecular lifetimes [THALHAMMER *et al.* (2006)]. The laser beams are polarized perpendicularly to each other, and their frequencies differ by several tens of MHz to avoid disturbing interference effects. The waists of

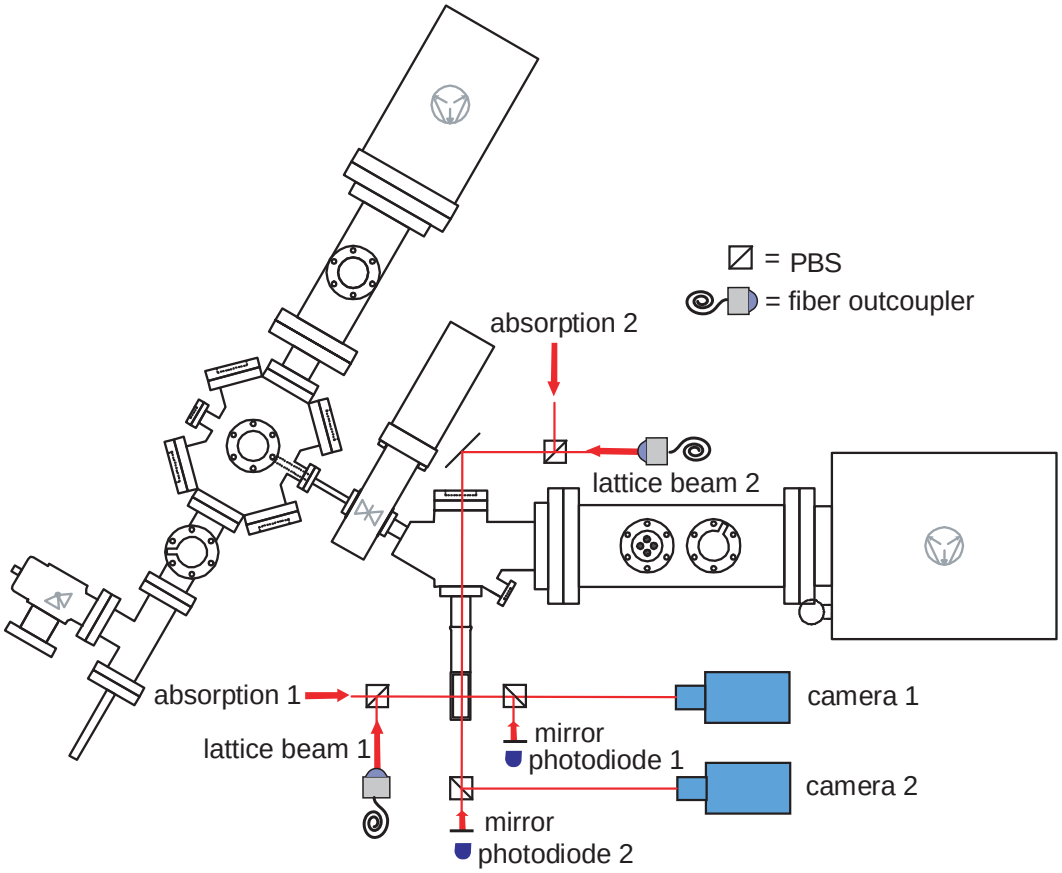

Figure 1.6:
Alignment of the lattice beams: We retro-reflect three independent laser beams to create a 3D optical lattice (shown are only two directions). We measure the intensity of the lattice beams with photodiodes behind the retro-reflecting mirrors which transmit 1% of the laser light. The photodiode signal is used to stabilize the lattice laser beam intensity. We overlap, by using polarizing beam splitters (PBS), all three lattice laser beams with laser beams for the absorption imaging. After passing the glass cell we separate the beams again with a second PBS. In this way we are able to independently observe the BEC in all three directions in space. Additionally we can also detect the lattice laser beams on the CCD-cameras. This has the big advantage that it is relatively easy to overlap the lattice laser beams with the BEC and also to control the beam-size.

all three beams are about 160 µm. The maximum obtainable power is about 110 mW per beam, which results in calculated lattice depths up to 40 recoil energies E_r. $E_r = h^2/2m\lambda^2$, where h is Planck's constant. We have verified the lattice depths by measuring the energy gap between bands of the lattice [HECKER DENSCHLAG *et al.* (2002)]. The relative uncertainty of our lattice depth is ±10%.
In our experimental setup we overlap, by using polarizing beams splitters (PBS), all three

lattice laser beams with laser beams for the absorption imaging (see Fig. 1.6). After passing the glass cell the beams are separated again with a second PBS. In this way we are able to independently observe the BEC in all three directions in space. Additionally we can also detect the lattice laser beams on the CCD-cameras because a small part of the lattice laser light arrives after passing the PBS at the camera. This has the big advantage that it is relatively easy to overlap the lattice laser beams with the BEC and also to control the beam-size. To create the optical lattice we retro-reflect the laser beams with plane cavity mirrors which transmit 1% of the laser light. This allows us to measure the intensity of the lattice beams with photodiodes behind the retro-reflecting mirrors. We use the photodiode signal to stabilize the lattice laser beam intensities.

1.4 Preparation of an ultracold pure molecular sample

In this section I will describe how we prepare an ultracold pure molecular sample in a 3D lattice. "Pure" means that the individual sites of the lattice are either empty or filled with a single molecule. "Ultracold" means that the molecules are in the vibrational ground state of the lattice.
To produce the molecules in the lattice we sweep across a so-called magnetic Feshbach resonance [STÖFERLE *et al.* (2006); THALHAMMER *et al.* (2006); VOLZ *et al.* (2006); OSPELKAUS *et al.* (2006)]. The key feature of this experimental technique is the adiabatic transfer of the scattering state of two atoms into the highest excited diatomic vibrational bound state (for an excellent review of molecule production with Feshbach resonances see [KÖHLER *et al.* (2006)]). The basic concept can be seen in Fig. 1.7: the scattering state of two free atoms crosses a bound state at a certain magnetic field strength. A coupling between the two states leads to an avoided crossing. By changing slowly enough the external homogeneous magnetic field, the scattering state can be transferred adiabatically into the bound state and vice-versa. The probability of creating a molecule is given by [KÖHLER *et al.* (2006)]

$$P_{mol} = 1 - \exp\left(-\frac{2\sqrt{6}\hbar}{m a_{ho}^3}\left|\frac{a_{bg}\Delta B}{\dot{B}}\right|\right), \tag{1.4}$$

where $a_{bg} = 100.5\,a_0$ is the background scattering length, $\Delta B = 0.21\,\mathrm{G}$ the width of the Feshbach resonance and $\dot{B}$ the ramp speed at the Feshbach resonance. $a_{ho} = \sqrt{\hbar/m\omega_{ho}}$ is the harmonic oscillator length, with ω_{ho} the trap frequency.

Experimental realization

In order to prepare an ultracold pure molecular sample, the atomic BEC is first adiabatically loaded into a $35\,\mathrm{E_r}$ deep 3D optical lattice within 100 ms. Afterwards we turn off the magnetic trap and by suddenly reversing the bias magnetic field of a few Gauss, we flip the spins of our atoms to the high field seeking state $|F = 1, m_F = +1\rangle$ with an efficiency higher than 99%. This state features a Feshbach resonance at 1007.4 G [VOLZ *et al.*

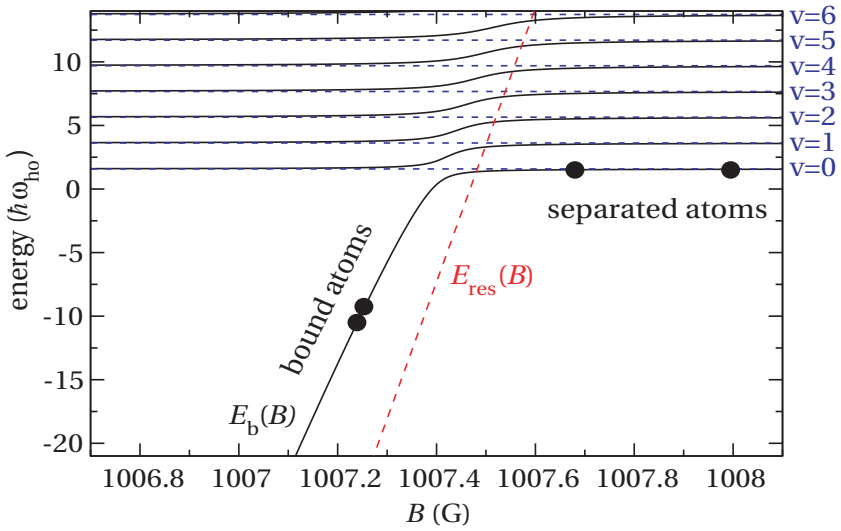

Figure 1.7:
Schematic illustration of the molecular association of a pair of ^{87}Rubidium atoms via a downward magnetic field sweep in a spherical harmonic atom trap with an trapping frequency of $\omega_{ho} = 2\pi \times 39$ kHz. This value corresponds to the trap frequency for Rubidium atoms in the sites of an optical lattice with a depth of 35 E_r and a wavelength λ = 830 nm. The dashed lines indicate the vibrational levels (v = 0, . . . , 6) of the harmonic trap and the energy $E_{res}(B)$ of the bound state without a coupling between the states. With the coupling (solid lines) we observe avoided crossings whereas the molecular bound state is connected with the lowest vibrational state. Picture from KÖHLER *et al.* (2006).

(2003)]. Afterwards, we ramp up a homogeneous magnetic field in 3 ms to about 1015 G using the QUIC quadrupole coils in Helmholtz configuration [THALHAMMER *et al.* (2006)]. The fast diabatic crossing of the Feshbach resonance has basically no effect on the atoms in the lattice. This means that the atoms remain in the vibrational ground state of the lattice. Afterwards we slowly ramp in 5 ms from 1015 G to 1000 G crossing the Feshbach resonance at 1007.4 G. Molecules are adiabatically produced in the multiply occupied lattice sites. At this stage typically 10-20% of the condensate atoms are grouped in pairs of two into the lattice sites. 50-60% of the condensate atoms are found in singly occupied sites, and another 20-30% of atoms are located in triply and more highly occupied lattice sites [THALHAMMER *et al.* (2006)]. Note, that these values strongly depend on the density of the BEC and trap parameters like the radial confinement of the lattice laser beams. We observed for a smaller atom number N in the BEC, corresponding to lower density $n_{BEC}(0) \propto N^{2/5}$ [DALFOVO *et al.* (1999)], a decreasing number of atoms in triply and more highly occupied lattice sites while the number of atoms in singly and doubly occupied lattice sites increases.

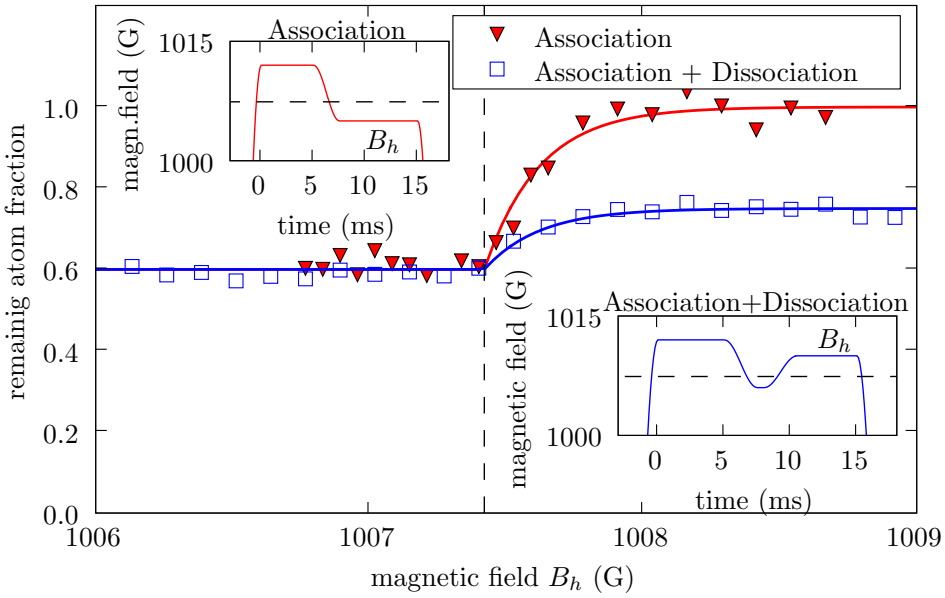

Figure 1.8:
Adiabatic association and dissociation of Feshbach molecules: After ramping the magnetic field to about 1013 G, we ramp the field in 2.5 ms to a variable hold value B_h as shown in the left hand side inset. Crossing the Feshbach resonance at 1007.4 G (dashed lines), we observe a decrease in atom numbers (red triangles). If we ramp the magnetic field back over the Feshbach resonance (right hand side inset in Fig. 1.8) we observe a reappearing of a part of the "missing" atoms (blue squares). This number corresponds to atoms in doubly occupied lattice sites which form molecules after the first Feshbach ramp and are dissociated again with second ramp. We attribute the irretrievable loss of certain number of the atoms (difference between red triangles and blue squares at $B_h > 1007.4$) to inelastic collisions involving molecules for sites initially occupied by three or more atoms.

Adiabatic association and dissociation of Feshbach molecules

We can investigate the number of atoms which are located in singly, doubly or multiply occupied lattice sites by an adiabatic association and dissociation of Feshbach molecules. The data in Fig. 1.8 are measured as follows [THALHAMMER (2007)]: after ramping the magnetic field to about 1013 G, we ramp the field in 2.5 ms to a variable hold value B_h, as shown in the left hand side inset in Fig. 1.8. Crossing the Feshbach resonance at 1007.4 G (dashed vertical line), we observe a decrease in atom numbers. If we ramp the magnetic field back over the Feshbach resonance (right hand side inset in Fig. 1.8) we observe a reappearance of a part of the "missing" atoms. This number corresponds to the atoms in doubly occupied lattice sites in which molecules are formed after the first Feshbach ramp. We can dissociate these molecules into atoms with near unity efficiency by ramping back over the Feshbach resonance [THALHAMMER *et al.* (2006)]. We attribute the irretrievable

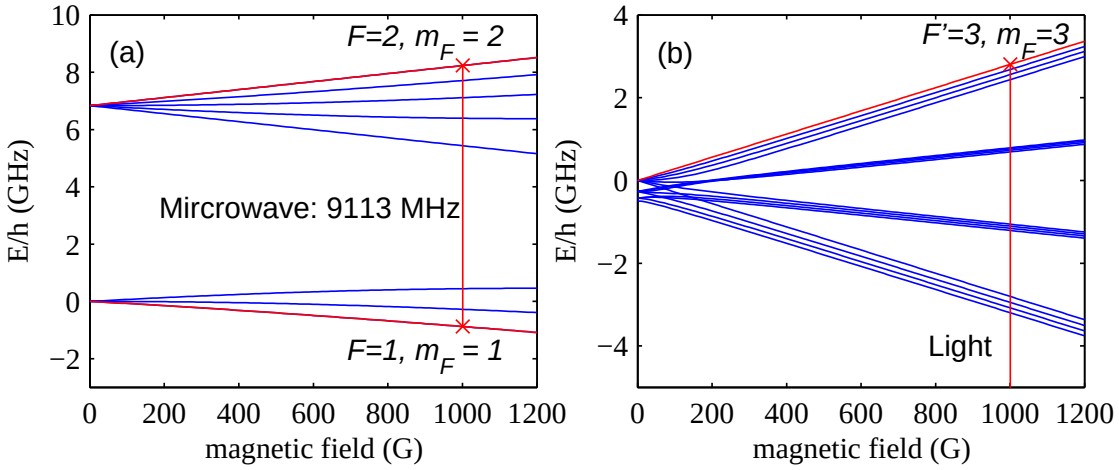

Figure 1.9:
Purification scheme: We apply a combined microwave and light pulse at a magnetic field of 1000 G for 3 ms. (a) The microwave drives the transition at a frequency of 9113 MHz between levels which correlate with $|F=1,m_F=+1\rangle$ and $|F=2,m_F=+2\rangle$. (b) The light pulse drives the closed transition $|F=2,m_F=+2\rangle \rightarrow |F'=3,m_F=+3\rangle$. Plotted is the magnetic field dependence of the $5P_{3/2}$ excited state. The optical transition frequency is 1402 MHz blue detuned compared to the transition at zero magnetic field.

loss of certain number of the atoms to inelastic collisions involving molecules for sites initially occupied by three or more atoms. Therefore, after the Feshbach ramp the remaining occupied sites each contain either a single atom or a single molecule.
We observe that reducing the atom number of the BEC leads to higher fraction of atoms in doubly occupied sites but not to a higher absolute number. Therefore we work in our experiments normally with large BECs with $\sim 5-10\times10^5$ atoms to maximize the molecule number. However, optimizing the trap parameters for a given atom number would lead to a higher percentage of doubly occupied sites even for large BECs and therefore also would improve the absolute molecule number.

Purification scheme

In order to create a pure molecular sample, we have developed an advanced purification scheme to remove all the single atoms that are not bound in molecules [THALHAMMER *et al.* (2006)]. This scheme combines the great selectivity of microwave excitation with the high efficiency of atom removal through resonant light pressure [XU *et al.* (2003)]. We apply a combined microwave and light pulse at a magnetic field of 1000 G for about 3 ms. The microwave drives the transition at a frequency of 9113 MHz between levels that correlate with $|F=1,m_F=+1\rangle$ and $|F=2,m_F=+2\rangle$.
We use a microwave waveguide as antenna. The waveguide has the form of a rectangular tube ($\sim 1.5\times3\times15$ cm) which is open at one side. We supply this waveguide with a 2 Watt

amplifier (for details see [THALHAMMER (2007)]). The light pulse drives the closed transition $|F = 2, m_F = +2\rangle \rightarrow |F' = 3, m_F = +3\rangle$ (see Fig. 1.9). The optical transition frequency is 1402 MHz blue detuned compared to the transition at zero magnetic field. We find the optimum light intensity by increasing the intensity until no more atoms can be detected after the combined pulse.
The direct effect of the microwave and light field pulse on the molecules is negligible because the radiation is off resonance. As an indirect effect, however, we find that we lose about 40% of the molecules, probably due to inelastic collisions with the blown away atoms. Further losses are not observed in subsequent purification pulses. We end up with a pure molecular sample formed from about 10% of the initial atoms, which corresponds to typically 3×10^4 molecules.

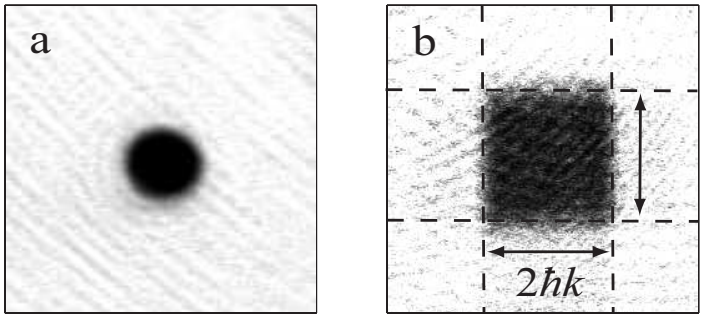

Figure 1.10:
Typical time of flight (~ 15 ms) absorption pictures of: (a) A BEC, released from a magnetic trap. (b) Atoms released from an optical three dimensional lattice. For this measurement the lattice is ramped down from a lattice depth of 35 E_r to zero in about 2 ms. The momentum distribution of the atoms, which is fully contained in a cube of width $2\hbar k$, corresponds to the first Brillouin zone of the lattice. This demonstrates that the atoms are in the vibrational ground state of the lattice sites. For a typical time of flight of 15 ms, the width of Brillouin zone corresponds to width of about 165 µm.

1.5 Measurement of atom and molecule numbers

Atom numbers are measured in our experiment with absorption imaging [KETTERLE *et al.* (1999)] at low magnetic fields (≈ 2 G) after release from the optical lattice and typically 15 ms of ballistic expansion. The absorption imaging investigates the shadow an atom cloud casts onto our CCD camera when we illuminate the cloud with a near resonant laser beam.
We apply the near resonant absorption laser beam for 100 µs. This beam drives the closed transition $|F = 2\rangle \rightarrow |F' = 3\rangle$ at $B \sim 0$ G. We detune the absorption laser beam from the atomic resonance typically by 0 to 15 MHz, depending on the atom numbers, to avoid a saturation effect [THEIS (2005)]. We simultaneously apply a repumping laser beam which drives the transition $|F = 1\rangle \rightarrow |F' = 1\rangle$ in order to transfer the atoms from the hyperfine state $|F = 1\rangle$, which we use normally for our experiments, to state $|F = 2\rangle$. Both laser beams are linearly polarized. In order to determine molecule numbers, the molecules are first dissociated into atoms by slowly ramping back across the Feshbach resonance and then quickly switching off the magnetic field. The atoms can then be detected as described before.
We also use absorption imaging to map out the band occupation of the lattice. For this purpose, the lattice is ramped down in 2 ms and we typically observe a momentum distribution, which is fully contained in a cube of width $2\hbar k$ (see Fig. 1.10 (b)), corresponding to the first Brillouin zone of the lattice [GREINER *et al.* (2001)]. This demonstrates that atoms and molecules are in the vibrational ground state of the lattice sites (a detailed discussion of atoms in the ground state of an optical lattice can be found in Sec. 3.1).

2 Coherent Optical Transfer of Feshbach Molecules to a Lower Vibrational State

Since molecules have more internal degrees of freedom than atoms, ultracold molecules lend themselves to an even larger number of interesting studies in, for instance, few body collision physics [CHIN *et al.* (2005); STAANUM *et al.* (2006); ZAHZAM *et al.* (2006)], chemistry in the ultracold regime, high resolution spectroscopy, as well as quantum computation [DEMILLE (2002)]. Furthermore, molecules in their vibrational ground state are of special interest, because they allow the formation of an intrinsically stable molecular BEC. Current pathways towards ultracold molecules in well-defined quantum states are either based on sympathetic cooling [DOYLE *et al.* (2004)] or association of ultracold neutral atoms, using photoassociation [JONES *et al.* (2006)] or Feshbach resonances [KÖHLER *et al.* (2006)]. The method of Feshbach ramping has proved especially successful and efficient, but it only produces molecules in the least bound vibrational level. In order to selectively convert molecules into more deeply bound states, it has been proposed [JAKSCH *et al.* (2002)] to use a sequence of stimulated optical Raman transitions to step molecules down the vibrational ladder. This process takes place while the molecules are kept in an optical lattice, which isolates them from each other and thus shields them from detrimental collisions.

In the experiments described in this chapter, we realized an efficient and highly selective transfer scheme, where an ensemble of $^{87}Rb_2$ Feshbach molecules in an optical lattice is coherently converted to a deeper bound molecular state. This chapter is organized as follows: First I give a basic introduction to the scheme we use to transfer the molecules to a deeper bound state. This transfer is based on an optical Raman transition and is called "STImulated Raman Adiabatic Passage (STIRAP)". Then I describe the experimental setup for the measurements presented in this chapter. Afterwards I show spectroscopy measurements which we performed to identify a suitable excited molecular state for STIRAP and discuss the observation of molecular dark resonances with a long lifetime. These long-living dark states are a necessary precondition for our STIRAP experiments. Subsequently I review the successful experimental realization of population transfer of the molecules with STIRAP and discuss the adiabaticity of the process. After that I present an interferometrical test of the coherence of a molecular superposition state and shortly discuss the lifetime of the molecules in both vibrational states. In the outlook I discuss the possibility to use STIRAP to transfer molecules to the vibrational ground state of the singlet and triplet potential.

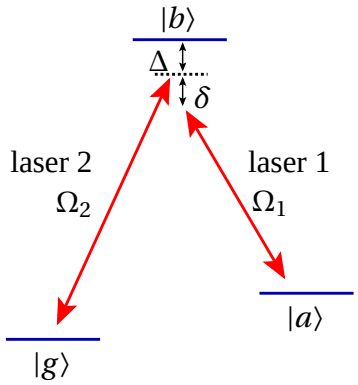

Figure 2.1:
Simple three level system for STIRAP: $|a\rangle$ and $|g\rangle$ are the electronic ground states, $|b\rangle$ is an excited state. These states are coupled with laser fields. $\Omega_{1,2}$ denote the corresponding Rabi frequencies. Δ and δ are the laser detunings (see text).

2.1 Stimulated Raman Adiabatic Passage

The stimulated Raman adiabatic passage (STIRAP) is known as a fast, efficient and robust process for population transfer based on a Raman transition [BERGMANN *et al.* (1998)]. The idea of STIRAP is to keep the molecules during the transfer in a dark superposition state, which decouples from the light and thus suppresses losses due to spontaneous light scattering.
The possibility of an efficient population transfer by appropriate delayed laser pulses was first recognized by OREG *et al.* (1984) in a theoretical work and is closely connected with the observation of dark states in 1976 [ARIMONDO AND ORRIOLS (1976)]. The first experimental realization of population transfer with STIRAP was demonstrated in the group of Klaas Bergmann at the university of Kaiserslautern [GAUBATZ *et al.* (1988)]. Gaubatz *et al.* showed an efficient excitation of molecules to specific high vibrational states when the molecules are flying through two displaced laser beams.
The method of population transfer with STIRAP can be understood with a relatively simple three level system [KUKLINSKI *et al.* (1989)], as discussed in the following:

Three level system

We label the three levels with $|a\rangle$, $|b\rangle$ and $|g\rangle$ (see Fig. 2.1). $|a\rangle$, $|g\rangle$ are electronic ground states while $|b\rangle$ is an excited state. State $|a\rangle$ is coupled with a laser field (laser 1) to state $|b\rangle$ and state $|g\rangle$ is coupled with another laser field (laser 2) to state $|b\rangle$.
$\Delta+\delta = (E_a - E_b)/\hbar - \omega_1$ is the detuning of the laser 1 from the resonance of the $|a\rangle \rightarrow |b\rangle$ transition. $\delta = (E_a - E_g)/\hbar - (\omega_1 - \omega_2)$ is the two photon detuning. ω_1 and ω_2 are the frequencies of the corresponding laser fields.
We can write the Hamilton matrix, which describes the coupling of the three states by two

coherent radiation fields, within the rotating wave approximation (RWA) [SHORE (1990)]

$$H = \hbar \begin{pmatrix} 0 & \Omega_1/2 & 0 \\ \Omega_1/2 & (\Delta+\delta) & \Omega_2/2 \\ 0 & \Omega_2/2 & \delta \end{pmatrix} \tag{2.1}$$

The coupling strength between the states is determined by the time dependent Rabi frequencies $\Omega_1(t)$ and $\Omega_2(t)$, while the detuning from the intermediate state or from the two-photon resonance appears as the elements on the diagonal. The Rabi frequencies $\Omega_1(t)$ and $\Omega_2(t)$ are given by

$$\Omega_{1,2}(t) = \frac{\mathbf{d}_{1,2}\mathbf{E}_{1,2}(t)}{\hbar}, \tag{2.2}$$

where $\mathbf{E}_{1,2}(t)$ is the time dependent electric-field amplitude of the corresponding laser field ($= \mathbf{E}_{1,2}(t)\sin(\omega_{1,2}t)$). $\mathbf{d}_{1,2}$ is the corresponding transition dipole matrix element.
The evolving system can be described by the time dependent Schrödinger equation

$$i\hbar\frac{\mathrm{d}}{\mathrm{d}t}|\psi\rangle = H|\psi\rangle \tag{2.3}$$

where

$$|\psi(t)\rangle = \begin{pmatrix} a(t) \\ b(t) \\ g(t) \end{pmatrix} \tag{2.4}$$

is a vector of time dependent probability amplitudes $a(t), b(t), g(t)$. The absolute square

$$P_n(t) = |n(t)|^2 \tag{2.5}$$

provides the probability of finding the system at time t in state $|n\rangle$ ($n = a, b, g$), with $P(t) = |a(t)|^2 + |b(t)|^2 + |g(t)|^2 = 1$.
Losses from the intermediate state $|b\rangle$ to other states out of the system are treated simply by including an imaginary decay rate in the Hamilton matrix (2.1):

$$H = \hbar \begin{pmatrix} 0 & \Omega_1/2 & 0 \\ \Omega_1/2 & (\Delta+\delta) - i\gamma_b/2 & \Omega_2/2 \\ 0 & \Omega_2/2 & \delta \end{pmatrix} \tag{2.6}$$

The resulting Hamiltonian (2.6) is non-Hermitian. However, within the Schrödinger equation it provides correct results if the molecules do not decay from $|b\rangle$ into the states $|a\rangle$ and $|g\rangle$ but into states out of the system [BERGMANN *et al.* (1998)]. To a very good approximation this is the case in our experiments.
A more complete description, allowing decay into $|a\rangle$ and $|g\rangle$, requires a treatment based on the density-matrix formalism [SHORE (1990)].

Dark States

A very interesting property of the three level system coupled with a coherent radiation field is the existence of a dark state [ARIMONDO AND ORRIOLS (1976)]. This dark state $|\psi_{\mathrm{DS}}\rangle$ is an eigenstate ("Dressed State") of the three level system and fulfils

$$i\hbar\frac{\mathrm{d}}{\mathrm{d}t}|\psi_{\mathrm{DS}}\rangle = H|\psi_{\mathrm{DS}}\rangle = E|\psi_{\mathrm{DS}}\rangle. \tag{2.7}$$

When the two photon detuning is zero ($\delta = 0$), equation (2.7) has the following solution:

$$|\psi_{\mathrm{DS}}\rangle = \frac{1}{\sqrt{{\Omega_1}^2 + {\Omega_2}^2}}\left(\Omega_2|a\rangle - \Omega_1|g\rangle\right). \tag{2.8}$$

The dark state is a coherent superposition of state $|a\rangle$ and $|g\rangle$, which has no contribution of the "leaky" state $|b\rangle$ and so ideally does not decay. The presence of a detuning $\Delta \neq 0$ does not prevent a dark state. The stationary eigenvector (2.8) has a constant eigenenergy E which is independent of the Rabi frequencies and a detuning Δ (see Sec. 2.5).

Population transfer with STIRAP

STIRAP is a method to coherently transfer population between states without losses. During the transfer the population is kept always in a dark state, which is at all times free of any contribution from the leaky state $|b\rangle$ [BERGMANN *et al.* (1998)]. The procedure can be explained with formula (2.8):
Let's assume that the population is initially in state $|a\rangle$. The state $|a\rangle$ is in a dark state $|\psi_{\mathrm{DS}}(t)\rangle$ if the probability

$$P_{DS}(t=0) = \left|\langle a|\psi_{\mathrm{DS}}\rangle\right|^2 = 1. \tag{2.9}$$

To fulfil this condition, initially only laser 2 (Ω_2), which couples state $|g\rangle$ with state $|b\rangle$, has to be switched on. Subsequently we can transfer the population from $|a\rangle$ to $|g\rangle$ by adiabatically changing the Rabi frequencies $\Omega_1(t)$ and $\Omega_2(t)$ (see Fig. 2.2), keeping the population always in a dark superposition state. At the end of the process only laser 1 has to be on, so that the probability is unity to find all the molecules in state $|g\rangle$:

$$P_{DS}(t_{end}) = \left|\langle g|\psi_{\mathrm{DS}}\rangle\right|^2 = 1. \tag{2.10}$$

This scheme seems to be "counterintuitive" because initially there is no population in $|g\rangle$ or $|b\rangle$, and so laser 2 does not change the population. However this does not mean that laser 2 has no effect. In fact, this laser creates a coherent superposition of the two unpopulated states $|g\rangle$ and $|b\rangle$. This coherent superposition state is then coupled to the populated state $|a\rangle$ by ramping up laser 1. By adiabatically changing the Rabi frequencies the population is transferred from $|a\rangle$ to $|g\rangle$ without transfer population to the radiative decaying intermediate state $|b\rangle$. The criteria for the adiabaticity of the process are discussed in detail in Sec. 2.5.

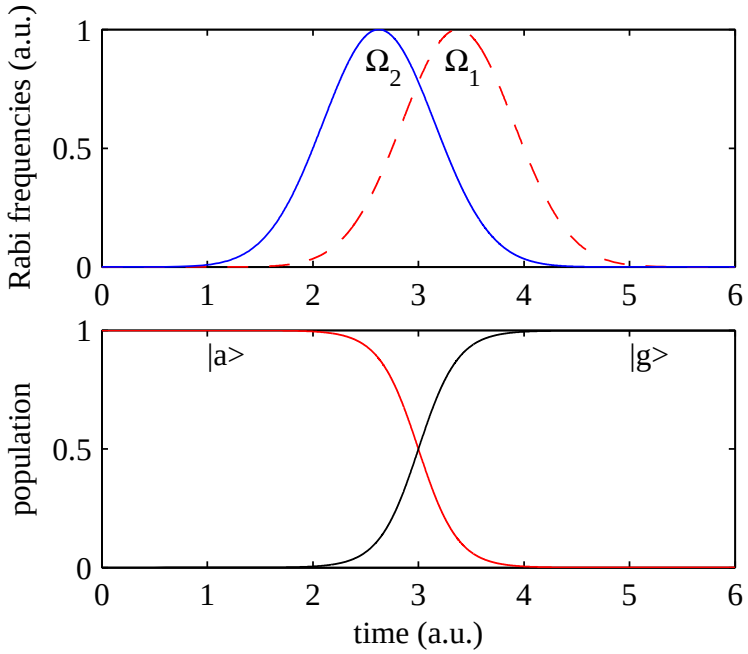

Figure 2.2:
(a) "Counterintuitive" pulse sequence. (b) Population transfer as a function of time. In the absence of losses a 100% population transfer is possible. The data are results from numerical calculations using the Schrödinger equation (2.7).

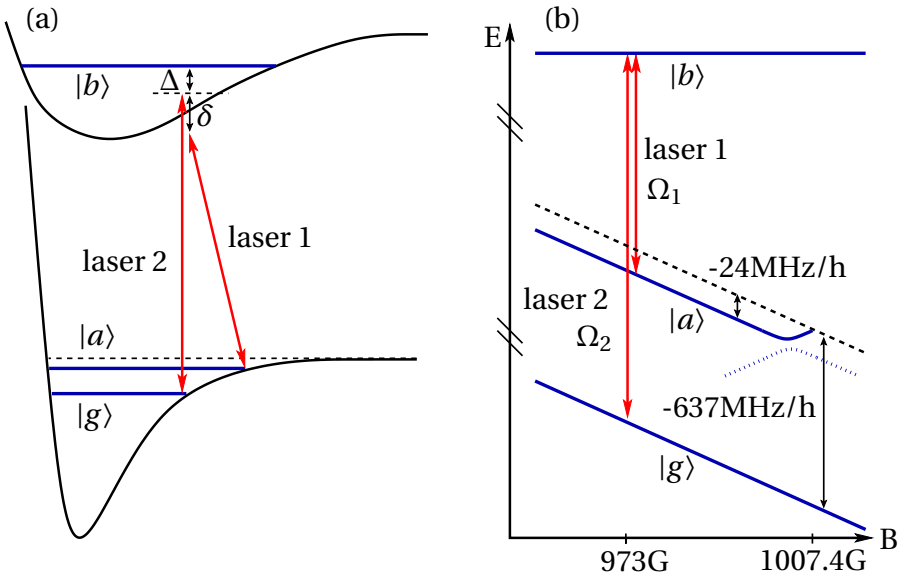

Figure 2.3:
(a) Level scheme for STIRAP. Lasers 1, 2 couple the ground state molecular levels $|a\rangle$, $|g\rangle$ to the excited level $|b\rangle$ with Rabi frequencies Ω_1 and Ω_2, respectively. Δ and δ denote detunings. (b) Zeeman diagram of relevant energy levels. At 1007.4 G a molecular state crosses the threshold of the unbound two atom continuum (dashed line) giving rise to a Feshbach resonance. From there this molecular state adiabatically connects to the last bound vibrational level $|a\rangle$, the state of the Feshbach molecules.

2.2 Experimental Setup

Preparation of an ultracold ensemble of Feshbach molecule

The starting point for our STIRAP experiments is a pure ensemble of typically $2-3\times10^4$ ultracold $^{87}Rb_2$ Feshbach molecules which are held in the lowest Bloch band of a cubic 3D optical lattice (for details see Sec. 1.4). There is no more than a single molecule per site and the whole molecular ensemble occupies a volume of about $20\times20\times20\,\mu m^3$. The lattice is $50\,E_r$ deep for molecules[1] ($E_r = 2\pi^2\hbar^2/m\lambda^2$, where m is the mass of the atoms and λ = 830.44 nm the wavelength of the lattice laser), suppressing tunneling between sites. The molecular ensemble is initially produced from an atomic ^{87}Rb Bose-Einstein condensate (BEC) after loading it into the lattice, subsequent Feshbach ramping at 1007.40 G [Volz *et al.* (2003)] and a final purification step which removes all chemically unbound atoms (see Sec. 1.4).

[1] The molecules experience twice the dipole potential compared to atoms.

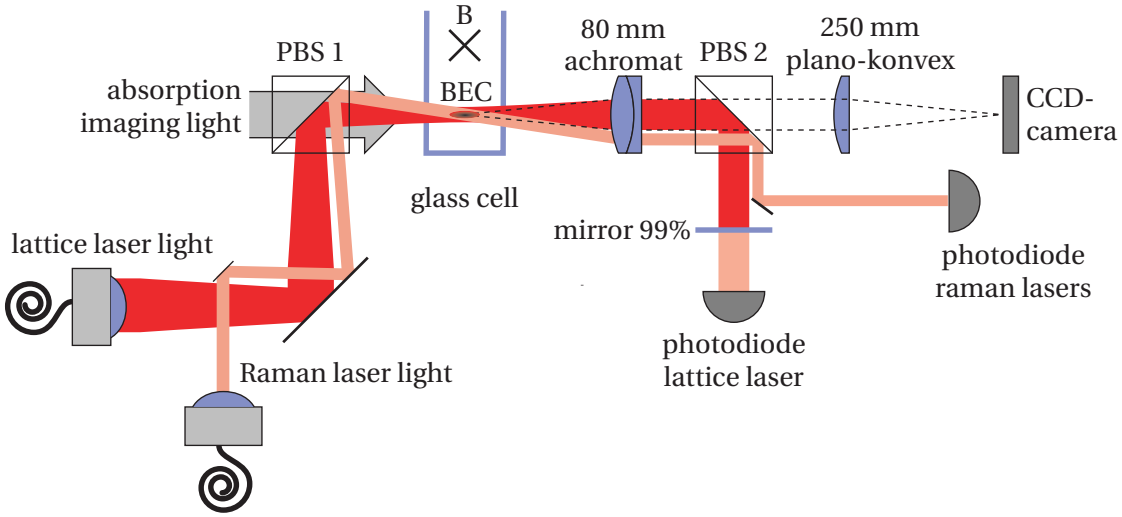

Figure 2.4:
Setup for the STIRAP experiments: we illuminate a cloud of ultracold molecules with Raman laser light pulses to coherently transfer them to a deeper molecular state. The molecules are held in a three dimensional lattice (plotted is only a lattice beam in one direction). The polarization of the Raman light is parallel to the magnetic field of 973 G.

Experimental three level system

In our experiment we transfer Feshbach molecules with a STIRAP pulse from their last bound vibrational level to the second to last bound vibrational level. We label for convenience the state of the Feshbach molecules $|a\rangle$ and the deeper molecular bound state $|g\rangle$. The excited molecular state is labeled with $|b\rangle$ (see Fig. 2.3). The Feshbach molecules in state $|a\rangle$ have a binding energy of $\sim 24\,\mathrm{MHz}\times h$ (below a magnetic field of about 1000 G), the second to last bound vibrational level $|g\rangle$ has a binding energy of $637\,\mathrm{MHz}\times h$ at 973 G. Both levels have a rotational quantum number $l = 0$ and a total spin $F = 2, m_F = 2$. The level $|g\rangle$ is known from previous experiments [WYNAR *et al.* (2000); ROM *et al.* (2004); THALHAMMER *et al.* (2005); WINKLER *et al.* (2005)].

Setup for the population transfer

In order to transfer the Feshbach molecules to the second to last bound vibrational level $|g\rangle$ we illuminate the molecules in the optical lattice with Raman laser light pulses (see Fig. 2.4).
To detect the more deeply bound molecules in $|g\rangle$, a second STIRAP pulse converts the molecules back to the last bound vibrational level $|a\rangle$, where they are detected as atoms after dissociation via Feshbach ramping (for details see Sec. 1.5).

Raman laser beam generation

The Raman laser beams used for the STIRAP process are both derived from a single Titanium Sapphire laser (model 899-01 from Coherent) with a short term line-width of less than 1 MHz. The Titanium Sapphire (Ti:Sa) laser is offset locked relative to the D_2-line of atomic rubidium with the help of a scanning optical cavity, which yields an absolute frequency stability of better than 5 MHz (for details of the locking scheme see [HELLWIG (2005)]). The frequency difference between the two beams is created with an acousto-optical modulator (AOM) with a frequency of about 307 MHz in a double-pass configuration (see Fig. 2.5). This allows precise control of the relative frequency difference between the beams over several tens of MHz and ensures phase-locking. By changing the RF-power used for the AOM we are able to control the relative intensity between the two laser beams. Both beams propagate collinearly and have a waist of about 290 µm at the location of the molecular ensemble. The polarization of the beams is parallel to the direction of the magnetic bias field (~ 1000 G).

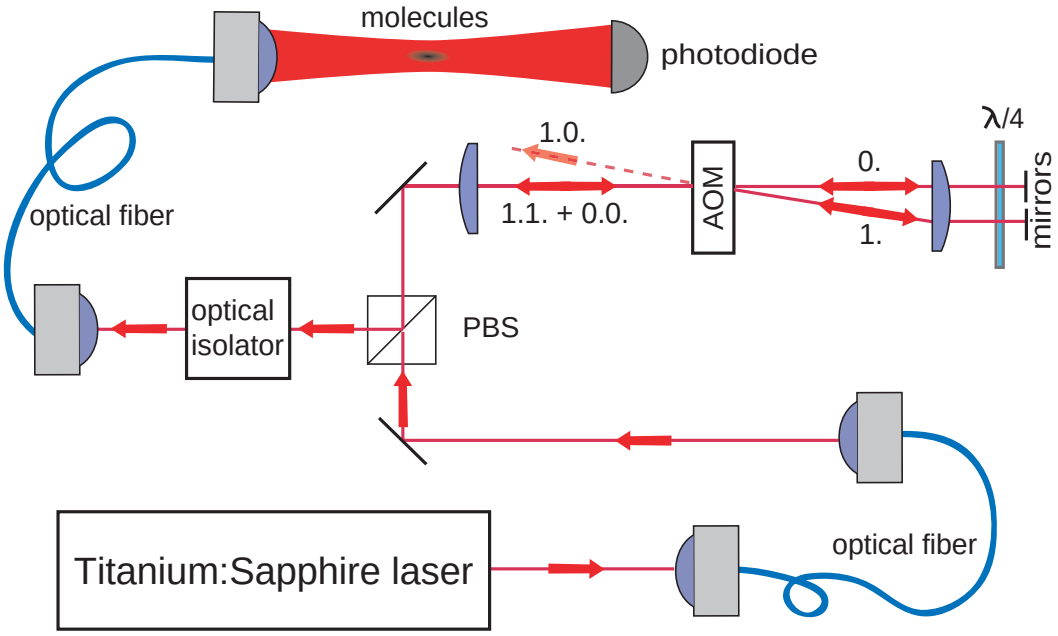

Figure 2.5:
Raman laser beam generation: The frequency difference between the two beams ($\Delta\nu \sim 614\,\mathrm{MHz}$) is created with an AOM with a frequency of about 307 MHz in a double-pass configuration. The zero (0.) and first (1.) diffraction order of the incoming laser beam, which is derived from a single Titanium Sapphire laser, are retro-reflected independently, after collimating them again with a second lens. The reflected first order beam gets diffracted again re-passing the AOM. The frequency of the resulting beam (1.1.) is changed by two times the AOM frequency. The beam (1.1.) is collinear with the zero order of the reflected zero order beam (0.0.). Passing two times the $\lambda/4$ plate, the polarization of the beams gets changed by $\pi/2$. This method allows us to spatially separate the two lasers beams (1.1. + 0.0.) from the incoming beam at the polarizing beam splitter (PBS) without losses. For a perfect spatial overlap of the two beams we couple them into the same optical fiber. By changing the RF-power used for the AOM we are able to control the relative intensity between the two laser beams. The maximum reachable power ratio between the (0.0.) and (1.1.) beam after the optical fiber is in the case of an optimal alignment about 1:1000. We measure the intensities of both beams with a photodiode.

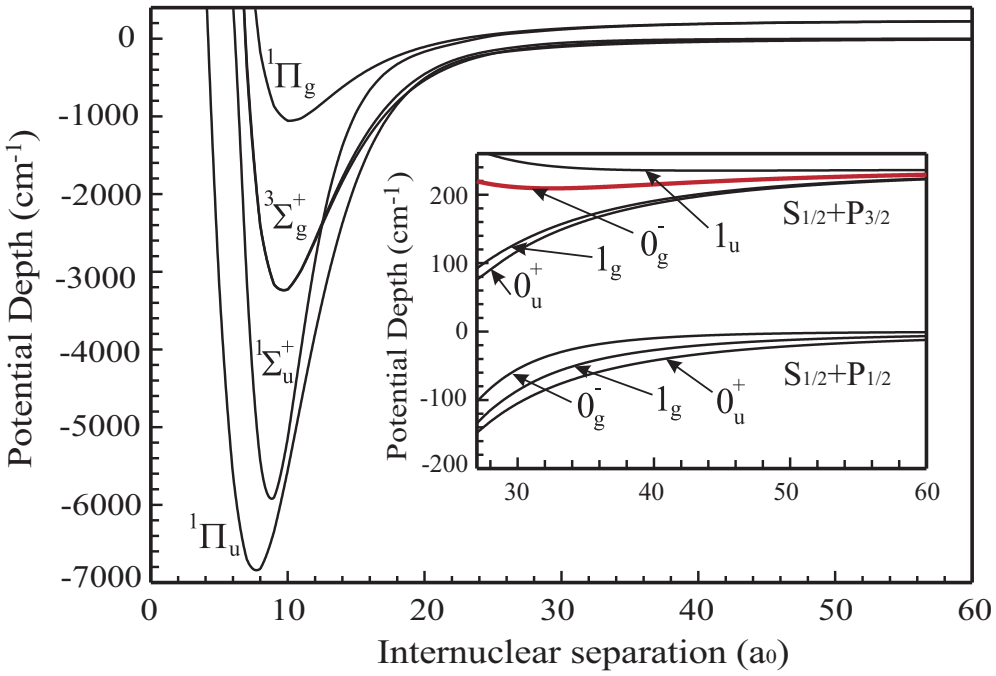

Figure 2.6:
The molecular excited state potentials of $^{87}Rb_2$ relevant to this experiment. The Hund's case (a) labels are shown at short range, the Hund's case (c) labels are shown for long range [JONES *et al.* (2006)]. For our experiments we use a level of the shallow upper 0_g^- long range potential (inset). Figure adapted from [WYNAR (2000)]

2.3 Finding the "right" excited state

In order to efficiently carry out STIRAP, a suitable excited molecular level, $|b\rangle$, has to be identified. Finding a "good" excited molecular level can be difficult because not only a strong coupling between the ground and excited state is needed, but also a level which has no other excited states in the direct vicinity. This is because coupling to other excited molecular states leads to a loss of the molecules, since these levels typically decay spontaneously into a variety of undetected vibrational levels in the ground state.
After testing several levels of the 0_g^- long range potential (see Fig. 2.6) for their suitability, we finally chose the electronically excited molecular state $|0_g^-, v = 31, J = 0\rangle$ located $6.87\,\mathrm{cm}^{-1}$ below the $S_{1/2}$+$P_{3/2}$ dissociation asymptote [FIORETTI *et al.* (2001)]. This line is strong and solitary, i.e. within a 2 GHz vicinity no other strong molecular lines are found which could interfere with STIRAP (see Fig. 2.7).
The coupling of an optical molecular transition crucially depends on the Franck-Condon factor[2], i.e. the square of the overlap between initial and final vibrational wavefunctions

[2]The dipole matrix element **d** for an optical molecular transition is given in a first approximation (and for an allowed transitions) by the value for the atomic transition times the square root of the Franck-Condon factor.

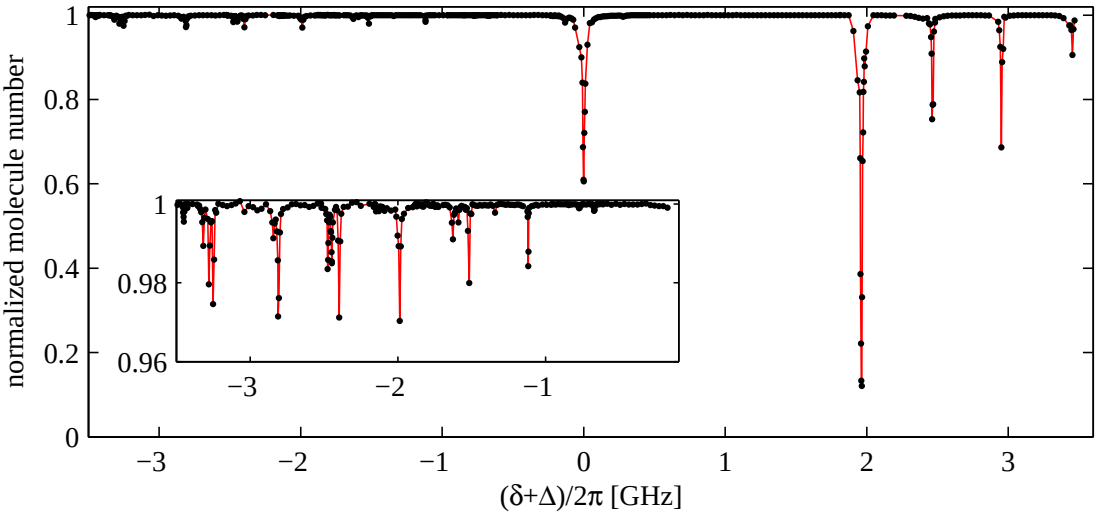

Figure 2.7:
One color spectrum as a function of the one photon detuning $(\delta+\Delta)$. The absorption line at $(\delta+\Delta)/2\pi = 0$ is the exited molecular state $|0_g^-, J=0, v=31\rangle$ which we are using for our experiments. A positive detuning $(\delta+\Delta>0)$ corresponds to a higher frequency ("blue" detuning) and a negative detuning $(\delta+\Delta<0)$ to a lower frequency ("red" detuning). The inset is a zoom on the weaker lines in the red.

[JONES *et al.* (2006)]. For STIRAP it is advantageous that the chosen level $|b\rangle$ has a similar Franck-Condon overlap with states $|a\rangle$ and $|g\rangle$. This can be understood as follows:
Let's assume that the Franck-Condon overlap $|g\rangle \rightarrow |b\rangle$ is by a factor of 100 smaller than $|a\rangle \rightarrow |b\rangle$. The power of laser 2 would have to be increased by a factor of 10000 to get the same Rabi frequencies Ω_1 and Ω_2, since the Rabi frequency scales with the root of the laser intensity. However, laser 2 also couples state $|a\rangle$ to the short-lived excited molecular state $|b\rangle$ with a detuning δ_1, with δ_1 the frequency difference of the two laser beams (see Fig. 2.8). This coupling leads to a loss of the molecules. The corresponding loss rate is given by

$$\gamma = \frac{\Omega_{\text{off}}^2 \cdot \gamma_b}{\gamma_b^2 + 4\delta_1^2}, \tag{2.11}$$

for $\Omega_{\text{off}} < \gamma_b$, with γ_b the decay rate of the excited state [METCALF AND VAN DER STRATEN (2002)]). Ω_{off} is given by $\Omega_{\text{off}} = \mathbf{d}_1 \cdot \mathbf{E}_2/\hbar$. In this numerical example Ω_{off} is 100 times larger than Ω_1 because $\mathbf{E}_2 = 100 \cdot \mathbf{E}_1$. Therefore, the loss rate γ is 10000 times stronger as in the case of equal Franck-Condon factors because $\gamma \propto \Omega_{\text{off}}^2$. For small frequency difference δ_1 of the two Raman lasers, as it is the case for our experiments ($\delta_1/2\pi \approx 614$ MHz), this loss channel cannot be neglected.
But also in the case of a larger frequency difference of the two Raman lasers this could be a limiting factor, because a coupling to other molecular states of the excited state potentials is possible (see Fig. 2.8). The state $|0_g^-, v=31, J=0\rangle$ was the best state we found to fulfill

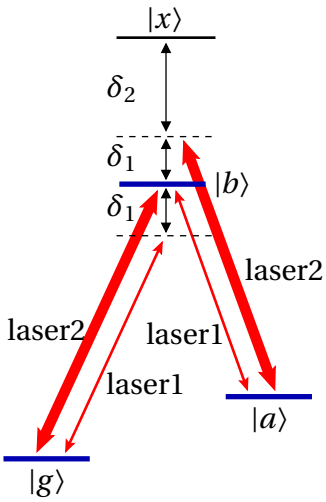

Figure 2.8:
Losses due to an assignment problem: laser 2 couples off-resonantly $|a\rangle \rightarrow |b\rangle$ and laser 1 $|g\rangle \rightarrow |b\rangle$. The detuning δ_1 is equal to the frequency difference of the two laser beams. Also a coupling to other excited molecular states has to be considered. Such a possible other excited state is labeled in this plot with $|x\rangle$. Laser 2 has a detuning δ_2 relative to this state.

all our requirements although ~ 2.0 GHz to the blue is another strong line and ~ 1 GHz to the red is the first of bundle of weak lines (see Fig. 2.7).

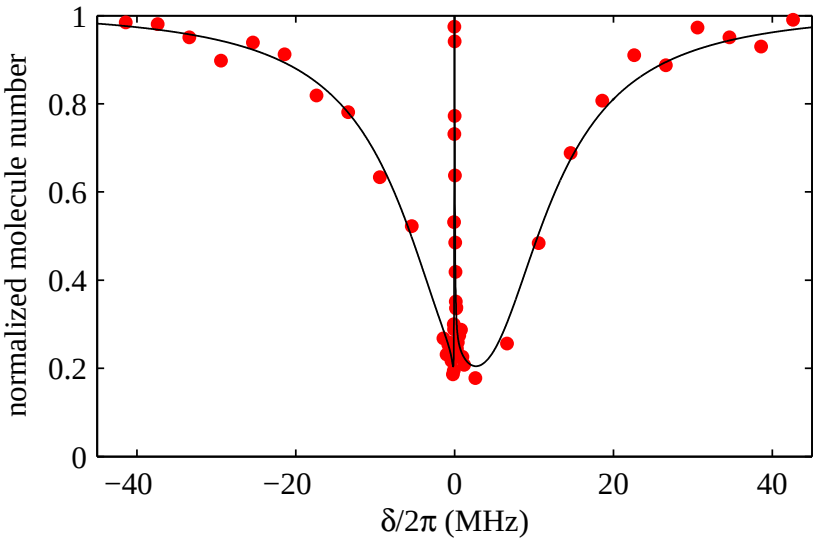

Figure 2.9:
Dark resonance. The data show the remaining fraction of Feshbach molecules in state $|a\rangle$, after subjecting them to a 200 µs square pulse of Raman laser light, as a function of the two-photon detuning δ. The strong suppression of loss at $\delta = 0$ is due to the appearance of a dark state. The laser intensities are $I_1 = 2.6\,\mathrm{mW/cm^2}$, $I_2 = 51\,\mathrm{mW/cm^2}$. The solid line is a fit curve with model (2.13).

2.4 Dark Resonances

With the choice of states $|a\rangle$, $|b\rangle$, $|g\rangle$, we observe a clear molecular dark resonance when coupling them with resonant Raman laser light (see Fig. 2.9). The data in Fig. 2.9 and Fig. 2.10 show the remaining fraction of Feshbach molecules in state $|a\rangle$, after subjecting them to a 200 µs square pulse of Raman laser light, as a function of the two-photon detuning δ. The strong suppression of loss at $\delta = 0$ is due to the appearance of a dark state. Δ is in general tuned close to zero and for the shown measurements happens to be $\Delta/2\pi \approx 2.5\,\mathrm{MHz}$, which gives rise to the slightly asymmetric line shape of the dark states (see Fig. 2.10). The corresponding molecular dark superposition states at $\delta = 0$ shows a long lifetime of several ms for typical intensities used in our measurements. This is a necessary precondition for our STIRAP experiments, because the molecules have to be kept in a dark state during the whole STIRAP process, which in our case typically takes hundreds of µs.

Extended three level model

We are able to understand the measured data by using an extended three level model in which we include, in contrast to Eq. (2.6), also decay of the molecular ground states $|a\rangle$

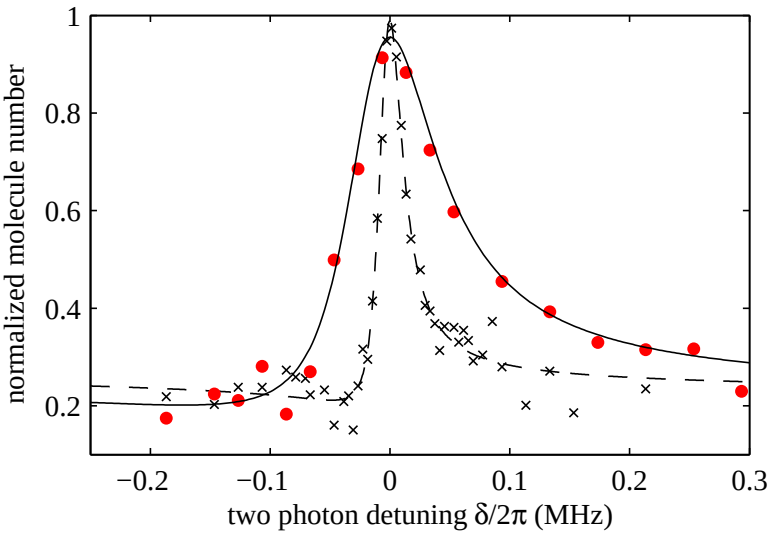

Figure 2.10:
Zoom on the dark resonance of figure 2.9 (red dots). For a direct comparison, the black crosses are measured with a different intensity $I_2 = 13\,\mathrm{mW/cm^2}$. The laser intensity $I_1 = 2.6\,\mathrm{mW/cm^2}$ is equal for both measurements. Δ is in general tuned close to zero and for the shown measurements happens to be $\Delta/2\pi \approx 2.5\,\mathrm{MHz}$, which gives rise to the slightly asymmetric line shape of the dark states. The solid line is a fit curve with model (2.13). For $\gamma_b \gg \Omega_2$ the width of the dark state is approximately given by Ω_2^2/γ_b, corresponding to power broadening [WINKLER *et al.* (2005)].

and $|g\rangle$:

$$H = \hbar \begin{pmatrix} -i\gamma_a/2 & \Omega_1/2 & 0 \\ \Omega_1/2 & (\Delta+\delta) - i\gamma_b/2 & \Omega_2/2 \\ 0 & \Omega_2/2 & \delta - i\gamma_g/2 \end{pmatrix} \tag{2.12}$$

The evolving system is described by the time dependent Schrödinger equation (2.3). We can then write the quantum mechanical probability amplitudes a, b, and g for a molecule in the respective states $|a\rangle$, $|b\rangle$ and $|g\rangle$ in terms of the following set of differential equations which we solve numerically with the program MATLAB:

$$\begin{aligned} i\dot{a} &= (-i\gamma_a/2)a - \tfrac{1}{2}\Omega_1 b, \\ i\dot{b} &= \left[(\Delta+\delta) - i\gamma_b/2\right] b - \tfrac{1}{2}(\Omega_1 a + \Omega_2 g), \\ i\dot{g} &= (\delta - i\gamma_g/2)g - \tfrac{1}{2}\Omega_2 b. \end{aligned} \tag{2.13}$$

Here, the Rabi frequencies Ω_1, Ω_2, the detunings Δ and δ are defined as shown in Fig. 2.3. $\gamma_b = 2\pi \cdot 12\,\mathrm{MHz}$ is the decay rate of the excited molecular state $|b\rangle$. The effective decay rates γ_a, γ_g are intensity dependent and are mainly due to the coupling of $|a\rangle$ with laser 2 and $|g\rangle$ with laser 1 (see Fig. 2.11). We determine γ_a (γ_g) by shining laser 2 (laser 1)

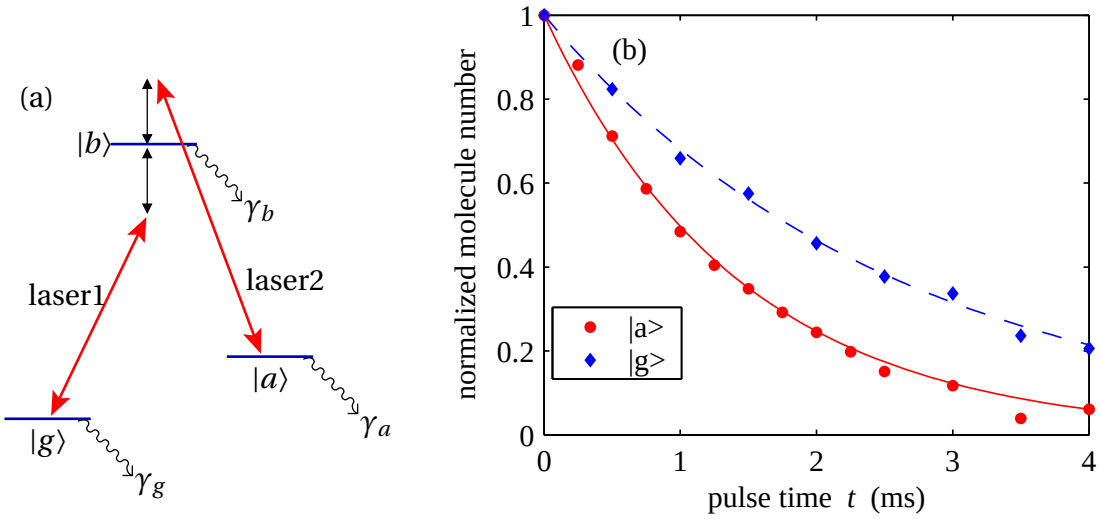

Figure 2.11:
(a) We determine the loss rates γ_a and γ_g, which are caused by an assignment problem (see Fig. 2.8), by shining laser 2 on the molecules in state $|a\rangle$ and laser 1 on the molecules in state $|g\rangle$, after preparation of the molecules in the respective states. The losses are treated in our model (2.13) as intensity dependent loss rates $\gamma_{a,g}$ of the molecular states $|a\rangle$ and $|g\rangle$ (see text). (b) Measured time dependent losses shining laser 2 on the molecules in state $|a\rangle$ (red dots) and laser 1 on the molecules in state $|g\rangle$ (blue diamonds). The intensity of the corresponding laser beam is for both measurements $I_{1,2} = 0.15\,\mathrm{W/cm^2}$. We fit the data with an exponential decay, $\exp(-t\cdot\gamma_{a,g})$, where $\gamma_{a,g}$ is intensity dependent ($\propto I_{2,1}$).

on the molecules in state $|a\rangle$ ($|g\rangle$) after preparation of the molecules in the respective states (see Sec. 2.5) and measuring the time dependent losses. We fit the data with an exponential decay, $\exp(-t\cdot\gamma_{a,g})$, where $\gamma_{a,g}$ is intensity dependent ($\propto I_{2,1}$). We find that $\gamma_a/I_2 = 2\pi\times 0.72\,\mathrm{kHz/(W\,cm^{-2})}$ and $\gamma_g/I_1 = 2\pi\times 0.40\,\mathrm{kHz/(W\,cm^{-2})}$. Fitting similar spectra as shown in Fig. 2.9, 2.10 we are able to obtain accurate values for the Rabi frequencies: $\Omega_1 = 2\pi\times 2.9\,\mathrm{MHz}(I_1/(\mathrm{W\,cm^{-2}}))^{1/2}$ and $\Omega_2 = 2\pi\times 6.0\,\mathrm{MHz}(I_2/(\mathrm{W\,cm^{-2}}))^{1/2}$. From these independent measurements, all parameters of Eqs. (2.13) are determined without further adjustable parameters.

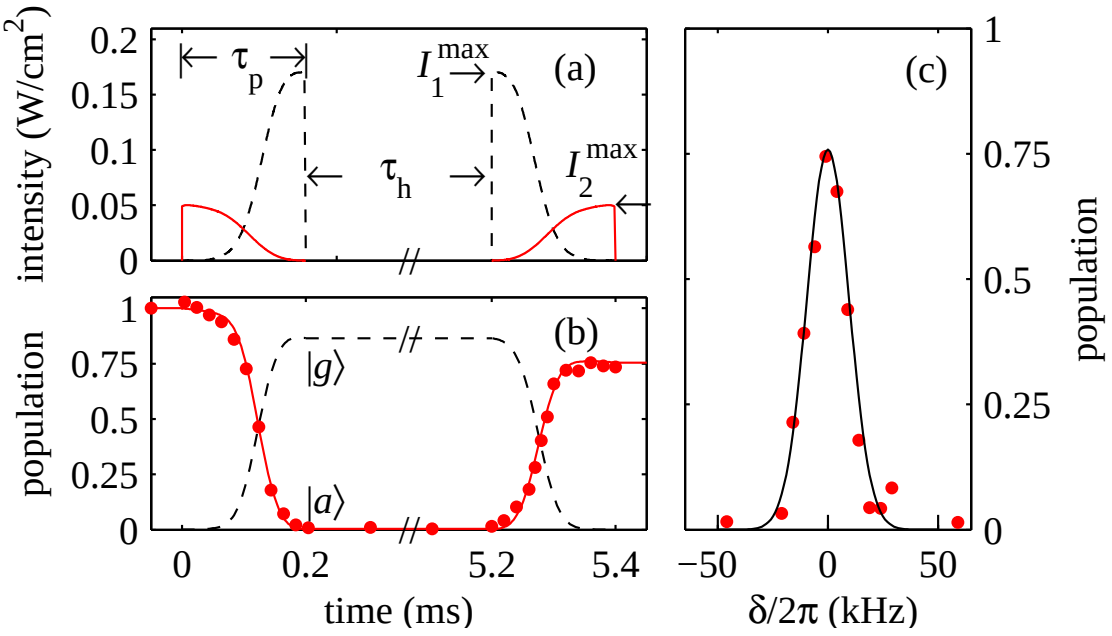

Figure 2.12:
STIRAP: (a) Counterintuitive pulse scheme. Shown are laser intensities as a function of time (laser 1: dashed line, laser 2: solid line). The first STIRAP pulse with length $\tau_p = 200\,\mu s$ transfers the molecule from state $|a\rangle$ to state $|g\rangle$. After a holding time $\tau_h = 5\,ms$, the second pulse (identical, but reversed) transfers the molecules back to $|a\rangle$. $I_{1,2}^{max}$ indicates the maximal intensity of laser 1 (2) in the pulse, respectively. (b) Corresponding population in state $|a\rangle$ (data points, solid line) and state $|g\rangle$ (dashed line). The data points are measurements where at a given point in time the STIRAP lasers are abruptly switched off and the molecule population in state $|a\rangle$ is determined. For these measurements $\Delta \approx 0 \approx \delta$. The lines are model calculations (see text). (c) Efficiency for population transfer from state $|a\rangle$ to state $|g\rangle$ and back via STIRAP as a function of the two photon detuning δ. The line is a model calculation, showing a Gaussian line shape with a FWHM width of $\approx 22\,kHz$.

2.5 Population transfer with STIRAP

In order to transfer the molecules from state $|a\rangle$ to state $|g\rangle$, we carry out a STIRAP pulse which consists of a succession of two phase locked laser pulses (see Fig. 2.12 (a)). We first switch on laser 2 and then ramp its intensity to zero within the pulse time $\tau_p = 200\,\mu s$. Simultaneously we ramp up the intensity of laser 1 from zero to its final value. We fix the ratio of the maximal pulse intensities of laser 1 and 2 to $I_2^{max}/I_1^{max} = 1/3.2$ in order to partially compensate for the unequal Franck-Condon factor of the $|a\rangle \rightarrow |b\rangle$ and $|g\rangle \rightarrow |b\rangle$ transitions. Ideally, after the first STIRAP pulse all molecules from state $|a\rangle$ should end up in state $|g\rangle$. In order to determine the population in state $|g\rangle$, we apply, after a holding time of $\tau_h = 5\,ms$, a second STIRAP pulse which is the mirror image in time of pulse 1. This

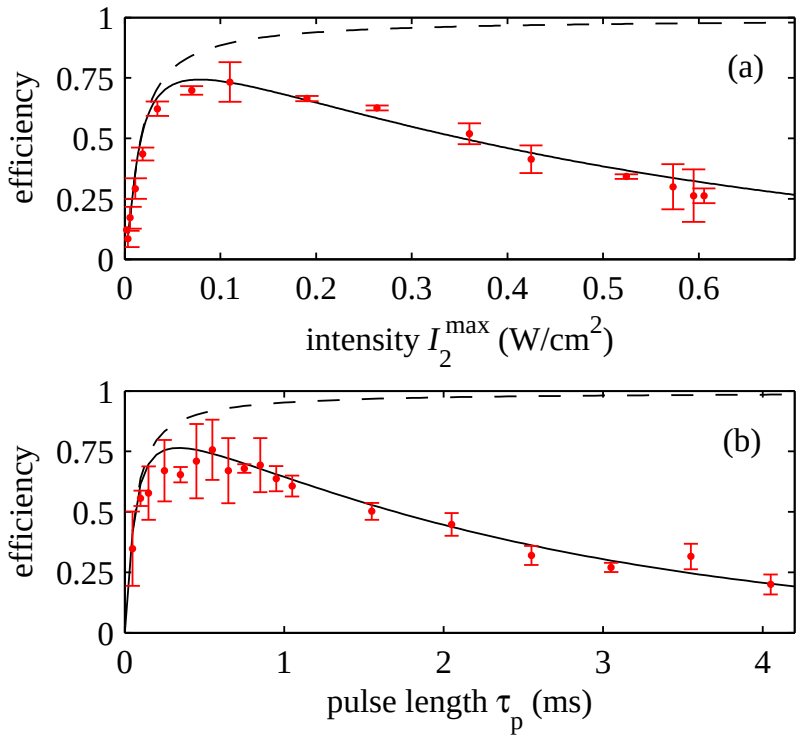

Figure 2.13:
Efficiency for population transfer from state $|a\rangle$ to state $|g\rangle$ and back with two STIRAP pulses. (a) Efficiency versus the laser intensity I_2^{max} (fixed pulse length of $\tau_p = 200\,\mu s$). (b) Efficiency versus the pulse length τ_p (fixed laser intensity $I_2^{max} = 44\,mW/cm^2$). For (a) and (b) the intensity ratio $I_2^{max}/I_1^{max} = 1/3.2$. The lines are from calculations without free parameters using Eqs. 2.13. Setting $\gamma_a = \gamma_g = 0$, the efficiency would reach unity for a fully adiabatic transfer (dashed lines). Using for γ_a, γ_g the experimentally determined values, the calculations (solid lines) are in good agreement with the data.

transfers the molecules back into state $|a\rangle$. We then ramp the magnetic field over the Feshbach resonance at 1007.4 G which dissociates the molecules with unit efficiency [THALHAMMER *et al.* (2006)] into pairs of atoms. These are subsequently detected with standard absorption imaging. Figure 2.12 (b) shows in a time resolved way how molecules in state $|a\rangle$ first disappear and then reappear during the course of the STIRAP sequence. After applying the first STIRAP pulse, no molecules can be observed in state $|a\rangle$. This is to be expected, since any molecule which is left over in state $|a\rangle$ at the end of the first STIRAP pulse is in a bright state and will be quickly removed by resonantly scattering photons from laser 1. This confirms, that after completion of the second STIRAP pulse we only detect molecules that were previously in state $|g\rangle$. We observe an efficiency of 75% for the full cycle of conversion into state $|g\rangle$ and back. Figure 2.12 (c) shows how this efficiency depends critically on the two photon detuning δ. The lines in Fig. 2.12 (b) and (c) are

model calculations without free parameter (see Eq. (2.13)). In the calculations the time dependent pulse shapes (see Fig. 2.12(a)) are included.
In Figure 2.13 we investigate further the complete STIRAP cycle efficiency as a function of the laser intensity and pulse length. In these measurements we use pulses with the same shape as in Fig. 2.12(a), which are re-scaled to adjust pulse time τ_{p} and laser intensity. Again, for the best settings we reach an efficiency of about 75% for the two pulses, which corresponds to a transfer efficiency to state $|g\rangle$ of about 87%. The dependence of the efficiency on intensity and pulse length can be qualitatively understood as follows. For short pulse lengths or low intensities, the dark state cannot adiabatically follow the STIRAP pulse, resulting in a low transfer efficiency. For very long pulse lengths and high intensities the losses due to an imperfect dark state become dominant, also resulting in a low transfer efficiency. Thus in order to find an optimum value for the transfer efficiency there is a trade-off between adiabaticity and inelastic photon scattering. The agreement between theory and experiment is very good as we are able to consistently describe all data in Figs. 2.9, 2.12 and 2.13 with a single set of parameters.

Adiabaticity of STIRAP

An insufficient coupling by the coherent radiation fields may prevent the state vector $|\psi\rangle$ from adiabatically following the evolution of the dark state $|\psi_{\mathrm{DS}}\rangle$, and loss of population due to non-adiabatic transfer to the bright states $|\psi_+\rangle$ and $|\psi_-\rangle$ may occur [Bergmann *et al.* (1998)]. $|\psi_\pm\rangle$ are the two other "eigenstates" of our three level system, which are linear combinations of the three bare states $|a\rangle$, $|b\rangle$ and $|g\rangle$:

$$\begin{aligned} |\psi_+\rangle &= \sin\Theta\sin\Phi|a\rangle + \cos\Phi|b\rangle + \cos\Theta\sin\Phi|g\rangle, \\ |\psi_-\rangle &= \sin\Theta\cos\Phi|a\rangle - \sin\Phi|b\rangle + \cos\Theta\cos\Phi|g\rangle. \end{aligned} \tag{2.14}$$

The dark state has in this notation the form

$$|\psi_{DS}\rangle = \cos\Theta|a\rangle - \sin\Theta|g\rangle. \tag{2.15}$$

The angles Θ and Φ are defined as

$$\tan\Theta = \frac{\Omega_1}{\Omega_2}, \tag{2.16}$$

$$\tan 2\Phi = \frac{2\cdot\Omega_{eff}}{\Delta}, \tag{2.17}$$

with $\Omega_{1,2}(t)$ the time dependent Rabi frequencies, Δ the one photon detuning and $\Omega_{eff} = \sqrt{\Omega_1^2+\Omega_2^2}$ the effective Rabi frequency. The Hamiltonian matrix element for non-adiabatic transfer between state $|\psi_{\mathrm{DS}}\rangle$, which carries the population and evolves in time, and either one of the states $|\psi_+\rangle$ or $|\psi_-\rangle$ is given by $\alpha = \langle\psi_\pm|\dot{\psi}_{\mathrm{DS}}\rangle$ [Messiah (1990)]. α characterizes the rotational speed of the eigenaxes of the corresponding Hamiltonian (2.1). Non adiabatic coupling is small if

$$\left|\frac{\alpha}{\omega}\right|^2 \ll 1, \tag{2.18}$$

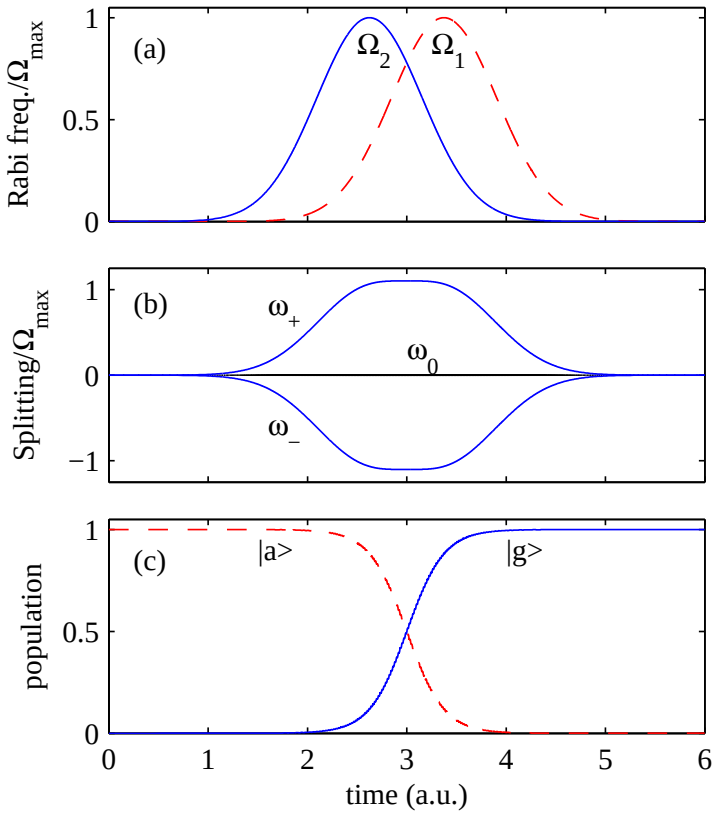

Figure 2.14:
STIRAP. (a) Gaussian pulse shapes $\Omega_{2,1}(t) = \Omega_{\max}\exp(-(t \pm t_0)^2/d^2)$ with d the pulse width and $2 \cdot t_0$ the time delay between the two pulses. (b) Splitting of the eigenvalues: For Gaussian pulse shapes the optimum time delay is equal to the pulse width, $2t_0 = d$. In this case the splitting ω of the eigenstates is optimized to fulfil the adiabatic criterion (2.19). (c) The population in the starting level $|a\rangle$ and final level $|g\rangle$.

where $\omega = |\omega_\pm - \omega_{\mathrm{DS}}|$ is the "Bohr frequency" of the transition $|\psi_{\mathrm{DS}}\rangle \rightarrow |\psi_\pm\rangle$ [MESSIAH (1990)]. $\omega_\pm = \Delta \pm \sqrt{\Delta^2 + \Omega_1^2 + \Omega_2^2}$ and ω_{DS} are the dressed state eigenvalues of the three level system (2.1). ω_{DS} is constant (normally set to zero) for all times and is independent of the Rabi frequencies Ω_1 and Ω_2 (see Fig. 2.14 (b)). For a $\Delta = 0$ the separation of the corresponding eigenvalues ω is given by the effective Rabi frequency Ω_{eff}. α can be calculated from Eqs. (2.14) and (2.15), resulting in $\alpha = -\dot{\Theta}\sin\Phi$. Setting $\sin\Phi = 1$ and using Eq. (2.16) the condition (2.18) can be written in the form [BERGMANN *et al.* (1998)]

$$\left|\frac{\dot{\Omega}_1\Omega_2 - \Omega_1\dot{\Omega}_2}{\Omega_1^2 + \Omega_2^2}\right| \ll |\omega|. \tag{2.19}$$

When the laser pulses have a smooth shape, a convenient "global" adiabaticity criterion may be derived from (2.19) by taking a time average of the left-hand side. This procedure

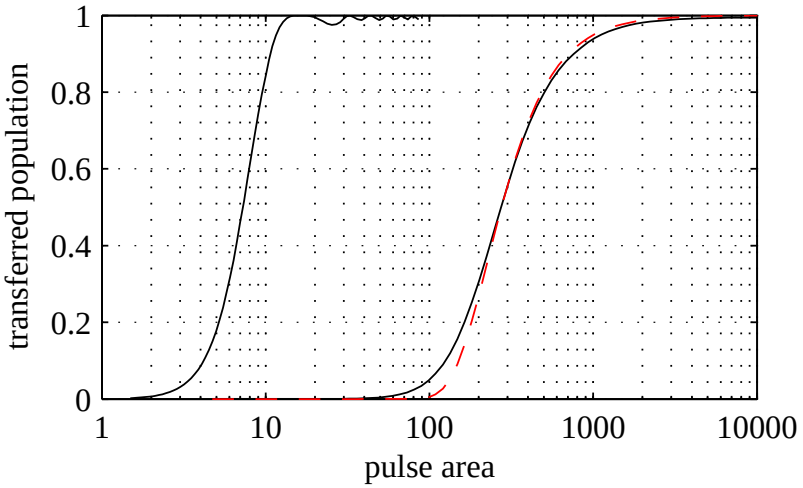

Figure 2.15:
Calculated population transfer efficiency for $\Delta = 0$ as a function of the pulse area $\widetilde{\Omega}_{\text{eff}} \cdot \tau_p$. The STIRAP pulse length τ_p is 100 µs, a typical value used in our experiments. For a $\gamma_b = 2\pi \times 12$ MHz one has to increase the mean effective Rabi frequency $\widetilde{\Omega}_{\text{eff}}$ by a factor of about 100 slower for being adiabatic (solid curve on the right) compared to the case where $\gamma_b = 0$ (solid curve on the left). The solid lines are calculated from numerical simulations using model (2.6). The red dashed line is a calculation with formula (2.21).

leads to the condition [BERGMANN *et al.* (1998)]

$$\widetilde{\Omega}_{\text{eff}} \cdot \tau_p > 10, \tag{2.20}$$

where $\widetilde{\Omega}_{\text{eff}} \cdot \tau_p = \int_0^{\tau_p} dt \sqrt{\Omega_1(t)^2 + \Omega_2(t)^2}$ is the STIRAP pulse area, with τ_p is the pulse time. The numerical value of 10 is obtained from numerical simulations (see Fig. 2.15) assuming Gaussian pulse shapes $\Omega_{1,2}(t) = \Omega_{\max 1,2} \cdot \exp(-(t \mp t_0)^2/d^2)$ with d the pulse width and $2t_0$ the time delay between the two pulses. For Gaussian pulse shapes the optimum time delay is equal to the pulse width, $2t_0 = d$. In this case the splitting ω of the eigenstates is optimal (see Fig. 2.14).
However, Eq. (2.20) is only valid for $\widetilde{\Omega}_{\text{eff}} \gg \gamma_b$, where γ_b is the decay rate of the excited state $|b\rangle$. In the adiabatic limit state $|b\rangle$ never gets populated and its decay is irrelevant. However, if the decay rate becomes sufficiently large compared to the splitting of the eigenstates adiabaticity breaks down and the transfer efficiency of STIRAP decreases. Hence, the transfer has to be much slower for being adiabatic. This is the case for our experiments where Ω_{eff} is typically smaller than γ_b. Numerical simulations with the extended Hamiltonian matrix (2.6), which includes the decay rate γ_b of the excited state, show for the case $\widetilde{\Omega}_{\text{eff}} < \gamma_b$ that we have to be slower by a factor of about 100 to be adiabatic compared to the case where $\gamma_b = 0$ (see Fig. 2.15). In the limit of $\widetilde{\Omega}^2_{\text{eff}} \cdot \tau_p \gg \gamma_b$ an

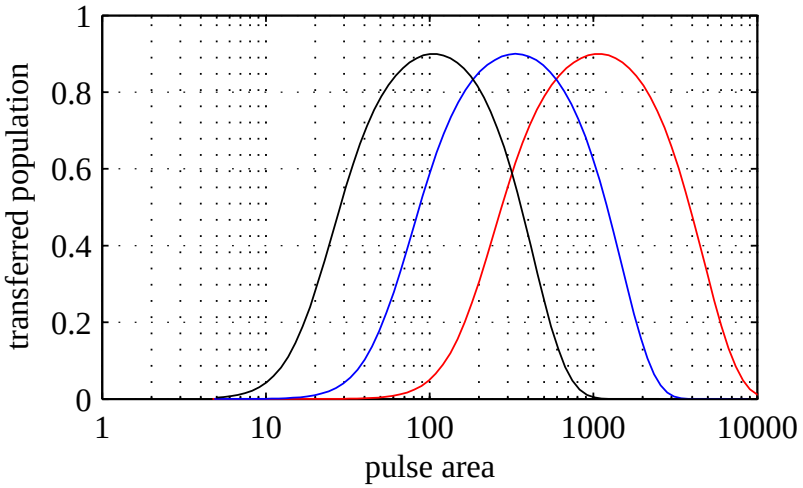

Figure 2.16:
Calculated population transfer efficiency as a function of the STIRAP pulse area $\widetilde{\Omega}_{\text{eff}} \cdot \tau_p$. In contrast to Fig. 2.15, intensity dependent loss ($\gamma_{a,b} \propto I_{2,1}$) is included. The population transfer efficiency is calculated for various STIRAP pulse lengths τ_p: 1 µs (left), 10 µs (middle), and 100 µs (right). Δ is set to zero. The maximum reachable population transfer remains constant. For this calculation we included the measured intensity dependent loss rates $\gamma_{a,g}$ (see Sec. 2.4).

approximate analytic solution is given by [VITANOV AND STENHOLM (1997)]:

$$P_g(t_{end}) = \exp(-\frac{\pi^2}{\sqrt{2}} \frac{\gamma_b}{\widetilde{\Omega}^2_{\text{eff}} \cdot \tau_p}), \tag{2.21}$$

where $P_g(t_{end})$ is the transferred population after the STIRAP pulse sequence. One could now assume that the best strategy to reach high transfer efficiencies is to use Rabi frequencies larger than γ_b. This would increase the splitting of the eigenvalues and one could again reduce the pulse area (see Fig. 2.14 (b)). However, additionally to the decay rate of the excited state, also losses due to spontaneous light scattering play a role for the "real" STIRAP, as pointed out already in Sec. 2.4. Hence, the gain in adiabaticity by using larger Rabi frequencies is compensated by a higher loss due to the light scattering, as shown in Fig. 2.16, since the loss rates $\gamma_{a,g}$ scale with the intensity of the laser beams (see e.g. Eq. (2.13)). Therefore, we find that the maximum reachable population transfer remains constant.
A detuning $\Delta \neq 0$ does not prevent STIRAP, but causes a weaker splitting ω of the eigenvalues. Thus, the population transfer efficiency decreases for an increasing one photon detuning Δ at a constant Rabi frequency and pulse length. In Fig. 2.17 we simulate this situation for Gaussian pulses shapes with a maximum Rabi frequency $\Omega_{\text{max}1,2} = 2\pi \times 1\,\text{MHz}$, a pulse length τ_p of 100 µs (pulse area $\widetilde{\Omega}_{eff} \cdot \tau_p \approx 500$) and without off resonant losses. For a $\Delta \gg \Omega_{\text{max}1,2}$ the population transfer efficiency decreases $\propto 1/\Delta^2$. Therefore, normally the best choice is a detuning Δ of zero, as it was the case for our STIRAP experiments.

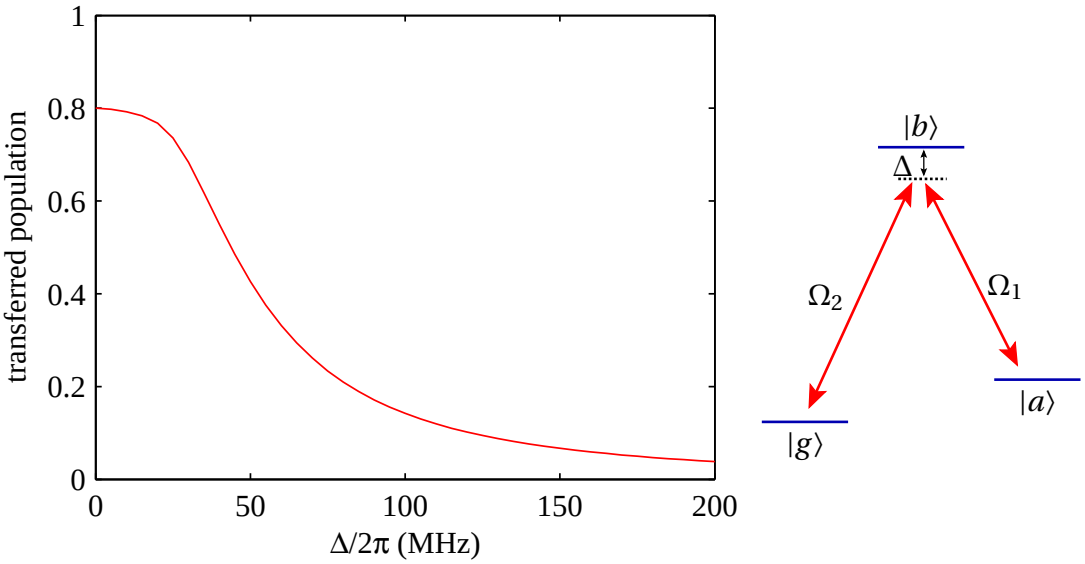

Figure 2.17:
Transferred population as a function of the detuning Δ, calculated for Gaussian pulses shapes with a maximum Rabi frequency $\Omega_{\max 1,2} = 2\pi \times 1\,\mathrm{MHz}$ and a pulse length τ_p of 100 µs. The decay rate γ_b of the excited state is $\gamma_b = 2\pi \times 12\,\mathrm{MHz}$. The decay rates $\gamma_{a,g}$ are set to zero for this simulation. The pulse area $\tilde{\Omega}_{\mathrm{eff}} \cdot \tau_p \approx 500$, which leads to a 80% population transfer efficiency for $\Delta = 0$ (see also Fig. 2.15). The values for $\Omega_{\max 1,2}$ and τ_p are comparable with the ones used in our STIRAP experiments.

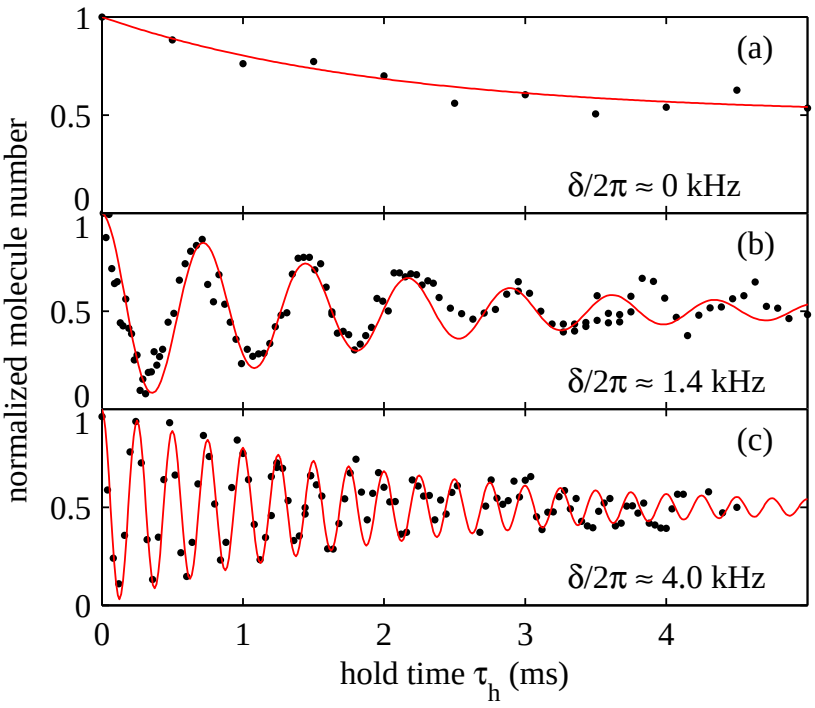

Figure 2.18:
Coherence of the $(|a\rangle - |g\rangle)$ superposition state. Shown is the molecule number in state $|a\rangle$ as a function of holding time τ_h for different detunings δ as indicated. The oscillations indicate coherent flopping of the molecular superposition state between the dark and a bright state. The lines are given by $1/2 \times (\exp(-\tau_h/\tau)\cos(\delta \cdot \tau_h) + 1)$, with a damping time $\tau = 2\,\text{ms}$.

2.6 Testing the Coherence

During STIRAP the molecules are in a quantum superposition, $\Omega_2|a\rangle - \Omega_1|g\rangle$, which is dynamically evolving with the intensities of the lasers. In order to probe the coherence of this superposition, we perform a Ramsey-type experiment. First, we create a dark superposition state with equal population in the two states,

$$\psi \approx \frac{1}{\sqrt{2}}(|a\rangle - |g\rangle), \tag{2.22}$$

by going halfway into the first STIRAP pulse of Fig. 2.12 (a)[3]. We then simultaneously switch off both STIRAP lasers for a variable holding time τ_h. After the hold time we switch the lasers on again and retrace in time the same STIRAP half pulse. As a result we observe oscillations in the number of molecules in level $|a\rangle$ as a function of the holding time τ_h

[3] (2.22) is valid even for a two-photon detuning $\delta \neq 0$ simply because the fraction which is not in the dark state decays. However, δ has to be small compared to the width of the dark resonance so that the losses are negligible.

(see Fig. 2.18). The interference signal is calculated in a straightforward manner [WEITZ *et al.* (1994)]: During the holding time, the superposition state ψ freely evolves:

$$\psi_{\tau_\mathrm{h}} = e^{-iH/\hbar\tau_\mathrm{h}}\psi = (|a\rangle - e^{i\delta\tau_\mathrm{h}}|g\rangle)/\sqrt{2}. \tag{2.23}$$

H is the Hamiltonian matrix in the rotating frame ("dressed state picture") without light interaction ($\Omega_1 = \Omega_2 = 0$) and is given by

$$H = \hbar\begin{pmatrix} 0 & 0 & 0 \\ 0 & \Delta+\delta & 0 \\ 0 & 0 & \delta \end{pmatrix}, \tag{2.24}$$

with $\delta = (E_a - E_g)/\hbar - (\omega_2 - \omega_1)$ the two photon detuning. Calculate the probability to find ψ_{τ_h} in a dark state after the hold time τ_h, we find that for a $\delta \neq 0$, ψ_{τ_h} is coherently flopping between the dark and a bright state with a frequency equal to the two-photon detuning δ:

$$\langle\psi_{\tau_\mathrm{h}}|\psi_\mathrm{DS}\rangle = \frac{1}{2}(\langle a| - e^{i\delta\tau_\mathrm{h}}\langle g|)(|a\rangle - |g\rangle) = \frac{1}{2}(1 + e^{i\delta\tau_\mathrm{h}}). \tag{2.25}$$

At the end of the hold time, when we switch on again the STIRAP lasers, the dark state is subsequently transferred back to state $|a\rangle$ whereas the bright state will be immediately destroyed by the light and leads to complete loss of the corresponding molecules. The measured molecule number in $|a\rangle$ after the second STIRAP pulse is the absolute square of (2.25):

$$|\langle\psi_{\tau_\mathrm{h}}|\psi_\mathrm{DS}\rangle|^2 = \frac{1}{2}(1 + e^{i\delta\tau_\mathrm{h}}) \times \frac{1}{2}(1 + e^{-i\delta\tau_\mathrm{h}}) = 1/2 \times (1 + \cos(\delta\tau_\mathrm{h})). \tag{2.26}$$

With a two photon detuning $\delta = 0$ (Fig. 2.18 (a)) we observe no oscillations because the phase of ψ_{τ_h} evolves equal to phase of the light field and the superposition state is always in a dark state. However, we observe for all the different detunings δ in Fig. 2.18 a damping on a time scale of about 2 ms. This damping can be explained due to a dephasing which is caused by a magnetic field inhomogeneity of about 20 mG over the molecular cloud. This inhomogeneity leads to a spatial variation of $2\pi \times 250$ Hz in the two-photon detuning δ. Therefore, the molecules in different lattice sites "see" a different two photon detuning δ and so each molecule is flopping differently between dark and bright state (see Eq. (2.26)). The observed population in the dark state is then an average of single oscillations, as indicated in Fig. 2.19.

Additionally we observe a slight shift of the oscillation frequency with time on the order of $2\pi \times 50$ Hz/ms. This can be attributed to a small drift of the magnetic field (~ 5 mG/ms) during the measurements. We suspect a power line problem of our power supplies, which leads to an oscillatory noise on the magnetic field, to be the origin of this drift. An independent measurement of this magnetic field noise (see [THALHAMMER (2007)]) agrees with the drift observed in these coherence measurements.

The black line shown in Fig. 2.19 is an average of 20000 calculated oscillations, each with a different detuning δ. The different detunings are chosen from a normal distribution with mean $\tilde{\delta}$ and a standard deviation of $\sigma = 100$ Hz. The mean value $\tilde{\delta}$ includes the time dependent frequency shift and is $\tilde{\delta}/2\pi = (1.48 - 0.05/\mathrm{ms} \times \tau_\mathrm{h})$ kHz. The red data points in Fig. 2.19 are the same as used in Fig. 2.18 (b).

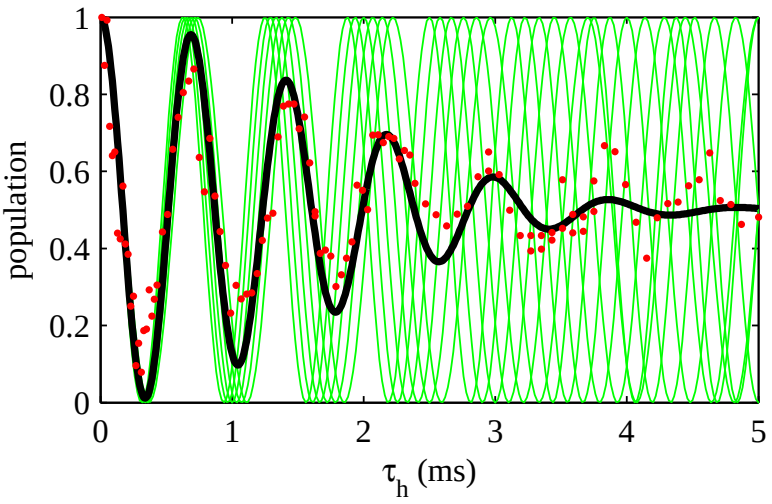

Figure 2.19:
Population in the dark state as function of time: A magnetic field inhomogeneity of ~ 20 mG over the molecule cloud leads to different two photon detunings δ (indicated with the green lines) for different lattice sites causing a "damping" due to dephasing. The black line is an average of 20000 oscillations, each with a different detuning δ. The different detunings are chosen from a normal distribution with mean $\tilde{\delta}$ and a standard deviation of $\sigma = 100$ Hz. The mean value $\tilde{\delta}$ includes the frequency shift and is $\tilde{\delta}/2\pi = (1.48 - 0.05/\text{ms} \times \tau_h)$ kHz. The red data points in Fig. 2.19 are the same as used in Fig. 2.18 (b).

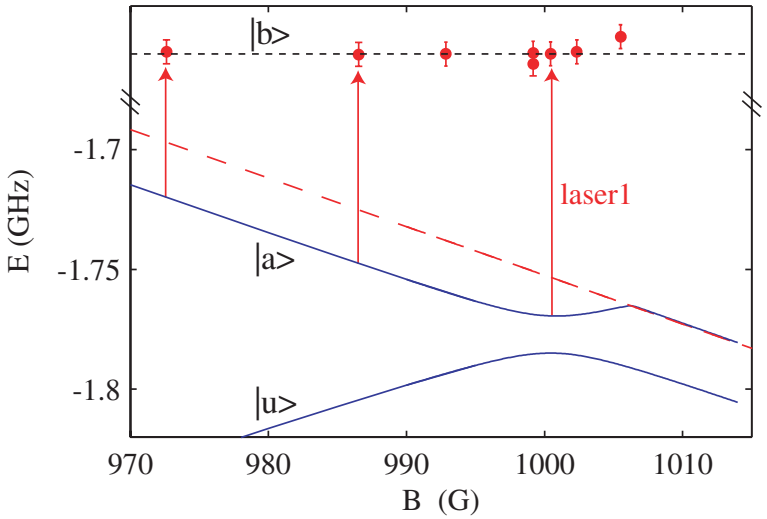

Figure 2.20:
Zeeman shift of the excited molecular state $|b\rangle$: We determine the data points by measuring the resonance frequency of the one photon transition $|a\rangle \rightarrow |b\rangle$ for different magnetic fields and afterwards subtracting the Zeeman shift of the molecular state $|a\rangle$ (upper blue line) from the measured resonance frequencies. The resulting data-points are constant with the magnetic field. This means that the shift of the resonance frequency can be mainly attributed to the Zeeman shift of the molecular state $|a\rangle$. Consequently the excited state $|b\rangle$ does not shift with the magnetic field (within the error bars). The dashed red line corresponds to the energy of the dissociation threshold. The lower blue line corresponds to a state $|u\rangle$ with the quantum numbers (F=2,F=2),v=-5,l=0,$m_F = 2$ assigned at zero magnetic field [MARTE *et al.* (2002)].

2.7 Additional measurements

2.7.1 Zeeman shift of the excited molecular state

We measure the magnetic field dependence of the resonance frequency of one photon transition $|a\rangle \rightarrow |b\rangle$ to determine the Zeeman shift of the excited molecular state $|b\rangle$. This measurement provides an additional hint that $|b\rangle$ is a state of the $|0_g^-\rangle$ potential. The data-points shown in Fig. 2.20 are determined as follows:
We measure the resonance frequency of one photon transition for different magnetic fields. Afterwards we subtract the Zeeman shift of the molecular state $|a\rangle$ from the measured resonance frequencies. The resulting data are constant with the magnetic field, as one can see in Fig. 2.20. This means that the shift of the resonance frequency can be mainly attributed to the Zeeman shift of our molecular state $|a\rangle$ (upper blue line). Consequently the excited state $|b\rangle$ does not shift with the magnetic field (within the error bars). This is what we expect from a $|0_g^-\rangle$ state because of its zero magnetic moment ($\Omega = 0$,

where Ω is the projection of the total electronic angular momentum $\mathbf{J} = \mathbf{L} + \mathbf{S}$ along the internuclear axis. $\mathbf{L}$ and $\mathbf{S}$ are the total orbital angular momentum and the total electron spin, respectively. Ω is a good quantum number for Hund's case c, which is valid for this long range potential [JONES *et al.* (2006)]).
Because of the zero magnetic moment, the spectrum of the pure long range state $|0_g^-\rangle$ has also no hyperfine splitting (see Fig. 2.7), while states with $\Omega > 0$ have a first order hyperfine structure.
The magnetic field dependence of the bound state energies (blue solid lines in Fig. 2.20) is calculated with a FORTRAN code obtained from Paul Julienne (NIST) which uses a Fourier grid method. The magnetic field dependence of the dissociation threshold, which corresponds to the energy of two atoms in the high field seeking state $|F = 1, m_F = 1\rangle$, is calculated with the Breit-Rabi formula (dashed red line in Fig. 2.20).

2.7.2 Magnetic field dependence of the two photon resonance frequency

The dark resonance (see Sec. 2.4) is an ideal tool to measure the two-photon resonance frequency because their position is independent on the laser intensities and on the one photon detuning Δ. We use this tool to measure the data points in Fig. 2.21 (a). We observe that the measured two-photon resonance frequencies ν, which correspond to the energy difference of the state $|a\rangle$ and $|g\rangle$ divided by the Planck's constant h, are not constant if we change the magnetic field. This variation of ν is caused by the coupling of state $|a\rangle$ and $|u\rangle$ (see Fig. 2.21 (c)).
We can model the dependence of measured resonance frequencies ν with a Landau-Zener model which determines the two-level dressed state energies [KÖHLER *et al.* (2006)]

$$E_{\pm} = \frac{E_1 + E_2}{2} \pm \frac{\sqrt{(E_2 - E_1)^2 + (2h\Omega_{au})^2}}{2}. \tag{2.27}$$

The energy $E_1 = E_{a0} - E_g = h\nu_0$ is the energy difference of the bare state $|a_0\rangle$ and state $|g\rangle$ (see Fig 2.21 (c)). ν_0 denotes the unperturbed two photon resonance frequency which is constant because the bare state $|a_0\rangle$ and state $|g\rangle$ have the same magnetic moment. $E_2 = E_{u0} - E_g = E_1 + \mu_{rel} \cdot (B - B_0)$ is the energy of the bare state $|u_0\rangle$ relative to $|g\rangle$. B_0 is the magnetic field position of the avoided molecule-molecule crossing and is $B_0 \approx 1001.7\,G$ [DÜRR *et al.* (2004A)]. $\mu_{rel} = \mu_{u0} - \mu_{a0}$ is the relative magnetic moment between the bare state $|u_0\rangle$ and the bare state $|a_0\rangle$. μ_{rel} is calculated independently with a program from Paul Julienne (NIST) which provides the bound state energies using a Fourier grid method and is $\mu_{rel} = h \times 3.9\,\mathrm{MHz/G}$. $2h\Omega_{au}$ is the energy splitting of the two dressed states $|a\rangle$ and $|u\rangle$. The data analysis results to a splitting $2\Omega_{au} = (12 \pm 0.5)\,\mathrm{MHz}$ and $\nu_0 = (613.035 \pm 0.025)\,\mathrm{MHz}$. The errors correspond to a 95% confidence interval. The value for Ω_{au} roughly agrees with a measurement of the Rempe-group at the Max-Planck institute in Garching ($2\Omega_{au} = 13\,\mathrm{MHz}$ [DÜRR *et al.* (2004A)]), and with a measurement for which we use a radio frequency transition between the two states to determine the energy splitting. This really precise measurement gives a splitting $2\Omega_{au} = 13.32\,\mathrm{MHz}$.

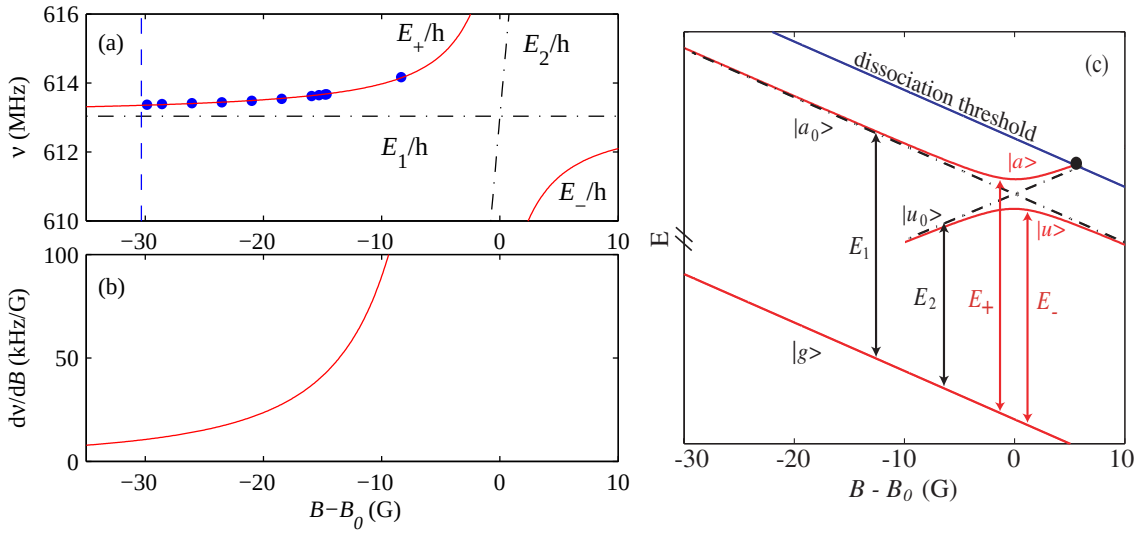

Figure 2.21:
(a) Two photon resonance frequency ν as a function of the magnetic field $(B - B_0)$. $B_0 \sim 1001.7\,\mathrm{G}$ is the magnetic field position of the avoided molecule-molecule crossing of the bare states $|a_0\rangle$ and $|u_0\rangle$ below the Feshbach resonance (see (c)). The data are fitted with a Landau-Zener model (2.27) (red solid lines). The upper red solid line asymptotically approaches the horizontal dashed line at $\nu = \nu_0 = 613.035\,\mathrm{MHz}$. The vertical dashed line shows the position of another molecule-molecule crossing which prevents a further ramping to lower magnetic field values. (b) The solid line is the derivative of the curve in (a). At a magnetic field value of 973 G ($\cong -29\,\mathrm{G}$), at which we normally do our STIRAP measurements, the dependence of the two-photon resonance frequency on the magnetic field is about 10 kHz/G. (c) Definition of the energies $E_{+,-}$ and $E_{1,2}$. The black dot indicates the position of the Feshbach resonance.

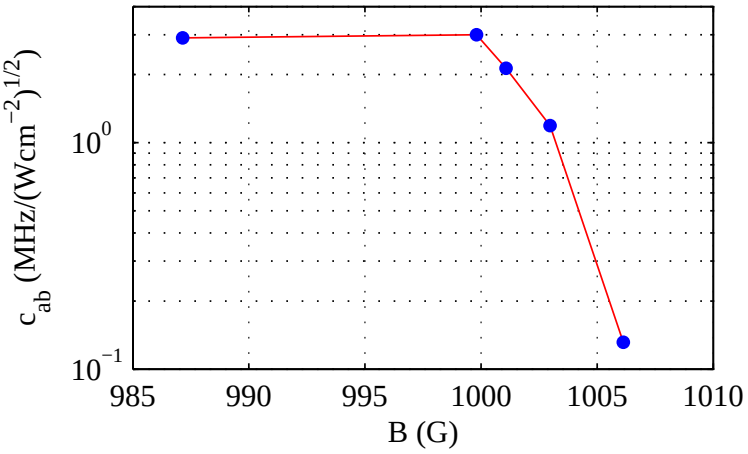

Figure 2.22:
Measured coupling strength c_{ab} ($\equiv \Omega_1/(2\pi \times I_1^{1/2})$) of the one photon transition $|a\rangle \rightarrow |b\rangle$ as a function of the magnetic field. At $\sim$ 1006 G the coupling strength is by a factor of about twenty weaker than for magnetic fields lower than 1000 G.

The solid line in Fig. 2.21 (b) is the derivative of the curve in (a). At a magnetic field value of 973 G ($\cong -29$ G in Fig. 2.21), at which we normally do our STIRAP measurements, the dependence of the two-photon resonance frequency on the magnetic field is about 10 kHz/G.

2.7.3 Magnetic field dependence of the coupling strength

On the avoided molecule-molecule crossing, which is located below the Feshbach resonance at 1007.4 G (see Fig. 2.20), the coupling strength of the transition $|a\rangle \rightarrow |b\rangle$ is modified because of the mixing of the two molecular states $|a\rangle$ and $|u\rangle$. The mixing changes the wavefunction of the molecules and therefore also the Franck-Condon factor of the transition, i.e. the square of the overlap between initial and final vibrational wavefunction. This is shown in Fig. 2.22: on the avoided crossing the measured coupling strength of the one photon transition $|a\rangle \rightarrow |b\rangle$ strongly depends on the magnetic field. At a magnetic field of e.g. $B \sim 1006$ G the coupling strength is by a factor of about twenty weaker than for magnetic fields lower than 1000 G (see Fig. 2.22).
The coupling strengths in Fig. 2.22 are defined as $c_{ab} = \Omega_1/(2\pi \cdot I_1^{1/2})$, where $\Omega_1 = 2\pi \cdot c_{ab} \cdot I_1^{1/2}$ is the Rabi frequency of the transition $|a\rangle \rightarrow |b\rangle$ and I_1 the intensity of the corresponding laser beam. c_{ab} is directly related to the dipole matrix element $\mathbf{d}$ and is

$$c_{ab} = \frac{1}{2\pi \cdot \hbar}\sqrt{\frac{2}{c \cdot \epsilon_0}}|\mathbf{d}_1|. \tag{2.28}$$

This follows from $\Omega_1 = \mathbf{d}_1 \cdot \mathbf{E}_1/\hbar$ and $I_1 = c \cdot \epsilon_0 |\mathbf{E}_1|^2/2$, with c being the speed of light and ϵ_0 the vacuum permittivity.

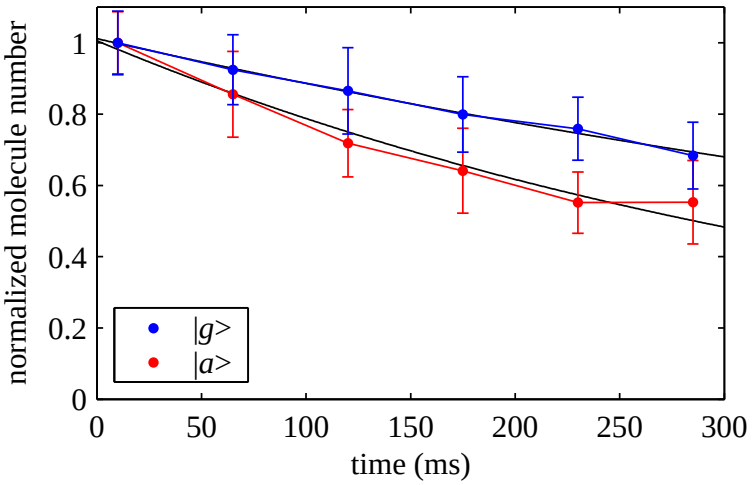

Figure 2.23:
Lifetime of the molecules in state $|g\rangle$ (blue points) and state $|a\rangle$ (red points) at a lattice depth of 60 E_r for molecules. The continuous lines are exponential fits to the data indicating a lifetime of $\tau_g = 750(\pm 110)$ ms and $\tau_a = 410(\pm 70)$ ms for the molecules in state $|g\rangle$ and $|a\rangle$, respectively. The error corresponds to a 95% confidence interval for the fit parameters $\tau_{a,g}$.

We determine the data in Fig. 2.22 by measuring the intensity I_1 and the Rabi frequency Ω_1. I_1 can be determined by measuring the beam power and the beam size at the position of the molecular cloud. Ω_1 can be determined from the molecular loss rate γ_{loss} at the one photon resonance position at $\delta = 0$ (see Fig. 2.7). The loss rate $\gamma_{loss} \approx \Omega_1^2/\gamma_b$ for $\Omega_1 \ll \gamma_b$ and $\delta = 0$ [METCALF AND VAN DER STRATEN (2002)]. For a given length t_p of the laser light pulse, the number of remaining particles N at the resonance position $\delta = 0$ is given by $N(t) = N_0 - N_{loss} = N_0 \cdot \exp(-\gamma_{loss} \cdot t_p)$. N_0 and N_{loss} can be determined from Lorentzian fits to one color spectra similar to the one shown in Fig. 2.7. The Lorentzian fit model has the form $N = N_0 - N_{loss} \cdot w^2/(4\delta^2 + w^2)$, with δ the detuning from the one photon resonance (for $\Delta = 0$, see Fig. 2.3) and w the width of the resonance. The coupling strength c_{ab} is then given by

$$c_{ab} = \sqrt{\ln\left(\frac{N_0}{N_0 - N_{loss}}\right) \cdot \frac{\gamma_b}{t_p \cdot I_1 \cdot (2\pi)^2}}. \tag{2.29}$$

2.7.4 Lifetime measurements

For a measurement of the lifetime of the molecules in state $|g\rangle$, the molecules are first transferred from $|a\rangle$ to $|g\rangle$ and after a variable hold time in state $|g\rangle$ they are transferred back to $|a\rangle$. This can be done by varying the time between the two STIRAP pulses (see Fig. 2.12 (a)). Immediately afterwards the molecules in state $|a\rangle$ are dissociated into atoms and then the optical lattice and the magnetic bias field are quickly switched off. The atoms are detected with absorption imaging as described in Sec. 1.5.

Figure 2.23 shows the measured lifetimes of the molecules in state $|g\rangle$ and state $|a\rangle$ for a lattice depth of 60 E_r for molecules. The hold time is limited to below 300 ms due to the heating up of the coils which produce the homogeneous bias field of about 1000 G. At the lattice depth of 60 E_r for molecules, we observe a lifetime τ_g of ~ 0.8 s for the molecules in state $|g\rangle$ (assuming exponential decay), which is longer than the lifetime τ_a of ~ 0.4 s for Feshbach molecules in state $|a\rangle$. At these deep lattices molecular decay is exclusively due to inelastic scattering of lattice photons.
The lattice laser light, which leads to the mentioned inelastic scattering of photons, has a wavelength of 830.44 nm. For this wavelength, the laser is detuned by about 100 GHz from the closest transition to an excited molecular level (for details see [THALHAMMER (2007)]). The difference between the lifetimes τ_g and τ_a can be explained by a weaker coupling of state $|g\rangle$ with the lattice laser light to the nearest excited molecular states.

2.8 Outlook for experiments with ultracold molecules

Using STIRAP we have demonstrated a coherent transfer of a molecular quantum gas from a weakly bound molecular level to a more deeply bound molecular level with a high transfer efficiency of 87%. The method can be in principle extended in a straight forward manner to create arbitrarily deeply bound molecules. Indeed, it seems to be very promising to transfer the Feshbach molecules to the vibrational ground state ($v = 0$) of the triplet potential $a^3\Sigma_u^+$ (see. Fig. 2.24) with a single STIRAP transition. The molecules in the triplet ground state could be stable under collisions because of their pure triplet character. A relaxation to vibrational states of the singlet potential should be strongly suppressed because of angular momentum conservation in a collision of two triplet molecules. The stability of the molecules under collision is crucial for the creation of a molecular Bose-Einstein condensate. Such a molecular BEC could be created by adiabatically ramping down the optical 3D lattice, if the molecules are in a Mott insulator state. The Mott insulator can be melted and a superfluid state of molecules can be directly created, as proposed by JAKSCH *et al.* (2002). Also in the case that the temperature of the sample is above the critical temperature T_c for Bose-Einstein condensation [DALFOVO *et al.* (1999)], a BEC of molecules could be created by subsequent evaporative cooling of the molecules.
The coupling for an optical molecular transition depends on the Franck-Condon factor, i.e. the square of the overlap between initial and final vibrational wavefunctions [JONES *et al.* (2006)]. Therefore, for a STIRAP transition to the triplet ground state a "good" excited molecular state $|b\rangle$ has to be found. For a "good" state $|b\rangle$ both couplings, $|a\rangle \rightarrow |b\rangle$ and $|g\rangle \rightarrow |b\rangle$, are large enough to obtain Rabi frequencies $\Omega_{1,2}$ in the order of 1 MHz with attainable laser light intensities (<1 kW/cm^2). Rabi frequencies on this order of magnitude are favorable for several reasons: First, the timescale for an adiabatic transfer of molecules remains short enough to avoid problems with the relative phase stability of the lasers used in the STIRAP process. Such phase fluctuations would lead to losses due to non-adiabatic coupling and could be significant on long STIRAP time scales. Second, the width w_{DS} of the dark state resonance is directly connected with the Rabi frequencies $\Omega_{1,2}$ of the two-photon transition, as discussed in Sec. 2.4. In the case of a small width w_{DS} ($w_{\mathrm{DS}}/2\pi \leq 10$ kHz, which corresponds to Rabi frequencies $\Omega_{1,2} \leq 2\pi \cdot 0.3$ MHz), the requirements on the stability of the magnetic- and light fields become very high. Additionally, the search for the two photon resonances becomes difficult if w_{DS} is small.
Calculations from Christiane Koch show that the vibrational levels v' of the excited state $^3\Sigma_g^+$, which is asymptotically connected to the $5S_{1/2} + 5P_{1/2}$ collisional state, are promising candidates for a STIRAP transition to the triplet ground state (see Fig. 2.25). Mainly one of the first excited states ($v' \approx 1 - 30$) of this $^3\Sigma_g^+$ potential seems to be suitable for STIRAP because the Franck-Condon factors for the transition $|a\rangle \rightarrow |b\rangle$ and $|g\rangle \rightarrow |b\rangle$ have a similar and reasonable value. The calculated coupling strengths ($\equiv \Omega/(2\pi \cdot I^{1/2})$ are on the order of 1 MHz/(Wcm^{-2})$^{1/2}$. The level $v' = 3$, e.g., has an energy of about 9500 cm^{-1} relative to dissociation threshold of the ground state (at E=0, see Fig. 2.24). This energy corresponds to a wavelength of ~ 1050 nm for the transition $|a\rangle \rightarrow |b\rangle$. The second laser, which connects the ground state $v = 0$ of the triplet potential $a^3\Sigma_u^+$ with the excited state $|b\rangle$, needs to have an about 25 nm shorter wavelength relative to laser 1 because of the

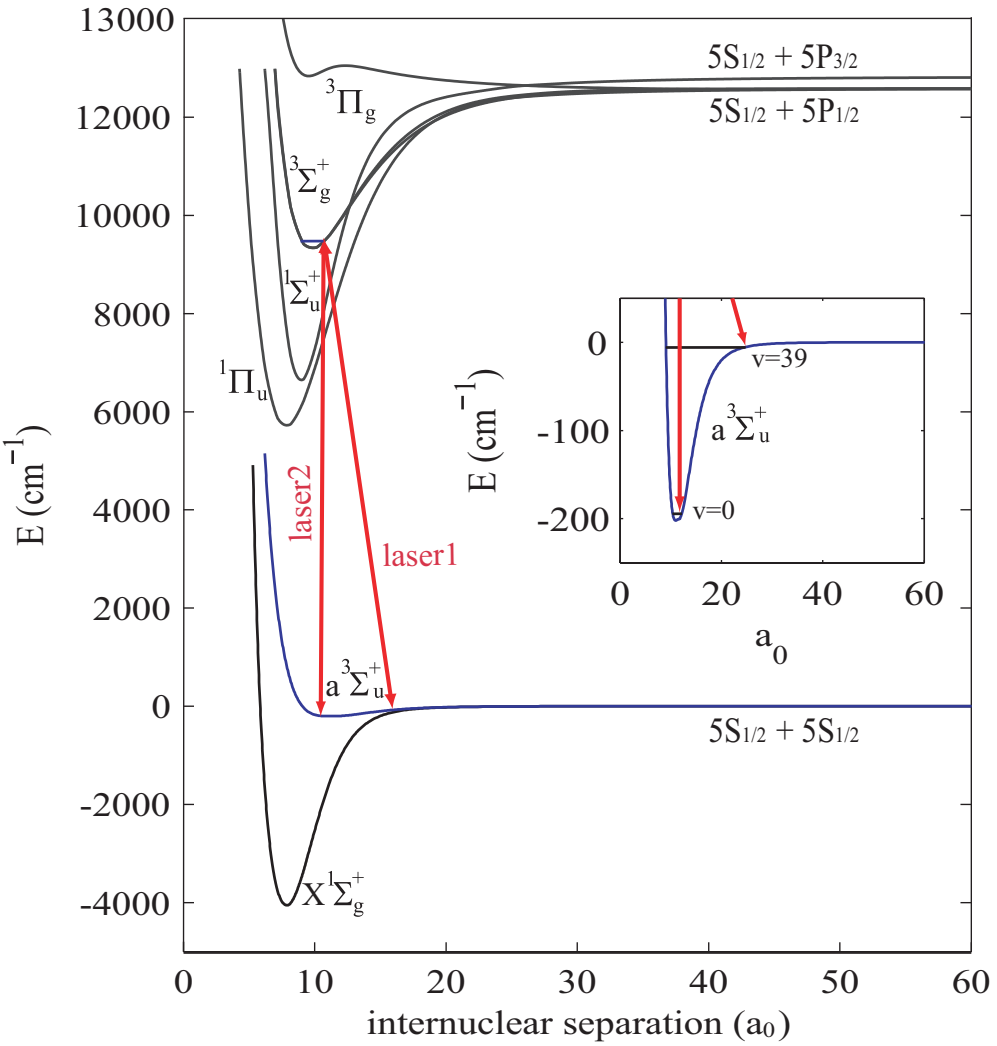

Figure 2.24:
The Born-Oppenheimer potentials of $^{87}Rb_2$ in the conventional Hund's case (a) notation for the molecular states. The shown excited state molecular potentials are asymptotically connected to the $5S_{1/2}+5P_{1/2}$ or $5S_{1/2}+5P_{3/2}$ collisional states. The red arrows indicate the lasers which couple the corresponding vibrational levels v of the triplet ground state potential $a^3\Sigma_u^+$ (see inset) with a level v' of the excited state potential $^3\Sigma_g^+$. Starting with Feshbach molecules in state $v=39$ (binding-energy $\approx 24\,\mathrm{MHz}\times h$) it should be possible to reach the vibrational ground state ($v=0$) of the triplet potential with a single STIRAP pulse (see text).

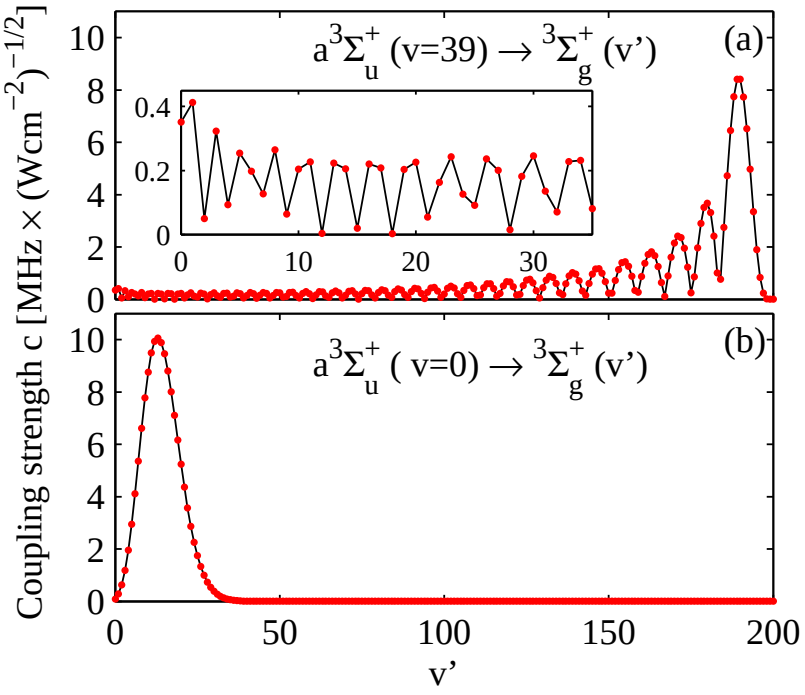

Figure 2.25:
Calculated coupling strengths c for the transitions (a) $|a\rangle \rightarrow |b\rangle$ and (b) $|g\rangle \rightarrow |b\rangle$ to the vibrational levels $|b\rangle = v'$ of the excited state potential $^3\Sigma_g^+$. $|a\rangle$ is our initial state ($v = 39$) of the Feshbach molecules and $|g\rangle$ is the vibrational ground state ($v = 0$) of the triplet potential $a^3\Sigma_g^+$. The coupling strengths c are defined as c= $\Omega/(2\pi \cdot I^{1/2})$, where Ω is the Rabi frequency and I the laser intensity. The data are based on calculations of Christiane Koch.

binding energy of this state (see Fig. 2.24, inset). However, lasers with both wavelength are easily available.
Taking one of the first vibrational levels v' of the exited state $^3\Sigma_g^+$ would have the advantage that laser 1, which connects $|a\rangle$ with $|b\rangle$, cannot couple the state $|g\rangle$ to other states of the $^3\Sigma_g^+$ potential since there are no more states available. Additionally a coupling to states of the $^1\Sigma_u^+$ or $^1\Pi_u$ potential is suppressed because of selection rules which allow only bound-bound transitions of g states to u states and vice versa [JONES *et al.* (2006)]. However, our initial Feshbach state $|a\rangle$ does not have a definite singlet or triplet character and so transitions to both g and u excited states are allowed. Hence, laser 2 could couple $|a\rangle$ to states of the $^3\Sigma_g^+$, $^3\Pi_g$, $^1\Sigma_u^+$ and $^1\Pi_u$ potentials. Therefore, a possible level v' has to be tested experimentally for its suitability, since exact data for the levels are not known.
The vibrational ground state $X^1\Sigma_g^+$ ($v = 0$) of the singlet potential is more difficult a reach, because it seems to not be possible to transfer the molecules with a single step to $v = 0$. In [JAKSCH *et al.* (2002)] the authors propose a three step scheme to transfer atoms (in our case molecules) to the singlet ground state. Jaksch *et al.* suggest to produce with a first

two photon transition molecules in the level $X^1\Sigma_g^+$ ($v = 120$)/$a^3\Sigma_u^+$ ($v = 35$) with a binding energy of 30 GHz$\times h$. The next step could be a two photon transition $X^1\Sigma_g^+$ ($v = 120$) $\longrightarrow^1$ $\Sigma_u^+(v' = 185) \longrightarrow X^1\Sigma_g^+$ ($v = 52$) and then subsequently $X^1\Sigma_g^+$ ($v = 52$) $\longrightarrow^1 \Sigma_u^+(v' = 24) \longrightarrow$ $X^1\Sigma_g^+$ ($v = 0$). Jaksch *et al.* propose to use a two photon Raman process with an intermediate detuning ($\Delta \neq 0$) for the transitions. However STIRAP, which is nothing else but a special kind of a Raman process (as already the name "STImulated Raman Adiabatic Passage" implies), should be more stable, because it is not sensitive on fluctuations of the pulse length, laser intensity or laser detunig. Thus STIRAP is also a promising tool for the creation of a molecular BEC in the singlet ground state.

3 Repulsively Bound Atom Pairs in an Optical Lattice

Throughout physics, stable composite objects are usually formed via attractive forces, which allow the constituents to lower their energy by binding together. Repulsive forces separate particles in free space. However, in a structured environment such as a periodic potential and in the absence of dissipation, stable composite objects can exist even for repulsive interactions.
In this part of my thesis I review an experiment [WINKLER *et al.* (2006)] in which we have observed such a novel kind of bound state of two atoms which is based on repulsive interactions between the particles. The repulsively bound pairs exhibit long lifetimes, even under conditions when they collide with one another. Stable repulsively bound objects should be viewed as a general phenomenon and their existence will be ubiquitous in cold atoms lattice physics. Although the experiment described here is based on bosonic ^{87}Rb atoms, other composites with fermions [HOFSTETTER *et al.* (2002)] or Bose-Fermi mixtures [LEWENSTEIN *et al.* (2004)] should exist in an analogous manner. Furthermore, repulsively bound objects could also be formed with more than two particles.
In the following I will first explain the theoretical background of interacting bosonic atoms in an optical lattice. Then I will show an analytic solution for a single repulsively atom pair in the lattice. Afterwards I will shortly discuss the numerical method we used to simulate a lattice gas of many interacting repulsively bound pairs. The analytic description of a single pair and the numerical simulations were done by a theoretical physics team in Innsbruck around Hans-Peter Büchler, Andrew Daley and Peter Zoller and will be shown here for the sake of completeness. Afterwards I will present our experimental results which demonstrate several key properties of the pairs. We experimentally investigate the lifetime, the quasi-momentum distribution and the binding energy of the pairs. By varying the effective interaction between the atoms with the help of the Feshbach resonance we can also create lattice induced bound atom pairs which are based on attractive interactions. Finally, I briefly discuss possible future experiments with repulsively bound pairs.

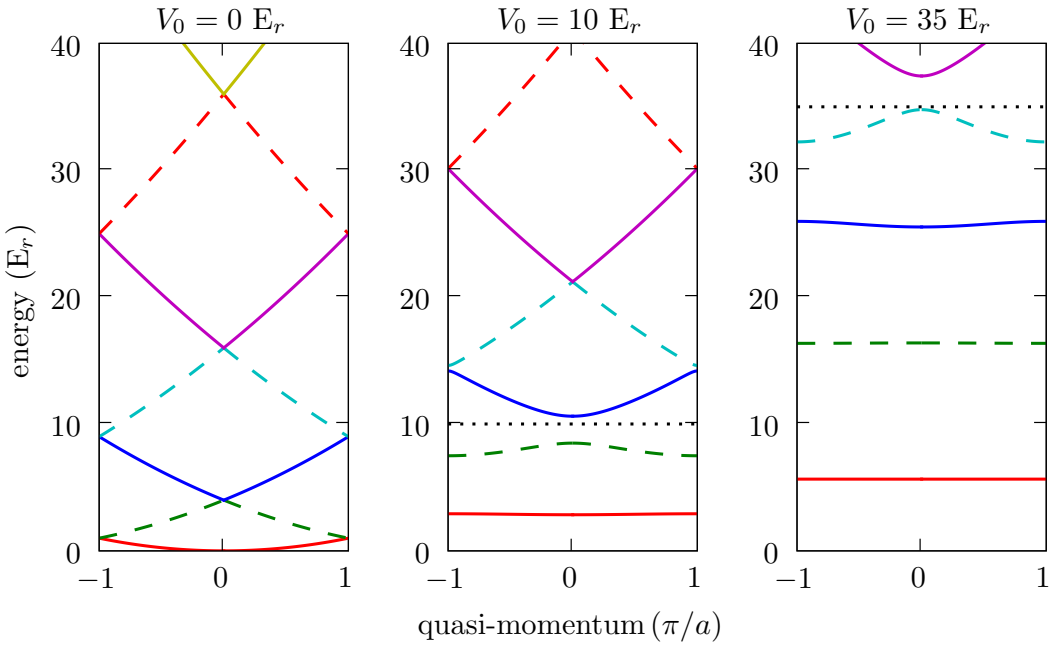

Figure 3.1:
Energy spectrum for a single particle in a 1D lattice for three different potential depths V_0 as a function of the quasi-momentum. The band width of the lowest Bloch band is given by $4J$, where J is the hopping energy (see Eq. (3.5)). a is the lattice period and $\mathrm{E_r} = \pi^2\hbar^2/2ma^2$ denotes the recoil energy. The dotted line corresponds to the lattice depth V_0.

3.1 Interacting bosons in an optical lattice

Optical lattices are generated by pairs of counter-propagating laser beams, where the resulting standing wave intensity pattern forms a periodic array of microtraps for the cold atoms, with period given by half the wavelength of the light, $a = \lambda/2$ (for details see Sec. 1.3). The periodicity of the potential V_{lat} gives rise to a band structure for the atom dynamics with Bloch bands separated by band gaps, which can be controlled via the laser parameters and configuration, as shown in Fig. 3.1. The Bloch bands are given by the eigenenergies $E_{n,q}$ of the Bloch functions $\Phi^n_q(x)$ (see e.g. [GREINER (2003)]):

$$H\Phi^n_q(x) = E_{n,q}\Phi^n_q(x) \qquad \text{with} \qquad H = \frac{1}{2m}\hat{p}^2 + V_{\mathrm{lat}}(x) \tag{3.1}$$

The dynamics of particles moving in well separated bands can be described by using Wannier functions (see e.g. [JAKSCH AND ZOLLER (2005)]). These are complete sets of orthogonal normalized real mode functions for each band n. The Wannier functions localized at lattice site x_j are defined by

$$w(x - x_j) = \theta^{-1/2}\sum_q e^{-iqx_j}\Phi^n_q(x) \tag{3.2}$$

with θ a normalization constant. The Wannier functions are used for describing particles trapped in the lattice since they allow to attribute to the particles a mean position x_j. Additionally, they easily account for local interactions between particles since the dominant contribution to the interaction energy arises from particles occupying the same lattice site x_j. The Wannier functions for a three dimensional lattice can be calculated simply from the product of the Wannier functions in the one dimensional case

$$w(\mathbf{r}) = \prod_{j=1}^{3} w(x_j). \tag{3.3}$$

The dynamics of an atomic Bose-Einstein condensate loaded into the lowest band of a sufficiently deep optical lattice is well described by a single band Bose-Hubbard model [FISHER *et al.* (1989)] considering only the Wannier function of the lowest Bloch band ($n = 0$). This leads to the Bose-Hubbard Hamiltonian [JAKSCH *et al.* (1998)]

$$\hat{H} = -J \sum_{\langle i\,j \rangle} \hat{b}_i^\dagger \hat{b}_j + \frac{U}{2} \sum_j \hat{b}_j^\dagger \hat{b}_j \left(\hat{b}_j^\dagger \hat{b}_j - 1 \right) + \sum_i \epsilon_i \hat{b}_j^\dagger \hat{b}_j. \tag{3.4}$$

This single band model is valid because the kinetic energy and interaction energy in this system are much smaller than the separation to the first excited Bloch band, which is $\hbar\omega_j = \sqrt{4 V_0 \mathrm{E_r}}$ in a harmonic approximation. ω_j is also the oscillation frequency in the wells and the resulting width of the Bloch band is $4J$.

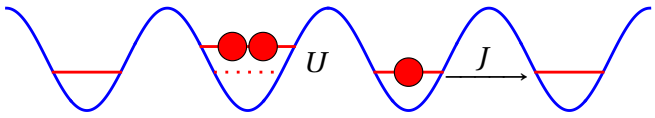

Figure 3.2:
J and U denote respectively the tunneling rate of atoms between neighboring sites, and the collisional energy shift from interactions between atoms on the same site.

In the Bose-Hubbard Hamiltonian (3.4) $\hat{b}_i$ ($\hat{b}_i^\dagger$) are destruction (creation) operators for the bosonic atoms at site i which obey the canonical commutation relations $[\hat{b}_i, \hat{b}_j^\dagger] = \delta_{ij}$. The operator $\hat{b}_j^\dagger \hat{b}_j = \hat{n}_j$ (also called number operator) counts the number of bosons on the j^{th} lattice site and $\langle i\,j \rangle$ denotes the summation which is carried out over nearest neighboring lattice sites. The first term in the Bose-Hubbard Hamiltonian (3.4) is called the hopping term and describes the tunneling of bosons between neighboring potential wells. $J/\hbar$ denotes the tunneling rate of atoms between neighboring sites and this rate is given by the tunnel matrix element

$$J = -\int d^3x\, w^*(\mathbf{r} - \mathbf{r}_i)[-\hbar^2\nabla/2m + V_{\mathrm{lat}}(\mathbf{r})]\, w(\mathbf{r} - \mathbf{r}_j). \tag{3.5}$$

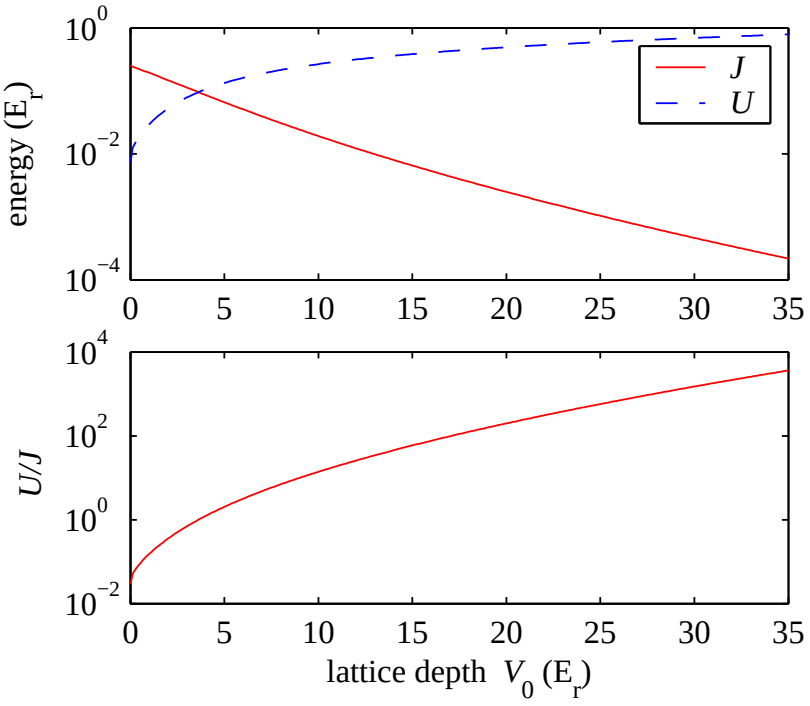

Figure 3.3:
Tunneling matrix element J and onsite interaction energy U (top) and U/J (bottom) versus lattice depth of an isotropic three dimensional lattice with the same depth in each direction. Changing the strength of the lattice potential, the ratio U/J can be continuously adjusted over several orders of magnitude.

$V_{\mathrm{lat}}(\mathbf{r})$ is the three dimensional optical lattice potential of the form

$$V_{\mathrm{lat}}(\mathbf{r}) = \sum_{j=1}^{3} V_0 \sin^2(k_{\mathrm{lat}} x_j), \tag{3.6}$$

with the wave number $k_{\mathrm{lat}} = 2\pi/\lambda$ and V_0 the lattice depth (see also Sec. 1.3). The hopping term of the Hamiltonian tends to delocalize each atom over the lattice. In the limit $J >> U$ the system is superfluid (SF) and possesses first order long range off diagonal correlations [JAKSCH AND ZOLLER (2005)].
The interaction of n atoms, each interacting with $n-1$ other atoms on the same lattice site, is described by the second term of the Bose-Hubbard Hamiltonian (3.4). The interaction potential between the atoms is approximated by a short-range pseudo-potential with as the s-wave scattering length and m the mass of the atoms. U denotes the collisional energy shift and quantifies the repulsion between two atoms on a single lattice site and is given by

$$U = (4\pi\hbar^2 a_s/m) \int d^3x \mid w(\mathbf{r}) \mid^4, \tag{3.7}$$

with a_s the s-wave scattering length. Due to the short range of the interactions compared to the lattice spacing, the interaction energy is well described by this term, which characterizes a purely on-site interaction. The interaction term tends to localize atoms to lattice sites. In the limit of a dominating U ($U >> J$) the system is not any more superfluid but becomes Mott isolating [GREINER *et al.* (2002)]. The quantum phase transition between superfluid and Mott isolating state takes place at about $U \approx 5.8J \times z$ with z the number of nearest neighbors of each lattice site [JAKSCH *et al.* (1998); JAKSCH AND ZOLLER (2005)]. The external confinement which gives rise to an energy offset $\epsilon_i \approx V_{\text{ext}}(x_i)$ on the ith lattice is described by the third term of the Bose-Hubbard Hamiltonian (3.4). For a homogenous system ϵ_i is zero.
For a given optical lattice potential U and J can be evaluated numerically (see Fig. 3.3). When the potential depth of the optical lattice is increased, the tunneling barrier between neighboring lattice sites is raised and therefore the tunneling matrix element J decreases exponentially. The on-site interaction U on the other hand is slightly increased in a deeper lattice due to a tighter confinement of the wavefunction on a lattice site. Therefore the ratio U/J can be continuously adjusted over a wide range by changing the strength of the lattice potential.

Repulsively bound atom pairs

The Bose-Hubbard Hamiltonian (3.4) predicts the existence of stable repulsively bound atom pairs. These are most intuitively understood in the limit of strong repulsive interaction $U >> J$ (where $U > 0$ but this energy is still smaller than the separation to the first excited Bloch band, $U \ll \omega$). If a state is prepared with two atoms occupying a single site, $|2_i\rangle \equiv (\hat{b}_i^{\dagger 2}|\text{vac}\rangle)/\sqrt{2}$, then it will have a potential energy offset $\approx U$ with respect to states where the atoms are separated (see Fig. 3.8 (a)). This state will be unable to decay by converting the potential energy into kinetic energy, as the Bloch band provides a maximum kinetic energy for two atoms both at the edge of the Brillouin zone given by $8J << U$. Instead, the atoms will remain together, and tunnel through the lattice as a bound composite object, a repulsively bound pair.

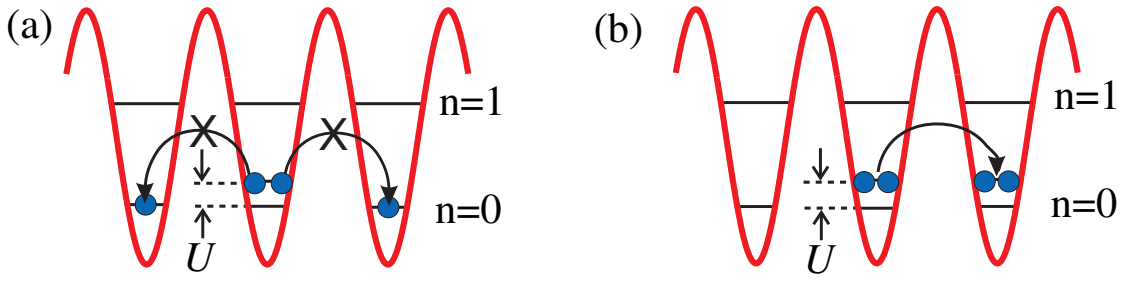

Figure 3.4:
(a) A state with two atoms located on the same site of an optical lattice has an energy offset $\approx U$ with respect to states where the atoms are separated. Breaking up of the pair is suppressed due to the lattice band structure and energy conservation, so that the pair remains bound as a composite object, which can tunnel through the lattice. In the figure, $n = 0$ denotes the lowest Bloch band and $n = 1$ the first excited band. (b) The atom pair can tunnel through the lattice as a composite object.

3.2 Analytical solution of two particle problem in an optical lattice

The analytic description of a single pair is based on notes of Hans-Peter Büchler. This analytic description is shown here for the sake of completeness and for a general understanding of the repulsively bound pairs. A similar discussion can be found in [HECKER DENSCHLAG AND DALEY (2006)]. I have added in the following description several intermediate steps to simplify the understanding.

General Discussion

Our understanding of the stable repulsively bound pairs can be made more formal by an exact solution of the two particle Lippmann-Schwinger scattering equation on the lattice corresponding to the Bose-Hubbard Hamiltonian Eq. (3.4). Denoting the primitive lattice vectors in each of the d dimensions by $\mathbf{e}_i$, we can write the position of the two atoms by $\mathbf{x} = \sum_{i=1}^{d} x_i \mathbf{e}_i$ and $\mathbf{y} = \sum_{i=1}^{d} y_i \mathbf{e}_i$, where x_i, y_i are integers, and we can write the two atom wavefunction in the form $\Psi(\mathbf{x},\mathbf{y})$. The related Schrödinger equation from the Bose-Hubbard model (3.4) with homogeneous background, $\epsilon_i = 0$, then takes the form

$$H\Psi(\mathbf{x},\mathbf{y}) = [H_{kin} + H_{int}]\,\Psi(\mathbf{x},\mathbf{y}) = \left[-J\left(\tilde{\Delta}_{\mathbf{x}} + \tilde{\Delta}_{\mathbf{y}}\right) + U\delta_{\mathbf{x},\mathbf{y}}\right]\Psi(\mathbf{x},\mathbf{y}) = E\,\Psi(\mathbf{x},\mathbf{y}), \tag{3.8}$$

where the operator

$$\tilde{\Delta}_{\mathbf{x}}\Psi(\mathbf{x},\mathbf{y}) = \sum_{i=1}^{d}\left[\Psi(\mathbf{x}+\mathbf{e}_i,\mathbf{y}) + \Psi(\mathbf{x}-\mathbf{e}_i,\mathbf{y}) - 2\Psi(\mathbf{x},\mathbf{y})\right] \tag{3.9}$$

denotes a discrete lattice Laplacian on a cubic lattice. Note that in order to express this in terms of the discrete lattice Laplacian we have added $4dJ\Psi(\mathbf{x},\mathbf{y})$ to each side of the Schrödinger equation. This effectively changes the zero of energy, so that $E \to E+4Jd$. We then introduce relative coordinates $\mathbf{r} = \mathbf{x}-\mathbf{y}$ existing on the same lattice structure as the co-ordinate $\mathbf{x}$, and center of mass coordinates $\mathbf{R} = (\mathbf{x}+\mathbf{y})/2$, existing on a lattice with the same symmetry as the original lattice but smaller lattice constant $a/2$. We then separate the wavefunction using the ansatz

$$\Psi(\mathbf{x},\mathbf{y}) = \exp(i\mathbf{K}\mathbf{R})\psi_{\mathbf{K}}(\mathbf{r}), \tag{3.10}$$

with $\mathbf{K} = \mathbf{k}_1+\mathbf{k}_2$ the center of mass quasi-momentum. This allows us to reduce the Schrödinger equation to a single particle problem in the relative coordinate,

$$\left[-2J\tilde{\Delta}^{\mathbf{K}}_{\mathbf{r}} + E_{\mathbf{K}} + U\delta_{\mathbf{r},0}\right]\psi_{\mathbf{K}}(\mathbf{r}) = E\psi_{\mathbf{K}}(\mathbf{r}) \tag{3.11}$$

where $E_{\mathbf{K}} = 4J\sum_{i=1}^{d}[1-\cos(\mathbf{K}\mathbf{e}_i/2)]$ is the kinetic energy of the center of mass motion, and where the discrete lattice Laplacian for a square lattice is now given by

$$\tilde{\Delta}^{\mathbf{K}}_{\mathbf{r}}\psi(\mathbf{r}) = \sum_{i=1}^{d}\cos(\mathbf{K}\mathbf{e}_i/2)\left[\psi(\mathbf{r}+\mathbf{e}_i)+\psi(\mathbf{r}-\mathbf{e}_i)-2\psi(\mathbf{r})\right]. \tag{3.12}$$

The solutions of this Schrödinger equation can be found using the Greens function of the non-interacting problem with $U = 0$, which is defined by

$$[E - E_{\mathbf{K}} - H_0]\,G_{\mathbf{K}}(E,\mathbf{r}) = \delta_{\mathbf{r},0}, \tag{3.13}$$

with $\delta_{\mathbf{r},0}$ the three-dimensional Kronecker delta, and $H_0 = -2J\tilde{\Delta}^{\mathbf{K}}_{\mathbf{r}}$ the Hamiltonian of the non-interacting system. Then any solution $\psi_{\mathbf{K}}(\mathbf{r})$ satisfies [COHEN TANNOUDJI *et al.* (1999)]

$$\psi_{\mathbf{K}}(\mathbf{r}) = \psi_0(\mathbf{r}) + \sum_{\mathbf{r}'}G(E,\mathbf{r}-\mathbf{r}')V(\mathbf{r}')\psi_{\mathbf{K}}(\mathbf{r}'), \tag{3.14}$$

where $\psi_0(\mathbf{r})$ is a solution of the homogeneous equation

$$[E - E_{\mathbf{K}} - H_0]\,\psi_0(\mathbf{r}) = 0. \tag{3.15}$$

The Green function $G(E,\mathbf{r})$ in Eq. (3.14) can be found by substituting $G(E,\mathbf{r})$ in Eq. (3.13) with its Fourier transform [CSERTI (2000)]:

$$\begin{aligned}
&[E - E_{\mathbf{K}} - H_0]\,G(E,\mathbf{r}) = [E - E_{\mathbf{K}} - H_0]\,[1/(2\pi)^d]\int_{-\pi}^{\pi}\mathrm{d}^d k\,\tilde{G}(E,\mathbf{k})\exp(i\mathbf{k}\mathbf{r}) = \\
&= [1/(2\pi)^d]\int_{-\pi}^{\pi}\mathrm{d}^d k\,[E - E_{\mathbf{K}} - H_0]\,\tilde{G}(E,\mathbf{k})\exp(i\mathbf{k}\mathbf{r}) = \\
&= [1/(2\pi)^d]\int_{-\pi}^{\pi}\mathrm{d}^d k\,[E - E_{\mathbf{K}} - \epsilon_{\mathbf{K}}(\mathbf{k})]\,\tilde{G}(E,\mathbf{k})\exp(i\mathbf{k}\mathbf{r}) = \delta_{\mathbf{r},0}.
\end{aligned} \tag{3.16}$$

$\mathbf{k} = (\mathbf{k}_2 - \mathbf{k}_1)/2$ is here the relative quasi-momentum, and $\epsilon_{\mathbf{K}}(\mathbf{k})$ accounts for the dispersion relation of the non-interacting system ($U = 0$),

$$\epsilon_{\mathbf{K}}(\mathbf{k}) = 4J \sum_{i=1}^{d} \cos\frac{\mathbf{K}\mathbf{e}_i}{2} \left[1 - \cos(\mathbf{k}\mathbf{e}_i)\right]. \tag{3.17}$$

$\epsilon_{\mathbf{K}}(\mathbf{k})$ can be calculated from the equation for the eigenvalues

$$\begin{aligned}
&\epsilon_{\mathbf{K}}(\mathbf{k}) \exp(i\mathbf{k}\mathbf{r}) = H_0 \exp(i\mathbf{k}\mathbf{r}) = -2J\tilde{\Delta}^{\mathbf{K}}_{\mathbf{r}} \exp(i\mathbf{k}\mathbf{r}) = \\
&= -2J \sum_{i=1}^{d} \cos\frac{\mathbf{K}\mathbf{e}_i}{2} \left[\exp(i\mathbf{k}(\mathbf{r}+\mathbf{e}_i)) + \exp(i\mathbf{k}(\mathbf{r}-\mathbf{e}_i)) - 2\exp(i\mathbf{k}\mathbf{r})\right] = \\
&= -2J \sum_{i=1}^{d} \cos\frac{\mathbf{K}\mathbf{e}_i}{2} \left[\exp(i\mathbf{k}\mathbf{e}_i) + \exp(-i\mathbf{k}\mathbf{e}_i) - 2\right] \exp(i\mathbf{k}\mathbf{r}) = \\
&= 4J \sum_{i=1}^{d} \cos\frac{\mathbf{K}\mathbf{e}_i}{2} \left[1 - \cos(\mathbf{k}\mathbf{e}_i)\right] \exp(i\mathbf{k}\mathbf{r}).
\end{aligned} \tag{3.18}$$

From the δ-function in Eq. (3.16)

$$\delta_{\mathbf{r},0} = [1/(2\pi)^d] \int_{-\pi}^{\pi} \mathrm{d}^d k \, \exp(i\mathbf{k}\mathbf{r}) \tag{3.19}$$

follows that

$$\tilde{G}_{\mathbf{K}}(E, \mathbf{k}) = \frac{1}{E - E_{\mathbf{K}} - \epsilon_{\mathbf{K}}(\mathbf{k})}. \tag{3.20}$$

$G(E, \mathbf{r})$ can be calculated from the Fourier transformation of $\tilde{G}(E, \mathbf{k})$ and we obtain the solution

$$G(E, \mathbf{r}) = [1/(2\pi)^d] \int_{-\pi}^{\pi} \mathrm{d}^d k \, \tilde{G}(E, \mathbf{k}) \exp(i\mathbf{k}\mathbf{r}). \tag{3.21}$$

The solutions of Eq. (3.11) can be divided into two classes: scattering states, and bound (localized) states. We we will first analyze the scattering states.

Scattering States

Similarly to scattering problems involving particles in free space, the scattering states of particles on the lattice with energy E obey the Lippmann-Schwinger equation

$$\psi_E(\mathbf{r}) = \psi^0_E(\mathbf{r}) + \sum_{\mathbf{r}_1} G_{\mathbf{K}}(E, \mathbf{r} - \mathbf{r_1}) V(\mathbf{r}_1) \psi_E(\mathbf{r}_1) \tag{3.22}$$

with $\psi^0_E = \exp(i\mathbf{k}\mathbf{r})$ an eigenstate of H_0 with energy $E = \epsilon_{\mathbf{K}}(\mathbf{k})$. The equation (3.22) can be solved with an iteration method [COHEN TANNOUDJI *et al.* (1999)]: renaming the variables ($\mathbf{r} \longrightarrow \mathbf{r_1}; \mathbf{r_1} \longrightarrow \mathbf{r_2}$) gives

$$\psi_E(\mathbf{r}_1) = e^{i\mathbf{k}\mathbf{r_1}} + \sum_{\mathbf{r_2}} G_{\mathbf{K}}(E, \mathbf{r_1} - \mathbf{r_2}) V(\mathbf{r}_2) \psi_E(\mathbf{r}_2) \tag{3.23}$$

If we put the expression in Eq.(3.23) in to Eq. (3.22) and repeat this step we get the Born series

$$\begin{aligned}\psi_E(\mathbf{r}) &= \psi_E^0(\mathbf{r}) + \sum_{\mathbf{r_1}} G_{\mathbf{K}}(E,\mathbf{r}-\mathbf{r_1})V(\mathbf{r_1})e^{i\mathbf{k}\mathbf{r_1}} \\ &+ \sum_{\mathbf{r_1}}\sum_{\mathbf{r_2}} G_{\mathbf{K}}(E,\mathbf{r}-\mathbf{r_1})V(\mathbf{r_1})e^{i\mathbf{k}\mathbf{r_1}} G_{\mathbf{K}}(E,\mathbf{r_1}-\mathbf{r_2})V(\mathbf{r_2})e^{i\mathbf{k}\mathbf{r_2}} \\ &+ \sum_{\mathbf{r_1}}\sum_{\mathbf{r_2}}\sum_{\mathbf{r_3}} G_{\mathbf{K}}(E,\mathbf{r}-\mathbf{r_1})V(\mathbf{r_1})e^{i\mathbf{k}\mathbf{r_1}} \\ &\times G_{\mathbf{K}}(E,\mathbf{r_1}-\mathbf{r_2})V(\mathbf{r_2})e^{i\mathbf{k}\mathbf{r_2}} G_{\mathbf{K}}(E,\mathbf{r_2}-\mathbf{r_3})V(\mathbf{r_3})e^{i\mathbf{k}\mathbf{r_3}} + ...\end{aligned} \tag{3.24}$$

A re-summation of the Born expansion results in:

$$\psi_E(\mathbf{r}) = \psi_E^0(\mathbf{r}) + \sum_{n=1}^{\infty}\sum_{\mathbf{r_1}...\mathbf{r_n}} G_{\mathbf{K}}(E,\mathbf{r}-\mathbf{r_1})V(\mathbf{r_1})e^{i\mathbf{k}\mathbf{r_1}}...G_{\mathbf{K}}(E,\mathbf{r_{n-1}}-\mathbf{r_n})V(\mathbf{r_n})G_{\mathbf{K}}(E,\mathbf{r_n})e^{i\mathbf{k}\mathbf{r_n}}. \tag{3.25}$$

In the present situation with a short range potential $V(\mathbf{r_n}) = U\delta_{\mathbf{r_n},0}$ we can then write Eq. (3.25) as

$$\begin{aligned}\psi_E(\mathbf{r}) &= \psi_E^0(\mathbf{r}) + \sum_{n=1}^{\infty} U^n G_{\mathbf{K}}(E,0)^{n-1} G_{\mathbf{K}}(E,\mathbf{r}) \\ &= \psi_E^0(\mathbf{r}) + 2J \times G_{\mathbf{K}}(E,\mathbf{r})\frac{U}{2J}\sum_{n=0}^{\infty}\left(\frac{U}{2J}\right)^n (2J \times G_{\mathbf{K}}(E,0))^n.\end{aligned} \tag{3.26}$$

The geometric series $\sum_{n=0}^{\infty} x^n = \frac{1}{1-x}$ for $|x| < 1$ and so the sum in Eq. (3.26) gives

$$\sum_{n=0}^{\infty}\left(\frac{\alpha_{\mathbf{K}}U}{2J}\right)^n = \frac{1}{1-\alpha_{\mathbf{K}}U/2J} \tag{3.27}$$

with $\alpha_{\mathbf{K}} = 2J \times G_{\mathbf{K}}(E,0)$ and we obtain

$$\psi_E(\mathbf{r}) = \exp(i\mathbf{k}\mathbf{r}) - 8\pi J f_E(\mathbf{K})G_{\mathbf{K}}(E,\mathbf{r}) \tag{3.28}$$

with scattering amplitude

$$f_E(\mathbf{K}) = -\frac{1}{4\pi}\frac{U/(2J)}{1-\alpha_{\mathbf{K}}U/(2J)}, \tag{3.29}$$

and

$$G_{\mathbf{K}}(E,0) = \frac{1}{2J}\int_{-\pi}^{\pi}\frac{d\mathbf{k}}{(2\pi)^d}\frac{1}{(E-E_{\mathbf{K}})/(2J) - 2\sum_{i=1}^{d}\cos\frac{\mathbf{K}\mathbf{e}_i}{2}(1-\cos(\mathbf{k}\mathbf{e}_i))}. \tag{3.30}$$

The scattering states $\psi_E(\mathbf{r})$ correspond to two free atoms moving on the lattice and undergoing scattering processes. The corresponding energies appear as a continuum in Fig. 3.6. In order to make a connection to the scattering length in free space, we can consider the

limit of small momenta of the incoming plane wave, i.e., $\mathbf{k} \to 0$, $\mathbf{K} \to 0$ and $E \to 0$. Then $G_{\mathbf{K}}(E, \mathbf{r})$ becomes in the limit $\mathbf{r} \to \infty$

$$G_{\mathbf{K}}(E, \mathbf{r}) \sim -\frac{1}{4\pi} \frac{e^{ikr}}{r} \tag{3.31}$$

and the solution (3.28) reduces to

$$\psi_E(\mathbf{r}) \sim \psi_E^0(\mathbf{r}) + f(\mathbf{k}, \mathbf{k}') \frac{e^{ikr}}{r} \tag{3.32}$$

with the scattering amplitude

$$f(\mathbf{k}, \mathbf{k}') = -a_s = -\frac{1}{4\pi} \frac{U/(2J)}{1 - \alpha_0 U/(2J)}, \tag{3.33}$$

equivalent to the s-wave scattering length a_s, while the constant $\alpha_0 = \lim_{E \to 0}(\alpha_{\mathbf{K}})$ becomes $\alpha_0 \approx -0.25$ [CSERTI (2000)].

Bound States

Note that the scattering amplitude in Eq. (3.28) contains a pole, associated with a bound state. We now focus on these bound states in the regime, $U > 0$, which will correspond to a repulsively bound pair. First we note that we can write Eq. (3.13) in the form

$$[E - E_{\mathbf{K}} - H_0] G_{\mathbf{K}}(E, \mathbf{r}) = \frac{1}{G_{\mathbf{K}}(E, 0)} \delta_{\mathbf{r},0} G_{\mathbf{K}}(E, \mathbf{r}), \tag{3.34}$$

because $G_{\mathbf{K}}(E, 0) = \delta_{\mathbf{r},0} G_{\mathbf{K}}(E, \mathbf{r}))$. As a consequence, the function $\psi_{\mathbf{K}}^{\mathrm{BS}}(\mathbf{r}) = G_{\mathbf{K}}(E, \mathbf{r})$ is a solution of the Schrödinger equation if the self-consistency relation is satisfied

$$U = \frac{1}{G_{\mathbf{K}}(E, 0)}, \tag{3.35}$$

which determines the energy E_{BS} of the bound state $\psi_{\mathbf{K}}^{\mathrm{BS}}$. The resulting bound state wavefunction, $\psi_{\mathbf{K}}^{\mathrm{BS}}(\mathbf{r})$ falls off exponentially for large r, and describes a bound two particle state traveling with center of mass momenta $\mathbf{K}$ through the lattice. The momentum distribution of this bound state is then given by $G_{\mathbf{K}}(E_{\mathrm{BS}}, \mathbf{k})$

$$\tilde{\psi}_{\mathbf{K}}^{\mathrm{BS}}(\mathbf{k}) = \frac{1}{E_{\mathrm{BS}} - E_{\mathbf{K}} - \epsilon_{\mathbf{K}}(\mathbf{k})}. \tag{3.36}$$

Note, that this wavefunction is not normalized. In three dimensions, Eq. (3.35) only has a solution for interaction strengths above a critical value, $U > U_c = -2J/G(0,0) \approx 8J$, and thus we require $U > U_c$ for the formation of the bound two-particle state. The energy E_{BS} can thereby be calculated from a integration over the first Brillouin zone with the volume $\mathcal{V}_0 = (2\pi/a)^d$ for a d-dimensional cubic lattice

$$G(E, 0) = \int \frac{\mathrm{d}\mathbf{k}}{\mathcal{V}_0} \frac{1}{E_{\mathrm{BS}} - E_{\mathbf{K}} - \epsilon_{\mathbf{K}}(\mathbf{k})} = \frac{1}{U}. \tag{3.37}$$

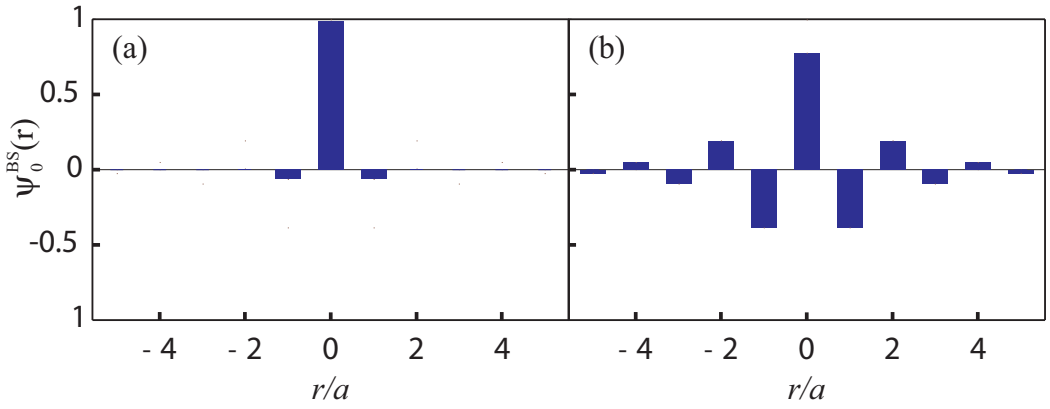

Figure 3.5:
Wavefunctions $\psi_{\mathbf{K}}^{\mathrm{BS}}(\mathbf{r})$ showing the amplitude for various site separations for repulsively bound pairs ($a_s = 100\,a_0$) in 1D with $K = 0$. r denotes the separation between the two atoms. (a) $U/J = 30$ ($V_0 = 10\,E_r$) and (b) $U/J = 3$ ($V_0 = 3\,E_r$).

The wavefunction $\psi_{\mathbf{K}}^{\mathrm{BS}}(\mathbf{r})$ which is the Fourier transform of $\tilde{\psi}_{\mathbf{K}}^{\mathrm{BS}}(\mathbf{k})$ in Eq. (3.36) is square-integrable, as shown in Fig. 3.5. For a deep lattice, i.e. $U/J \gg 1$, bound pairs essentially consist of two atoms occupying the same site, whereas for small U/J, the pair is delocalized over several lattice sites. A main feature of the repulsive pair wavefunction is its oscillating character: the wavefunction amplitude alternates sign from one site to the next, as shown in Fig. 3.5. In quasi-momentum space this corresponds to a wavefunction which is peaked at the edges of the first Brillouin zone, which is discussed in detail in Sec. 3.5.2.
When motion is confined to one dimension the bound two particle state exists for arbitrarily small repulsive interaction $U > 0$, in contrast to the three-dimensional situation. Eq. (3.35) reduces to

$$G(E,0) = \frac{a}{4\pi J}\int_{-\pi/a}^{\pi/a} \frac{dk}{E_{\mathrm{BS}}/2J - 2\,[1-\cos(Ka/2)] - 2\cos(Ka/2)\,[1-\cos(ka)]} = \frac{1}{U}. \quad (3.38)$$

The integral in Eq. (3.38) can be easily solved (e.g. with Maple, Mathematica) and the energy of the bound pairs, computed from Eq. (3.38) is

$$E_{\mathrm{BS}}(K) = 4J\left(1+\sqrt{(\cos\frac{Ka}{2})^2 + (U/4J)^2}\right), \quad (3.39)$$

which can be seen plotted in Fig. 3.6 as Bloch band of a stable composite object *above* the continuum of two particle scattering states. The figure shows how the binding energy (separation of these states from the continuum) increases as U/J is increased, and how the curvature of the band becomes less pronounced. In the limit of strong interaction, $U \gg J$ the bound state energy reduces to $E_{\mathrm{BS}}(K) \sim 4J + U + (4J^2/U)(1+\cos Ka)$, which is consistent with our expectation of a positive binding energy U, and the center of mass energy of a composite object with an effective tunneling matrix element J^2/U.

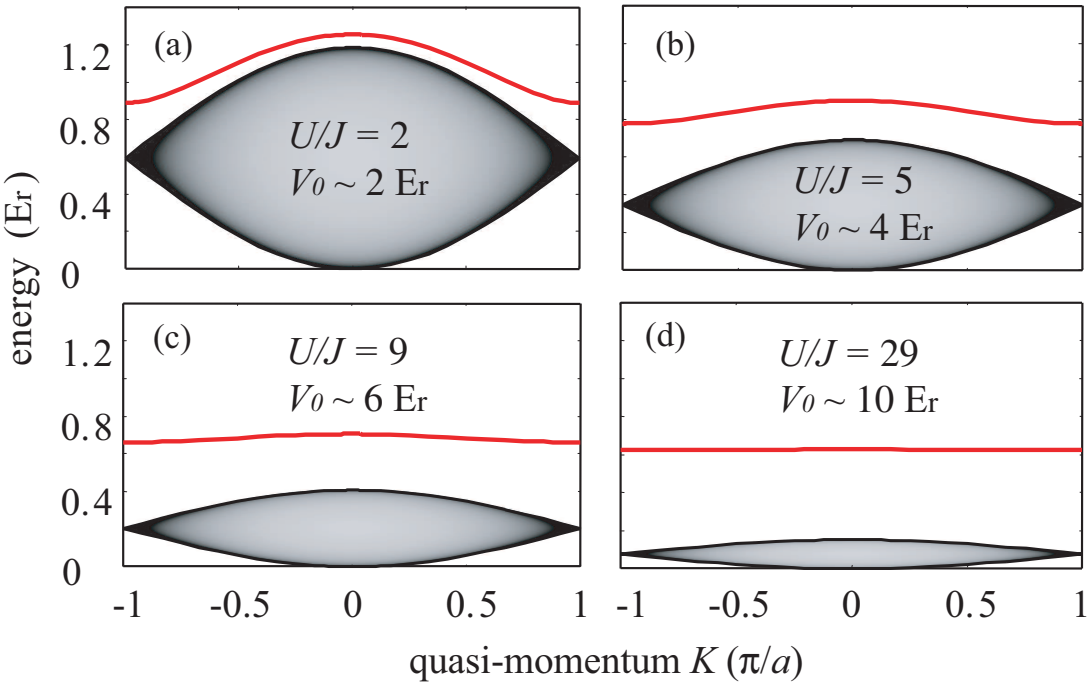

Figure 3.6:
Two particle energy spectrum in a 1D lattice for four different potential depths V_0 as a function of center of mass quasi-momentum K. The Bloch band for repulsively bound pairs is located above the continuum of unbound scattering states. The grey level for the shading of the continuum is proportional to the density of states.

3.3 Numerical simulations

We want to be able to treat not just a single repulsively bound pair, but a lattice gas of many interacting repulsively bound pairs. This is important both in order to properly describe the effects of interactions on experimental measurements, and to investigate many-body effects on the behavior of the pairs.
For that purpose, Andrew Daley and collaborators have performed numerical calculations to simulate a lattice gas of pairs. Here I only briefly discuss their approach. A more detailed discussion can be found in [HECKER DENSCHLAG AND DALEY (2006)].
In brief, the system of interacting repulsively bound pair in one spatial dimension can be treated by directly simulating the Bose-Hubbard model time-dependently, using time-dependent Density Matrix Renormalisation Group (DMRG) methods (for a review see [SCHOLLWÖCK (2005)]). Typically $10-30$ pairs in 60 lattice sites are studied. The starting point is an initial product state, corresponding to a random distribution of doubly-occupied and unoccupied lattice sites. Reducing the values of U and increasing the value of J, the same time dependence for the depth of the lattice $V_0(t)$ as in the experiment is used. The single particle momentum distributions can then be calculated efficiently from the matrix product state representation, and the results are averaged over different initial configurations, to match the averaging over different 1D tubes in the experiment. Also lattice modulation spectroscopy (see also Sec. 3.5.3) can be performed, computing the time evolution of the many-body state when the parameters U and J vary as a function of time, based on the time dependence of the lattice depth $V_0(t)$ used in our experiments.
The results of the numerical simulations are shown in the following sections in comparison with the experimental results (see e.g. Fig. 3.17 and Fig. 3.22).

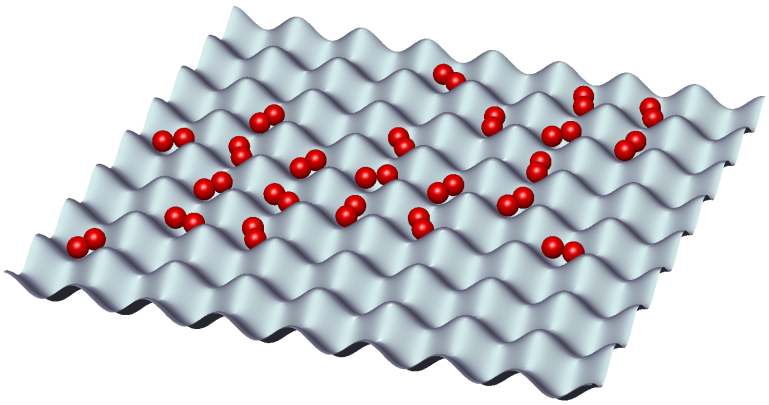

Figure 3.7:
Atom pairs in an optical lattice: the lattice sites are either empty or filled with exactly two atoms.

3.4 Production of repulsively bound pairs

In this section I will explain how we experimentally produce a sample of repulsively bound pairs. The procedure is as follows: We start with a pure sample of Rb_2 Feshbach molecules in the vibrational ground state of a three dimensional lattice. Each lattice site is occupied by not more than a single molecule (for details see section 1.4). Sweeping across a Feshbach resonance at 1007.4 G we adiabatically dissociate the molecules and obtain a lattice correspondingly filled with 2×10^4 atom pairs. Away from the Feshbach resonance, the effective interaction U between the atoms is repulsive with scattering length $a_s = +100\,a_0$. Therefore an atom pair has a positive potential energy offset $\approx U$ with respect to a state where the two atoms are separated.
We estimate the distribution of pairs in the lattice from a typical distribution of atoms in a Mott insulating state [FISHER *et al.* (1989); JAKSCH *et al.* (1998); GREINER *et al.* (2002)]. A Mott insulator with our experimental parameters has a shell like structure of singly and doubly occupied lattice sites and a core of triply occupied sites [JAKSCH *et al.* (1998)]. Crossing a Feshbach resonance, we create molecules in the multiply occupied lattice sites. Only the atoms in doubly occupied lattice sites form stable molecules. The atoms in the higher occupied lattice sites are lost due to inelastic atom-molecule collisions (for details see Sec. 1.4). Applying a cleaning procedure we are able to remove all the single atoms. Therefore we expect a shell of molecules/atom pairs. However, we loose in our cleaning procedure about 50% of the molecules (see Sec. 1.4). This leads to an estimated effective filling factor of pairs in the lattice of typically $0.3 - 0.5$.

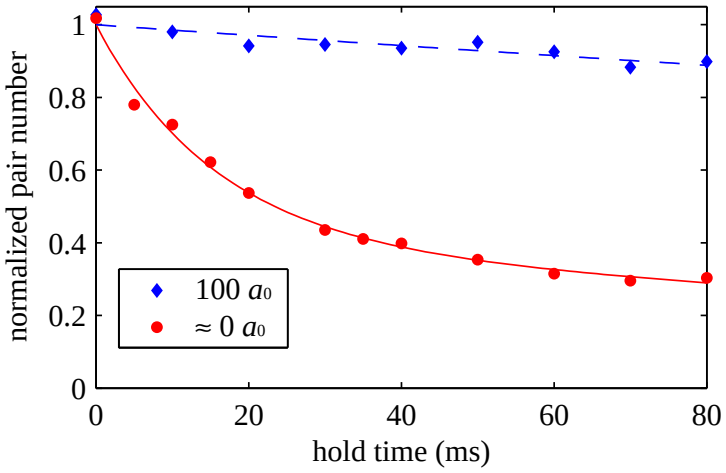

Figure 3.8:
Long lifetime of repulsively bound atom pairs that are held in a 3D optical lattice. The potential depth is $(10 \pm 0.5)\,E_r$ in one direction and $(35 \pm 1.5)\,E_r$ in the perpendicular directions. Shown is the remaining fraction of pairs for a scattering length a_s of $100\,a_0$ (diamonds) and a scattering length of about $(0 \pm 10)\,a_0$ (circles) as a function of the hold time. The lines are fitted curves of an exponential (dashed line) and the sum of two exponentials (solid line).

3.5 Experiments with repulsively bound pairs

In the following sections I will discuss the properties of the repulsively bound pairs which we experimentally investigate by measuring their lifetime, quasi-momentum distribution and binding energies. By varying the effective interaction between the atoms with the help of the Feshbach resonance we can also create lattice induced bound atom pairs which are based on attractive interactions.

3.5.1 Measurement of the pair lifetime

We measure the lifetime of the repulsively bound pairs to study their stability in various regimes. These lifetime measurements are based on adiabatically lowering the lattice depth V_0 from typically $V_0 = 35\,E_r$ to a chosen height. Then we hold the pairs for a variable time at this lattice depth. During the hold time, the pair can then potentially dissociate into two free atoms. In order to measure the remaining pair number, the lattice is adiabatically raised again to its full initial depth of $V_0 = 35\,E_r$ after the hold time. Using the Feshbach resonance, atoms in doubly occupied sites are converted to Feshbach molecules with near unit efficiency. A combined rf-light purification pulse then removes all remaining single atoms, which stem from the dissociated pairs, as in the original preparation step (see Sec. 1.4). Afterwards the molecules are again converted back into atoms, and can then be detected via conventional absorption imaging (see Sec. 1.5).

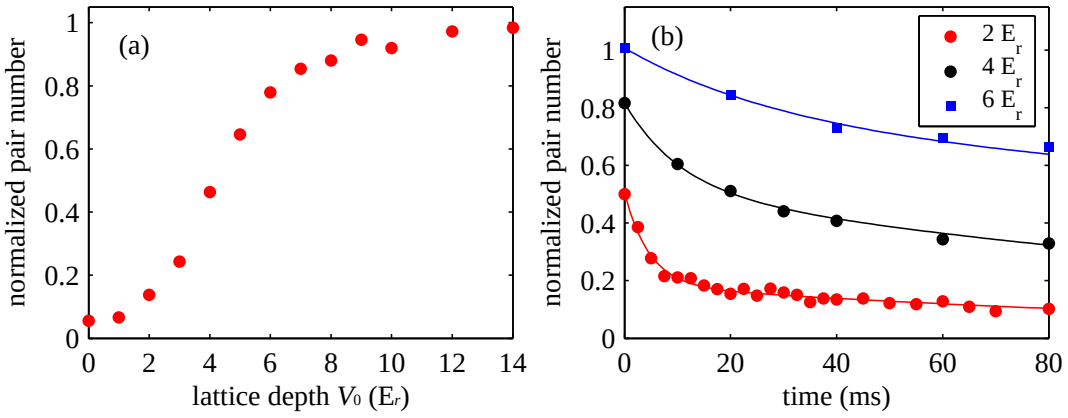

Figure 3.9:
(a) Pair stability in 1D as a function of the lattice depth V_0. For this measurement we adiabatically ramp the lattice depth V_0 in one direction in 25 ms from 35 E_r to a chosen value. After a hold time of 20 ms we ramp the lattice in another 25 ms back to 35 E_r and count the number of remaining pairs. At a V_0 below 7 E_r we observe increasing losses of pairs. (b) Loss as a function of time for a given lattice depth ($V_0 \sim 2\,E_r, 4\,E_r$ and $6\,E_r$): the decay exhibits two timescales: a fast decay within a few ms on top of a slow decay of hundreds of ms. The lines are fit curves given by the sum of two exponentials, $N_{\text{pairs}} = N_{\text{fast0}} \exp(-t/\tau_{\text{fast}}) + N_{\text{slow}} \exp(-t/\tau_{\text{slow}})$

We can observe the nature of the repulsive binding nicely in the following experiment (see Fig. 3.8): After production of the atom pairs, we allow the atoms to tunnel through the lattice along one dimension. This is done by decreasing the lattice depth in one (horizontal) direction to about 10 E_r, while the perpendicular directions remain at 35 E_r. If the on-site interaction U of the atoms is tuned to zero with the help of the Feshbach resonance, the pairs break up within a few ms, corresponding to the tunneling timescale. However, if the effective interaction between the atoms is repulsive, we observe a remarkably long lifetime of $t = 700$ ms (determined by an exponential fit). This lifetime is mainly limited by inelastic scattering of lattice photons and greatly exceeds the calculated time for an atom to tunnel from one site to the next, $h/(4J) \sim 4$ ms.
However, we observe in our experiments an increasing loss of pairs as we lower the lattice potential V_0 below a certain value. This is shown in Fig. 3.9. For this measurement we adiabatically change the lattice depth V_0 (one horizontal direction) in 25 ms from 35 E_r to a chosen value. After a hold time of 20 ms we ramp the lattice in another in 25 ms back to 35 E_r and count the number of remaining pairs. As one can see in Fig. 3.9, the loss of pairs starts below a 1D lattice depth of $\sim 7\,E_r$.
The decay of pairs below this lattice height of 7 E_r exhibits two timescales: a fast decay within a few ms on top of a slow decay of hundreds of ms (see Fig. 3.9 (b)). We fit the data in Fig. 3.9 (b) with the sum of two exponentials, $N_{\text{pairs}} = N_{\text{fast0}} \exp(-t/\tau_{\text{fast}}) + N_{\text{slow}} \exp(-t/\tau_{\text{slow}})$. The timescale of the fast decay (τ_{fast}) depends on the lattice depth

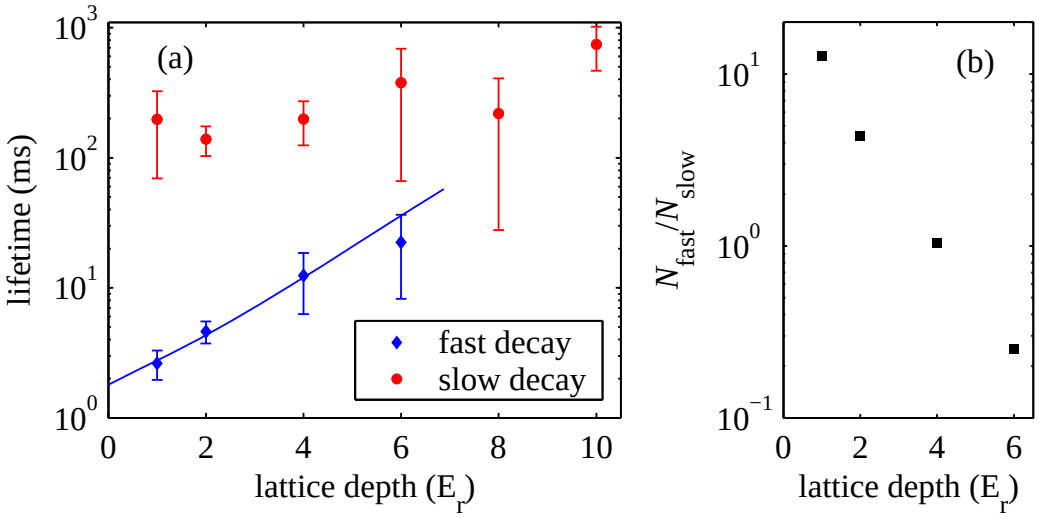

Figure 3.10:
(a) Lifetime of the pairs as a function of lattice depth. The data points are the results of fitting a sum of two exponential curves to data similar to the one shown in Fig. 3.9 (b). The experimental error bars correspond to the 95% confidence interval for the fit parameters. The blue line is given by $h/(\Delta E_{\mathrm{BS}} \cdot 4.8)$ (see text). (b) The number of fast decaying (N_{fast}) and slow decaying pairs (N_{slow}) crucially depends on the lattice depth.

while the timescale of the slow decay (τ_{slow}) is constant within the error-bars (see Fig. 3.10 (a)). The initial number of pairs is reduced for lattice depths below $6\,E_r$, as one can see in Fig. 3.9 (b). This is because some of the pairs decay already while we ramp the lattice to its final depth in 25 ms. Therefore, the "correct" number of fast decaying pairs is given by $N_{\mathrm{fast}} = N_0 - N_{\mathrm{slow}}$, where N_0 is the number of pairs without changing the lattice depth. The number of fast decaying (N_{fast}) and slow decaying pairs (N_{slow}) crucially depends on the lattice depth, as one can see in Fig. 3.10 (b).

Possible explanation for the pair decay

Theoretically, single repulsively bound pairs in 1D can not spontaneously decay into the continuum even for arbitrarily low lattice depths because the binding gap never completely vanishes (see Fig. 3.11). In the following, I conceptualize possible scenarios which could explain a decay of pairs as inelastic scattering processes and a resonant decay due to external gradients.

Inelastic scattering

It is possible that the pairs decay in an inelastic scattering process. This can be explained best with an example: Let's assume, two pairs with a total momentum of $K_1 = \pi/a$ and $K_2 = -\pi/a$ scatter. In the scattering process of the two pairs the momentum has to be

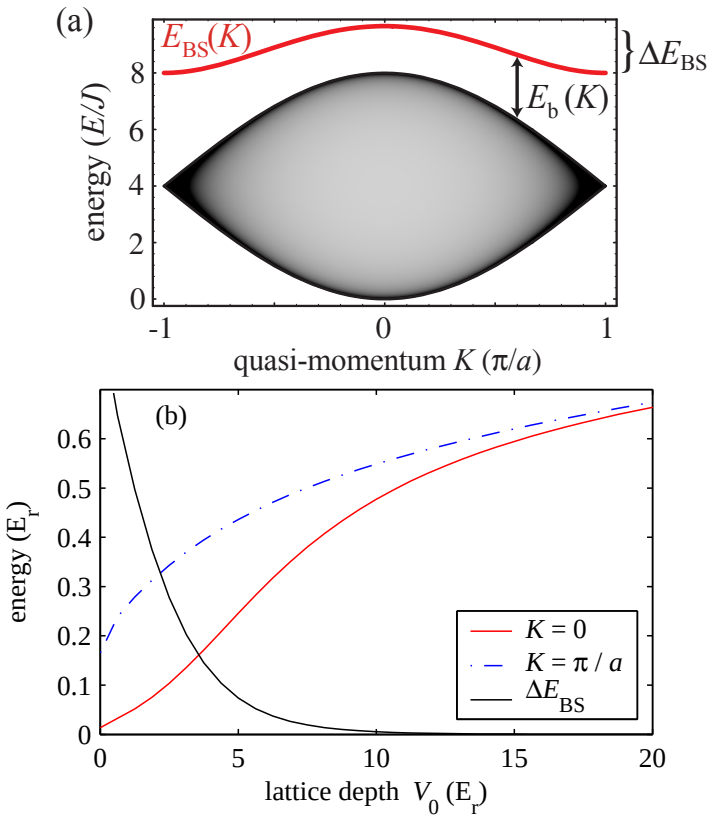

Figure 3.11:
(a) Two particle energy spectrum in a 1D lattice as a function of center of mass quasi-momentum K. The Bloch band for repulsively bound pairs (red line) is located above the continuum of unbound scattering states (grey area). The width of the Bloch band for pairs is ΔE_{BS}. (b) Positive "binding" energy of the pairs in 1D as a function of the lattice depth V_0 for a total quasi-momentum K of 0 (red solid line) and π/a (blue dashed line). This binding energy is dependent on the total momentum of the pair and is given by $E_b(K) = E_{BS}(K) - 8J(1+\cos(K\,a/2))$. Black line: Width of the Bloch band for pairs ΔE_{BS} as a function of the lattice depth.

conserved, $K_1 + K_2 = \tilde{K}_1 + \tilde{K}_2$. For $\tilde{K}_1 = \tilde{K}_2 = 0$, one of the pairs can increase its energy by ΔE_{BS}. ΔE_{BS} is the width of the Bloch band for a pair (see Fig. 3.11). Due to energy conservation the second pair can now decay into the scattering continuum of two free atoms (grey area in Fig. 3.11 (a)) if its resulting energy

$$E_{BS}(K = \pm\pi/a) - \Delta E_{BS} \leq 8J, \tag{3.40}$$

with $8J$ the kinetic energy which two free atoms in the lowest Bloch band of the lattice can maximally have. This energy is equal to two times of the width of the lowest Bloch band for atoms which is given by $4J$.
The calculated critical lattice depth for the condition ($E_{BS}(K = \pm\pi/a) - \Delta E_{BS} = 8J$) is about

$4.5\,E_r$. Below this value we can expect inelastic two body scattering processes which lead to a decay of pairs. This value of $4.5\,E_r$ is calculated for a three dimensional lattice with a variable lattice depth in one direction. The lattice depth in the two perpendicular directions is kept at $35\,E_r$. These are typical settings for our 1D measurements.
Initially only pairs with a $K \sim \pm\pi/a$ can decay, because in a inelastic scattering process one of the pairs can increase/decrease its energy by the maximum possibly energy ΔE_{BS}. In a scattering processes of two pairs with a $K < \pm\pi/a$ this amount of energy is smaller, corresponding to their momentum K (see Fig. 3.11 (b)). Two pairs with an initial momentum $K = 0$ can not decay in the two body scattering process, because an increase/decrease of energy is not possible.
We can explain the fast decay by the fact that initially only pairs with a $K \sim \pm\pi/a$ can decay in an inelastic scattering process, as discussed before. With a decreasing lattice depth more and more pairs have a momentum K which allows the decay in a scattering process. The timescale of the fast decay should depend on the tunneling rate of the pairs, but also on the distribution of the pairs in the lattice. In fact, we observe an exponentially decreasing τ_{fast} for a decreasing lattice depth (see Fig. 3.10 (a), blue diamonds). This is what we expect since the tunneling rate exponentially decreases with a decreasing lattice depth. The tunneling rate for pairs is proportional to the width of the Bloch band for pairs ΔE_{BS} ($\approx 4J^2/U$ for $U \gg J$) (see Fig. 3.11 (b), black line) and is given by $\Delta E_{BS}/4\hbar$. The calculated time for a pair to tunnel from one site to the next is given approximately by $h/\Delta E_{BS}$. In fact, the measured timescale of the fast decay τ_{fast} scales like the calculated tunneling time for pairs ($\propto 1/J^2$) and not like the tunneling time for atoms ($\propto 1/J$). This is shown in Fig. 3.10 (a): the calculated tunneling times for pairs agree with the measured timescale of the fast decay (τ_{fast}) if we multiply the calculated values with a certain factor (= 4.8) (blue line). Note that this factor is taken just to compare the scaling of the data.
The slow decay could stem from a momentum re-distribution in the lattice under the influence of an external force F. An external force could lead to Bloch oscillations of the pairs with a timescale which is proportional to this force. The timescale of the oscillations is given by $\tau_{Bloch} = h/(|F|a)$, with a the lattice spacing [BEN DAHAN *et al.* (1996)]. The pairs constantly change their momentum K during the Bloch oscillations. With the "right" momentum K the pairs can decay again in a scattering process.
The origin of the force F could be the radial confinement due to the beam shape of the lattice laser beams. The effective potential of this radial confinement is in a harmonic approximation $V_{ext} \approx V_0 \cdot 2r^2/w^2$, with r the distance from the trap center and w the waist of the lattice laser beams (see also Sec. 1.3). If we lower the lattice in 1D the radial confinement of the two perpendicular lattice beams is always present. This confinement leads to an effective potential of $V_{ext} = 4 \cdot 35\,E_r \cdot r^2/w^2$ for a lattice depth of $35\,E_r$ of the perpendicular lattices. The external force, which is given by the gradient of the potential V_{ext}, is $F = dV_{ext}/dr = 8 \cdot 35\,E_r \cdot r/w^2$. This force leads e.g. to a oscillation timescale $\tau_{Bloch} \approx 7$ ms for atoms which are 10 µm displaced from the trap center.
The energy difference ΔE_{lat} from lattice site to lattice site due to the radial confinement of the lattice laser beams is about $\pm 0.1\,E_r$ for a this distance ($r \approx \pm 10$µm) from the trap center.
The time scale of the oscillation should be independent of the one dimensional lattice

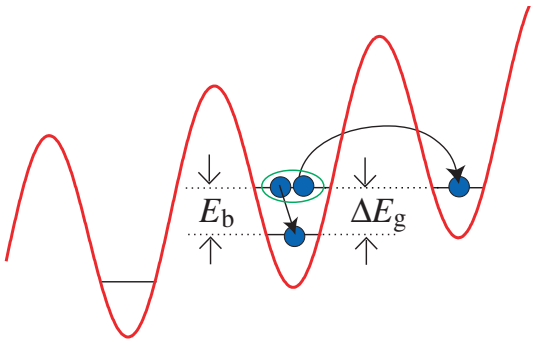

Figure 3.12:
Lattice with a gradient: an atom pair can resonantly decay if its energy is equal to the energy of two free atoms in the lattice. This is the case for $E_b = \Delta E_g$, where ΔE_g is the energy difference from lattice site to lattice site. Note, that the energy of the pair as a compound object shifted by E_b relative to the energy of a single atom in the lattice.

depth because the external confinement is mainly determined by the perpendicular lattice laser beams. In fact, we observe in our measurements that the timescale τ_{slow} of the slow decay does not depend on the 1D lattice depth within the error bars (see Fig. 3.10 (a), red circles).
Additionally to the gradient which is caused by radial confinement of the laser beams, we have a magnetic field gradient due to the inhomogeneity of the "homogeneous" bias field of about 1000 G. The magnetic field gradient leads to a inhomogeneity of about $\Delta B \approx 20\,\mathrm{mG}$ over the molecular cloud (see also Sec. 2.6). However, in a current measurement we found out that the magnetic field gradient is mainly along one horizontal lattice direction where we keep the lattice high during the 1D measurements[1]. In the lattice direction where we lower the lattice depth, the magnetic field gradient ΔB should be $< 5\,\mathrm{mG}$. This value corresponds to an energy $\Delta E_{mag} = \mu \cdot \Delta B < 10\,\mathrm{kHz} \cdot h$, with $\mu \approx h \cdot 2\,\mathrm{MHz/G}$ the magnetic moment of the atoms at a magnetic field of about 1000 G. Assuming a cloud size of about 20 µm in 1D, the energy difference ΔE_{mag} would lead to energy shift $< 0.05\,E_r$ from lattice site to lattice site.

Resonant decay

The external gradients could be the origin of an additional decay channel for the pairs. This can be explained as follows: The decay of the atom pair occurs as one of the atoms "tunnels" into a neighboring lattice site. However, the neighboring sites are shifted due to the gradients by $|\Delta E_g| = |\Delta E_{lat} + \Delta E_{mag}|$ (see Fig. 3.12). A single atom pair can resonantly decay if its energy is equal to the energy of two free atoms in the lattice. This is the case for $E_b = |\Delta E_g|$ (see Fig. 3.12). Assuming an external gradient $|\Delta E_g|$ of up to $0.3\,E_r$ per lat-

[1]The position of the cloud was displaced by about 150 µm relative to the symmetry center of the quadrupole coils in the direction of the lattice beam 1 (see Fig. 1.6)

tice constant (from site to site), the pairs could decay due to this resonant process below a lattice depth of $7\,E_r$. Note, that ΔE_g depends on the position of the pairs in the lattice and $E_b(K)$ depends on the total moment K of the pair (see Fig. 3.9). Therefore also the pair decay due to this resonant process should be dependent on the total momentum K and the pair position in the lattice.
The effect of an external gradient can be seen when we lower the lattice depth V_0 simultaneously in all three directions. In this case we have a known energy difference $|\Delta E_g|$ of about $0.27\,E_r$ from lattice site to lattice site in the vertical direction due to the gravitation potential. Additionally we have a gradient due the radial confinement of the laser beams and a magnetic field gradient, as discussed before. However, if we lower the lattice depth V_0 in all three directions also the radial confinement is reduced and $|\Delta E_{lat}|$ should be $< 0.05\,E_r$.
As shown in Fig. 3.13 (a), we observe increasing losses of pairs already below a V_0 of $\sim 15\,E_r$. For this measurement we adiabatically ramp the lattice depth V_0 in 5 ms from $35\,E_r$ to a chosen value. After a hold time of 5 ms we ramp the lattice in another 5 ms back to $35\,E_r$.
The pairs can resonantly break up if the binding energy of the pair is equal to this energy difference $|\Delta E_g|$ of about $0.27\,E_r$ from site to site (horizontal dashed line). For pairs with a total momentum $\mathbf{K} = 0$ this breaking up can already happen at a lattice depth of $\sim 15\,E_r$ (Fig. 3.13 (b), right vertical dashed line), for pairs with a total momentum $\mathbf{K} = (\pi, \pi, \pi)/a$ this happens at $\sim 11\,E_r$ (Fig. 3.13 (b), left vertical dashed line). This assumption explains very well the observed behavior in Fig. 3.13. The "positive" binding energies of the pairs in 3D are calculated with Eq. (3.37).
However, we observe that we do not loose more than $\sim 80\%$ of the pairs even if we go to low values of the lattice potential ($V_0 < 10$). A possible explanation is that some of the atoms could be randomly paired in the lattice sites when we ramp up again the lattice.
Additional measurements and numerical simulations of the Hubbard model should be able to test these assumptions on the pair decay.

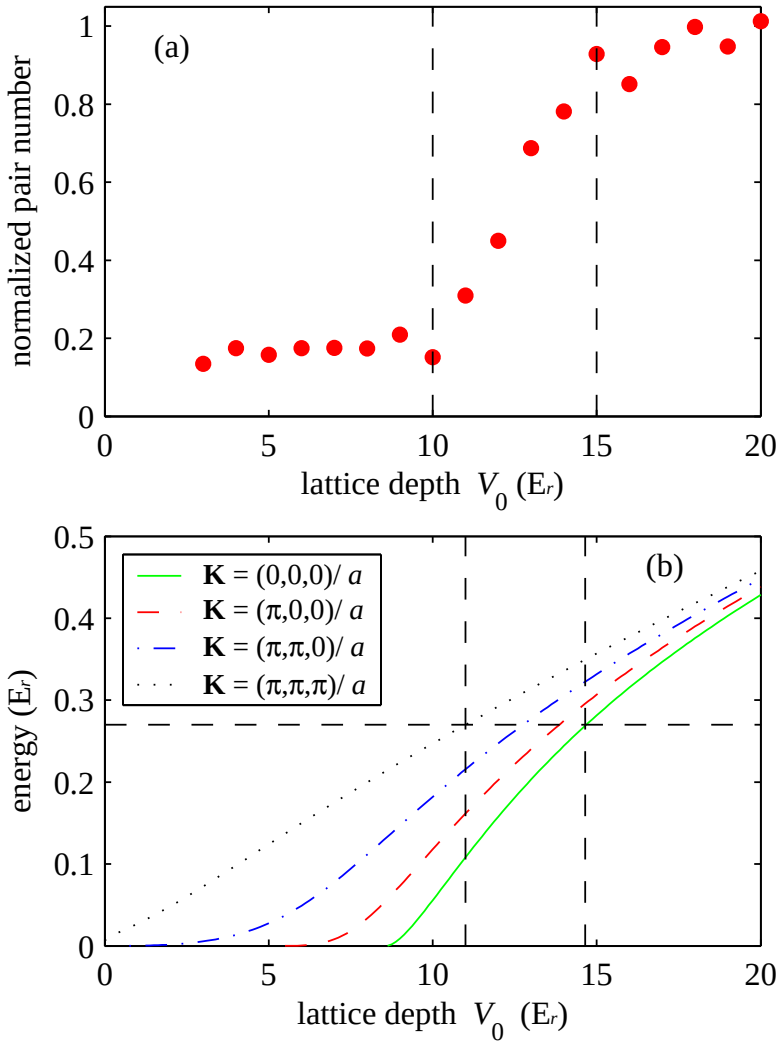

Figure 3.13:
(a) Pair stability as a function of the 3D lattice depth V_0. For this measurement we adiabatically ramp the lattice depth of all three lattice beams in 5 ms from 35 E_r to a chosen value V_0. After a hold time of 5 ms we ramp the lattice in another in 5 ms back to 35 E_r. We observe increasing losses of pairs already below a V_0 of ~ 15 E_r (right dashed line) compared to the case where we lower the lattice only in one dimension (see Fig. 3.9). For lattice depths below ~ 10 E_r (left dashed line) the number of remaining pairs is constant (see text). (b) Positive "binding" energy of the pairs as a function of the 3D lattice depth V_0 for different total momenta **K**. Due to the gravitation potential we have a mean energy difference of about 0.27 E_r from lattice site to lattice site in the vertical direction. If the binding energy of the pair is equal to this mean energy difference of 0.27 E_r (horizontal dashed line) the pair can break up. For pairs with a total momentum **K** = 0 this happens already at ~ 15 E_r (right vertical dashed line), for pairs with a total momentum **K** = $(\pi,\pi,\pi)/a$ this happens at ~ 11 E_r (left vertical dashed line).

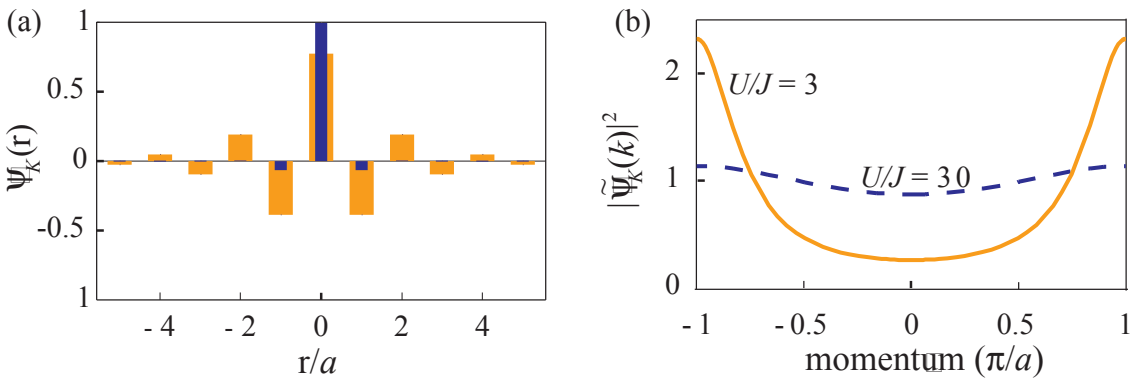

Figure 3.14:
(a) The pair wavefunction $\psi_K^{\mathrm{BS}}(r)$ for $K = 0$, showing the amplitude at each site with $U/J = 30$ ($V_0 \approx 10\,\mathrm{E_r}$, blue bars) and $U/J = 3$ ($V_0 \approx 3\,\mathrm{E_r}$, orange bars). (b) The square modulus of the corresponding momentum space wavefunctions $|\psi_K^{\mathrm{BS}}(k)|^2$ for $K = 0$. This momentum space wavefunctions are equivalent to the single-particle momentum distributions. Note the characteristic peaks at the edge of the Brillouin zone.

3.5.2 Quasi-momentum distribution

For a deep lattice an atom pair consists of two atoms occupying a single lattice site. However, for a shallow lattice the single atoms of a pair are not any more localized in one lattice site: the atom pair wavefunction is "smeared out" over many lattice sites. This one can see in Fig. 3.14 (a): the pair wavefunction $\psi_K^{\mathrm{BS}}(r)$ in relative coordinates is delocalized over many lattice sites, depending on the lattice depth V_0. A main feature of the repulsive pair wavefunction $\psi_K^{\mathrm{BS}}(r)$ is its oscillating character: the wavefunction amplitude alternates sign from one site to the next. However, this wavefunction $\psi_K^{\mathrm{BS}}(r)$ is not directly measurable.
But how can we get experimentally information on the pair wavefunction? It turned out that we can measure the quasi-momentum distribution of the pairs by a time of flight measurement. For such a measurement we simply have to ramp down the lattice potential. The ramp speed has to be rapidly enough for the pair wavefunction not to change, but slow enough such that the population of the energy bands is not changed during the ramp. A state with quasi-momentum q is then mapped to a state with free particle momentum $p = q$ as the lattice is turned off. The free particle momentum p is finally converted onto a spatial distribution by making a picture of the expanded cloud after ballistic expansion [GREINER *et al.* (2001); HECKER DENSCHLAG *et al.* (2002); GREINER (2003)].
The quasi-momentum distribution of individual atoms is directly given by the square modulus of the corresponding momentum space wavefunction $|\tilde{\psi}_K^{\mathrm{BS}}(k)|^2$ (see Fig. 3.14 (b)). The momentum space wavefunction $\tilde{\psi}_K^{\mathrm{BS}}(k)$ is given by the Fourier transform of $\psi_K^{\mathrm{BS}}(r)$. The alternating sign of the amplitude of $\psi_K^{\mathrm{BS}}(r)$ leads to a momentum space wavefunction $\tilde{\psi}_K^{\mathrm{BS}}(k)$ which shows characteristic peaks at the edges of the Brillouin zone (see Fig. 3.14 (b)).

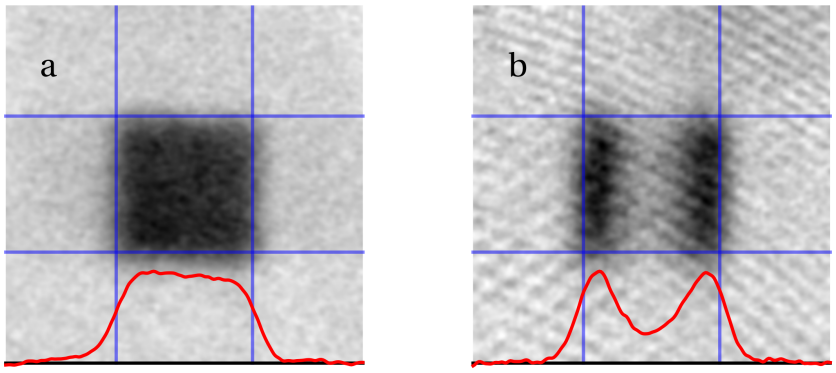

Figure 3.15:
Absorption images of the atomic distribution after release from a 3D lattice and a subsequent 15 ms time of flight. The horizontal and vertical dashed lines enclose the first Brillouin zone. (a) For this measurement we prepared atoms in a 3D lattice with only singly occupied sites. The observed momentum distribution is flat. This is reminiscent for a dephased ensemble of ultracold atoms in the lowest band of a lattice [GREINER *et al.* (2001)]. (b) The repulsively bound pairs show a momentum distribution which is peaked at the edges of the Brillouin zone. This characteristic is a clear signature of the wavefunction for repulsively bound pairs. For both measurements the lattice depth is adiabatically lowered in 1D to a value below 3 E_r.

The amplitude of the peaks grows with increasing width $4J$ of the Bloch band.
Using this technique of mapping the quasi-momentum to free particle momentum we have experimentally investigated the quasi-momentum distribution of the pairs in various regimes. For these measurements, we first adiabatically lower the lattice depth in a horizontal direction at a rate of 1.3 E_r/ms to a pre-chosen height V_0 while the lattice depth in the other two directions are kept high (35 E_r). This will prepare repulsively bound pairs at the chosen lattice depth. We then turn off the lattice rapidly with linear ramps with rates of 0.2 E_r/µs. The resulting momentum distribution is then converted onto a spatial distribution after typically 15 ms time of flight.
In Figure 3.15 one can nicely see the the different momentum distribution of atom pairs and single atoms after release from a 3D lattice and a subsequent 15 ms time of flight. For the single atoms the observed momentum distribution is flat (see Fig. 3.15 (a)). This is reminiscent for a dephased ensemble of ultracold atoms in the lowest band of a lattice [GREINER *et al.* (2001)]. However, the repulsively bound pairs show a momentum distribution which is peaked at the edges of the Brillouin zone (see Fig. 3.15 (b)). This characteristic pattern is a clear signature of the wavefunction for repulsively bound pairs.

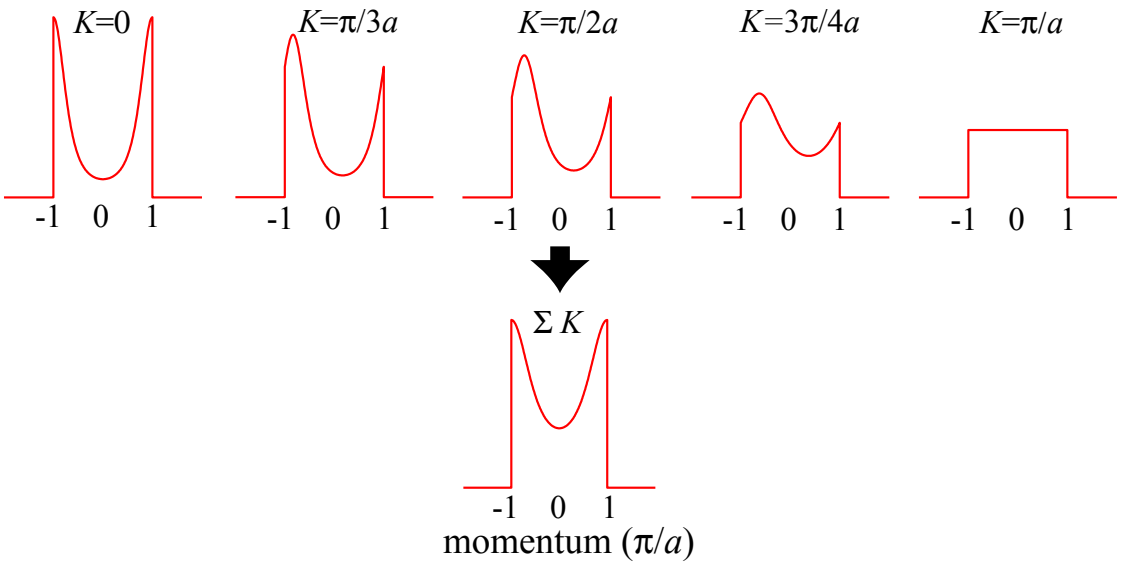

Figure 3.16:
Calculated single atom quasi-momentum distributions for different total quasi-momenta K and a lattice depth $V_0 = 5\,\mathrm{E_r}$. The curve below is the sum of all the different quasi-momentum distributions for different K, assuming a homogeneous distribution of K from $-\pi/a$ to π/a.

It is important to note that we measure the distribution of single atom quasi-momenta in a large sample. For atom pairs with a fixed center of mass quasi-momentum $K = k_1 + k_2$ ($\rightarrow k = k_1 - K/2$), the quasi-momentum distribution of the individual atoms is given by

$$\begin{aligned} \mathrm{P} &= \left|\tilde{\psi}_K^{\mathrm{BS}}(k)\right|^2 = \left|\tilde{\psi}_K^{\mathrm{BS}}(k_1 - K/2)\right|^2 = \left|\frac{1}{E_{\mathrm{BS}} - E_K - \epsilon_K(k_1 - K/2)}\right|^2 \\ &= \left|\frac{1}{4J} \cdot \frac{1}{\sqrt{(\cos(Ka/2))^2 + (U/4J)^2} + \cos(Ka/2)\cos((k_1 - K/2)\cdot a)}\right|^2, \end{aligned} \tag{3.41}$$

where k_1 ranges from $-\pi/a$ to π/a.
Note, that Eq. (3.41) provides the same result for $k = -(k_2 - K/2)$ as for $k = k_1 - K/2$ because of the symmetry of the cosine-function ($\cos(k\,a) = \cos(-k\,a)$).
The observed momentum distribution of the atoms is an average over a distribution of center of mass quasi momenta K. That we still obtain the peaked distribution characteristic of repulsively bound pairs is non-trivial. In fact, if we just take a single repulsively bound pair with center of mass quasi-momentum $K \neq 0$, its single atom quasi-momentum distribution will not be peaked anymore at the edges of the first Brillouin zone (see Fig. 3.16). The peak will be somewhat translated towards the center of the first Brillouin zone. Fortunately, with increasing $|K|$, the peak in the single-particle quasi-momentum distribution also becomes less pronounced and vanishes at $K = \pi/a$. As a

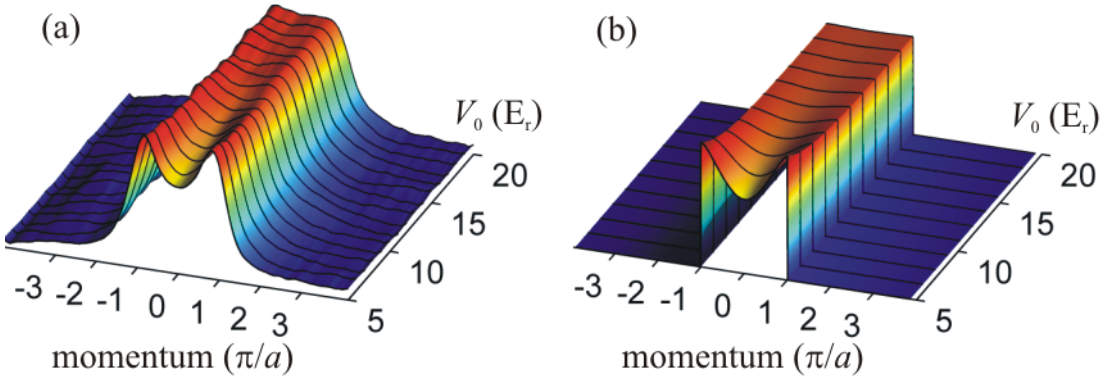

Figure 3.17:
Quasi-momentum distributions of atoms in the lattice as a function of lattice depth V_0. (a) The single lines show the corresponding quasi-momentum distributions in the horizontal-direction, after integration over the vertical-direction of the absorption pictures (see e.g. Fig. 3.15). (b) For comparison numerical simulations are shown. The density values have been scaled to facilitate comparison between experimental and theoretical results.

result, when we average over a roughly uniform distribution of center of mass quasi momenta K for a dilute gas of repulsively bound pairs, we still observe the pronounced peaks at the edges of the Brillouin zone.
Figure 3.17 shows in a continuous fashion the dependence on the 1D lattice depth V_0 of the quasi-momentum distribution for repulsively bound pairs for both experiment and numerical simulation. The peak structure is more pronounced for lower values of V_0, and diminishes for larger V_0. When the two particles are localized on the same site, the quasi-momentum distribution is essentially flat. This one can see in Fig. 3.17: for deep lattices we observe a homogenously filled first Brillouin zone and the quasi-momentum distribution has a flat top shape. However, for a shallow lattice the pair wavefunction $\psi_K^{\mathrm{BS}}(r)$ is delocalized over many lattice sites and the quasi-momentum distribution shows the characteristic peaks at the edges of the Brillouin zone.
The agreement between experimental data and theoretical simulations is quite good, as one can see in Fig. 3.17. However, it turned out that the simulated momentum distributions depend on the distribution of the pairs in the lattice. This is because the interaction between the single pairs can influence the distribution of the total momentum K. Therefore, the numerical simulations do not provide exactly the same results as the calculations for a single pair (see Fig. 3.16).
Additionally one can see in Fig. 3.17 that the experimental distributions appear to extend beyond the first Brillouin zone. This is an experimental artifact related to the quick turning off of the lattice and can be understood as follows: The adiabaticity criterion for the transfer from the lowest into the n^{th} energy band of a non interacting gas is given by

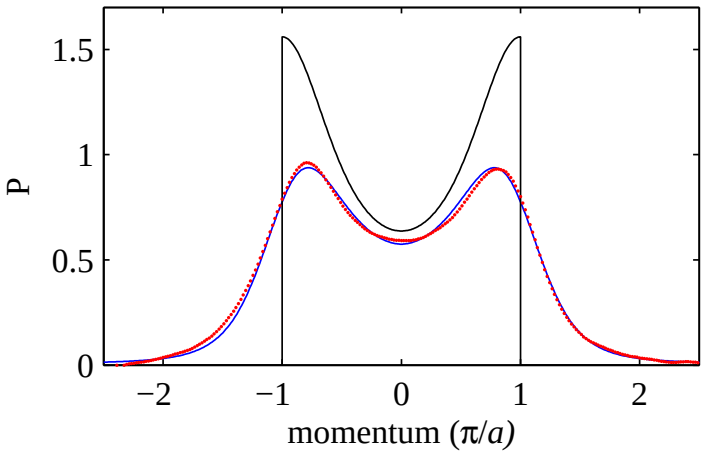

Figure 3.18:
Comparison between a measured and a calculated momentum distribution. We prepare for the measurement the repulsively bound pairs at the 1D lattice depth of $5\,E_r$. We then turn off the lattice rapidly with linear ramps with rates of $0.2\,E_r/\mu s$. The measured distribution (red dots) is the same as in Fig. 3.17 at that initial lattice depth V_0. The measured momentum distribution nicely agrees with the simulated single atom momentum distribution which includes the excitation into higher bands (blue solid line). The single atom momentum distribution without excitation is given by the black solid line (see text).

[HECKER DENSCHLAG *et al.* (2002)]:

$$|\langle n,q|dH/dt|0,q\rangle| \ll |E_{n,q}-E_{0,q}|^2/\hbar, \tag{3.42}$$

where $|n,q\rangle$ is the Bloch state with the quasi momentum q in the n^{th} energy band. H is the Hamilton operator for a particle in a periodic potential (see Eq.(3.1)).
In the case of ($q \sim 0$) the energy difference of first ($n=0$) and second ($n=1$) band remains finite even for very low lattice depths V_0 ($(E_{1,0}-E_{0,0}) \geq 4\,E_r$ for any V_0). Condition (3.42) then reads [HECKER DENSCHLAG *et al.* (2002)]

$$\frac{d}{dt}V_0/E_r \ll 16\,E_r/\hbar \sim 5\cdot 10^5 s^{-1}. \tag{3.43}$$

However, at the borders of the first Brillouin zone ($q \sim \pm\pi/a$), the gap between the the first and second Bloch band gets very small for low lattice depths since $|E_{1,(\pm\pi/a)}-E_{0,(\pm\pi/a)}|=0$ for $V_0=0$. Therefore, our turning off of the lattice with a ramp speed of $\frac{d}{dt}V_0/E_r \sim 2\cdot 10^5 s^{-1}$ is too fast as q approaches the Brillouin zone boundary.
This means that especially the single atoms with a quasi-momentum $q=k_{1,2}\sim\pm\pi/a$ can populate the second Bloch band. This leads to smearing out of the sharp structure at the edge of the Brillouin zone what can be clearly seen in Fig. 3.18: The measured momentum

distribution (red dots) extends beyond the first Brillouin zone and does not agree exactly with the calculated single atom quasi-momenta (black line) for that lattice depth (~5 E_r). However, we can simulate the turning off of the lattice and determine the probability to excite a particle with a certain momentum q to higher Bloch bands. This is realized by numerically calculating the time dependent evolution of the single particle Hamiltonian H of a 1D lattice. We can determine with this method the probability, as a function of the initial quasi-momentum q, that an atom has a momentum $p = q + 2n\hbar k_{\mathrm{lat}}$ after switching off the lattice. The atom distribution in the corresponding Brillouin zones is determined by multiplying this probability with the single atom quasi-momentum distribution for an initial lattice depth V_0 (see Fig. 3.18, black line). The result of this calculation is given by the blue solid line in Fig. 3.18. The observed momentum distribution nicely agrees with this prediction of the single atom momentum distribution which includes the excitation into higher bands (blue solid line).

Quasi-momentum distribution in 3D

Figure 3.17 shows the peaked structure of the momentum distribution in the 1D case. But what happens if we lower the lattice simultaneously in all three directions from the same lattice depth? It turns out, that such a measurement is much more complicated for us because the pairs decay below a 3D lattice depth of about 15 E_r, as discussed in Sec. 3.5.1. Therefore, we are not able to prepare the sample of pairs at a certain 3D lattice depth below 15 E_r and above this value the momentum distribution is essentially flat. However, if we ramp the lattice relatively fast (in a few ms) from a lattice depth above 15 E_r to zero we observe a momentum distribution which is peaked at the corners of the Brillouin zone, as shown in Fig. 3.19 (a). We are able observe this feature because the ramp speed is faster then the pair decay occurs. However, we can not attribute the momentum distribution to a certain 3D lattice depth. The observed momentum distribution corresponds presumably to a pair quasi-momentum distribution for a lattice depth below 5 E_r.
Figure 3.19 (b) shows for a comparison the calculated quasi-momentum distribution of pairs in a lattice with a depth of 5 E_r. The simulated quasi-momentum distribution shows also prominent peaks in the corners of the first Brillouin zone. This confirms the peaked structure of the observed momentum distribution.

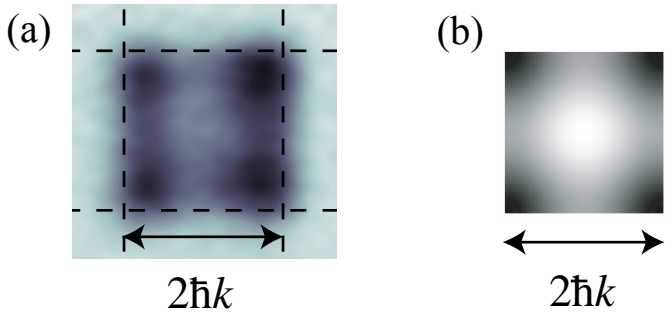

Figure 3.19:
(a) Absorption image of the atomic distribution after release from the 3D lattice and a subsequent 15 ms time of flight. The horizontal and vertical dashed lines enclose the first Brillouin zone. For the this measurement the lattice depth in all three directions is ramped simultaneously in 5 ms from 35 E_r to zero. (b) Numerical calculation of the quasi-momentum distribution for a 3D lattice depth of 5 E_r.

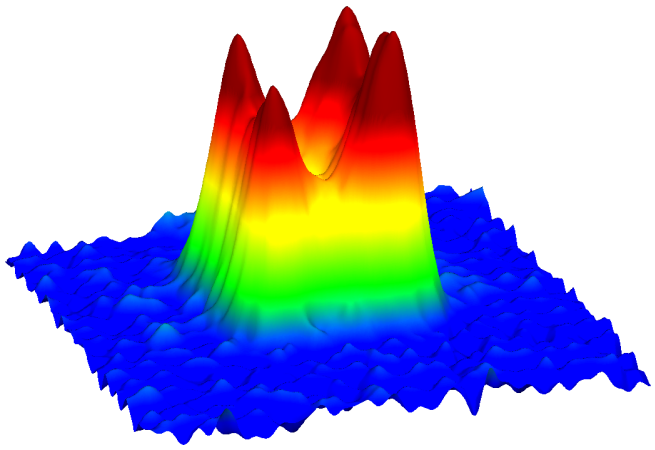

Figure 3.20:
3D picture of the experimental data of Fig. 3.19 (a). The peak height and the color represent the atomic density.

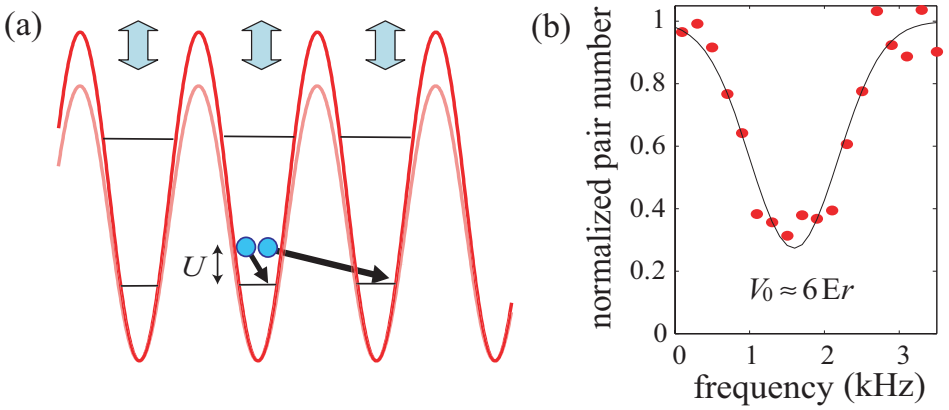

Figure 3.21:
Modulation spectroscopy of repulsively bound pairs. (a) By modulating the optical lattice amplitude with the proper frequency, the pair can dump its binding energy into the lattice motion and subsequently break up. (b) Typical resonance dip showing the remaining number of atom pairs as a function of the modulation frequency, for $V_0 \approx 6\,E_r$. The black line is a Gaussian fit, a choice which was justified by numerical calculations.

3.5.3 Modulation spectroscopy

By modulating the depth of the lattice at a chosen frequency we can determine the binding energy of the pairs (see Fig. 3.21 (a)). For appropriate modulation frequencies, the pairs can "dump" their binding energy into the lattice motion and dissociate. The dissociation occurs as one of the atoms "tunnels" in a neighboring lattice site. Figure 3.21 (b) shows a typical resonance curve of the number of remaining pairs as a function of the modulation frequency. The resonance frequency of about 1.5 kHz (for a lattice depth of $V_0 = 6\,E_r$) agrees well with the calculated binding energy of a pair.
We perform this modulation spectroscopy for a variety of lattice depths V_0 in one direction while keeping the lattice in the other two directions at about $30\,E_r$ (see Fig. 3.22). For these measurements we sinusoidally modulate the intensity of one lattice beam in horizonal direction for 40 ms. The modulation amplitude corresponds to a lattice depth of 1 to $4\,E_r$. The amplitude is adjusted for different 1D lattice depths to get reasonable resonance dips.
The behavior of the binding energy as a function of the lattice depth provides an additional key signature of repulsively bound pairs. As shown in Fig. 3.22 (b), the resonance positions are in good agreement with numerical simulations, which are performed by Andrew Daley. For a lattice depth above $10\,E_r$ the resonance positions essentially coincide with the interaction energy U. For a lattice depth below $10\,E_r$ both the experimental data and the numerical simulations show a significantly larger frequency as given by U/h. As the pairs decay into a scattering continuum of free atoms, the center of the resonance

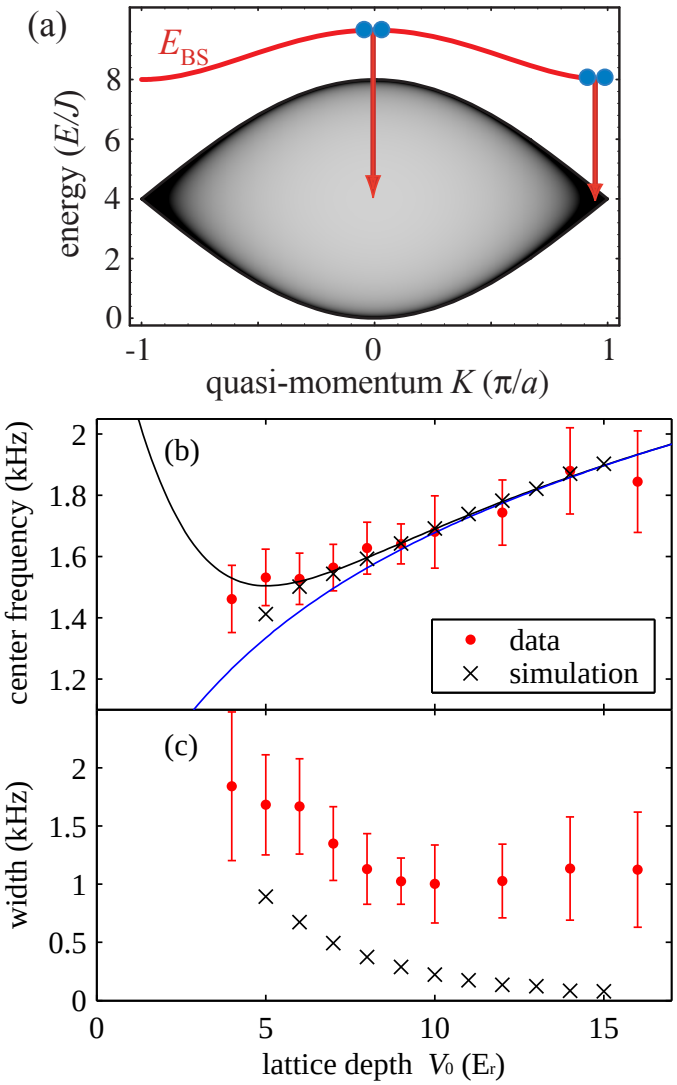

Figure 3.22:
(a) Two particle energy spectrum in a 1D lattice as a function of center of mass quasi-momentum K. Modulating the lattice, the repulsively bound pairs can decay into two free atoms. The possible energy of the two free atom is given by the continuum of scattering states (grey area). (b) Measured resonance frequencies of the modulation spectroscopy as a function of the 1D lattice depth. The resonance frequency was determined from resonance curves similar to the one in Fig. 3.21 (b). The experimental points (filled circles) show good agreement with numerical simulations (crosses). The experimental error bars correspond to the 95% confidence interval for the Gaussian fit parameters of the resonance dips. The data points coincide with the mean energy difference of the bound state energy $E_{BS}(K)$ to the center of the scattering continuum ($= 4J$) (black solid line). The blue solid line is given by U/h, with U the on-site collisional energy shift. (c) Corresponding measured and simulated widths (FWHM) of the resonance dips.

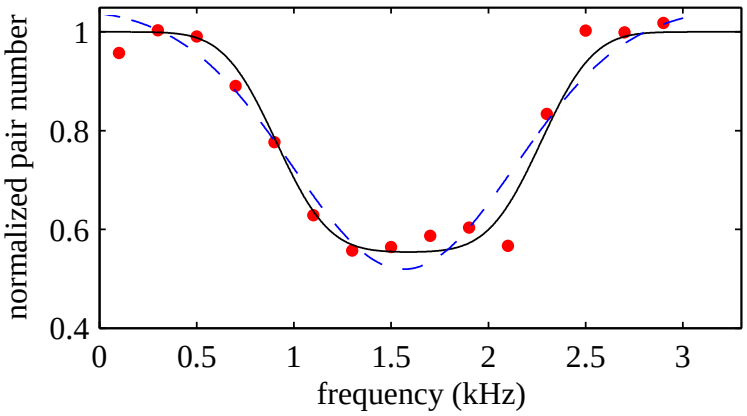

Figure 3.23:
Simulation of the broadening of the resonance dips (black line). The dashed blue line is a fit of a Gaussian curve to the data (red dots). The resulting FWHM-width of the Gaussian fit curve is ~ 1.35 kHz. The data are from a modulation spectroscopy measurement at lattice depth of about 7 E_r.

dips is given by the average energy difference of the pair energy $E_{BS}(K)$ to the center of the scattering continuum $4J$ (see Fig. 3.22 (a)). This energy difference is given by

$$\Delta\tilde{E} = \frac{a}{2\pi}\int_{-\pi/a}^{\pi/a}(E_{BS}(K) - 4J)\,dK, \tag{3.44}$$

assuming a homogeneous distribution of the total momentum K. The measured resonance positions nicely coincide with $\Delta\tilde{E}/h$ (black solid line), as one can see in Fig. 3.22 (b). We could not perform modulation spectroscopy measurements below a lattice depth of ~4 E_r because the lifetime of the pairs is strongly reduced below this value (see Sec. 3.5.1). The width of the resonance dips can be understood, as the pair will decay into a continuum of scattering states which has an energy width of up to $8J$, depending on the initial center of mass quasi-momentum K (see Fig. 3.22 (a)). However, as one can see in Fig. 3.22 (b), the measured widths (FWHM) of the resonance curves do not agree with the calculated widths. We observe an experimental minimum width of about 1 kHz also for a lattice depth $V_0 > 10\,E_r$.
This broadening of the resonance dips could be explained by inhomogeneity effects in the lattice due to gradients. These gradients are caused by the radial confinement of the lattice laser beams and by an inhomogeneity of the magnetic bias field (see Sec. 3.5.1) and lead to a position dependent energy difference from lattice site to lattice site. Modulating the lattice, the decay of an atom pair occurs as one of the atoms "tunnels" in a neighboring lattice site. However, the resonance frequency is then different for each pair, depending on the position of the pair in the lattice. This effect would lead to a broadening of the resonance dips.
We can simulate this broadening by summing single resonance curves, each of them shifted by a different frequency from the center frequency position ($\Delta\tilde{E}/h$). This is shown in Fig. 3.23: Assuming a homogeneous distribution of energy difference from 0 to 0.2 E_r

from site to site, the calculations show a broadening of the resonance dips which is consistent with the observed one (see Fig. 3.23). The calculated curve (black line) is given by the sum of single Gaussian curves[2]. The width of the single Gaussian curves (FWHM = 0.5 kHz) corresponds to the expected width of the resonance dip for this lattice depth, which is roughly given by $4J/h$. The single Gaussian curves are homogeneously shifted by -0.65 kHz to +0.65 kHz (corresponding to -0.2 to 0.2 E_r) from the center resonance frequency position (1.56 kHz). The resulting curve does not have any more a Gaussian shape. This can also be observed in the measured spectra (see e.g. Fig. 3.23 and Fig. 3.22 (b)). This broadening effect due to external gradients is able to explain the measured widths shown in Fig. 3.21 (c).

Determination of the scattering length

The modulation spectroscopy is also an interesting application for measuring the scattering length a_s in the lattice. This is possible because the measured resonance frequencies, which coincide with $U/\hbar$ for a deep enough lattice (see Fig. 3.22), are directly proportional to a_s (see Eq. (3.7)).
We measure the resonance frequencies of the modulation spectra near the Feshbach resonance at 1007.4 G at a lattice depth V_0 of 10 E_r. We normalize these resonance frequencies relative to a measurement of the resonance frequency at a magnetic field of about 1020 G to avoid an error due to a non exactly known lattice depth. At this magnetic field the value of scattering length is $a_s = a_{bg} = 100\,a_0$, where a_{bg} is the background scattering length. We can determine the scattering lengths by multiplying the normalized resonance frequencies with a_{bg}. The resulting data points (filled circles) are fitted with a model which determines the magnetic-field dependence of the scattering length:

$$a_s = a_{bg} \cdot \left(1 - \frac{\Delta_B}{B - B_0}\right),$$

with Δ_B the width and B_0 the position of the Feshbach resonance [GÓRAL *et al.* (2004)]. We calibrate the position of B_0 to the position given in [MARTE *et al.* (2002)]. The width Δ_B, the only free fit parameter, is 215(±15) mG. The error corresponds to a 95% confidence interval. Our measured width Δ_B nicely agrees with a measurement (Δ_B = 210(±20) mG) of the Rempe group [DÜRR *et al.* (2004B)]. DÜRR *et al.* (2004B) determined the width of the Feshbach resonance by measuring the kinetic energy released in a dissociation process of molecules.
We can measure with the modulation spectroscopy only the absolute value of the scattering length but not the sign. However, we can extract the sign from time of flight absorption images because the quasi-momentum distribution changes for a negative scattering length. This will be explained in the following section 3.5.4.

[2] The numerical simulations show that the shape of the resonance curves is well described by a Gaussian curve.

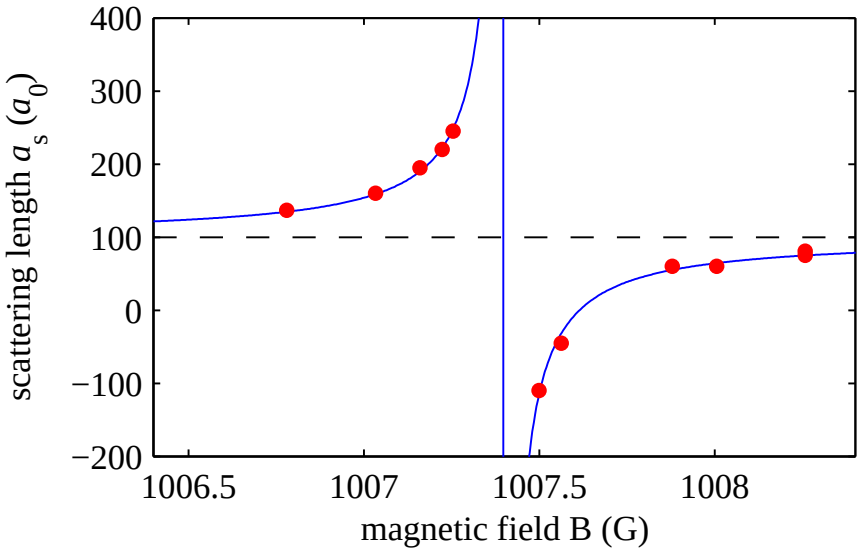

Figure 3.24:
Measurement of the scattering length near the Feshbach resonance at 1007.4 G using modulation spectroscopy. The 1D lattice depth V_0 is 10 E_r. The experimental points (filled circles) are fitted with a model which determines the magnetic-field dependence of the scattering length: $a_s = a_{bg} \cdot (1 - \Delta_B/(B - B_0))$, with $a_{bg} = 100\,a_0$ the background scattering length (horizontal dashed line), Δ_B the width and B_0 the position of the Feshbach resonance [GÓRAL *et al.* (2004)]. The width Δ_B, the only free fit parameter, is 215(±15) mG. The error corresponds to a 95% confidence interval.

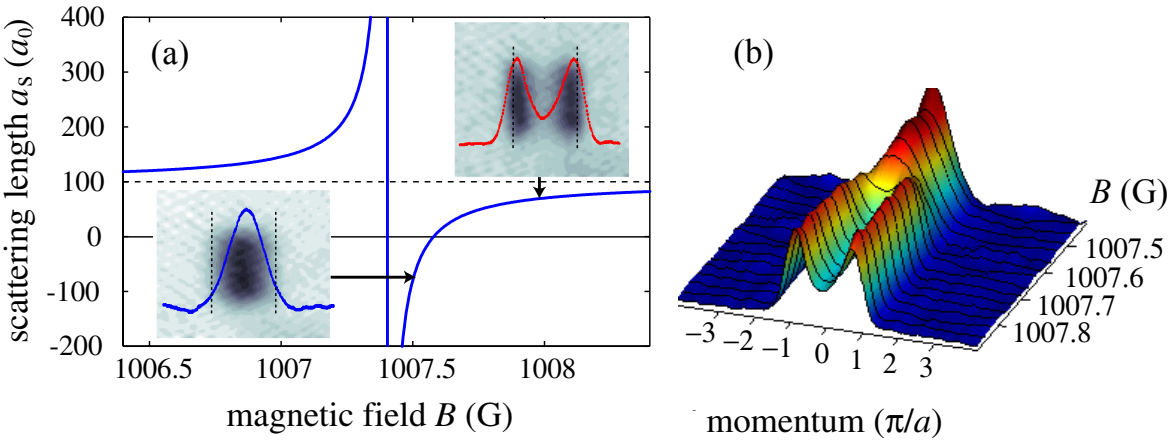

Figure 3.25:
From repulsively to attractively bound atom pairs. (a) With the help of a Feshbach resonance around 1007.4 G, we can choose the effective interaction of the paired atoms by controlling the scattering length a_s. The inserted images show momentum distributions similar to the ones of Fig. 3.15. For effectively attractive interaction the momentum distribution is peaked around zero momentum. (b) The momentum distribution for atom pairs as a function of magnetic field. One can see in a continuous fashion the change of the momentum distribution if the magnetic field is ramped below ~ 1007.6. Below this value the scattering length is negative (see (a)). At zero scattering length the distribution has a flat top shape. The shown data correspond to experiments where the lattice depth V_0 had been adiabatically lowered in 1D below 3 E_r.

3.5.4 Attractively bound pairs

Making use of the Feshbach resonance at 1007.4 G we can tune the effective interaction of the atoms within the pair (see Fig. 3.25 (a)). It is then possible to also create bound atom pairs which are based on attractive interaction. After initial production of repulsively bound atom pairs in the deep lattice ($V_0 = 35\,E_r$) at about 1015 G, we adiabatically lower the homogenous magnetic offset field to certain value. This tunes, depending on magnetic field value, the scattering length of the atomic pair from its default value of $a_s = 100\,a_0$ to negative scattering lengths of up to $a_s = -110\,a_0$ (see Fig. 3.24). Afterwards we measure the quasi-momentum distribution of the pairs by lowering the optical lattice, as discussed in Sec. 3.5.2. In contrast to repulsively bound pairs where the momentum distribution is peaked at the edges of the first Brillouin zone, the momentum distribution for attractively bound pairs is peaked in the center of the first Brillouin zone.
The Bloch band for attractively bound pairs is located below the continuum of scattering states (see Fig. 3.26 (a)). The bound state energy can be simply calculated by replacing

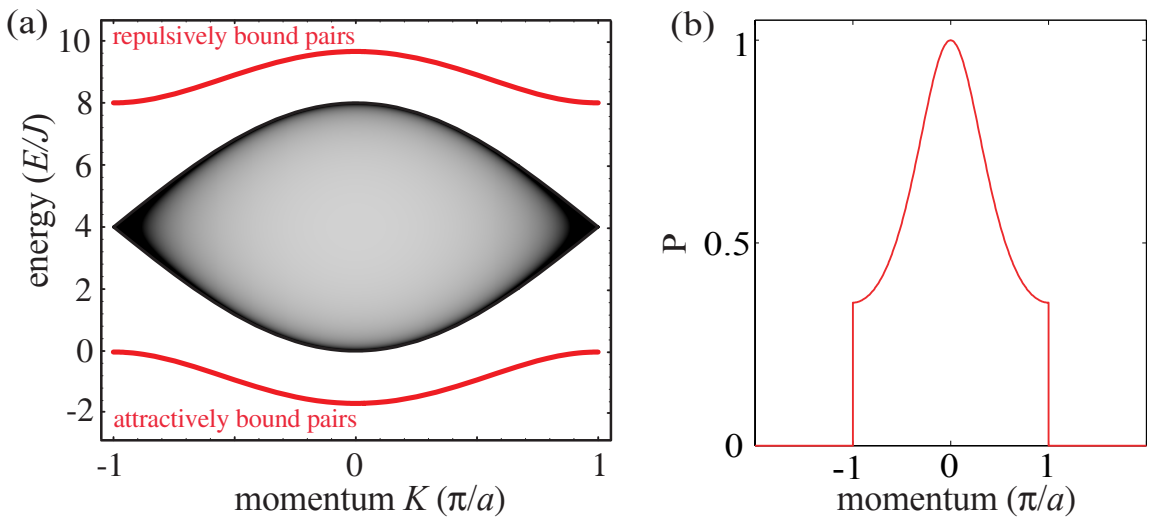

Figure 3.26:
(a) Two particle energy spectrum in a 1D lattice as a function of center of mass quasi-momentum K. The Bloch band for attractively bound pairs is located below the continuum of scattering states (grey area). (b) Calculated single atom quasi-momentum distribution for attractively bound pairs at a 1D lattice depth of 5 E_r, assuming a homogeneous distribution of K.

$U \rightarrow -U$ in the derivation for the analytic solution in Sec. 3.2 (see Eq. (3.35)). The bound state energy for attractively bound pairs is then

$$E_{\text{attr BS}}(K) = 4J\left(1 - \sqrt{(\cos\frac{Ka}{2})^2 + (U/4J)^2}\right). \tag{3.45}$$

The corresponding wavefunction (1D) in momentum space is given by

$$\tilde{\psi}_K^{\text{attr BS}}(k) = \frac{1}{E_{\text{attr BS}} - E_K - \epsilon_K(k)}. \tag{3.46}$$

The calculated single atom momentum distribution after release from the lattice (see Sec. 3.5.2) is in fact peaked at the center of the Brillouin zone in the case of attractively bound pairs (see Fig. 3.26 (b)).
Fig. 3.25 (b) shows how the quasi-momentum distribution of the pairs changes continuously as the scattering length is changed. Interestingly, for non-interacting atoms ($a_s = 0 \rightarrow U = 0$) the distribution again becomes a flat top shape. With respect to stability, we find that lifetimes of bound atom pairs are similar for scattering lengths of equal size but opposite sign.
It is to note, that attractively bound pairs are directly related to so-called "confinement-induced molecules". Such "molecules" were first observed in a 1D Fermi gas by the group of Tilmann Esslinger at the ETH in Zürich [MORITZ *et al.* (2005)]. Moritz *et al.* provided

evidence of these "confinement-induced molecules" by measuring their binding energy with rf-spectroscopy.

3.6 Outlook for experiments with atom pairs

In our experiments we have demonstrated the formation of a novel composite object in an optical lattice: a stable bound state that arises from the lattice band structure and repulsion between the constituents.
A possible next experimental step could be to study the stability of pairs for different on-site interaction potentials U. This can be realized by changing the scattering length a_s with the help of the Feshbach resonance. In the case of a large U the stability of pairs should increase because of a larger gap between the bound state and the continuum of scattering states. Therefore, the lifetime limiting effects discussed in Sec. 3.5.1 should be suppressed. With such a method it could be possible to realize a condensate of pairs, together with the means to characterize long-range order in this system.
A condensate of pairs would have not anymore a homogeneous distribution of the total momentum K, but a specific value of K. Therefore it could be also possible to observe Bloch oscillations of the pairs and so observe the different momentum distribution for different K's (see Sec. 3.5.2).

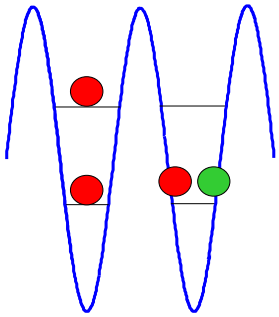

Figure 3.27:
Possible realization of repulsively bound pairs with fermionic atoms. In the case of two identical fermions (same spin) the atoms have to be in different bands due to the Pauli exclusion principle (left). Fermions of different spins or Bose-Fermi mixtures, however, can occupy the same band (right).

Also it would be very interesting to study repulsively bound pairs formed from fermions or boson-fermion mixtures. These systems will exhibit interesting physics based on their composite nature and the quantum statistics of their components.
In a single species fermion experiment it is not possible to put two identical fermions into the same site and band due to the Pauli exclusion principle. The two atoms would have to be at least in different bands (see Fig. 3.27, left), and even then the interaction between them typically would be very small in the ultracold regime.
These problems do not arise using a two-component spin mix of fermions (see Fig. 3.27, right), as two atoms of different spin can share the same site and band and can also interact strongly [CHIN *et al.* (2006); STÖFERLE *et al.* (2006)]. The fact that a higher site occupancy than two is again strictly forbidden could be advantageous in the initial production

of pairs. Furthermore, the pairing of two fermions can result in a pair with bosonic character. In a 3D environment pairing of fermions recently lead to interesting experiments studying the BEC-BCS transition (see e.g. [REGAL *et al.* (2004); CHIN *et al.* (2004); ZWIERLEIN *et al.* (2004)]). It would be interesting to study similar properties to this transition with repulsive pairing, investigating the system as the interaction strength is changed.
Also it would be very interesting to study repulsive pairs which are a composite objects of a fermion and a boson [OTT *et al.* (2004); GÜNTER *et al.* (2006); OSPELKAUS *et al.* (2006)]. One question would be how these bound states would interact with each other, and how, for example, the bosonic atoms within the pair would mediate next neighbor interactions [LEWENSTEIN *et al.* (2004)].

A Publications

The following articles have been published in the framework of this PhD thesis and are attached in the following order:

1. K. Winkler, F. Lang, G. Thalhammer, P.v.d. Straten, R. Grimm, and J. Hecker Denschlag.
   Coherent optical transfer of Feshbach molecules to a lower vibrational state.
   Phys. Rev. Lett. **98**, 043201, 2007.

2. K. Winkler, G. Thalhammer, F. Lang, R. Grimm, J. Hecker Denschlag, A. J. Daley, A. Kantian, H. P. Büchler, and P. Zoller.
   Repulsively bound atom pairs in an optical lattice.
   Nature **441**, 853, 2006.

3. S. Schmid, G. Thalhammer, K. Winkler, F. Lang, and J. Hecker Denschlag.
   Long distance transport of ultracold atoms using a 1D optical lattice.
   New Journal of Physics **8**, 159, 2006

4. G. Thalhammer, K. Winkler, F. Lang, S. Schmid, R. Grimm, and J. Hecker Denschlag.
   Long-lived Feshbach molecules in a three-dimensional optical lattice.
   Phys. Rev. Lett. **96**, 050402, 2006.

5. K. Winkler, G. Thalhammer, M. Theis, H. Ritsch, R. Grimm, and J. Hecker Denschlag.
   Atom-molecule dark states in a Bose-Einstein condensate.
   Phys. Rev. Lett. **95**, 063202, 2005.

6. G. Thalhammer, M. Theis, K. Winkler, R. Grimm, and J. Hecker Denschlag.
   Inducing an optical Feshbach resonance via stimulated Raman coupling.
   Physical Review A **71**, 033403, 2005.

7. M. Theis, G. Thalhammer, K. Winkler, M. Hellwig, G. Ruff, R. Grimm and J. Hecker Denschlag.
   Tuning the scattering length with an optically induced Feshbach resonance.
   Phys. Rev. Lett. **93**, 123001, 2004.

Coherent Optical Transfer of Feshbach Molecules to a Lower Vibrational State

K. Winkler,[1] F. Lang,[1] G. Thalhammer,[1] P. v. d. Straten,[2] R. Grimm,[1,3] and J. Hecker Denschlag[1]
[1]*Institut für Experimentalphysik, Forschungszentrum für Quantenphysik, Universität Innsbruck, 6020 Innsbruck, Austria*
[2]*Debye Institute, Universiteit Utrecht, 3508 TA Utrecht, Netherlands*
[3]*Institut für Quantenoptik und Quanteninformation, Österreichische Akademie der Wissenschaften, 6020 Innsbruck, Austria*
(Received 8 November 2006; published 25 January 2007)

Using the technique of stimulated Raman adiabatic passage (STIRAP) we have coherently transferred ultracold $^{87}Rb_2$ Feshbach molecules into a more deeply bound vibrational quantum level. Our measurements indicate a high transfer efficiency of up to 87%. Because the molecules are held in an optical lattice with not more than a single molecule per lattice site, inelastic collisions between the molecules are suppressed and we observe long molecular lifetimes of about 1 s. Using STIRAP we have created quantum superpositions of the two molecular states and tested their coherence interferometrically. These results represent an important step towards Bose-Einstein condensation of molecules in the vibrational ground state.

DOI: 10.1103/PhysRevLett.98.043201 PACS numbers: 34.50.Rk, 03.75.Nt, 32.80.Pj, 42.50.Gy

Recently, there has been a rapidly growing interest in ultracold molecules since they lend themselves to a large number of interesting studies in, for instance, few body collision physics [1–3], chemistry in the ultracold regime, high resolution spectroscopy, as well as quantum computation [4]. Furthermore, molecules in their vibrational ground state are of special interest, because they allow for the formation of an intrinsically stable molecular Bose-Einstein condensate (BEC). Current pathways towards the production of ultracold molecules in well-defined quantum states are either based on sympathetic cooling [5] or association of ultracold neutral atoms using photoassociation [6] or Feshbach resonances [7]. The method of Feshbach ramping has proved especially successful and efficient, but it only produces molecules in the last bound vibrational level. In order to selectively convert molecules into more deeply bound states, it has been proposed [8] to use a sequence of stimulated optical Raman transitions to step molecules down the vibrational ladder. This process takes place while the molecules are held in an optical lattice isolating them from each other and thus shielding them from detrimental collisions. Recently, optical transfer of molecules into their vibrational ground state was demonstrated experimentally using a "pump-dump" method without a lattice at a moderate efficiency and selectivity [9].

Here we report the realization of an efficient and highly selective transfer scheme, where an ensemble of $^{87}Rb_2$ Feshbach molecules in an optical lattice is coherently converted to a deeper bound molecular state via stimulated Raman adiabatic passage (STIRAP). STIRAP is known as a fast, efficient, and robust process for population transfer based on a Raman transition [10]. During transfer it keeps the molecules in a dark superposition state, which decouples from the light and thus suppresses losses due to spontaneous light scattering. In our proof-of-principle experiment we transfer the Feshbach molecules with a STIRAP pulse from their last bound vibrational level (binding energy 24 MHz $\times h$), which we denote $|a\rangle$, to the second-to-last bound vibrational level, $|g\rangle$ [see Fig. 1(a) and 1(b)]. Both levels have a rotational quantum number $l = 0$ and a total spin $F = 2$, $m_F = 2$. The level $|g\rangle$ is known from previous experiments [11–14]. It has a binding energy of 637 MHz $\times h$ at 973 G and can be conveniently reached via Raman beams generated with an acousto-optic modulator (AOM). In order to detect the more deeply bound molecules, a second STIRAP pulse converts the

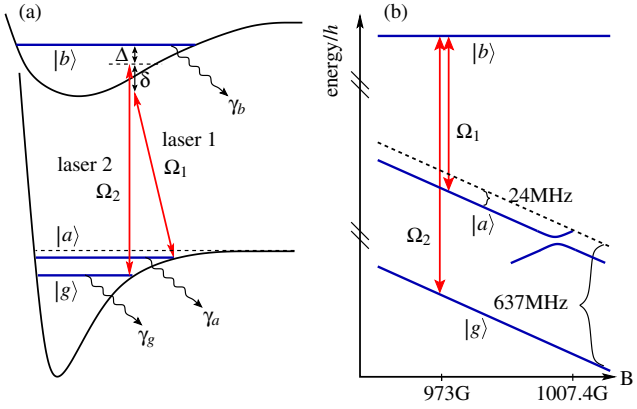

FIG. 1 (color online). (a) Level scheme for STIRAP. Lasers 1, 2 couple the ground state molecular levels $|a\rangle$, $|g\rangle$ to the excited level $|b\rangle$ with Rabi frequencies Ω_1, Ω_2, respectively. Δ and δ denote detunings. γ_a, γ_b, γ_g give effective decay rates of the levels. (b) Zeeman diagram of relevant energy levels. At 1007.4 G a molecular state crosses the threshold of the unbound two atom continuum (dashed line) giving rise to a Feshbach resonance. From there this molecular state adiabatically connects to the last bound vibrational level $|a\rangle$, the state of the Feshbach molecules.

molecules back to the last bound vibrational level, where they are detected as atoms after dissociation via Feshbach ramping. The complete cycle has an efficiency of 75%, indicating a single STIRAP efficiency of 87%.

We use essentially the same setup as in Ref. [15]. Starting point for the experiments is a pure ensemble of 2×10^4 ultracold $^{87}Rb_2$ Feshbach molecules which are held in the lowest Bloch band of a cubic 3D optical lattice. There is no more than a single molecule per site and the whole molecular ensemble occupies a volume of about $20 \times 20 \times 20\ \mu m^3$. The lattice is 50 E_r deep for molecules ($E_r = 2\pi^2\hbar^2/m\lambda^2$, where m is the mass of the atoms and $\lambda = 830.44$ nm the wavelength of the lattice laser), suppressing tunneling between sites. The molecular ensemble is initially produced from an atomic ^{87}Rb BEC after loading it into the lattice, subsequent Feshbach ramping at 1007.40 G [16] and a final purification step [15] which removes all chemically unbound atoms. Lowering the magnetic field to 973 G transfers the atoms to the adiabatically connected state $|a\rangle$, which has nearly the same magnetic moment as $|g\rangle$ (see Fig. 1). This results in an almost magnetic field insensitive Raman transition [17].

In order to efficiently carry out STIRAP, a suitable excited molecular level, $|b\rangle$, has to be identified (see Fig. 1). We chose the electronically excited molecular state $|0_g^-, \nu = 31, J = 0\rangle$ located 6.87 cm^{-1} below the $S_{1/2} + P_{3/2}$ dissociation asymptote [18]. The corresponding line is strong and solitary; i.e., within a 2 GHz vicinity no other strong molecular lines are found which could interfere with STIRAP. Coupling to other excited molecular states leads to loss of the molecules, since these levels typically decay spontaneously into a variety of undetected vibrational levels in the ground state. Furthermore, it is advantageous that the chosen level $|b\rangle$ has a similar Franck-Condon overlap with states $|a\rangle$ and $|g\rangle$. It can be shown that this also helps to minimize losses through off-resonant coupling channels.

With this choice of states $|a\rangle$, $|b\rangle$, $|g\rangle$, we observe a clear molecular dark resonance when coupling the states with resonant Raman laser light (see Fig. 2). The corresponding molecular dark superposition state shows a long lifetime. This is a necessary precondition for our STIRAP experiments, because the molecules have to be kept in a dark state during the whole STIRAP process which in our case typically takes hundreds of μs. The Raman laser beams are both derived from a single Ti:sapphire laser with a short term linewidth of less than 1 MHz. The Ti:sapphire laser is offset locked relative to the D_2 line of atomic rubidium with the help of a scanning optical cavity, which yields an absolute frequency stability of better than 5 MHz. The frequency difference between the two beams is created with an acousto-optical modulator (AOM) with a frequency of about 307 MHz in a double-pass configuration. This allows precise control of the relative frequency difference between the beams over several tens of MHz and ensures phase locking. Both beams propagate collinearly and have a waist of about 290 μm at the location of the molecular ensemble. The polarization of the beams is parallel to the direction of the magnetic bias field of 973 G.

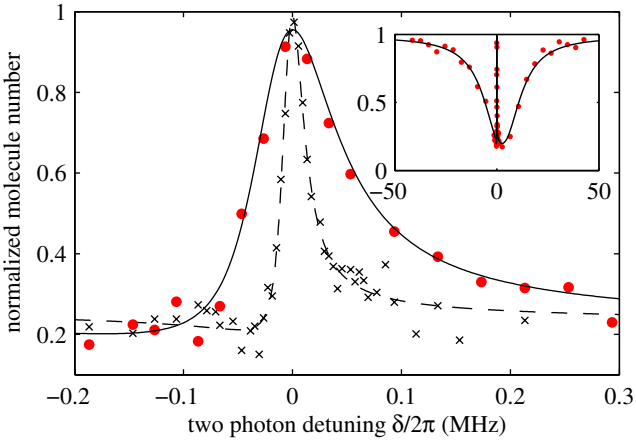

FIG. 2 (color online). Dark resonance. The data show the remaining fraction of Feshbach molecules in state $|a\rangle$, after subjecting them to a 200 μs square pulse of Raman laser light in a narrow range around 0 of the two-photon detuning δ. The inset shows the scan over the whole line of state $|b\rangle$. The strong suppression of loss at $\delta = 0$ is due to the appearance of a dark state. The laser intensities are $I_1 = 2.6$ mW/cm^2, $I_2 = 13$ mW/cm^2 (×), $I_2 = 51$ mW/cm^2 (●). Δ is in general tuned close to zero and for the shown measurements happens to be $\Delta/2\pi \approx 2.5$ MHz, which gives rise to the slightly asymmetric line shape of the dark states. The solid and dashed lines are model calculations (see text).

In order to transfer the molecules from state $|a\rangle$ to state $|g\rangle$, we carry out a STIRAP pulse which consists of a so-called counterintuitive succession of two laser pulses [see Fig. 3(a)]. We first switch on laser 2 and then ramp its intensity to zero within the pulse time $\tau_p = 200\ \mu$s. Simultaneously we ramp up the intensity of laser 1 from zero to its final value. We fix the ratio of the maximal pulse intensities of laser 1 and 2 to $I_2^{\max}/I_1^{\max} = 1/3.2$ in order to partially compensate for the unequal Franck-Condon factor of the $|a\rangle - |b\rangle$ and $|g\rangle - |b\rangle$ transitions. Ideally, after the first STIRAP pulse all molecules from state $|a\rangle$ should end up in state $|g\rangle$. In order to determine the population in state $|g\rangle$, we apply, after a holding time of $\tau_h = 5$ ms, a second STIRAP pulse which is the mirror image in time of pulse 1. This transfers the molecules back into state $|a\rangle$. We then ramp the magnetic field over the Feshbach resonance at 1007.4 G which dissociates the molecules with unit efficiency [15] into pairs of atoms. These are subsequently detected with standard absorption imaging. Figure 3(b) shows in a time resolved way how molecules in state $|a\rangle$ first disappear and then reappear during the course of the STIRAP sequence. After applying the first STIRAP pulse, no molecules can be observed in state $|a\rangle$. This is to be expected, since any molecule which is left over in state $|a\rangle$ at the end of the first STIRAP pulse is in a bright state and will be quickly removed by resonantly scattering photons from laser 1. This confirms, that after completion of the

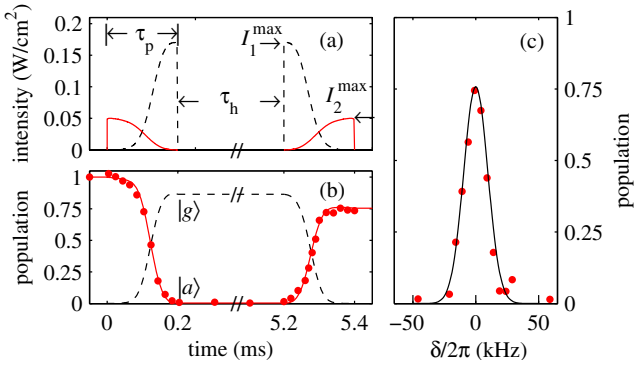

FIG. 3 (color online). STIRAP. (a) Counterintuitive pulse scheme. Shown are laser intensities as a function of time (laser 1: dashed line, laser 2: solid line). The first STIRAP pulse with length $\tau_p = 200$ μs transfers the molecule from state $|a\rangle$ to state $|g\rangle$. After a holding time $\tau_h = 5$ ms, the second pulse (identical, but reversed) transfers the molecules back to $|a\rangle$. $I_{1,2}^{max}$ indicates the maximal intensity of laser 1 (2) in the pulse, respectively. (b) Corresponding population in state $|a\rangle$ (data points, solid line) and state $|g\rangle$ (dashed line). The data points are measurements where at a given point in time the STIRAP lasers are abruptly switched off and the molecule population in state $|a\rangle$ is determined. For these measurements $\Delta \approx 0 \approx \delta$. The lines are model calculations (see text). (c) Efficiency for population transfer from state $|a\rangle$ to state $|g\rangle$ and back via STIRAP as a function of the two-photon detuning δ. The line is a model calculation, showing a Gaussian line shape with a FWHM width of ≈ 22 kHz.

second STIRAP pulse we only detect molecules that were previously in state $|g\rangle$. We observe an efficiency of 75% for the full cycle of conversion into state $|g\rangle$ and back. Figure 3(c) shows how this efficiency depends critically on the two-photon detuning δ.

In Fig. 4 we investigate further the complete STIRAP cycle efficiency as a function of the laser intensity and pulse length. In these measurements we use pulses with the same shape as in Fig. 3(a), which are rescaled to adjust pulse time τ_p and laser intensity. Again, for the best settings we reach an efficiency of about 75% for the two pulses, which corresponds to a transfer efficiency to state $|g\rangle$ of about 87%. The dependence of the efficiency on intensity and pulse length can be qualitatively understood as follows. For short pulse lengths or low intensities, the dark state cannot adiabatically follow the STIRAP pulse, resulting in a low transfer efficiency. For very long pulse lengths and high intensities the losses due to an imperfect dark state become dominant, also resulting in a low transfer efficiency. Thus in order to find an optimum value for the transfer efficiency there is a trade off between adiabaticity and inelastic photon scattering.

We are also able to quantitatively understand our data by using a three level model. It describes the evolution of the quantum mechanical probability amplitudes a, b, and g for a molecule in the respective states $|a\rangle$, $|b\rangle$, and $|g\rangle$ in terms of the following set of differential equations:

$$\begin{aligned} i\dot{a} &= (-i\gamma_a/2)a - \tfrac{1}{2}\Omega_1 b, \\ i\dot{b} &= [(\Delta + \delta) - i\gamma_b/2]b - \tfrac{1}{2}(\Omega_1 a + \Omega_2 g), \\ i\dot{g} &= (\delta - i\gamma_g/2)g - \tfrac{1}{2}\Omega_2 b. \end{aligned} \quad (1)$$

Here, the Rabi frequencies Ω_1, Ω_2, the detunings Δ and δ, and the decay rates γ_a, γ_b, γ_g are defined as shown in Fig. 1. After experimentally determining Ω_1, Ω_2 and γ_a, γ_g and using $\gamma_b = 2\pi \times 12$ MHz, we are able to consistently describe all data in Figs. 2–4 with a single set of parameters. From one-photon and two-photon scans (as, e.g., in Fig. 2) we obtain $\Omega_1 = 2\pi \times 2.9\ \mathrm{MHz}[I_1/(\mathrm{W\,cm^{-2}})]^{1/2}$ and $\Omega_2 = 2\pi \times 6.0\ \mathrm{MHz}[I_2/(\mathrm{W\,cm^{-2}})]^{1/2}$. The effective decay rates γ_a, γ_g are intensity dependent and are mainly due to the off-resonant coupling of $|a\rangle$ with laser 2 and $|g\rangle$ with laser 1. We determine γ_a (γ_g) by shining laser 2 (laser 1) on the molecules in state $|a\rangle$ ($|g\rangle$) and measuring the off-resonant losses. We find that $\gamma_a/I_2 = 2\pi \times 0.72\ \mathrm{kHz/(W\,cm^{-2})}$ and $\gamma_g/I_1 = 2\pi \times 0.40\ \mathrm{kHz/(W\,cm^{-2})}$. From these independent measurements, all parameters of Eqs. (1) are determined without further adjustable parameters. In the calculations shown in Fig. 3(b), 3(c), and 4 the time dependent pulse shapes [see Fig. 3(a)] are included. The agreement between theory and experiment is very good.

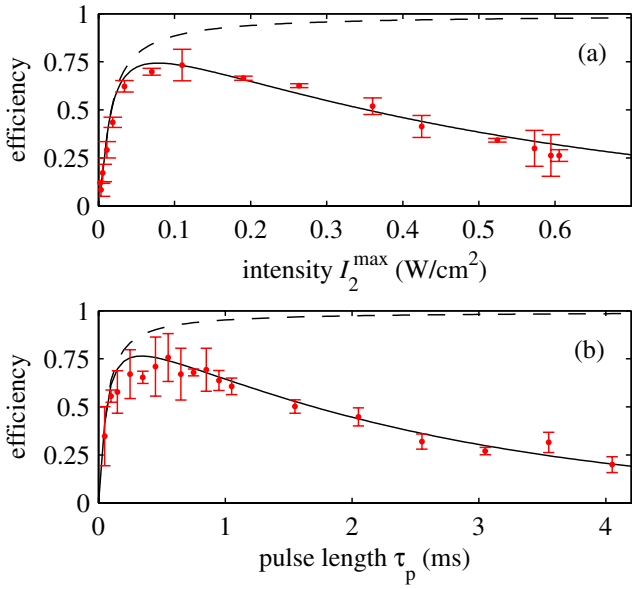

FIG. 4 (color online). Efficiency for population transfer from state $|a\rangle$ to state $|g\rangle$ and back with two STIRAP pulses. (a) Efficiency vs the laser intensity I_2^{max} (fixed pulse length of $\tau_p = 200$ μs). (b) Efficiency vs the pulse length τ_p (fixed laser intensity $I_2^{max} = 44\ \mathrm{mW/cm^2}$). For (a) and (b) the intensity ratio $I_2^{max}/I_1^{max} = 1/3.2$. The lines are from calculations without free parameters using Eqs. (1). Setting $\gamma_a = \gamma_g = 0$, the efficiency would reach unity for a fully adiabatic transfer (dashed lines). Using for γ_a, γ_a the experimentally determined values, the calculations (solid lines) are in good agreement with the data. The error bars represent a 1σ statistical error.

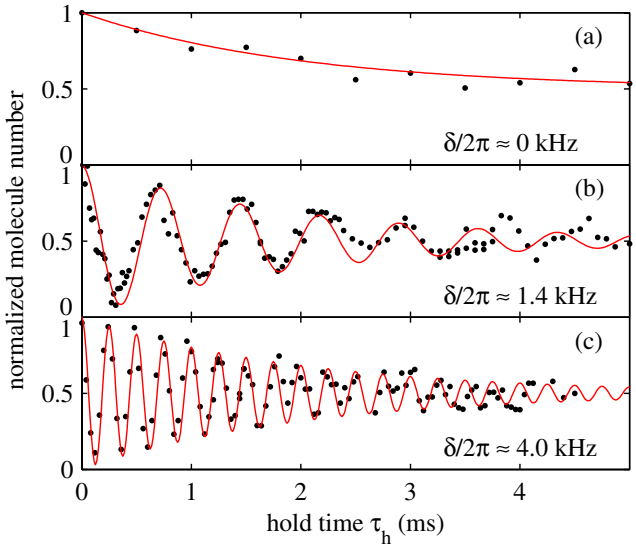

FIG. 5 (color online). Coherence of the $(|a\rangle - |g\rangle)$ superposition state. Shown is the molecule number in state $|a\rangle$ as a function of holding time τ_h for different detunings δ as indicated. The oscillations indicate coherent flopping of the molecular superposition state between the dark and a bright state. The lines are given by $0.5\exp(-\tau_h/\tau)\cos(\delta\tau_h) + 0.5$, with a damping time $\tau = 2$ ms.

During STIRAP the molecules are in a quantum superposition, $\Omega_2|a\rangle - \Omega_1|g\rangle$. In order to probe the coherence of this superposition, we perform a Ramsey-type experiment. First we create a dark superposition state with equal population in the two states, $|a\rangle - |g\rangle$, by going halfway into the first STIRAP pulse of Fig. 3(a). We then simultaneously switch off both STIRAP lasers for a variable holding time τ_h, after which we retrace in time the same STIRAP half pulse. As a result we observe oscillations in the number of molecules in level $|a\rangle$ as a function of the holding time τ_h (see Fig. 5). During the holding time, the superposition state freely evolves, coherently flopping between the dark and a bright state with a frequency equal to the two-photon detuning δ. At the end of the holding time, when we switch on again the STIRAP lasers, the dark state is transferred back to state $|a\rangle$ whereas the bright state will be immediately destroyed by the light and leads to complete loss of the corresponding molecules. The observed oscillations are exponentially damped on a time scale of about 2 ms. This damping can be explained by a magnetic field inhomogeneity of about 20 mG over the molecular cloud, which leads to a spatial variation of $2\pi \times 250$ Hz in the two-photon detuning δ. Additionally we observe a slight shift of the oscillation frequency with time on the order of $2\pi \times 50$ Hz/ms. This can be attributed to a small drift of the magnetic field.

Furthermore, we have performed lifetime measurements of the molecules in state $|g\rangle$ by varying the holding time τ_h between the two STIRAP pulses [see Fig. 3(a)]. At a lattice depth of 60 E_r for molecules, we observe a long lifetime of 0.8 s (assuming exponential decay), which is longer than the lifetime of 0.4 s for Feshbach molecules in state $|a\rangle$. At these deep lattices molecular decay is exclusively due to inelastic scattering of lattice photons.

To conclude, using STIRAP we have demonstrated a coherent transfer of a molecular quantum gas from a weakly bound molecular level to a more deeply bound molecular level with a high transfer efficiency of 87%. The method can be extended in a straightforward manner to create arbitrarily deeply bound molecules. With a *single* STIRAP pulse all vibrational levels down to level $X^1\Sigma_g^+(v = 116)/a^3\Sigma_u^+(v = 32)$ should be easily reached since the Franck-Condon factors to state $|b\rangle$ are of similar order as for level $|g\rangle$ [19]. This includes the level $X^1\Sigma_g^+(v = 119)/a^3\Sigma_u^+(v = 35)$ with its binding energy of 30 GHz $\times h$, from which the vibrational ground state $X^1\Sigma_g^+(v = 0)$ of the singlet potential can be reached with two additional Raman (or STIRAP) transitions [8]. Thus STIRAP is a promising tool for the creation of a molecular BEC in the molecular ground state.

We thank Christiane Koch for providing Franck-Condon factors and Helmut Ritsch for valuable discussions. This work was supported by the Austrian Science Fund (FWF) within SFB 15 (project part 17) and the Cold Molecules TMR Network under Contract No. HPRN-CT-2002-00290. P. v. d. S. acknowledges support within the ESF-program QUDEDIS during his stay in Innsbruck.

[1] C. Chin *et al.*, Phys. Rev. Lett. **94**, 123201 (2005).
[2] P. Staanum, S. D. Kraft, J. Lange, R. Wester, and M. Weidemüller, Phys. Rev. Lett. **96**, 023201 (2006).
[3] N. Zahzam, T. Vogt, M. Mudrich, D. Comparat, and P. Pillet, Phys. Rev. Lett. **96**, 023202 (2006).
[4] D. DeMille, Phys. Rev. Lett. **88**, 067901 (2002).
[5] For an overview, see J. Doyle, B. Friedrich, R. V. Krems, and F. Masnou-Seeuws, Eur. Phys. J. D **31**, 149 (2004).
[6] For an overview, see K. M. Jones, E. Tiesinga, P. D. Lett, and P. S. Julienne, Rev. Mod. Phys. **78**, 483 (2006).
[7] For an overview, see T. Köhler, K. Goral, and P. S. Julienne, Rev. Mod. Phys. **78**, 1311 (2006).
[8] D. Jaksch, V. Venturi, J. I. Cirac, C. J. Williams, and P. Zoller, Phys. Rev. Lett. **89**, 040402 (2002).
[9] J. M. Sage, S. Sainis, T. Bergeman, and D. DeMille, Phys. Rev. Lett. **94**, 203001 (2005).
[10] K. Bergmann, H. Theuer, and B. W. Shore, Rev. Mod. Phys. **70**, 1003 (1998).
[11] R. Wynar, R. S. Freeland, D. J. Han, C. Ryu, and D. J. Heinzen, Science **287**, 1016 (2000).
[12] T. Rom *et al.*, Phys. Rev. Lett. **93**, 073002 (2004).
[13] K. Winkler *et al.*, Phys. Rev. Lett. **95**, 063202 (2005).
[14] G. Thalhammer *et al.*, Phys. Rev. A **71**, 033403 (2005).
[15] G. Thalhammer *et al.*, Phys. Rev. Lett. **96**, 050402 (2006).
[16] T. Volz, S. Dürr, S. Ernst, A. Marte, and G. Rempe, Phys. Rev. A **68**, 010702(R) (2003).
[17] At 973 G the dependence of the two-photon resonance on the magnetic field is about 12 kHz/G.
[18] A. Fioretti *et al.*, Eur. Phys. J. D **15**, 189 (2001).
[19] C. Koch (private communication).

LETTERS

Repulsively bound atom pairs in an optical lattice

K. Winkler[1], G. Thalhammer[1], F. Lang[1], R. Grimm[1,3], J. Hecker Denschlag[1], A. J. Daley[2,3], A. Kantian[2,3], H. P. Büchler[2,3] & P. Zoller[2,3]

Throughout physics, stable composite objects are usually formed by way of attractive forces, which allow the constituents to lower their energy by binding together. Repulsive forces separate particles in free space. However, in a structured environment such as a periodic potential and in the absence of dissipation, stable composite objects can exist even for repulsive interactions. Here we report the observation of such an exotic bound state, which comprises a pair of ultracold rubidium atoms in an optical lattice. Consistent with our theoretical analysis, these repulsively bound pairs exhibit long lifetimes, even under conditions when they collide with one another. Signatures of the pairs are also recognized in the characteristic momentum distribution and through spectroscopic measurements. There is no analogue in traditional condensed matter systems of such repulsively bound pairs, owing to the presence of strong decay channels. Our results exemplify the strong correspondence between the optical lattice physics of ultracold bosonic atoms and the Bose–Hubbard model[1,2]—a link that is vital for future applications of these systems to the study of strongly correlated condensed matter and to quantum information.

Cold atoms loaded into a three-dimensional (3D) optical lattice provide a realization of a quantum lattice gas[1,2]. An optical lattice can be generated by pairs of counterpropagating laser beams, where the resulting standing wave intensity pattern forms a periodic array of microtraps for the cold atoms, with period a given by half the wavelength of the light, $\lambda/2$. The periodicity of the potential gives rise to a band structure for the atom dynamics with Bloch bands separated by bandgaps, which can be controlled by the laser parameters and beam configuration. The dynamics of ultracold atoms loaded into the lowest band of a sufficiently deep optical lattice is well described by the Bose–Hubbard model with hamiltonian[1,3]:

$$\hat{H} = -J\sum_{\langle i,j\rangle}\hat{b}_i^{\dagger}\hat{b}_j + \frac{U}{2}\sum_i \hat{n}_i(\hat{n}_i - 1) + \sum_i \varepsilon_i \hat{n}_i \qquad (1)$$

Here $\hat{b}_i$ ($\hat{b}_i^{\dagger}$) are destruction (creation) operators for the bosonic atoms at site i, and $\hat{n}_i = \hat{b}_i^{\dagger}\hat{b}_i$ is the corresponding number operator. $J/\hbar$ denotes the nearest-neighbour tunnelling rate, U the on-site collisional energy shift, and ε_i the background potential. The high degree of control available over the parameters in this system—for example, changing the relative values of U and J by varying the lattice depth, V_0—has led to seminal experiments on strongly correlated gases in optical lattices. These experiments include the study of the superfluid–Mott insulator transition[4], the realization of one-dimensional (1D) quantum liquids with atomic gases[5,6] (see also refs 7 and 8), and the investigation of disordered systems[9]. 3D optical lattices have also opened new avenues in cold collision physics and chemistry[10–13].

A striking prediction of the Bose–Hubbard hamiltonian (equation (1)) is the existence of stable repulsively bound atom pairs. These are most intuitively understood for strong repulsive interaction $|U| \gg J$, $U > 0$, where an example of such a pair is a state of two atoms occupying a single site, $|2_i\rangle \equiv (\hat{b}_i^{\dagger 2}|\mathrm{vac}\rangle)/\sqrt{2}$, where $|\mathrm{vac}\rangle$ is the vacuum state. This state has a potential energy offset U with respect to states where the atoms are separated (Fig. 1a). The pair is unable to decay by converting the potential energy into kinetic energy, as the Bloch band allows a maximum kinetic energy for two atoms given by $8J$, twice its width. The pair can move around the lattice, with both atoms tunnelling to a neighbouring site (Fig. 1b), but the atoms cannot move independently. The stability of repulsively bound pairs is intimately connected with the absence of dissipation, in contrast to solid state lattices, for example, where interactions with phonons typically lead to rapid relaxation.

We obtain experimental evidence for repulsively bound pairs with a sample of ultracold ^{87}Rb atoms in a cubic 3D optical lattice with lattice period $a = 415.22$ nm. The key tool used to prepare and observe the pairs is their adiabatic conversion into chemically

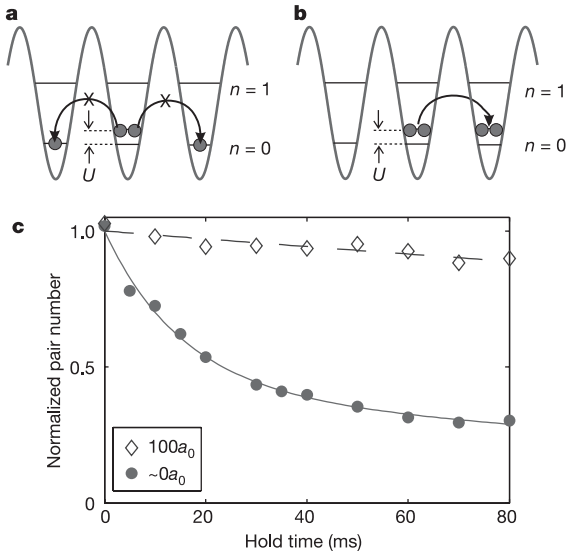

Figure 1 | Atom pairs in an optical lattice. a, Repulsive interaction (scattering length $a > 0$) between two atoms sharing a lattice site in the lowest band ($n = 0$) gives rise to an interaction energy U. Breaking up of the pair is suppressed owing to the lattice band structure and energy conservation. **b**, The pair is a composite object that can tunnel through the lattice. **c**, Long lifetime of repulsively bound atom pairs that are held in a 3D optical lattice. The potential depth is $(10 \pm 0.5)E_r$ in one direction and $(35 \pm 1.5)E_r$ in the perpendicular directions. Shown is the remaining fraction of pairs for a scattering length of $100a_0$ (open diamonds; a_0 is the Bohr radius) and a scattering length of about $(0 \pm 10)a_0$ (filled circles) as a function of the hold time. The lines are fitted curves of an exponential (dashed line) and the sum of two exponentials (solid line).

[1]Institute for Experimental Physics, [2]Institute for Theoretical Physics, University of Innsbruck, A-6020 Innsbruck, Austria. [3]Institute for Quantum Optics and Quantum Information of the Austrian Academy of Sciences, A-6020 Innsbruck, Austria.

bound dimers using a magnetic-field sweep across a Feshbach resonance[13–20] at 1,007.40 G. The initial state is prepared from a pure sample of Rb_2 Feshbach molecules in the vibrational ground state of the lattice where each lattice site is occupied by not more than a single molecule (see Methods). Sweeping across the Feshbach resonance, we adiabatically dissociate the dimers and obtain a lattice correspondingly filled with 2×10^4 atom pairs, at an effective filling factor of typically 0.3. Away from the Feshbach resonance, the effective interaction between the atoms is repulsive with scattering length $a_s = +100a_0$ (where a_0 is the Bohr radius).

In order to demonstrate the stability of repulsively bound pairs, we lower the lattice potential in one direction from its initial depth of $V_0 = 35E_r$ (corresponding to $J/\hbar \approx 2\pi \times 0.7$ Hz and $U/J \approx 3{,}700$, where $E_r = 2\pi^2\hbar^2/m\lambda^2$ and m is the mass of the atoms) in 1 ms to a depth of $V_0 = 10E_r$. This increases dramatically the tunnelling rates along this direction to $J/\hbar \approx 2\pi \times 63$ Hz ($U/J \approx 30$), potentially allowing the atom pairs to quickly separate. After a variable hold time we determine the number of remaining pairs. This is done by adiabatically raising the lattice to its full initial depth of $V_0 = 35E_r$, and converting doubly occupied sites to Feshbach molecules with near unit efficiency[13]. A purification pulse[13] then removes all remaining atoms due to dissociated pairs. Afterwards the molecules are again converted back into atoms, and can then be detected by conventional absorption imaging.

The results of these lifetime measurements are shown in Fig. 1c. For repulsive interaction ($a_s = 100a_0$), the atom pair sample exhibits the remarkably long lifetime of 700 ms (exponential fit). This lifetime is mainly limited by inelastic scattering of lattice photons[13], and greatly exceeds the calculated time for an atom to tunnel from one site to the next, $2\pi\hbar/(4J) \approx 4$ ms. In contrast, if we turn off the on-site interaction by tuning the scattering length near zero, we observe a much faster decay in the number of doubly occupied sites owing to the rapid diffusion of unbound atoms through the lattice (Fig. 1c). This observation clearly demonstrates that the stability of the pairs is induced by the on-site interaction U.

We can more deeply understand these repulsively bound pairs through an exact solution of the two-particle Lippmann–Schwinger scattering equation based on the Bose–Hubbard model. We write the two-atom wavefunction as $\Psi(\mathbf{x}, \mathbf{y})$, where the positions of the two particles are denoted $\mathbf{x} = \Sigma_i x_i \mathbf{e}_i$ and $\mathbf{y} = \Sigma_i y_i \mathbf{e}_i$, with $\mathbf{e}_i$ being the primitive lattice vectors, and x_i, y_i integer numbers. Introducing centre of mass, $\mathbf{R} = (\mathbf{x} + \mathbf{y})/2$, and relative coordinates, $\mathbf{r} = \mathbf{x} - \mathbf{y}$, we can solve the Schrödinger equation with the ansatz $\Psi(\mathbf{x}, \mathbf{y}) = \exp(i\mathbf{KR})\psi_K(\mathbf{r})$, where $\mathbf{K}$ is the quasi-momentum of the centre of mass motion and $\psi_K(\mathbf{r})$ is the pair wavefunction. We derive two types of solutions (for details see Methods), each of which are eigenstates of $\mathbf{K}$. These states, as illustrated in Fig. 2a, correspond to (1) unbound scattering solutions (shaded area in Fig. 2a), where the two particles move on the lattice, and scatter from each other according to the interaction U, and (2) repulsively bound pairs for which $\psi_K(\mathbf{r})$ is square integrable. In one and two dimensions, states of repulsively bound pairs always exist for non-zero U, while in three dimensions they exist above a critical value $U_{crit} \approx 0.5J$.

In this Letter, we focus primarily on the 1D situation, which in the experiment corresponds to a low depth of the lattice along one direction, whilst the lattice in the perpendicular directions remains very deep ($35E_r$). Here the energy of the bound pairs is $E(K) = 2J\left[\sqrt{4(\cos\frac{Ka}{2})^2 + (U/2J)^2} + 2\right]$. This is plotted in Fig. 2a as the Bloch band of a stable composite object above the continuum of two-particle scattering states. In the limit of strong interaction, $U \gg J$, this reduces to $E(K) \approx 4J + U + (4J^2/U)(1 + \cos Ka)$, which shows that the bound pairs indeed have binding energy of $\sim U$ and hop through the lattice with an effective tunnelling rate $J^2/(\hbar U)$.

Figure 2b shows the pair wavefunctions $\psi_K(r)$ for repulsively bound pairs ($a_s = 100a_0$) in one dimension with $K = 0$, for $U/J = 30$ ($V_0 \approx 10E_r$) and $U/J = 3$ ($V_0 \approx 3E_r$). For large U/J, bound pairs essentially consist of two atoms occupying the same site, whereas for small U/J, the pair is delocalized over several lattice sites. The corresponding quasi-momentum distribution can be found from the Fourier transform $\tilde{\psi}_0(k)$ of the pair wavefunction (Fig. 2c), where k is the relative quasi-momentum. Because $K = 0$, $|\tilde{\psi}_0(k)|^2$ is also equal to the single-particle quasi-momentum distribution. When the two particles are localized on the same site, the quasi-momentum distribution is essentially flat. However, for lower U/J the wavefunction is characteristically peaked at the edges of the Brillouin zone. This occurs because the energy of the repulsively bound state is above that of the continuum, and thus the contribution to the corresponding wavepacket of single-particle quasi-momentum states with higher energy is favoured. In contrast, if we had $U < 0$, the pair would be attractively bound, and would have energy lower than that in the continuum. Thus contributions from the low-energy quasi-momentum states would be favoured, leading to a single peak in the centre of the Brillouin zone. In both cases, the amplitude of the peaks grows with increasing width $4J$ of the Bloch band. In general, the stable bound pairs will not be prepared in a fixed quasi-momentum state K in an experiment, but rather in a superposition of different momentum states. For non-zero K, the peaks in the single-particle quasi-momentum distribution are translated by K, but their strength is also reduced. As a consequence, for typical symmetric distributions of K, the peak at the edge of the Brillouin zone remains present, but is less strong than in the optimal case of vanishing K. We have verified this using many-body numerical simulations, which were performed using time-dependent density-matrix renormalization group methods[21–23].

We have experimentally investigated the quasi-momentum distribution of the pairs in various regimes by mapping it onto a spatial distribution, which we measured using standard absorption imaging. For this, we first adiabatically lower the lattice depth in the X

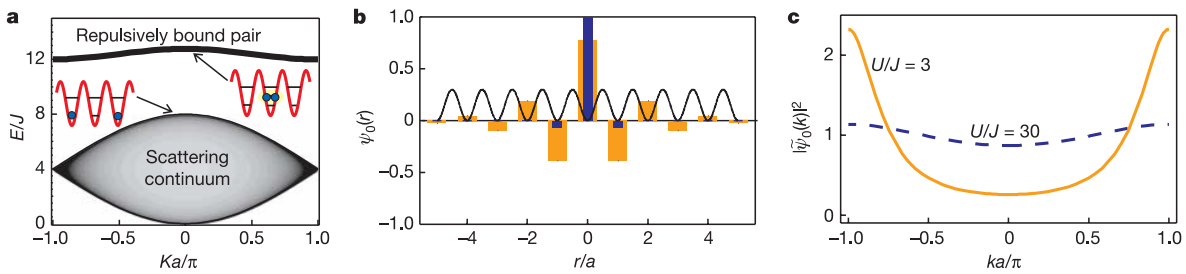

Figure 2 | Atom pair states in one dimension. **a**, Spectrum of energy E of the 1D hamiltonian for $U/J = 8$ ($V_0 \approx 6E_r$) as a function of centre of mass quasi-momentum K. The Bloch band for repulsively bound pairs is located above the continuum of unbound states. The grey level for the shading of the continuum is proportional to the density of states. **b**, The pair wavefunction $\psi_0(r)$, showing the amplitude at each site with $U/J = 30$ ($V_0 \approx 10E_r$, blue bars) and $U/J = 3$ ($V_0 \approx 3E_r$, orange bars). **c**, The square modulus of the corresponding momentum space wavefunctions $|\tilde{\psi}_0(k)|^2$, which are equivalent to the single-particle momentum distributions, as $K = 0$. Note the characteristic peaks at the edge of the Brillouin zone.

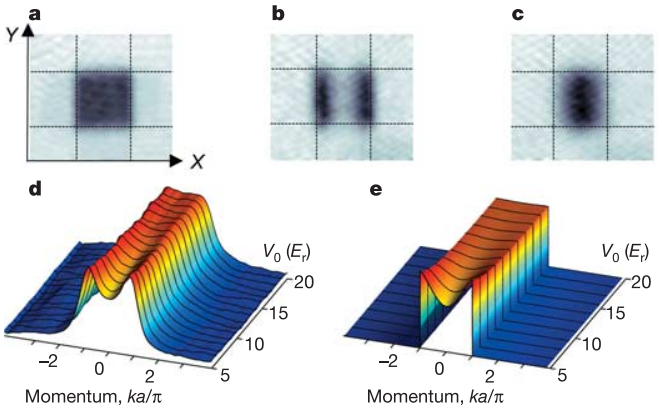

Figure 3 | Quasi-momentum distribution of atoms in the lattice. **a–c**, Absorption images of the atomic distribution after release from the 3D lattice and a subsequent 15-ms time of flight. The horizontal and vertical black lines enclose the first Brillouin zone. **a**, Distribution when lattice sites are occupied by single atoms; **b**, distribution for repulsively bound atom pairs (see text for details); **c**, same as **b** but pairs are attractively bound. **d**, **e**, The quasi-momentum distribution for pairs in the X direction as a function of lattice depth V_0, after integration over the Y direction. **d**, Experiment; **e**, numerical calculation. See Methods for a definition of E_r.

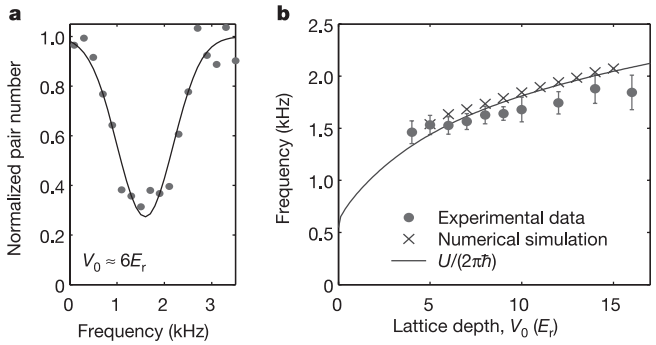

Figure 4 | Modulation spectroscopy of repulsively bound pairs. **a**, Typical resonance dip showing the remaining number of atom pairs as a function of the modulation frequency, for $V_0 \approx 6E_r$. The solid line is a gaussian fit, a choice that was justified by numerical calculations. **b**, Plot showing the measured resonance frequencies (filled circles) as a function of the lattice depth. They show good agreement with numerical simulations (crosses) and also coincide with the on-site collisional energy shift U (line). Experimental error bars correspond to the 95% confidence interval for the gaussian fit parameters of the resonance dips.

direction (Fig. 3a) at a rate of $1.3E_r$ (ms^{-1}) to a pre-chosen height while the lattice depth in the other two directions is kept high ($35E_r$). This will prepare repulsively bound pairs at the chosen lattice depth. We then turn off the lattice rapidly enough for the pair wavefunction not to change, but slowly with respect to the bandgap, so that single-particle quasi-momenta are mapped to real momenta[24,25]. We have typically employed linear ramps with rates of $0.2E_r\,\mu s^{-1}$. The resulting momentum distribution is converted to a spatial distribution after ~15 ms time of flight.

Figure 3a–c shows typical measured quasi-momentum distributions that were obtained after adiabatically lowering the lattice depth in the X direction to the lowest values, below $3E_r$. If only empty sites and sites with single atoms are present in the lattice, then the first Brillouin zone is homogeneously filled[24] (Fig. 3a). For repulsively bound pairs, the momentum distribution is, in general, peaked at the edges of the first Brillouin zone (Fig. 3b), whereas for attractively bound pairs, it is peaked in the centre of the first Brillouin zone (Fig. 3c). In order to change the interaction between the atoms from repulsive to attractive, we change the scattering length, making use of the Feshbach resonance[26] at 1,007.40 G. Figure 3d and e shows the dependence on lattice depth V_0 of the single-particle quasi-momentum distribution for repulsively bound pairs from experiment and numerical simulation, respectively. As expected, the peak structure is more pronounced for lower values of V_0, and diminishes for larger V_0. This characteristic is a clear signature of the pair wavefunction for repulsively bound pairs.

We also performed spectroscopic measurements, determining the binding energy from pair dissociation produced by modulating the depth of the lattice at a chosen frequency. On resonance, the modulation allows pairs to release their binding energy. Figure 4a shows the number of remaining pairs as a function of the modulation frequency. This was repeated for a variety of lattice depths V_0 in one direction while keeping the lattice in the other two directions at $35E_r$. The behaviour of the binding energy as a function of the lattice depth provides an additional key signature of repulsively bound pairs. As shown in Fig. 4b, the resonance positions are in good agreement with numerical simulations and essentially coincide with the interaction energy, U.

It is important to note that for sufficiently large U/J, repulsively bound pairs are stable under collisions with each other. This is particularly evident in the limit $U \gg J$ where, by energy arguments, the elastic scattering between pairs is the only open channel. This means that even a relatively dense quantum lattice gas of these objects can be long-lived. When the lattice height is lowered so that U/J becomes sufficiently small, it is possible for a certain fraction of the pairs to dissociate by collision with other pairs. In our experiments, we observe the onset of this behaviour for lattice depths lower than $6E_r$, that is, $U/J \approx 9$. The dynamics of the collisions and details of the decay depend crucially on lattice depth and the local density of pairs across the lattice. Further details of these processes will be discussed elsewhere.

In conclusion, we have demonstrated the formation of a novel composite object in an optical lattice: a stable bound state that arises from the lattice band structure and repulsion between the constituents. Although no direct analogue to repulsively bound atomic pairs is known to exist, the formation of a metastable state is reminiscent of trapping light in photonic bandgap materials[27], or extended lifetimes of excited atoms in cavity quantum electrodynamics[28]. In both cases, decay is suppressed by restriction of the accessible light field modes. Stable repulsively bound objects should be viewed as a general phenomenon, and their existence will be ubiquitous in cold atom lattice physics. They also give rise to new potential composites with fermions[29] or Bose–Fermi mixtures[30], and can be formed in an analogous manner with more than two particles. The stability of repulsively bound objects could thus be the basis of a wealth of new quantum many-body states or phases. In particular, the next experimental step in investigating repulsively bound atomic pairs is the possible realization of a condensate of pairs, together with the means to characterise long-range order in this system.

METHODS

Preparation of pure molecular sample. We use a set-up which was described in detail in ref. 13, starting with a Bose–Einstein condensate of 6×10^5 ^{87}Rb atoms in an Ioffe-type magnetic trap with trap frequencies $\omega_{x,y,z} = 2\pi \times (7, 19, 20)$ Hz). Within 100 ms the Bose–Einstein condensate is adiabatically loaded into the cubic 3D optical lattice which is $35E_r$ deep. After turning off the magnetic trap, we flip the spins of our atoms from their initial state $|F = 1, m_F = -1\rangle$ to $|F = 1, m_F = +1\rangle$ by suddenly reversing the bias magnetic field of a few gauss. This spin state features a 210-mG-wide Feshbach resonance at 1,007.40 G (ref. 26). By adiabatically ramping over this resonance we convert pairs of atoms in multiply occupied lattice sites into Rb_2 Feshbach molecules. Fast inelastic collisions of molecules within lattice sites and a subsequent combined radio-frequency and optical purification pulse remove all chemically unbound atoms, thus creating a pure molecular sample of about 2×10^4 molecules.

Exact solution for single pair bound state. Within the Bose–Hubbard model (equation (1)), the Schrödinger equation describing two particles in a

homogenous optical lattice takes the form

$$\left[-J\left(\tilde{\Delta}_{\mathbf{x}}^{0}+\tilde{\Delta}_{\mathbf{y}}^{0}\right)+U\delta_{\mathbf{x},\mathbf{y}}\right]\Psi(\mathbf{x},\mathbf{y})=E\Psi(\mathbf{x},\mathbf{y}) \quad (2)$$

where the vectors $\mathbf{x}$ and $\mathbf{y}$ describe the positions of the two particles as defined in the main text. The operator $\tilde{\Delta}_{\mathbf{x}}^{\mathbf{K}}\Psi(\mathbf{x})=\sum_{i=1}^{d}\cos(\mathbf{K}\mathbf{e}_i/2)[\Psi(\mathbf{x}+\mathbf{e}_i)+\Psi(\mathbf{x}-\mathbf{e}_i)-2\Psi(\mathbf{x})]$ denotes the discrete lattice laplacian with d the dimensionality in the cubic lattice, and $\delta_{\mathbf{x},\mathbf{y}}$ is a Kronecker delta. Writing the wavefunction in relative and centre of mass coordinates $\Psi(\mathbf{x},\ \mathbf{y})=\exp(i\mathbf{K}\mathbf{R})\psi_K(\mathbf{r})$, the Schrödinger equation (2) then reduces to a single-particle problem in the relative coordinate

$$\left[-2J\tilde{\Delta}_{\mathbf{r}}^{\mathbf{K}}+E_{\mathbf{K}}+U\delta_{\mathbf{r},0}\right]\psi_K(\mathbf{r})=E\psi_K(\mathbf{r}) \quad (3)$$

with $E_{\mathbf{K}}=4J\Sigma_i[1-\cos(\mathbf{K}\mathbf{e}_i/2)]$ being the kinetic energy of the centre of mass motion.

The short range character of the interaction potential allows for a resummation of the perturbation expansion generated by the corresponding Lippmann–Schwinger equation. We obtain the scattering states

$$\psi^{(+)}(\mathbf{r})=\exp(i\mathbf{k}\mathbf{r})-8\pi J f_E(\mathbf{K})G_{\mathbf{K}}(E,\mathbf{r}) \quad (4)$$

with scattering amplitude

$$f_E(\mathbf{K})=-\frac{1}{4\pi}\frac{U/(2J)}{1-G_{\mathbf{K}}(E,0)U} \quad (5)$$

where the total energy $E=\varepsilon_{\mathbf{k},\mathbf{K}}+E_{\mathbf{K}}$, and $\varepsilon_{\mathbf{k},\mathbf{K}}=4J\Sigma_i\cos(\mathbf{K}\mathbf{e}_i/2)[1-\cos(\mathbf{k}\mathbf{e}_i)]$. Furthermore, $G_{\mathbf{K}}(E,\ \mathbf{r})$ denotes the Green's function of the non-interacting problem, which in Fourier space takes the form $\tilde{G}_{\mathbf{K}}(E,\mathbf{k})=1/(E-\varepsilon_{\mathbf{k},\mathbf{K}}+i\eta)$.

The energy spectrum for these states in one dimension is shown as a function of K by the shaded region in Fig. 2a. In addition, the pole in the scattering amplitude indicates the presence of an additional bound state. The energy E_{bs} of the bound state is determined by $G_{\mathbf{K}}(E_{\mathrm{bs}},0)U=1$ and the bound state wavefunction takes the form $\psi^{\mathrm{bs}}(\mathbf{r})=cG_{\mathbf{K}}(E_{\mathrm{bs}},\mathbf{r})$, with c being a normalization factor.

Received 1 April; accepted 18 May 2006.

1. Jaksch, D. & Zoller, P. The cold atom Hubbard toolbox. *Ann. Phys.* **315,** 52–79 (2005).
2. Bloch, I. Ultracold quantum gases in optical lattices. *Nature Phys.* **1,** 23–30 (2005).
3. Fisher, M. P. A., Weichman, P. B., Grinstein, G. & Fisher, D. S. Boson localization and the superfluid insulator transition. *Phys. Rev. B.* **40,** 546–570 (1989).
4. Greiner, M., Mandel, O., Esslinger, T., Hänsch, T. W. & Bloch, I. Quantum phase transition from a superfluid to a Mott insulator in a gas of ultracold atoms. *Nature* **415,** 39–44 (2002).
5. Paredes, B. *et al.* Tonks–Girardeau gas of ultracold atoms in an optical lattice. *Nature* **429,** 277–281 (2004).
6. Stöferle, T., Moritz, H., Schori, C., Köhl, M. & Esslinger, T. Transition from a strongly interacting 1D superfluid to a Mott insulator. *Phys. Rev. Lett.* **92,** 130403 (2004).
7. Kinoshita, T., Wenger, T. & Weiss, D. S. Observation of a one-dimensional Tonks-Girardeau gas. *Science* **305,** 1125–1128 (2004).
8. Laburthe Tolra, B. *et al.* Observation of reduced three-body recombination in a correlated 1D degenerate Bose gas. *Phys. Rev. Lett.* **92,** 190401 (2004).
9. Fallani, L., Lye, J. E., Guarrera, V., Fort, C. & Inguscio, M. Onset of a Bose-glass of ultra-cold atoms in a disordered crystal of light. Preprint at ⟨http://arxiv.org/abs/cond-mat/0603655⟩ (2006).
10. Fedichev, P. O., Bijlsma, M. J. & Zoller, P. Extended molecules and geometric scattering resonances in optical lattices. *Phys. Rev. Lett.* **92,** 080401 (2004).
11. Ryu, C. *et al.* Raman-induced oscillation between an atomic and a molecular quantum gas. Preprint at ⟨http://arxiv.org/abs/cond-mat/0508201⟩ (2005).
12. Stöferle, T., Moritz, H., Günter, K., Köhl, M. & Esslinger, T. Molecules of fermionic atoms in an optical lattice. *Phys. Rev. Lett.* **96,** 030401 (2006).
13. Thalhammer, G. *et al.* Long-lived Feshbach molecules in a 3D optical lattice. *Phys. Rev. Lett.* **96,** 050402 (2006).
14. Donley, E. A., Claussen, N. R., Thompson, S. T. & Wieman, C. E. Atom–molecule coherence in a Bose–Einstein condensate. *Nature* **417,** 529–533 (2002).
15. Regal, C. A., Ticknor, C., Bohn, J. L. & Jin, D. S. Creation of ultracold molecules from a Fermi gas of atoms. *Nature* **424,** 47–50 (2003).
16. Herbig, J. *et al.* Preparation of a pure molecular quantum gas. *Science* **301,** 1510–1513 (2003).
17. Xu, K. *et al.* Formation of quantum-degenerate sodium molecules. *Phys. Rev. Lett.* **91,** 210402 (2003).
18. Cubizolles, J., Bourdel, T., Kokkelmans, S. J. J. M. F., Shlyapnikov, G. V. & Salomon, C. Production of long-lived ultracold Li_2 molecules from a Fermi gas. *Phys. Rev. Lett.* **91,** 240401 (2003).
19. Dürr, S., Volz, T., Marte, A. & Rempe, G. Observation of molecules produced from a Bose-Einstein condensate. *Phys. Rev. Lett.* **92,** 020406 (2004).
20. Koehler, T., Goral, K. & Julienne, P. S. Production of cold molecules via magnetically tunable Feshbach resonances. Preprint at ⟨http://arxiv.org/abs/cond-mat/0601420⟩ (2006).
21. Vidal, G. Efficient classical simulation of slightly entangled quantum computations. *Phys. Rev. Lett.* **91,** 147902 (2003).
22. Daley, A. J., Kollath, C., Schollwöck, U. & Vidal, G. Time-dependent density-matrix renormalization-group using adaptive effective Hilbert spaces. *J. Stat. Mech. Theor. Exp.* P04005 (2004).
23. White, S. R. & Feiguin, A. E. Real-time evolution using the density matrix renormalization group. *Phys. Rev. Lett.* **93,** 076401 (2004).
24. Greiner, M., Bloch, I., Mandel, O., Hänsch, T. W. & Esslinger, T. Exploring phase coherence in a 2D lattice of Bose-Einstein condensates. *Phys. Rev. Lett.* **87,** 160405 (2001).
25. Hecker Denschlag, J. *et al.* A Bose-Einstein condensate in an optical lattice. *J. Phys. B.* **35,** 3095–3110 (2002).
26. Volz, T., Dürr, S., Ernst, S., Marte, A. & Rempe, G. Characterization of elastic scattering near a Feshbach resonance in ^{87}Rb. *Phys. Rev. A* **68,** 010702 (2003).
27. Joannopoulos, J. D., Meade, R. D. & Winn, J. N. *Photonic Crystals: Molding the Flow of Light* (Princeton Univ. Press, Princeton, 1995).
28. Berman, P. (ed.) *Cavity Quantum Electrodynamics* (Academic, New York, 1994).
29. Hofstetter, W., Cirac, J. I., Zoller, P., Demler, E. & Lukin, M. D. High-temperature superfluidity of fermionic atoms in optical lattices. *Phys. Rev. Lett.* **89,** 220407 (2002).
30. Lewenstein, M., Santos, L., Baranov, M. A. & Fehrmann, H. Atomic Bose-Fermi mixtures in an optical lattice. *Phys. Rev. Lett.* **92,** 050401 (2004).

Acknowledgements We thank H. Ritsch for discussions, and M. Theis and S. Schmid for help in setting up the experiment. We acknowledge support from the Austrian Science Fund (FWF) within the Spezialforschungsbereich 15, from the European Union within the OLAQUI and SCALA networks, from the TMR network 'Cold Molecules', and from the Tiroler Zukunftsstiftung.

Author Contributions This work is a collaboration between teams of experimental (K.W., G.T., F.L., R.G. and J.H.D.) and theoretical (A.J.D., A.K., H.P.B. and P.Z.) physicists.

Author Information Reprints and permissions information is available at npg.nature.com/reprintsandpermissions. The authors declare no competing financial interests. Correspondence and requests for materials should be addressed to J.H.D. (Johannes.Denschlag@uibk.ac.at).

New Journal of Physics
The open-access journal for physics

Long distance transport of ultracold atoms using a 1D optical lattice

Stefan Schmid, Gregor Thalhammer, Klaus Winkler, Florian Lang and Johannes Hecker Denschlag

Institut für Experimentalphysik, Universität Innsbruck, Technikerstraße 25, 6020 Innsbruck, Austria
E-mail: johannes.denschlag@uibk.ac.at

New Journal of Physics **8** (2006) 159
Received 30 May 2006
Published 30 August 2006
Online at http://www.njp.org/
doi:10.1088/1367-2630/8/8/159

Abstract. We study the horizontal transport of ultracold atoms over macroscopic distances of up to 20 cm with a moving 1D optical lattice. By using an optical Bessel beam to form the optical lattice, we can achieve nearly homogeneous trapping conditions over the full transport length, which is crucial in order to hold the atoms against gravity for such a wide range. Fast transport velocities of up to $6\,\mathrm{m\,s^{-1}}$ (corresponding to about 1100 photon recoils) and accelerations of up to $2600\,\mathrm{m\,s^{-2}}$ are reached. Even at high velocities the momentum of the atoms is precisely defined with an uncertainty of less than one photon recoil. This allows for construction of an atom catapult with high kinetic energy resolution, which might have applications in novel collision experiments.

Contents

PII: S1367-2630(06)25646-5

1. Introduction

Fast, large-distance transport of Bose–Einstein condensates (BEC) from their place of production to other locations is of central interest in the field of ultracold atoms. It allows for exposure of BECs to all different kinds of environments, spawning progress in BEC manipulation and probing.

Transport of cold atoms has already been explored in various approaches using magnetic and optical fields. Magnetic fields have been used to shift atoms, e.g. on atom chips (for a review see [1]) and to move laser-cooled clouds of atoms over macroscopic distances of tens of centimetres, e.g. [2, 3]. By changing the position of an optical dipole trap, a BEC has been transferred over distances of about 40 cm within several seconds [4]. This approach consisted of mechanically relocating the focusing lens of the dipole trap with a large translation stage. A moving optical lattice offers another interesting possibility to transport ultracold atoms. Acceleration of atoms with lattices is intimately connected to the techniques of Raman transitions [5], STIRAP [6, 7] and the phenomenon of Bloch oscillations [8, 9]; (for a recent review on atoms in optical lattices see [10]). Acceleration with optical lattices allows for precise momentum transfer in multiples of two photon recoils to the atoms. Transport of single, laser-cooled atoms in a deep optical lattice over short distances of several mm has been reported in [11]. Coherent transport of atoms over several lattice sites has been described in [12]. Even beyond the field of ultracold atoms, applications of optical lattices for transport are of interest, e.g. to relocate submicron sized polystyrene spheres immersed in heavy water [13].

Here, we experimentally investigate transporting BECs and ultracold thermal samples with an optical lattice over macroscopic distances of tens of centimetres. Our method features the combination of the following important characteristics. The transport of the atoms is in the quantum regime, where all atoms are in the vibrational ground state of the lattice. With our setup, mechanical noise is avoided and we achieve precise positioning (on the order of the imaging resolution of 1 μm). We demonstrate high transport velocities of up to 6 m s^{-1}, which are accurately controlled on the quantum level. The velocity spread of the atoms is not more than 2 mm s^{-1}, corresponding to 1/3 of a photon recoil.

2. Basic principle of transport

Horizontal transport of atoms over larger distances holds two challenges: how to move the atoms and how to support them against gravity. Our approach here is to use a special 1D optical lattice trap, which is formed by a Bessel laser beam and a counterpropagating Gaussian beam. The lattice part of the trap moves the atoms axially, whereas the Bessel beam leads to radial confinement holding the atoms against gravity.

In brief, lattice transport works like this. We first load the atoms into a 1D optical lattice, which in general is a standing wave interference pattern of two counterpropagating laser beams far red-detuned from the atomic resonance line (see figure 1). Afterwards the optical lattice is carefully moved, 'dragging' along the atoms. Upon arrival at the destination, the atoms are released from the lattice.

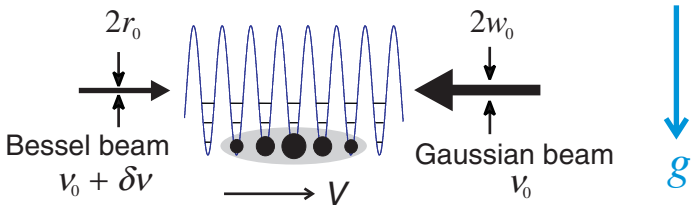

Figure 1. Scheme for atom transport. Two counterpropagating laser beams form a standing wave dipole trap. A BEC is loaded adiabatically into the vibrational ground state of this 1D optical lattice. A relative frequency detuning $\Delta\nu$ between the two laser beams results in a lattice motion at a velocity $v = \Delta\nu \cdot \lambda/2$ which drags along the trapped atoms. We chose the counterpropagating laser beams to consist of a Gaussian beam with diameter $2w_0$ and a Bessel beam with a central spot diameter of $2r_0$. The (in principle) diffraction-free propagation of the Bessel beam leads to tight radial confinement of the atoms over long distances, which supports the atoms against gravity during horizontal transport.

The lattice motion is induced by dynamically changing the relative frequency detuning $\Delta\nu$ of the two laser beams, which corresponds to a lattice velocity

$$v = \frac{\lambda}{2}\Delta\nu, \tag{1}$$

where λ is the laser wavelength of the lattice.

In comparison to the classical notion of simply 'dragging' along the atoms in the lattice, atom transport is more subtle on the quantum level. Here, only momenta in multiples of two photon recoil momenta, $2\hbar k = 4\pi\hbar/\lambda$ can be transferred to the atoms. This quantized momentum transfer can be understood in several ways, e.g. based on stimulated Raman transitions or based on the concept of Bloch-like oscillations in lattice potentials. For a more thorough discussion in this context, the reader is referred to [14].

In order to prevent the atoms from falling in the gravitational field, the lattice has to act as an optical dipole trap in the radial direction. It turns out that for radial trapping, optical lattices formed by Bessel beams have a clear advantage over Gaussian beam lattices. To make this point clear, we now show, that a standard optical lattice based on Gaussian beams is not well suited for long distance transports on the order of 50 cm. During transport, we require the maximum radial confining force $F_{\max}$ to be larger than gravity mg, where m is the atomic mass and $g \approx 9.81\,\mathrm{m\,s^{-2}}$ is the acceleration due to gravity. For a Gaussian beam this is

$$F_{\max} = \frac{3}{4\pi^3\sqrt{\mathrm{e}}}\frac{\lambda^3}{c}\frac{\Gamma}{\Delta}\frac{P_0}{w(z)^3} > mg, \tag{2}$$

where Γ is the natural linewidth of the relevant atomic transition, Δ the detuning from this transition, $w(z)$ the beam radius and P_0 the total power of the beam. The strong dependence on the beam radius $w(z)$ suggests, that $w(z) = w_0\sqrt{1 + (z/z_\mathrm{R})^2}$ should not vary too much over the transport distance. If we thus require the Rayleigh range $z_\mathrm{R} = \pi w_0^2/\lambda$ to equal the distance of 25 cm, the waist has to be $w_0 \approx 260\,\mu$m. For a lattice beam wavelength of e.g. $\lambda = 830$ nm, the detuning from the D-lines of ^{87}Rb is $\Delta \approx 2\pi \times 130$ THz. To hold the atoms against gravity for

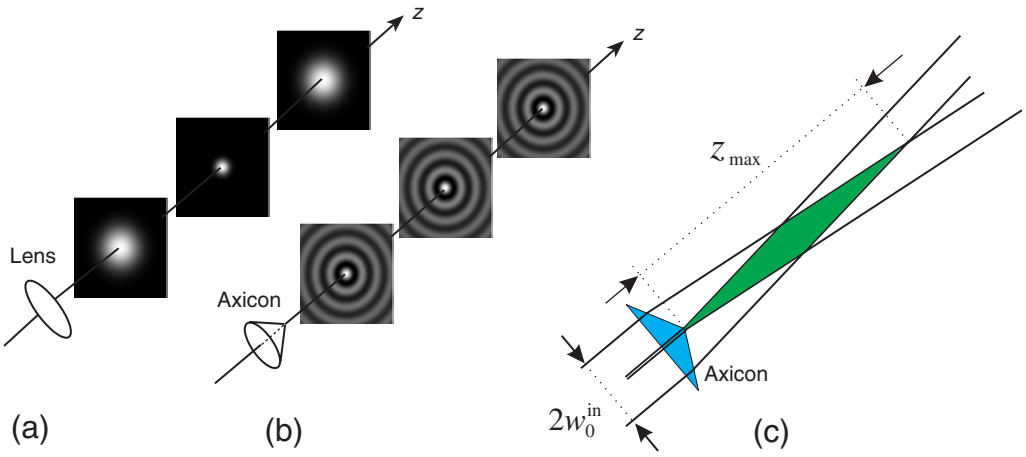

Figure 2. Gaussian and Bessel beams. (a) The radial intensity distribution of a Gaussian beam changes as it propagates. The smaller the waist w_0 of the beam, the higher its divergence (for a given wavelength). (b) Bessel beam: the radial distribution and in particular the radius of the central spot r_0 do not change with z (see equation (8)). (c) Within a certain axial range z_{max} a Bessel-like beam can be produced by illuminating an axicon lens with a collimated laser beam.

all z, where $|z| < z_R$, a total laser power of $P_0 \approx 10\,\mathrm{W}$ is needed, which is difficult to produce. In addition, the spontaneous photon scattering rate

$$\Gamma_{\mathrm{scatt}} = \frac{3}{8\pi^3\hbar}\frac{\lambda^3}{c}\left(\frac{\Gamma}{\Delta}\right)^2\frac{P_0}{w(z)^2} \tag{3}$$

would reach values on the order of $\Gamma_{\mathrm{scatt}} = 2\,\mathrm{s}^{-1}$. For typical transport times of 200 ms, this means substantial heating and atomic losses.

A better choice for transport are zero order Bessel beams (figure 2). They exhibit an intensity pattern which consists of an inner intensity spot surrounded by concentric rings and which does *not* change during propagation. In our experiments, we have formed a standing light wave by interfering a Bessel beam with a counterpropagating Gaussian beam, giving rise to an optical lattice which is radially modulated according to the Bessel beam.[1] Atoms loaded into the tightly confined inner spot of the Bessel beam can be held against gravity for moderate light intensities, which minimizes the spontaneous photon scattering rate. In comparison to the transport with a Gaussian beam, the scattering rate in a Bessel beam transport can be kept as low as $0.05\,\mathrm{s}^{-1}$ by using the beam parameters of our experiment.

3. Bessel beams

Bessel beams are a solution of the Helmholtz equation and were first discussed and experimentally investigated about two decades ago [15, 16].

[1] In principle, one could also use a pure Bessel lattice (produced by two counterpropagating Bessel beams) for transport. This would improve radial confinement, however, alignment is more involved.

In cylindrical coordinates, the electric field distribution of a Bessel beam of order l is given by

$$E(r, \varphi, z) = E_0 \, \mathrm{e}^{\mathrm{i}\beta z} \, \mathrm{e}^{\mathrm{i}l\varphi} J_l(\alpha r), \tag{4}$$

where $J_l(\alpha r)$ is the Bessel function of the first kind with integer order l. The beam is characterized by the parameters α and β. In the following, we restrict the discussion to order $l = 0$ which we have used in the experiment. By taking the absolute square of this expression, one gets the intensity distribution given by

$$I(r, z) = I_0 J_0^2(\alpha r), \tag{5}$$

where α determines the radius r_0 of the central spot via the first zero crossing of $J_0(\alpha r)$

$$r_0 \approx \frac{4.81}{2\alpha}. \tag{6}$$

As pointed out before, r_0 and I_0 do not change with the axial position z. Because of this axial independence, the Bessel beams are said to be 'diffraction-free'.

Bessel-like beams were realized experimentally for the first time by illuminating a circular slit [16]. Since this method is very inefficient, two other ways are common now-a-days. To generate Bessel beams of arbitrary order, holographic elements, such as phase-gratings, are used [17]. In our setup, we use a zero order Bessel beam, which can be produced efficiently by simply illuminating an axicon (conical lens) with a collimated laser beam [18]. How this comes about can be understood by looking at the Fourier transform of the Bessel field

$$\widetilde{E}(k_\perp, \varphi_k, k_z) = \int \mathrm{d}^3 r E(r, \varphi, z) \mathrm{e}^{-\mathrm{i}k_\perp r \cos(\varphi - \varphi_k)} \mathrm{e}^{-\mathrm{i}k_z z} \propto \mathrm{e}^{\mathrm{i}l\varphi_k} \delta(k_z - \beta)\delta(k_\perp - \alpha). \tag{7}$$

Thus a Bessel beam is a superposition of plane waves with $(k_\perp, k_z) = (\alpha, \beta)$. The $\mathbf{k}$-vectors of the plane waves all have the same magnitude $|\mathbf{k}| = k = 2\pi/\lambda = \sqrt{\alpha^2 + \beta^2}$ and they are forming a cone with radius $k_\perp$ and height k_z. Using an axicon with apex angle δ and index of refraction n, α and β are given by

$$\alpha = \frac{\pi(n-1)}{2\lambda \tan \delta/2} \tag{8}$$

and

$$\beta = \sqrt{k^2 - \alpha^2}. \tag{9}$$

These experimentally produced Bessel beams are not ideal in the sense that their range $z_{\max} = k w_0^{\mathrm{in}}/\alpha$ is limited by the finite size (waist w_0^{in}) of the beam impinging on the axicon lens (see figure 2(c)). Also, the intensity of the Bessel beams might not be independent of the axial coordinate z, as it is also determined by the radial intensity distribution of the impinging beam (e.g. see figure 4(b)).

4. Experimental setup

We work with a ^{87}Rb-BEC in the internal state $|F = 1, m_F = -1\rangle$, initially held in a Ioffe-type magnetic trap with trap frequencies of $2\pi\nu_{x,y,z} = 2\pi$ (7, 19 and 20 Hz) [19, 20]. From

the magnetic trap, the condensate is adiabatically loaded in about 100 ms into the inner core of the 1D optical lattice formed by a Bessel beam of central spot radius $r_0 = 36\,\mu$m and a counterpropagating Gaussian beam with a waist of $w_0 = 85\,\mu$m. About 70 lattice sites are occupied with atoms in the vibrational ground state. The lattice periodicity is 415 nm, corresponding to the laser wavelength of 830 nm. For our geometry (see below) the total power needed for the Bessel beam to support the atoms against gravity is typically 200 mW, since only a few per cent ($\approx$10 mW) of the total power are stored in the central spot. For the Gaussian beam, a power of roughly 20 mW is chosen, leading to an optical trapping potential at the centre ($r = 0$) of $U(z) = -U_0 + U_{\mathrm{latt}} \sin^2(kz)$, where the lattice depth (effective axial trap depth) is $U_{\mathrm{latt}} \approx 10 E_{\mathrm{r}}$ and the total trap depth $U_0 \approx 11 E_{\mathrm{r}}$. Here, $E_{\mathrm{r}} = (\hbar k)^2/(2m)$ is the recoil energy.

The corresponding trap frequencies are $\nu_\perp = 4.81\sqrt{U_0/(8mr_0^2)}/(2\pi) = 97$ Hz in the radial direction and $\nu_z = k\sqrt{2U_{\mathrm{latt}}/m}/(2\pi) = 21$ kHz in the axial direction. In order to better analyse the transport properties, we mostly perform round trips, where the atoms are first moved to a distance D and then back to their initial spot, which lies in the field of vision of our CCD camera. Once back, the atoms are adiabatically reloaded into the Ioffe-type magnetic trap. To obtain the resulting atomic momentum distribution, a standard absorption imaging picture is taken after sudden release from the magnetic trap and typically 12 ms of time-of-flight.

The lattice beams for the optical lattice are derived from a Ti:Sapphire-laser operating at 830 nm. The light is split into two beams, each of which is controlled in amplitude, phase and frequency with an acousto-optical modulator (AOM). For both AOMs, the radio-frequency (RF) driver consists of a home-built 300 MHz programmable frequency generator, which gives us full control over amplitude, frequency and phase of the radio-wave at any instant of time. The frequency generator is based on an AD9854 digital synthesizer chip from Analogue Devices and a 8-bit micro-controller ATmega162 from Atmel, on which the desired frequency ramps are stored and from which they are sent to the AD9854 upon request. After passing the AOMs, the two laser beams are mode-cleaned in single-mode fibres and converted into collimated Gaussian beams. One of the Gaussian beams passes the axicon lens (apex angle = 178°, radius = 25.4 mm, Del Mar Photonics) with a waist of $w_0^{\mathrm{in}} = 2$ mm, producing the Bessel beam. From there the beam propagates towards the condensate, which—before transport—is located 5 cm away.

5. Transport of ultracold atoms

Figure 3 shows results of a first experiment, where we have transported atoms over short distances of up to 1 mm (round trip), so that they never leave the field of view of the camera. The atoms move perpendicularly to the direction of observation. *In situ* images of the atomic cloud in the optical lattice are taken at various times during transport and the centre of mass position of the cloud is determined. As is clear from figure 3(a), we find very good agreement between the expected and the measured position of the atoms. In figures 3(b) and (c), calculations are shown for the corresponding velocity $v(t)$ and acceleration $a(t)$ of the optical lattice, respectively. As discussed before (see equation (1)), the velocity v of the lattice translates directly into a relative detuning $\Delta\nu$ of the laser beam, which we control via the AOMs. In order to suppress unwanted heating and losses of atoms during transport, we have chosen very smooth frequency ramps $\Delta\nu(t)$ such that the acceleration is described by a cubic spline interpolation curve which is continuously differentiable (details are given in the appendix). In this way, also the derivative of the acceleration (commonly called the jerk) is kept small.

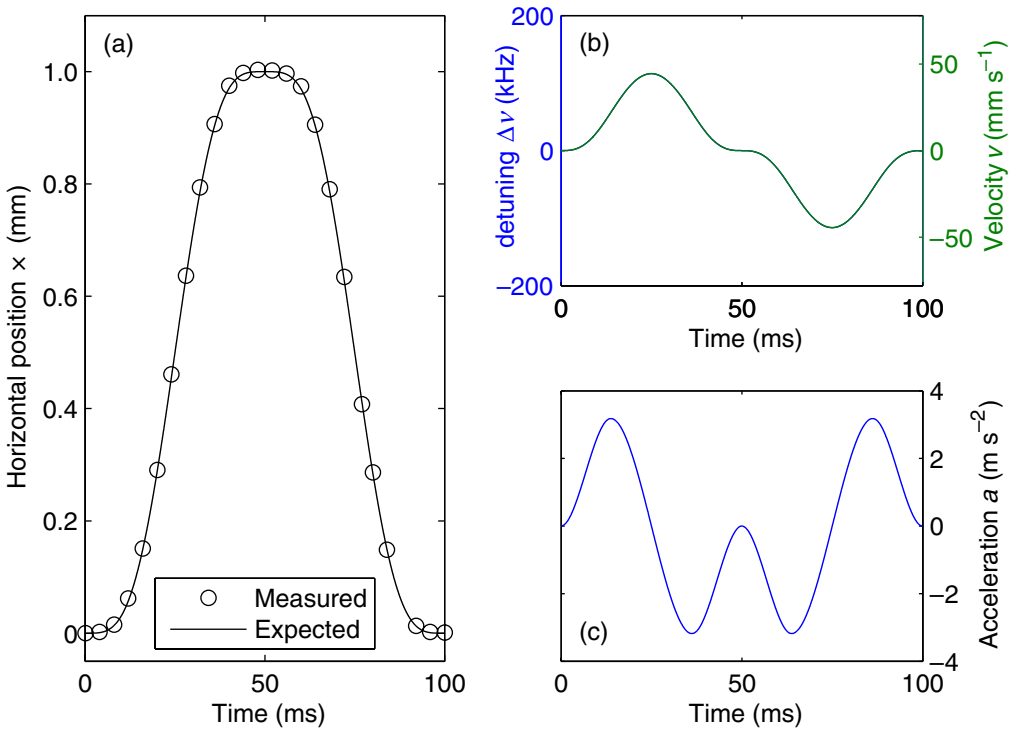

Figure 3. (a) Position, (b) velocity and (c) acceleration of the atomic cloud as a function of time for a typical transport sequence, here a round-trip over a short distance of 1 mm. Piecewise defined cubic polynomials are used for the acceleration ramp (see appendix for an analytical expression). By integrating over time, velocity and position are obtained. The frequency detuning $\Delta\nu$, which is used to program the RF synthesizers, corresponds directly to the velocity v via equation (1). The position ramp is compared with *in situ* measurements of the cloud's position (○).

In the next set of experiments, we extended the atomic transport to more macroscopic distances of up to 20 cm (40 cm round trip), where we moved the atoms basically from one end of the vacuum chamber to the other and back. However, the transport distance was always limited by the finite range $z_{\max}$ of the Bessel beam (see figures 2(c) and 4). As shown in figure 4, the total number of atoms abruptly decreases at the axial position, where the maximum radial force drops below gravity. It is also clear from the figure how the range of the Bessel beam is increased by enlarging the waist w_0^{in} of the incoming Gaussian beam. Of course, for a given total laser power, the maximum radial force decreases as the Bessel beam diameter is increased. For the transport distances of 12 and 20 cm, the total power in the Bessel beam was approximately 400 mW. For comparison, we have also transported atoms with a lattice formed by two counterpropagating Gaussian beams (see figure 4(a)). For this transport, both laser beams have a Rayleigh range of $z_{\text{R}} \approx 2$ cm corresponding to a waist of 70 μm. The laser power of the two beams was ≈130 and ≈35 mW, respectively. We observe a sudden drop in atom number when the transport distance exceeds the Rayleigh range. Using the scaling law given in equation (2), it should be clear that transports of atoms over tens of centimetres with a Gaussian lattice is hard to achieve.

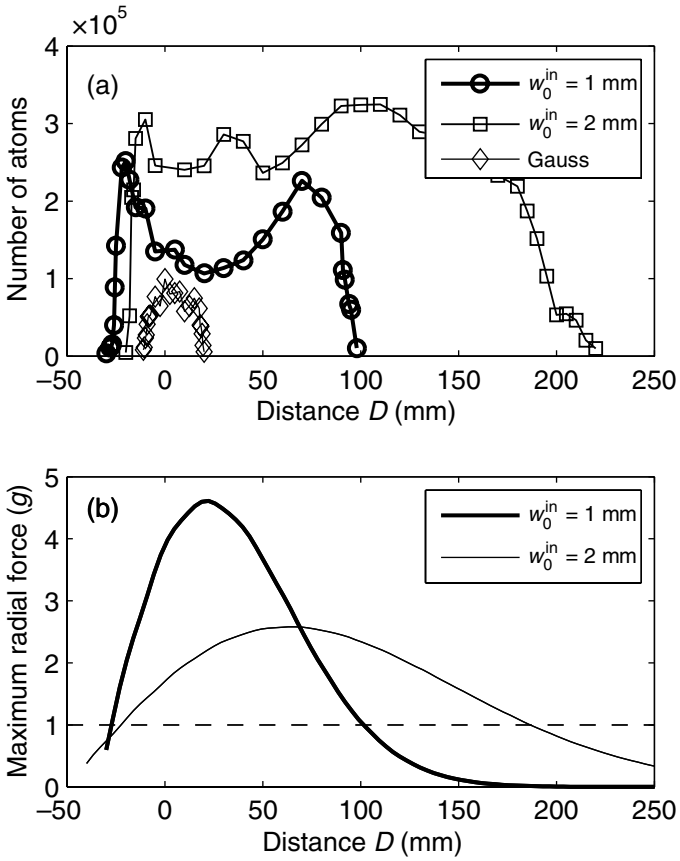

Figure 4. Long distance transports. (a) Shown is the number of remaining atoms after a round-trip transport (see figure 3) over various one-way distances D. The first two data sets are obtained with two different Bessel beams which are created by illuminating an axicon with a Gaussian beam with a waist $w_0^{\text{in}} = 1$ and 2 mm, respectively. The transport time T was kept constant at $T = 130$ ms and $T = 280$ ms, respectively. The third data set ($\diamond$) corresponds to a transport in a Gaussian beam lattice (see text). The calculated maximum radial trapping force of the two Bessel beam lattice traps is shown in (b) in units of mg, where $g \approx 9.81\ \text{m s}^{-2}$ denotes the gravitational acceleration. The variation of the trapping force with distance is an imperfection of the Bessel beam and reflects its creation from a Gaussian beam. When the maximum radial force drops below $1\,g$, gravity pulls the atoms out of the trap, as can be clearly seen in (a).

Interestingly, the curve corresponding to the Bessel beam with waist $w_0^{\text{in}} = 1$ mm in figure 4(a) exhibits a pronounced minimum in the number of remaining atoms at a distance of about 3 cm. The position of this minimum coincides with the position, where the lattice depth has a maximum (see figure 4(b)). This clearly indicates, that high light intensities adversely affect atom lifetimes in the lattice. Although we have not studied in detail the origin of the atomic losses in this work, they should partially originate from spontaneous photon scattering and three body recombination. In the deep lattice here ($60E_{\text{r}}$), the calculated photon scattering rate is $\Gamma_{\text{scatt}} = 0.4\ \text{s}^{-1}$. The tight lattice confinement leads to a high calculated atomic density

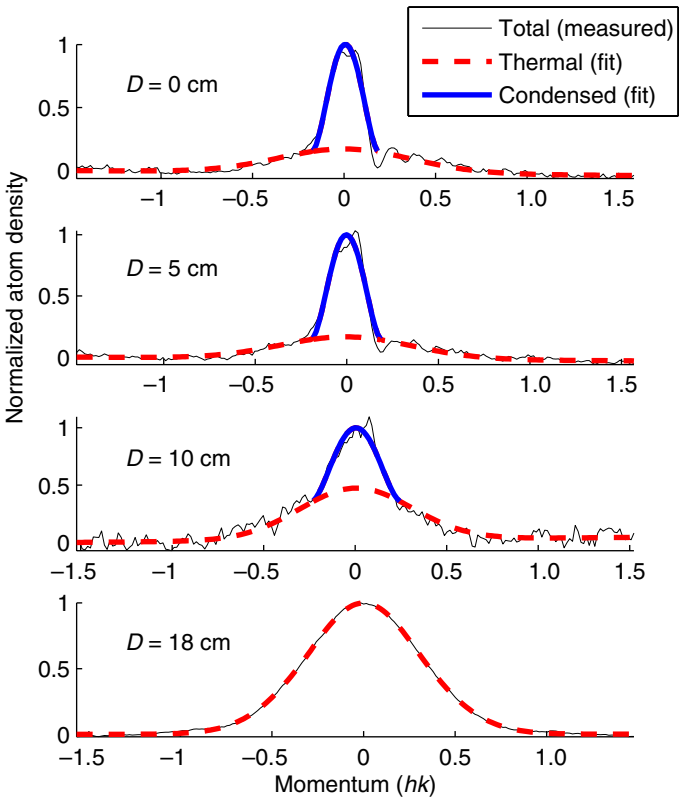

Figure 5. Transporting BEC. Shown are the momentum distributions (thin black lines) of the atoms after a return-trip transport over various one-way distances D. A bimodal distribution (a blue parabolic distribution for the condensed fraction and a red Gaussian distribution for the thermal fraction) is fit to the data. For D below 10 cm, a significant fraction of the atomic cloud is still condensed. For $D = 18$ cm, ($\approx$ the limit in our experiments) only a thermal cloud remains, however, with a temperature below the recoil limit ($T < 0.2E_r/k_B \approx 30$ nK).

of $n_0 \approx 2 \times 10^{14}\,\mathrm{cm}^{-3}$. Adopting $L = 5.8 \times 10^{-30}\,\mathrm{cm}^6\,\mathrm{s}^{-1}$ as rate coefficient for the three body recombination [21], we expect a corresponding loss rate $Ln_0^2 = 0.3\,\mathrm{s}^{-1}$.

In figure 5, we have studied the transport of a BEC, which is especially sensitive to heating and instabilities. It is important to determine, whether the atoms are still Bose-condensed after the transport and what their temperature is afterwards. Figure 5 shows momentum-distributions for various transport distances D, which were obtained after adiabatically reloading the atoms into the magnetic trap by ramping down the lattice and subsequent time-of-flight measurements.

Before discussing these results, we point out that loading the BEC adiabatically into the stationary optical lattice is already critical. We observe a strong dependence of the condensate fraction on the lattice depth. For too low lattice depths, most atoms fall out of the lattice trap due to the gravitational field. For too high lattice depths, all atoms are trapped but the condensate fraction is very small. One explanation for this is that high lattice depths lead to the regime of 2D pancake shaped condensates where tunnelling between adjacent lattice sites is suppressed. Relative dephasing of the pancake shaped condensates will then reduce the condensate fraction after release from the lattice. We obtain the best loading results for a $11\,E_r$ deep trap, where we lose

about 65% of the atoms, but maximize the condensate fraction. Because high lattice intensities are detrimental for the BEC, we readjust the power of the lattice during transport, such that the intensity is kept constant over the transport range. The adjustments are based on the calculated axial intensity distribution of the Bessel beam. In this way, we reach transport distances for BEC of 10 cm. We believe, that more sophisticated fine tuning of the power adjustments should increase the transport length considerably. After transport distances of $D = 18$ cm (36 cm round trip), the atomic cloud is thermal. Its momentum spread, however, is merely $0.3\hbar k$, which corresponds to a temperature of 30 nK. Additionally, we want to point out that the loss of atoms due to the transport is negligible ($<10\%$) compared to the loss through loading and simply holding in such a low lattice potential ($\approx 65\%$).

An outstanding feature of the lattice transport scheme is the precise positioning of the atomic cloud. Aside from uncontrolled phase shifts due to residual mechanical noise, such as vibrating optical components, we have perfect control over the relative phase of the lattice lasers with our RF/AOM setup. This would in principle result in an arbitrary accuracy in positioning the optical lattice. We have experimentally investigated the positioning capabilities in our setup. For this, we measured in many runs the position of the atomic cloud in the lattice after it had undergone a return trip with a transport distance of $D = 10$ cm. The position jitter, i.e. the standard deviation from the mean position, was slightly below 1 μm. For comparison, we obtain very similar values for the position jitter when investigating BECs in the lattice before transport. Hence, the position jitter introduced through the transport scheme is negligible.

Another important property of the lattice transport scheme is its high speed. For example, for a transport over 20 cm (40 cm round trip) with negligible loss, a total transport time of 200 ms turns out to be sufficient. This is more than an order of magnitude faster than in the MIT experiment [4], where an optical tweezer was mechanically relocated. The reason for this speed up as compared to the optical tweezer is mainly the much higher axial trapping frequency of the lattice and the non-mechanical setup.

In order to determine experimentally the lower limit of transportation time, we have investigated round-trip transports ($D = 5$ mm), where we have varied the maximum acceleration and the lattice depth (figure 6(a)). The number of atoms, which still remain in the lattice after transport, is measured. As soon as the maximum acceleration exceeds a critical value, the number of atoms starts to drop. For a given lattice depth, we define a critical acceleration a_{crit} as the maximum acceleration of the particular transport where 50% of the atoms still reach their final destination. Figure 6(b) shows the critical acceleration a_{crit} as a function of lattice depth. The upper bound on acceleration observed here can be understood from classical considerations. In our lattice, the maximum confining force along the axial direction is given by $U_{\mathrm{latt}}k$, where k is the wave vector of the light field. Thus in order to keep an atom bound to the lattice, we require the acceleration a to be small enough such that

$$ma < U_{\mathrm{latt}}k. \tag{10}$$

Our data in figure 6 are in good agreement with this limit.[2]

There is in principle also a lower bound on the acceleration, which is due to instabilities exhibited by BECs with repulsive interactions loaded into periodic potentials [23]–[26]. Due to the fact that these instabilities mainly occur at the edge of the Brillouin zones, the time spent

[2] In the weak lattice regime ($U_{\mathrm{latt}} \ll 10E_{\mathrm{r}}$) transport losses would be dominated by Landau–Zener tunnelling, see e.g. [14, 22].

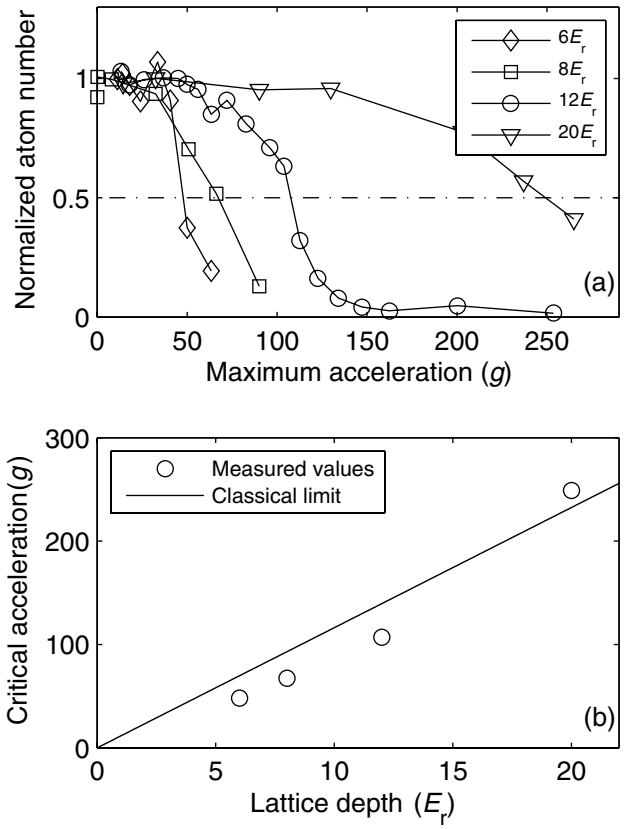

Figure 6. Critical acceleration in lattice. (a) For several round-trip transports with varying maximum acceleration a and lattice depth (see legend), the number of remaining atoms after transport is shown. As the maximum acceleration exceeds a critical value, the number of atoms starts to drop significantly. We define a critical acceleration as the maximum acceleration for transports in which 50% of the atoms still reach their final destination. This critical acceleration is shown as a function of the lattice depth in (b). The experimentally determined values are compared with the limit expected from classical considerations: $a_{\mathrm{crit}} = U_{\mathrm{latt}}k/m$.

in this critical momentum range should be kept small. For our lattice parameters, nearly half of the Brillouin zone is an unstable region, where the lifetime of the BEC is only on the order of 10 ms [25]. Thus we tend to sweep through the Brillouin zone in much less than $\Delta t = 20\,\mathrm{ms}$, which corresponds to an acceleration of $a = \dot{v} \gg 2v_{\mathrm{r}}/\Delta t \simeq 0.6\,\mathrm{m\,s^{-2}}$. In this way, BECs may be transported without introducing too much heating through these instabilities.

In contrast to acceleration, the transport velocity in our experiment is only technically limited due to the finite AOM bandwidth. As discussed before, the lattice is set in motion by introducing a detuning between the two beams via AOMs (equation (1)). For detunings exceeding the bandwidth of the AOM, the diffraction efficiency of the modulator starts to drop significantly. Consequently the lattice confinement vanishes, and the atoms are lost. In our setup, we can conveniently reach velocities of up to $v = 6\,\mathrm{m\,s^{-1}} \approx 1100v_{\mathrm{r}}$, corresponding to a typical AOM bandwidth of 15 MHz. This upper bound actually limits the transport time for long distance transports ($D > 5\,\mathrm{cm}$).

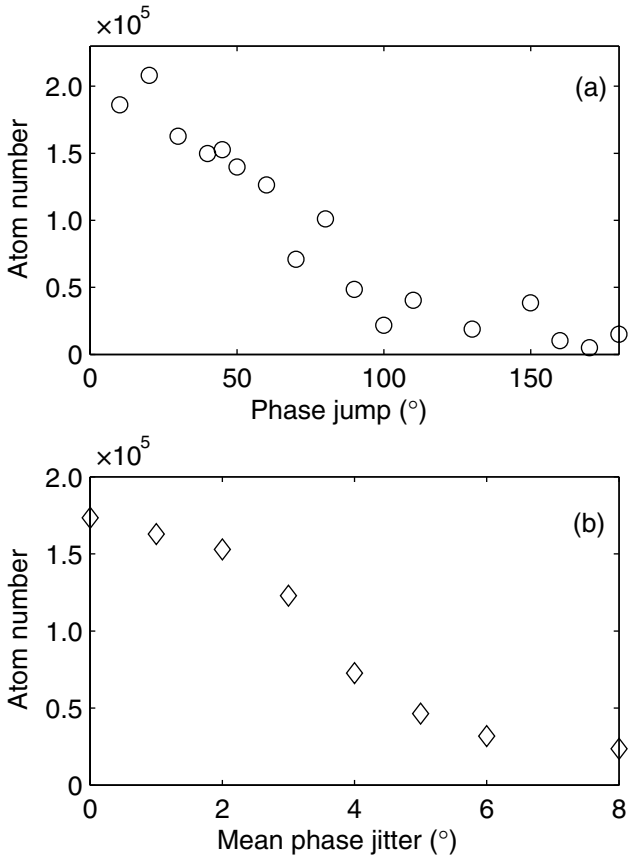

Figure 7. Stability requirements for transport. Sudden phase jumps are introduced in the relative phase of the two counterpropagating lattice laser beams. The corresponding abrupt displacements of the optical lattice lead to heating and loss of the atoms. We measure the number of atoms which remain in the lattice after transport. (a) Data obtained after a single relative phase jump of variable magnitude. (b) A phase jitter (200 positive Poissonian-distributed phase jumps with a variable mean value) is introduced during transport. Mean values on the order of a few degrees already lead to a severe loss of atoms.

Finally we have investigated the importance of phase stability of the optical lattice for the transport (see figure 7). For this, we purposely introduced sudden phase jumps during transport to one of the lattice beams. The timescale for the phase jumps, as given by AOM response time of about 100 ns, was much smaller than the inverse trapping frequencies. The phase jumps lead to abrupt displacements of the optical lattice, causing heating and loss of atoms. In figure 7(a), the atomic losses due to a single phase jump during transport are shown. Phase jumps of 60° typically induce a 50% loss of atoms. For continuous phase jitter (see figure 7(b)), the sensitivity is much larger.

6. Atom catapult

In addition to transport of ultracold atoms, acceleration of atoms to precisely defined velocities is another interesting application of the moving optical lattice. For instance, it could be used

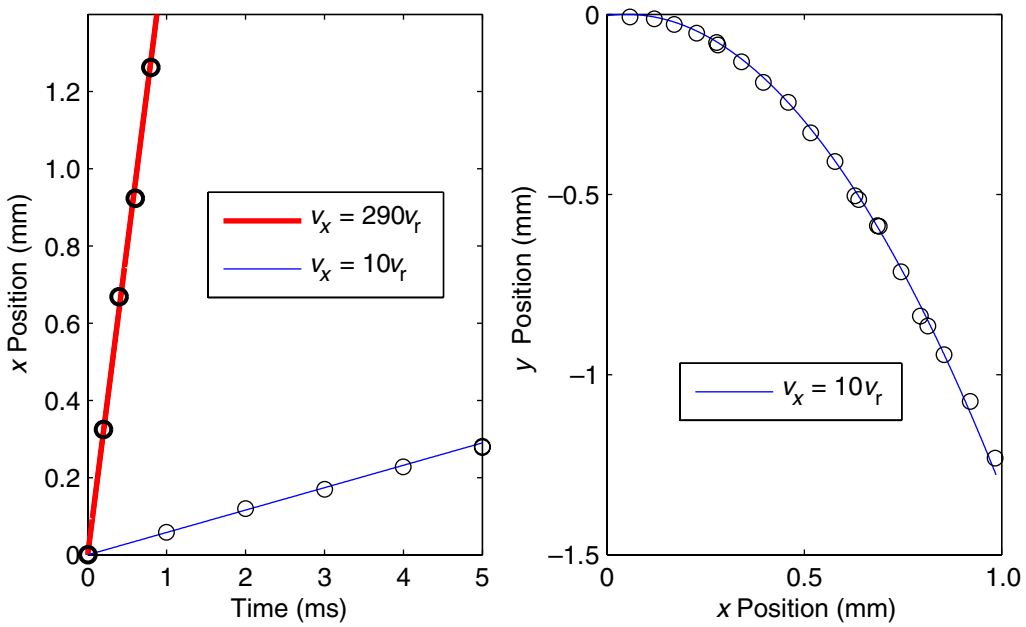

Figure 8. Atom catapult. After acceleration in x-direction and subsequent release from the lattice, the position of the atomic cloud is tracked as it flies ballistically through the field of view of the CCD camera. Shown are two data sets where atoms were accelerated to velocities of either $v_x = 10v_r$ or $v_x = 290v_r$. (a) The horizontal position x as a function of time. (b) For the slower cloud ($v_x = 10v_r$) a parabolic trajectory $y = -g/2 \cdot (x/v_x)^2$ is observed as it falls under the influence of gravity.

to study collisions of BECs with a very high but well-defined relative velocity, similar to the experiments described in [27, 28]. As already shown above, we have precise control to impart a well-defined number of up to 1100 photon recoils to the atoms. This corresponds to a large kinetic energy of $k_B \times 200\,\mathrm{mK}$. At the same time, the momentum spread of the atoms is about 1/3 of a recoil (see figure 5). To illustrate this, we have performed two sets of experiments, where we accelerate a cloud of atoms to velocities $v = 10v_r$ and $v = 290v_r \approx 1.6\,\mathrm{m\,s^{-1}}$. After adiabatic release from the lattice, we track their position in free flight (see figure 8). Initially the atomic cloud is placed about 8 cm away from the position of the magnetic trap. It is then accelerated back towards its original location. Before the atoms pass the camera's field of vision, the lattice beams are turned off within about 5 ms, to allow a ballistic flight of the cloud. Using absorption imaging, the position of the atomic cloud as a function of time is determined. The slope of the straight lines in figure 8(a) corresponds nicely to the expected velocity. However, due to a time jitter problem, individual measurements are somewhat less precise than one would expect.[3] For $v = 10v_r$, figure 8(b) shows the trajectory of the ballistic free fall of the atoms in gravity.

[3] This is linked to the fact that our clock for the system control is synchronized to the 50 Hz of the power grid. Fluctuations of the line frequency lead to shot to shot variations in the ballistic flight time of the atoms, which translates into an apparent position jitter.

7. Conclusion

In conclusion, we have realized a long distance optical transport for ultracold atoms, using a moveable standing wave dipole trap. With the help of a diffraction-free Bessel beam, macroscopic distances are covered for both BEC and ultracold thermal clouds. The lattice transport features a fairly simple setup, as well as a fast transport speed and high positional accuracy. Limitations are mainly technical and leave large room for improvement. In addition to transport, the lattice can also be used as an accelerator to impart a large but well-defined number of photon recoils to the atoms.

Acknowledgments

We thank U Schwarz for helpful information on the generation of Bessel beams and for lending us phase-gratings for testing purposes. Furthermore, we thank R Grimm for discussions and support. This work was supported by the Austrian Science fund (FWF) within SFB 15 (project part 17) and the Tiroler Zukunftsstiftung.

Appendix. Transport ramp

We give here the analytic expression for the lattice acceleration $a(t)$ as a function of time t which was implemented in our experiments (see for example figure 3). $a(t)$ is a smooth piecewise defined cubic polynomial,

$$a(t) = \begin{cases} \dfrac{D}{T^2}\left(-\dfrac{7040}{9}\left(\dfrac{t}{T}\right)^3 + 320\left(\dfrac{t}{T}\right)^2\right) & \text{for } 0 < t \leqslant T/4, \\ \dfrac{D}{T^2}\left(\dfrac{3200}{9}\left(\dfrac{t}{T}\right)^3 - \dfrac{1600}{3}\left(\dfrac{t}{T}\right)^2 + \dfrac{640}{3}\dfrac{t}{T} - \dfrac{160}{9}\right) & \text{for } T/4 < t \leqslant 3T/4, \\ \dfrac{D}{T^2}\left(-\dfrac{7040}{9}\left(\dfrac{t}{T}\right)^3 + \dfrac{6080}{3}\left(\dfrac{t}{T}\right)^2 - \dfrac{5120}{3}\dfrac{t}{T} + \dfrac{4160}{9}\right) & \text{for } 3T/4 < t \leqslant T. \end{cases}$$

Here, D is the distance over which the lattice is moved and T is the duration of the transport. From $a(t)$, both the velocity $v(t)$ and the location $x(t)$ may be derived via integration over time. Our choice for the acceleration $a(t)$ features a very smooth transport. The acceleration $a(t)$ and its derivative $\dot{a}(t)$ are zero at the beginning ($t = 0$) and at the end ($t = T$) of the transport. At $t = T/4$ and $t = 3T/4$, the absolute value of the acceleration reaches a maximum.

References

[1] Folman R, Krüger P, Schmiedmayer J, Denschlag J and Henkel C 2002 *Adv. At. Mol. Opt. Phys.* **48** 263–352
[2] Greiner M, Bloch I, Hänsch T W and Esslinger T 2001 *Phys. Rev.* A **63** 031401
[3] Lewandowski H J, Harber D M, Whitaker D L and Cornell E A 2002 *Phys. Rev. Lett.* **88** 070403
[4] Gustavson T L, Chikkatur A P, Leanhardt A E, Görlitz A, Gupta S, Pritchard D E and Ketterle W 2002 *Phys. Rev. Lett.* **88** 020401
[5] Kasevich M and Chu S 1991 *Phys. Rev. Lett.* **67** 000181
[6] Berg-Sørensen K and Mølmer K 1998 *Phys. Rev.* A **58** 1480

[7] Pötting S, Cramer M, Schwalb C H, Pu H and Meystre P 2001 *Phys. Rev.* A **64** 023604
[8] Dahan M B, Peik E, Reichel J, Castin Y and Salomon C 1996 *Phys. Rev. Lett.* **76** 4508–11
[9] Morsch O, Müller J H, Cristiani M, Ciampini D and Arimondo E 2001 *Phys. Rev. Lett.* **87** 140402
[10] Morsch O and Oberthaler M 2006 *Rev. Mod. Phys.* **78** 179–215
[11] Kuhr S, Alt W, Schrader D, Müller M, Gomer V and Meschede D 2001 *Science* **293** 278
[12] Mandel O, Greiner M, Widera A, Rom T, Hänsch T W and Bloch I 2003 *Phys. Rev. Lett.* **91** 010407
[13] Cizmar T, Garces-Chavez V, Dholakia K and Zemanek P 2005 *Appl. Phys. Lett.* **86** 174101
[14] Denschlag J H, Simsarian J E, Häffner H, McKenzie C, Browaeys A, Cho D, Helmerson K, Rolston S L and Phillips W D 2002 *J. Phys. B: At. Mol. Opt. Phys.* **35** 3095–110
[15] Durnin J 1987 *J. Opt. Soc. Am.* B **4** 651–4
[16] Durnin J, Miceli J J and Eberly J H 1987 *Phys. Rev. Lett.* **58** 1499–501
[17] Niggl L, Lanzl T and Maier M 1997 *J. Opt. Soc. Am.* A **14** 27–33
[18] Niggl L 1999 *PhD Thesis* Universität Regensburg
[19] Thalhammer G, Winkler K, Lang F, Schmid S, Grimm R and Denschlag J H 2006 *Phys. Rev. Lett.* **96** 050402
[20] Thalhammer G, Theis M, Winkler K, Grimm R and Denschlag J H 2005 *Phys. Rev.* A **71** 033403
[21] Söding J, Guéry-Odelin D, Desbiolles P, Chevy F, Inamori H and Dalibard J 1999 *Appl. Phys.* B **69** 257–61
[22] Peik E, Dahan M B, Bouchoule I, Castin Y and Salomon C 1997 *Phys. Rev.* A **55** 4
[23] Choi D I and Niu Q 1999 *Phys. Rev. Lett.* **82** 2022
[24] Wu B and Niu Q 2003 *New J. Phys.* **5** 104.1–104.24
[25] Fallani L, De Sarlo L, Lye J E, Modugno M, Saers R, Fort C and Inguscio M 2004 *Phys. Rev. Lett.* **93** 140406
[26] Cristiani M, Morsch O, Malossi N, Jona-Lasinio M, Anderlini M, Courtade E and Arimondo E 2004 *Opt. Express* **12** 4
[27] Thomas N R, Kjaergaard N, Julienne P S and Wilson A C 2004 *Phys. Rev. Lett.* **93** 173201
[28] Buggle C, Léonard J, von Klitzing W and Walraven J T M 2004 *Phys. Rev. Lett.* **93** 173202

Long-Lived Feshbach Molecules in a Three-Dimensional Optical Lattice

G. Thalhammer,[1] K. Winkler,[1] F. Lang,[1] S. Schmid,[1] R. Grimm,[1,2] and J. Hecker Denschlag[1]
[1]*Institut für Experimentalphysik, Universität Innsbruck, 6020 Innsbruck, Austria*
[2]*Institut für Quantenoptik und Quanteninformation, Österreichische Akademie der Wissenschaften, 6020 Innsbruck, Austria*
(Received 27 October 2005; published 8 February 2006)

We have created and trapped a pure sample of $^{87}Rb_2$ Feshbach molecules in a three-dimensional optical lattice. Compared to previous experiments without a lattice, we find dramatic improvements such as long lifetimes of up to 700 ms and a near unit efficiency for converting tightly confined atom pairs into molecules. The lattice shields the trapped molecules from collisions and, thus, overcomes the problem of inelastic decay by vibrational quenching. Furthermore, we have developed an advanced purification scheme that removes residual atoms, resulting in a lattice in which individual sites are either empty or filled with a single molecule in the vibrational ground state of the lattice.

DOI: 10.1103/PhysRevLett.96.050402 PACS numbers: 03.75.Lm, 03.75.Nt, 32.80.Lg, 34.50.−s

Using magnetic Feshbach resonances [1] to create ultracold diatomic molecules in their highest rovibrational state has become a key to exciting developments and breakthroughs. Feshbach molecules made of bosonic atoms behave in a strikingly different way from Feshbach molecules made of fermionic atoms. For weakly bound dimers of fermionic atoms, vibrational quenching and inelastic decay are strongly suppressed by a Pauli blocking effect in a close encounter of two molecules [2]. This has been vital to the experimental creation of molecular Bose-Einstein condensates (BEC) and investigations of the crossover to a strongly interacting fermionic superfluid [3]. For dimers of bosonic atoms [4–7], however, progress has been hampered by strong inelastic decay due to atom-molecule and molecule-molecule collisions. Therefore, the experiments have been focused on the transient regime, studying, e.g., the collision and dissociation dynamics [6–11].

A three-dimensional optical lattice offers many interesting opportunities for research on ultracold molecules. Lattice sites occupied with exactly two atoms represent a perfectly controlled quantum system which can be rigorously treated theoretically. Matrix elements for atom-molecule coupling are strongly enhanced with the prospect of efficient atom-molecule conversion. Moreover, it is expected that the lattice can isolate molecules from each other and shield them from detrimental collisions so that a long-lived sample can be created also with dimers of bosonic atoms. Recently, first experiments with molecules in a lattice have studied photoassociation [12,13] or demonstrated modifications of the binding energy of tightly confined Feshbach molecules [14].

In this Letter, we report on the creation of a pure sample of ultracold Rb_2 Feshbach molecules trapped in a 3D optical lattice. The observed long lifetimes of up to 700 ms greatly exceed previous values reported for dimers of bosonic atoms [6,7,9,10]. Further, we experimentally investigate association and dissociation of the Feshbach molecules and reach efficiencies of 95% for converting pairs of atoms into molecules. In brief, we adiabatically load a ^{87}Rb BEC into the vibrational ground state of the lattice. For our experimental conditions, about 20% of the condensate atoms are grouped in pairs of two into the lattice sites. By ramping adiabatically over a magnetic Feshbach resonance at 1007.4 G, we convert these pairs into molecules. Another 20% of atoms are located in triply and more highly occupied lattice sites. After the Feshbach ramp, however, inelastic collisions between the created molecules and atoms within the high occupancy sites quickly remove these particles from the lattice. Finally, the remaining 60% of the condensate atoms are found in singly occupied sites and are unaffected by the Feshbach ramp. Using a novel resonant purification scheme, we can remove these atoms from the lattice, which results in a pure molecular sample with each molecule being shielded from the others by the lattice potential.

The starting point for our experiments is an almost pure BEC of about 6×10^5 ^{87}Rb atoms in the spin state $|F = 1, m_F = -1\rangle$ [15]. It is transferred from a quadrupole Ioffe configuration trap (QUIC) into another Ioffe-type magnetic trap with trap frequencies $\omega_{x,y,z} = 2\pi \times (7, 19, 20)$ Hz, leading to a peak density of the BEC of about 4×10^{13} cm^{-3}. Our 3D lattice is cubic and consists of three retroreflected intensity-stabilized laser beams which propagate orthogonally to each other. They are derived from a frequency-stable single-mode Ti:sapphire laser ($\approx$500 kHz linewidth) with a wavelength of $\lambda =$ 830.44 nm. For this wavelength, the laser is detuned by about 100 GHz from the closest transition to an excited molecular level, minimizing light induced losses as a precondition for long molecular lifetimes. The laser beams are polarized perpendicularly to each other, and their frequencies differ by several tens of megahertz to avoid disturbing interference effects. The waists of all three beams are about 160 μm, and the maximum obtainable power is about 110 mW per beam, which results in calculated lattice depths of up to 40 recoil energies ($E_r = h^2/2m\lambda^2$, where m is the atomic mass of ^{87}Rb and h is Planck's constant). We have verified the lattice depths by measuring the energy

gap between bands of the lattice [16]. The relative uncertainty of our lattice depth is $\pm 15\%$.

After the BEC is adiabatically loaded into a $35E_r$ deep 3D optical lattice within 100 ms, we turn off the magnetic trap. By suddenly reversing the bias magnetic field of a few gauss, we flip the spins of our atoms to the high field seeking state $|F = 1, m_F = +1\rangle$ with an efficiency higher than 99% (see also [17]). This state features the Feshbach resonance at 1007.4 G. Afterwards, we ramp up a homogeneous magnetic field in 3 ms to about 1015 G using the QUIC quadrupole coils in Helmholtz configuration. The current through the coils is actively stabilized to a relative accuracy of about 10^{-4}. The fast diabatic crossing of the Feshbach resonance has basically no effect on the atoms in the lattice. If we slowly ramp in 5 ms from 1015 to 1000 G (crossing the Feshbach resonance at 1007 G), molecules are adiabatically produced in the multiply occupied lattice sites. If, however, we cross the Feshbach resonance very quickly, e.g., by simply switching off the magnetic field, less than 10% of the atoms are converted into molecules. Note that, after the first Feshbach ramp, we observe an immediate irretrievable loss of 20% of the atoms. We attribute this loss to inelastic collisions involving molecules for sites initially occupied by 3 or more atoms. The remaining occupied sites each contain either a single atom or a single molecule.

Atom numbers are measured with absorption imaging at low magnetic fields (≈ 2 G) after release from the optical lattice and 11 ms of ballistic expansion. In order to determine molecule numbers, they are first dissociated into atoms by slowly ramping back across the Feshbach resonance and then quickly switching off the magnetic field. We also use absorption imaging to map out the band occupation of the lattice. For this, the lattice is ramped down in 2 ms, and we typically observe a momentum distribution which is fully contained in a cube of width $2\hbar k$ corresponding to the first Brillouin zone of the lattice [18]. This demonstrates that atoms and molecules are in the vibrational ground state of the lattice sites.

In order to create a pure molecular sample, we have developed an advanced purification scheme to remove all atoms which combines the great selectivity of microwave excitation with the high efficiency of atom removal through resonant light pressure [7]. We apply a combined microwave and light pulse at a magnetic field of 1000 G for 3 ms. The microwave drives the transition at a frequency of 9113 MHz between levels which correlate with $|F = 1, m_F = +1\rangle$ and $|F = 2, m_F = +2\rangle$. The light pulse drives the closed transition $|F = 2, m_F = +2\rangle \rightarrow |F = 3, m_F = +3\rangle$. The optical transition frequency is 1402 MHz blue detuned compared to the transition at zero magnetic field. After this pulse, which heats the atoms out of the lattice and an additional hold time (~ 20 ms), no more atoms can be detected. The direct effect of the microwave and light field pulse on the molecules is negligible because the radiation is off resonance. As an indirect effect, however, we find that during the first purification pulse we still lose about 40% of the molecules, probably due to inelastic collisions with the blown away atoms. Further losses are not observed in subsequent purification pulses. We end up with a pure molecular sample formed from about 10% of the initial atoms, which corresponds to 3×10^4 molecules.

We have investigated the lifetimes of the Feshbach molecules in the lattice under various conditions (see Figs. 1 and 2). Figure 1 shows the decay of molecules at a lattice depth of $10E_r$. The pure molecular sample exhibits a remarkably long lifetime of 700 ms. For the case of an unpurified sample, where the atoms at singly occupied sites have not been removed, the lifetime of the molecules is considerably reduced to ≈ 35 ms. This observation suggests that the molecular decay is based on a process where an atom tunnels to a site occupied by a molecule and inelastically collides with it. These inelastic collisions can, in principle, also happen between two molecules. However, compared to an atom, a molecule has a much lower tunneling rate, since it experiences twice the dipole potential and has twice the mass of a single atom. Using simple scaling arguments, for a molecule to have the same tunneling rate as an atom, the lattice light intensity needs to be more than 4 times smaller. This explains the comparatively long lifetime of the purified molecular samples. We note that, if molecular decay is based on inelastic collisions, its time dependence is intrinsically nonexponential. However, exact modeling of the decay would be quite involved and requires precise knowledge of atom or molecule distributions in the lattice. Since these distributions are not known to us, we simply base our estimates for the molecular lifetimes on an exponential decay law.

Figure 2 shows the measured lifetimes of the molecules for various lattice depths. For sufficiently high lattice

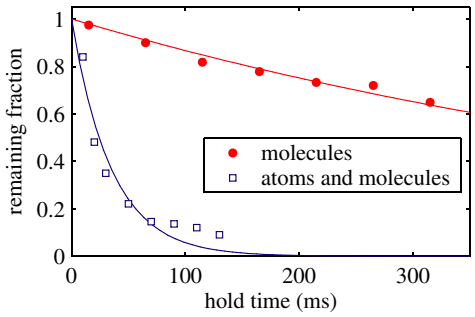

FIG. 1 (color online). Decay of molecules in a 3D optical lattice with a potential depth of $(10 \pm 2)E_r$. Shown is the remaining fraction of molecules in purified (solid circles) and unpurified (squares) samples as a function of hold time. The continuous lines are exponential fits to the data indicating a lifetime of 700 and 35 ms for purified and unpurified molecular samples, respectively. In order to determine molecule numbers in the unpurified sample, purification was performed at the end of the hold time. The hold time was limited to below 400 ms due to the heating up of the coils.

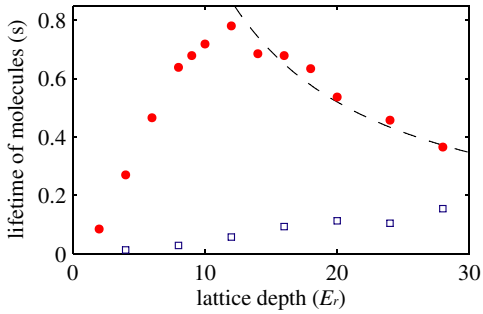

FIG. 2 (color online). Molecular lifetimes for purified molecular samples (circles) and for unpurified samples (squares) as a function of the lattice depth. For this measurement, the lattice depth was reduced from $35E_r$ to the given value after the creation of the molecules. The dashed line is inversely proportional to the lattice depth.

depths, we observe a lifetime for the purified molecular sample inversely proportional to the lattice depth (see dashed line in Fig. 2). From this, we conclude that above a lattice depth of about $12E_r$ the tunneling of the molecules is strongly suppressed, and the lifetime is limited by light induced losses due to off-resonant transitions to an excited molecular state which subsequently decays. Below this value, decay is dominated by tunneling [19] and following inelastic collisions. Thus, the molecular lifetime is maximized in a tradeoff between tunneling and light induced losses. As already shown in Fig. 1, the presence of atoms considerably reduces the lifetime of the molecules, even at larger lattice depths. In the limit of vanishing lattice depths, our experimental lifetimes decrease to values similar to those observed in Refs. [6–10]. Figure 2 clearly demonstrates that shielding of the molecules against inelastic collisions grows with increasing lattice depth.

We now investigate the dynamics for both association and dissociation of a single Feshbach molecule in a lattice site during Feshbach ramping. This fundamental system is of special interest since it can be theoretically treated exactly and solved analytically [21]. We prepare a purified sample of molecules at 1000 G in a lattice of $35E_r$ depth. We then ramp the magnetic field in a symmetric way across the Feshbach resonance up to 1015 G and back (see Fig. 3). Afterwards, purification is applied to remove atoms which have not recombined to form molecules. In a last step, the molecule number is measured. If dissociation and association are not fully adiabatic in a conversion cycle, a loss of molecules will result; e.g., during the association ramp, a pair of atoms might not be converted into a molecule or during dissociation the molecule might break up into two atoms which, after tunneling, are located in separate sites. For slow ramps, we observe small loss signals indicating high adiabaticity for the dissociation-association cycle. In order to increase the loss signal, to improve its accuracy, and to check for consistency, we repeated this experiment with a higher number of cycles (see Fig. 3). The two data

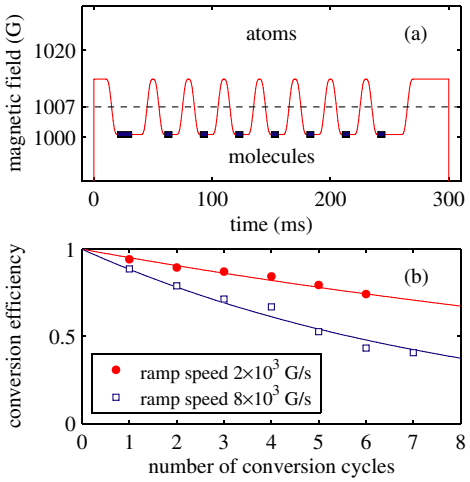

FIG. 3 (color online). (a) Scheme for measurement of conversion efficiency, shown for 7 dissociation-association cycles. The shaded areas indicate the application of our purification procedure to remove atoms. The dashed line at 1007 G shows the position of the Feshbach resonance. (b) Conversion efficiency for a given number of complete dissociation-association cycles for two different ramp speeds of the magnetic field. We measure a conversion efficiency of 95% per cycle for the slow ramp and 89% per cycle for the fast ramp. The solid lines are described by exponential fit curves as described in the text. The lattice depth is $35E_r$.

sets in Fig. 3(b) correspond to two different ramp speeds (2×10^3 G/s, 8×10^3 G/s) and can be described by the exponential functions 0.95^n and 0.89^n, respectively, where n is the number of cycles. Thus, for a slow Feshbach ramp (2×10^3 G/s), we observe an unprecedented high efficiency of up to 95% for the whole dissociation-association cycle. For a faster ramp (8×10^3 G/s), the efficiency drops to 89%. We have taken care that light induced losses have been corrected for in the data [Fig. 3(b)]. Our high conversion efficiencies in the optical lattice are in strong contrast to the low values of $\sim$10% observed previously in a ^{87}Rb BEC [10] which were presumably limited by strong inelastic collisions. In our deep lattice, however, inelastic collisions are suppressed.

After having determined the efficiency for the full dissociation-association cycle, we now study dissociation and association individually. Figure 4(a) shows the measured conversion efficiency of atom pairs to molecules for different ramp speeds. The atom pairs were prepared by creating a pure molecular sample and then dissociating the molecules by slowly (2×10^3 G/s) ramping backward over the Feshbach resonance. Then, again, the magnetic field was swept across the Feshbach resonance at various speeds, and, finally, after switching off completely the magnetic field, the remaining nonconverted atoms are detected. The dashed line in Fig. 4(a) is based on a Landau-Zener expression without adjustable parameters [21] and is given by

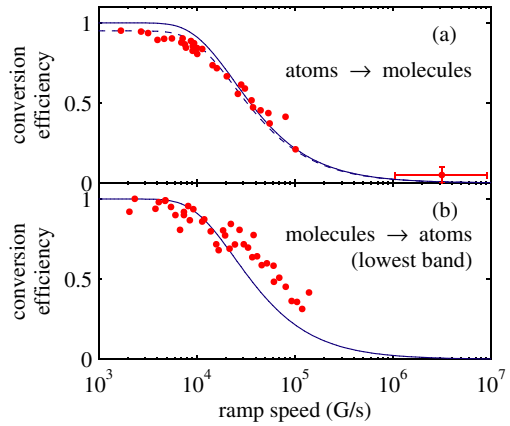

FIG. 4 (color online). (a) Conversion efficiency of atoms (mostly pairs) into molecules as a function of the ramp speed. (b) A purified sample of molecules is dissociated into atom pairs at different ramp speeds. We measure the number of atoms which are observed in the first Brillouin zone of the lattice after release, i.e., atoms that populate the lowest energy band of the lattice. The data is normalized to the atom number at the lowest ramp speeds. The continuous lines in (a) and (b) are calculations as described in the text.

$$p = 1 - \exp\left(-\frac{2\sqrt{6}\hbar}{m a_{\mathrm{ho}}^3}\left|\frac{a_{\mathrm{bg}}\Delta B}{\dot{B}}\right|\right), \qquad (1)$$

where p is the probability of creating a molecule, $a_{\mathrm{bg}} = 100.5a_0$ the background scattering length, $\Delta B = 0.21$ G [10] the width of the Feshbach resonance, $\dot{B}$ the ramp speed at the Feshbach resonance, and $a_{\mathrm{ho}} = \sqrt{\hbar/m\omega}$ the harmonic oscillator length. Using the best estimate for our trapping frequency of $\omega = 2\pi \times (39 \pm 3)$ kHz (corresponding to a lattice depth of $35 \pm 5E_r$), we get good agreement with our data. We note that, even for the slowest ramp speeds, the measured conversion efficiency never reaches unity but levels off at 95%, in agreement with the results in Fig. 3. This, however, does not exclude a true unit conversion efficiency for atom pairs into molecules, because it is possible that 5% of the atoms are not grouped in pairs, e.g., due to nonadiabaticity in dissociation and tunneling. In order to facilitate the comparison of the data distribution and theory, we have scaled the Landau-Zener curve by a factor of 0.95 (dashed line). The maximum controllable ramp speed ($\sim 10^5$ G/s; see Fig. 4) is limited by the performance of our current supply for the magnetic field coils. The data point at 3×10^6 G/s was obtained by simply switching off the coil currents with an external switch. The abrupt switching induces eddy currents, which results in a less controlled ramp with a large error margin. For fast switching, we measured a conversion efficiency of $5 \pm 5\%$.

In Fig. 4(b), we study the dissociation of a purified sample of molecules. We measure the number of atoms which populate the lowest band of the lattice after dissociation. At low ramp speeds, Feshbach molecules get adiabatically converted to pairs of atoms in the lattice ground state. At higher speeds, molecules are energetically lifted above the molecule threshold and can decay into higher lattice bands or into the continuum. Assuming the reversibility of the Landau-Zener transition, we use the same theory curve as in Fig. 4(a). For higher ramp speeds, we measure larger atom numbers than expected. This is probably due to imperfections of our data analysis which can overestimate the atom number in the lowest band by adding in some atoms from higher bands.

To summarize, we have demonstrated that ultracold Feshbach molecules can be created with high conversion efficiency in a 3D optical lattice. After purification, we observe long molecular lifetimes up to 700 ms. These strong improvements over previous experiments open promising perspectives for applications, e.g., in high resolution molecular spectroscopy and quantum information processing in optical lattices. They may also represent an important step in the creation of a stable BEC of molecules in their vibrational ground state.

We appreciate the assistance of Matthias Theis and Carlo Sias. We thank Thorsten Köhler and Todd Meyrath for fruitful discussions. This work was supported by the Austrian Science Fund (FWF) within SFB 15 (project part 17) and the European Union in the frame of the Cold Molecules TMR Network under Contract No. HPRN-CT-2002-00290.

[1] D. Kleppner, Phys. Today **57**, No. 8, 12 (2004).
[2] D. S. Petrov, C. Salomon, and G. V. Shlyapnikov, Phys. Rev. Lett. **93**, 090404 (2004).
[3] F. Chevy and C. Salomon, Phys. World **18**, 43 (2005).
[4] E. A. Donley *et al.*, Nature (London) **417**, 529 (2002).
[5] J. Herbig *et al.*, Science **301**, 1510 (2003).
[6] S. Dürr *et al.*, Phys. Rev. Lett. **92**, 020406 (2004).
[7] K. Xu *et al.*, Phys. Rev. Lett. **91**, 210402 (2003).
[8] E. Hodby *et al.*, Phys. Rev. Lett. **94**, 120402 (2005).
[9] T. Mukaiyama *et al.*, Phys. Rev. Lett. **92**, 180402 (2004).
[10] S. Dürr, T. Volz, and G. Rempe, Phys. Rev. A **70**, 031601(R) (2004).
[11] C. Chin *et al.*, Phys. Rev. Lett. **94**, 123201 (2005).
[12] T. Rom *et al.*, Phys. Rev. Lett. **93**, 073002 (2004).
[13] C. Ryu *et al.*, cond-mat/0508201.
[14] T. Stöferle *et al.*, Phys. Rev. Lett. **96**, 030401 (2006).
[15] G. Thalhammer *et al.*, Phys. Rev. A **71**, 033403 (2005).
[16] J. Hecker Denschlag *et al.*, J. Phys. B **35**, 3095 (2002).
[17] T. Volz *et al.*, Phys. Rev. A **68**, 010702(R) (2003).
[18] M. Greiner *et al.*, Phys. Rev. Lett. **87**, 160405 (2001).
[19] Tunneling rates can be calculated (see [20]); e.g., lattice depths of 5, 8, and $16E_r$ correspond to molecular tunneling rates J of 4, 0.6, and 0.009 Hz, respectively, which are consistent with our measured lifetimes.
[20] D. Jaksch *et al.*, Phys. Rev. Lett. **81**, 3108 (1998).
[21] P. Julienne, E. Tiesinga, and T. Köhler, J. Mod. Opt. **51**, 1787 (2004); cond-mat/0312492.

Atom-Molecule Dark States in a Bose-Einstein Condensate

K. Winkler,[1] G. Thalhammer,[1] M. Theis,[1] H. Ritsch,[2] R. Grimm,[1,3] and J. Hecker Denschlag[1]

[1]*Institut für Experimentalphysik, Universität Innsbruck, 6020 Innsbruck, Austria*

[2]*Institut für Theoretische Physik, Universität Innsbruck, 6020 Innsbruck, Austria*

[3]*Institut für Quantenoptik und Quanteninformation, Österreichische Akademie der Wissenschaften, 6020 Innsbruck, Austria*

(Received 30 May 2005; published 5 August 2005)

We have created a dark quantum superposition state of a Rb Bose-Einstein condensate and a degenerate gas of Rb_2 ground-state molecules in a specific rovibrational state using two-color photoassociation. As a signature for the decoupling of this coherent atom-molecule gas from the light field, we observe a striking suppression of photoassociation loss. In our experiment the maximal molecule population in the dark state is limited to about 100 Rb_2 molecules due to laser induced decay. The experimental findings can be well described by a simple three mode model.

DOI: 10.1103/PhysRevLett.95.063202 PACS numbers: 34.50.Rk, 03.75.Nt, 32.80.Pj, 42.50.Gy

The phenomenon of coherent dark states is well known in quantum optics and is based on a superposition of long-lived system eigenstates which decouple from the light field. Since their discovery [1] dark states have found numerous applications. Prominent examples are electromagnetically induced transparency and lasing without inversion [2], subrecoil laser cooling [3], and ultrasensitive magnetometers [4]. A particular application is the coherent transfer of population between two long-lived states by a stimulated Raman adiabatic passage (STIRAP) [5].

In the emerging field of ultracold molecules, the conversion of atomic into molecular Bose-Einstein condensates (BECs) is a central issue. A series of recent experiments on the creation of molecular quantum gases rely on the application of Feshbach resonances [6]. This coupling mechanism, however, is restricted to the creation of molecules in the highest rovibrational level and is only practicable for a limited number of systems. As a more general method, a stimulated optical Raman transition can directly produce deeply bound molecules as demonstrated a few years ago [7,8]. STIRAP was proposed as a promising way for a fast, efficient, and robust process to convert a BEC of atoms into a molecular condensate [9–15]. The central prerequisite for this kind of STIRAP is a dark superposition state of a BEC of atoms and a BEC of molecules.

In this Letter, we report the observation of such a collective multiparticle dark state in which atoms in a BEC are pairwise coupled coherently to ground-state molecules. This dark atom-molecule BEC shows up in a striking suppression of photoassociative loss, as illustrated by the spectra in Fig. 1. In one-color photoassociation, the excitation of a molecular transition produces a resonant loss feature that reflects the optical transition linewidth; see Fig. 1(a). The presence of a second laser field coupling the electronically excited molecular state to a long-lived ground-state level can drastically reduce this loss, as shown in Fig. 1(b) and 1(c). In Fig. 1(b), for example, we observe a striking loss suppression by about a factor of 70 on resonance.

Already the mere observation of an atom-molecule dark resonance in a BEC proves that a coherent, quantum degenerate gas of molecules has been formed. This follows from the facts that (1) the dark state is by definition a coherent superposition of atoms and molecules and (2) the atomic BEC is a coherent matter wave. In this fully coherent situation, the molecular fraction itself must be quantum degenerate with a phase-space density corresponding to the number of molecules. The very narrow resonance lines indicate the high resolution of our measurements and the potential sensitivity of the dark state as an analysis tool. Using a BEC allows direct interpretation

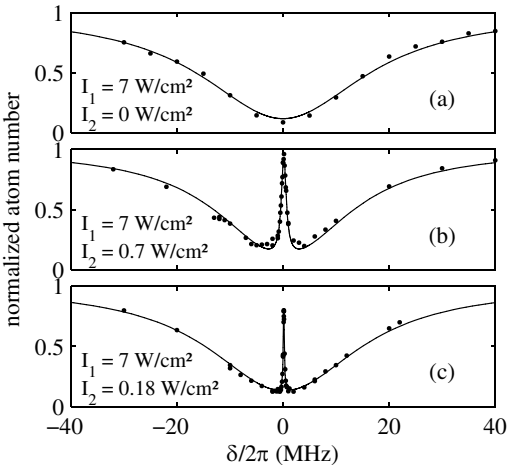

FIG. 1. Dark resonances in two-color photoassociation. (a) Atomic loss signal in one-color photoassociation as a function of the laser detuning from the electronically excited molecular line. (b), (c) When we apply a second laser (fixed frequency) which resonantly ($\Delta = 0$) couples the excited molecular state to a long-lived molecular ground state, the losses are strongly suppressed at $\delta = 0$. Depending on the intensity of laser 2, this dark resonance can get very narrow. The atom lifetime on the dark resonance in (b) is 140 ms whereas in (a) atoms have an initial decay time of about 2 ms. Intensities of laser 1 (I_1) and 2 (I_2) are as indicated.

and clear understanding of our data without ambiguity. Thermal averaging of signal features plays no role in contrast to previous measurements in thermal gases [8,16,17].

The starting point of our measurements is a BEC of 4×10^5 ^{87}Rb atoms in the spin state $|F = 1, m_F = -1\rangle$ [18]. In the level scheme of Fig. 2 the atomic BEC state is represented by $|a\rangle$. Laser 1 couples this state to the excited molecular state $|b\rangle$. Laser 2 couples $|b\rangle$ to the molecular ground state $|g\rangle$. We choose level $|b\rangle$ to be the electronically excited molecular state $|0_g^-, v = 1, J = 2\rangle$ located 26.8 cm^{-1} below the $S_{1/2} + P_{3/2}$ dissociation asymptote [18]. For level $|g\rangle$ we choose the second to last bound state in the ground-state potential. It has a binding energy of $E_b/h = 636$ MHz [7]. $|a\rangle$, $|b\rangle$, and $|g\rangle$ form the lambda system for the atom-molecule dark states.

We illuminate the trapped condensate for typically 10 ms with two phase-locked laser beams in a Raman configuration as shown in Fig. 2. Both laser beams are derived either from a single diode laser or, for higher optical powers, from a Ti:sapphire laser. The frequency difference between the two beams is created with an acousto-optical modulator at a center frequency of about 320 MHz in a double-pass configuration. This allows precise control of the beams' relative frequency difference over several tens of MHz. Both beams propagate collinearly and are aligned along the weak axis of the trap. They have a waist of about 100 μm, and their linear polarization is perpendicular to the magnetic bias field of the trap. The diode laser and the Ti:sapphire laser both have linewidths of less than 1 MHz. They are offset locked relative to the D_2 line of atomic rubidium with the help of a scanning optical cavity. This yields an absolute frequency stability of better than 10 MHz.

We are able to describe all of our spectra with a relatively simple three-mode model. Although the atom-molecule dark states are intrinsically complicated and entangled, in a first approximation the atoms and molecules can be represented as coherent matter fields [9–15]. Using the notation of Mackie *et al.* [11] we obtain a set of differential equations for the normalized field amplitudes a, b, and g of the BEC state, the excited molecular and ground state, respectively:

$$i\dot{a} = -\Omega_1 a^* b, \tag{1a}$$

$$i\dot{b} = [(\Delta + \delta) - i\gamma_b/2]b - \tfrac{1}{2}(\Omega_1 aa + \Omega_2 g), \tag{1b}$$

$$i\dot{g} = (\delta - i\gamma_g/2)g - \tfrac{1}{2}\Omega_2 b. \tag{1c}$$

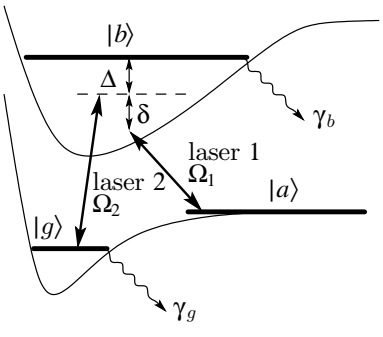

FIG. 2. Level scheme. Δ and δ denote the detunings. Ω_1 and Ω_2 are the Rabi frequencies. The excited molecular state $|b\rangle$ spontaneously decays with a rate γ_b to levels outside this scheme. The molecular state $|g\rangle$ is attributed a decay rate γ_g which phenomenologically takes into account losses through inelastic collisions and laser induced dissociation, e.g., when laser 1 couples $|g\rangle$ to the unstable state $|b\rangle$. In all our measurements laser 1 is scanned (varying δ) while laser 2 is held fixed at a particular detuning Δ.

We refer to Ω_1 as the free-bound Rabi frequency (see Fig. 2). It scales with intensity I_1 of laser 1 and initial atom density ρ as $\Omega_1 \propto \sqrt{I_1}\sqrt{\rho}$, where the factor $\sqrt{\rho}$ follows directly from the transition matrix element of a free-bound transition [13]. The bound-bound Rabi frequency $\Omega_2 \propto \sqrt{I_2}$ only depends on the intensity I_2 of laser 2. The detunings Δ and δ are defined as depicted in Fig. 2. γ_b and γ_g denote the effective decay rates of state $|b\rangle$ and $|g\rangle$ (for details, see Fig. 2). $|a|^2$, $|b|^2$ and $|g|^2$ give the ratio between the respective atom (molecule) number and the initial atom number. In the absence of losses, i.e., $\gamma_b = \gamma_g = 0$, particle numbers are conserved globally, $|a|^2 + 2|b|^2 + 2|g|^2 = 1$. Unlike the previous theoretical treatments [9–15] where the decay rate γ_g was basically neglected, we find that γ_g is relatively large and intensity dependent, $\gamma_g = \gamma_g(I_1)$. In our simple model we do not include atomic continuum states other than the BEC state. We neglect inhomogeneity effects due to the trapping potentials and finite size laser beams. Energy shifts caused by the mean-field interaction of atoms and molecules are small and neglected.

In order to determine the parameters of our model and to check it for consistency, we performed measurements in a broad parameter range of intensities and detunings. Fits to the photoassociation curves determine all unknown parameters of the system such as Ω_1, Ω_2, γ_b, and γ_g. Figure 3 shows photoassociation spectra for a relatively high laser power $I_2 = 20$ W/cm^2 and various detunings Δ. For a small detuning Δ [Fig. 3(a)] the dark resonance line from Fig. 1 has broadened considerably. This spectrum can also be viewed as two absorption lines resulting from a strong Autler-Townes splitting which was also observed in thermal gases [8,17]. From the 30 MHz separating the two resonance dips, the magnitude of the Rabi frequency Ω_2 can be directly determined. For a larger detuning Δ, the resulting spectrum becomes asymmetric and turns into a narrow and a broad dip; see Fig. 3(b) and 3(c). The narrow loss feature is related to the two-photon Raman transition while the broad dip is due to the one-photon transition $|a\rangle \rightarrow |b\rangle$. Note that similar to Fig. 1, losses are suppressed at $\delta = 0$.

Figure 4 shows the dark resonances in the low power limit where I_1 is held constant and I_2 is lowered in 4 steps.

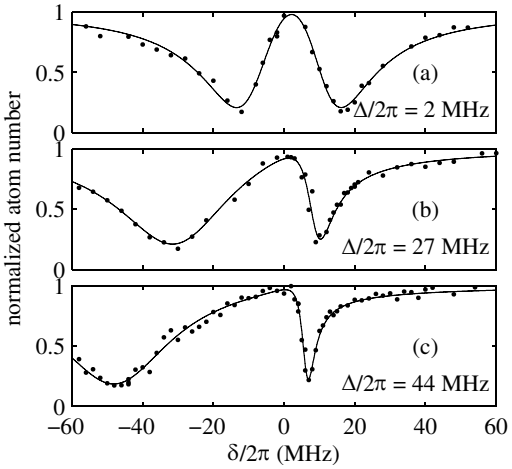

FIG. 3. Two-color photoassociation spectra for various detunings Δ at a large intensity $I_2 = 20\ \mathrm{W/cm^2}$. Here $I_1 = 80\ \mathrm{W/cm^2}$. The solid lines are fit curves based on our theoretical model.

The dark state transforms more and more into a gray state, because losses become more dominant due to a nonzero decay rate γ_g. The height of the dark resonance decreases when the pumping rate Ω_2^2/γ_b comes in the range of the decay rate of the molecular ground state γ_g. This allows for a convenient determination of γ_g. From Fig. 4 it is also clear that the width of the dark resonance decreases with Ω_2. For $\Omega_2 \ll \gamma_b$ the width is given by $\Omega_2^2/\gamma_b + \gamma_g$, corresponding to power broadening and the effective ground-state relaxation. The following set of parameters describes all our measurements quite accurately. It was used, in particular, for the calculated solid lines in Fig. 4 and it is consistent with previous measurements [18]: $\Omega_1/(\sqrt{I_1}\sqrt{\rho/\rho_0}) = 2\pi \times 8\ \mathrm{kHz/(W\,cm^{-2})^{1/2}}$ at a peak density of $\rho_0 = 2 \times 10^{14}\ \mathrm{cm^{-3}}$, $\Omega_2/\sqrt{I_2} = 2\pi \times 7\ \mathrm{MHz/(W\,cm^{-2})^{1/2}}$, and $\gamma_b = 2\pi \times 13$ MHz. We find that the decay rate γ_g of the ground-state molecular level increases with the intensity I_1 of laser 1 as shown in Fig. 5. A dependence of γ_g on I_2 was negligible in our experiments where typically $I_2/I_1 \sim 1/5 \ldots 1/500$. We model the behavior of γ_g as $\gamma_g = 2\pi \times 6\ \mathrm{kHz/(W\,cm^{-2})} I_1 + \gamma_{\mathrm{bg}}$, the sum of a light-induced decay rate proportional to I_1 and a background decay rate γ_{bg} due to inelastic collisions in the absence of light. From measurements at low intensities we can estimate an upper value for the background decay rate of about $\gamma_{\mathrm{bg}} \approx 2\pi \times 1$ kHz for $\rho_0 = 2 \times 10^{14}\ \mathrm{cm^{-3}}$. This value for γ_{bg} is consistent with previous experimental results for ^{87}Rb at similar atom densities [7]. The increase of γ_g with I_1 is due to several imperfections which break the ideal three-level lambda system. Laser 1 also couples the molecular ground state $|g\rangle$ to the short-lived excited molecular state $|b\rangle$, which leads to an incoherent loss of the molecules due to spontaneous decay. Because of the rather small frequency difference ($\approx 2\pi \times 636$ MHz) of the two Raman lasers and the strong bound-bound transition, this cannot be neglected. In addition, only 290 MHz below level $|b\rangle$ exists another excited molecular state $|0_g^-, v = 1, J = 0\rangle$ which represents an additional loss channel [18]. These two contributions explain about one third of our observed losses. Furthermore, losses can also stem from a photodissociation transition which couples ground-state molecules directly to the continuum above the $S_{1/2} + P_{1/2}$ dissociation asymptote.

Having determined the parameters we can use model (1) to calculate the fraction of ground-state molecules $|g|^2$. For the measurements presented in Fig. 4 we have a peak molecular fraction of 2×10^{-4} corresponding to about 100 molecules (at $\delta = 0$ and $I_2/I_1 = 1/500$). For comparison, for $I_2/I_1 = 1/40$ the molecule number is only about 25 at $\delta = 0$. It is interesting to note how few molecules are needed to stabilize almost a million atoms against photoassociation. This large asymmetry of the particle numbers reflects the different coupling strengths of the free-bound and bound-bound transitions. Naturally the question arises how the experimental parameters should be chosen to optimize the number of molecules. This is nontrivial due to the finite decay rate γ_g. With model (1) we have numerically mapped out molecule numbers as a function of time, detuning, and laser intensities, starting

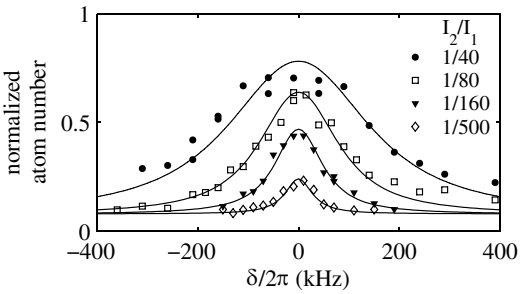

FIG. 4. Dark resonances [blowup of the central part of Fig. 1(c) and similar curves] for different intensity ratios I_2/I_1 (see legend) at a fixed intensity $I_1 = 7\ \mathrm{W/cm^2}$. The solid curves are calculations based on our theoretical model. $\Delta = 0$.

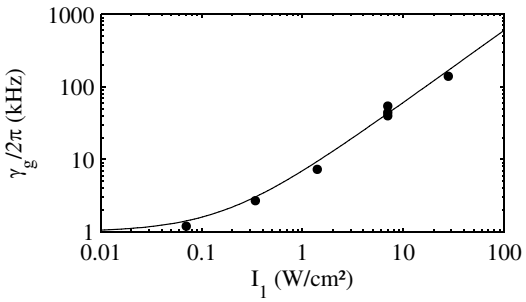

FIG. 5. Dependence of the decay rate γ_g of the ground-state molecules on the laser intensity I_1, measured with an intensity ratio $I_2/I_1 = 1/40$. The solid curve is given by $\gamma_g = 2\pi \times 6\ \mathrm{kHz/(W\,cm^{-2})} I_1 + 2\pi \times 1$ kHz.

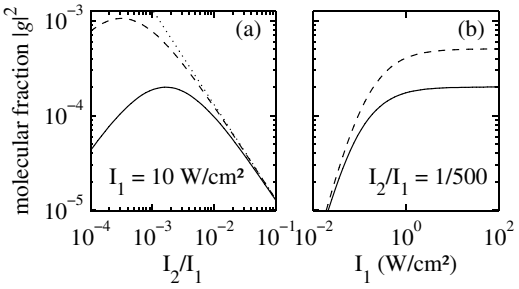

FIG. 6. (a) Maximum molecular fraction as function of the intensity ratio I_2/I_1 at a fixed intensity $I_1 = 10\ \mathrm{W/cm^2}$ and (b) as a function of intensity I_1 at a fixed intensity ratio $I_2/I_1 = 1/500$. The solid lines show the molecule fraction for the measured decay rate $\gamma_g = 2\pi \times 6\ \mathrm{kHz}/(\mathrm{W\,cm^{-2}})I_1 + \gamma_{\mathrm{bg}}$. The dashed lines show the molecule fraction assuming a lower decay rate $\gamma_g = 2\pi \times 1\ \mathrm{kHz}/(\mathrm{W\,cm^{-2}})I_1 + \gamma_{\mathrm{bg}}$. The dotted line corresponds to $\gamma_g = 0$. The calculations are based on Eqs. (1) with $\Delta = 0$.

out with a pure atomic BEC and simply switching on the lasers. In general, within a few μs of evolution, the dark state is formed. This involves only negligible losses of atoms since the dark state is very close to our initial BEC state. The maximum number of molecules of every evolution is then determined. We find that we can optimize the molecular production by working at $\Delta = 0$ although other values for Δ can be used. For $\Delta = 0$ the maximum number of molecules corresponds to $\delta = 0$, hence both lasers are on resonance. Figure 6 shows the molecular fraction as a function of the laser intensities. In Fig. 6(a), as I_2/I_1 is lowered from high values, the molecule fraction initially grows and follows a straight dotted line. Because of the finite γ_g the molecular fraction curve rolls over for some value of I_2/I_1, when the molecule loss rate is larger than its production rate. A smaller γ_g would lead to a larger number of molecules (dashed line). In the limit $\gamma_g = 0$ the molecular fraction is located on the dotted line. We note that for our parameter range, this line coincides with the ideal ($\gamma_g = 0$) route for a STIRAP conversion from atoms to molecules. The finite γ_g in our experiments leads to a maximum molecule number at $I_2/I_1 \sim 1/500$, a ratio which we also used in our measurements (see Fig. 4, open diamonds). For this optimum value the dependence of the molecular fraction on I_1 is shown in Fig. 6(b). Here it becomes clear that the laser intensities have to be kept above a certain threshold so that losses are not dominated by the background decay rate γ_{bg} of the molecular state.

To summarize, we have created a novel multiparticle dark state where an optical Raman transition coherently couples an atomic Rb BEC of about 4×10^5 atoms to a quantum degenerate gas of up to 100 Rb_2 ground-state molecules. Our investigations can be extended in a straight forward manner to create and study BECs of arbitrarily deeply bound molecules and coherent atom-molecule mixtures. The dark resonance has proven itself as a useful tool to analyze the atom-molecule system and to optimize the optical conversion of atomic to molecular BECs. An increase of the number of molecules by several orders of magnitude should be possible by choosing better suited ground and excited molecular states for the free-bound Raman transition.

We appreciate the help of George Ruff and Michael Hellwig at an early stage of the experiment. We thank Paul Julienne, Eite Tiesinga, Peter Drummond, and Karen Kheruntsyan for valuable discussions. This work was supported by the Austrian Science Fund (FWF) within SFB 15 (project parts 12 and 17) and the European Union in the frame of the Cold Molecules TMR Network under Contract No. HPRN-CT-2002-00290.

Note added.—Recently, atom-molecule dark states have also been observed in a sodium gas [19].

[1] E. Arimondo and G. Orriols, Lett. Nuovo Cimento Soc. Ital. Fis. **17**, 333 (1976).
[2] For a review, see, e.g., S. E. Harris, Phys. Today **50**, No. 7, 36 (1997).
[3] A. Aspect *et al.*, Phys. Rev. Lett. **61**, 826 (1988).
[4] M. Stähler *et al.*, Opt. Lett. **27**, 1472 (2002).
[5] K. Bergmann, H. Theuer, and B. W. Shore, Rev. Mod. Phys. **70**, 1003 (1998).
[6] For a review, see, e.g., D. Kleppner, Phys. Today **57**, No. 8, 12 (2004).
[7] R. Wynar, R. S. Freeland, D. J. Han, C. Ryu, and D. J. Heinzen, Science **287**, 1016 (2000).
[8] B. Laburthe Tolra, C. Drag, and P. Pillet, Phys. Rev. A **64**, 061401 (2001).
[9] A. Vardi, D. Abrashkevich, E. Frishman, and M. Shapiro, J. Chem. Phys. **107**, 6166 (1997); A. Vardi, V. A. Yurovsky, and J. R. Anglin, Phys. Rev. A **64**, 063611 (2001).
[10] P. S. Julienne, K. Burnett, Y. B. Band, and W. C. Stwalley, Phys. Rev. A **58**, R797 (1998).
[11] J. Javanainen and M. Mackie, Phys. Rev. A **58**, R789 (1998); M. Mackie, A. Collin, and J. Javanainen, Phys. Rev. A **71**, 017601 (2005).
[12] J. J. Hope, M. K. Olsen, and L. I. Plimak, Phys. Rev. A **63**, 043603 (2001).
[13] P. D. Drummond, K. V. Kheruntsyan, D. J. Heinzen, and R. H. Wynar, Phys. Rev. A **65**, 063619 (2002); **71**, 017602 (2005).
[14] B. Damski *et al.*, Phys. Rev. Lett. **90**, 110401 (2003).
[15] H. Y. Ling, H. Pu, and B. Seaman, Phys. Rev. Lett. **93**, 250403 (2004).
[16] C. Lisdat, N. Vanhaecke, D. Comparat, and P. Pillet, Eur. Phys. J. D **21**, 299 (2002).
[17] U. Schlöder, T. Deuschle, C. Silber, and C. Zimmermann, Phys. Rev. A **68**, 051403 (2003).
[18] For details, see, e.g., G. Thalhammer *et al.*, Phys. Rev. A **71**, 033403 (2005).
[19] R. Dumke, J. D. Weinstein, M. Johanning, K. M. Jones, and P. D. Lett, cond-mat/0508077.

Inducing an optical Feshbach resonance via stimulated Raman coupling

Gregor Thalhammer,[1] Matthias Theis,[1] Klaus Winkler,[1] Rudolf Grimm,[1,2] and Johannes Hecker Denschlag[1]
[1]*Institut für Experimentalphysik, Universität Innsbruck, Technikerstraße 25, 6020 Innsbruck, Austria*
[2]*Institut für Quantenoptik und Quanteninformation, Österreichische Akademie der Wissenschaften, 6020 Innsbruck, Austria*
(Received 23 September 2004; published 8 March 2005; publisher error corrected 11 March 2005)

We demonstrate a method of inducing an optical Feshbach resonance based on a coherent free-bound stimulated Raman transition. In our experiment atoms in a ^{87}Rb Bose-Einstein condensate are exposed to two phase-locked Raman laser beams which couple pairs of colliding atoms to a molecular ground state. By controlling the power and relative detuning of the two laser beams, we can change the atomic scattering length considerably. The dependence of scattering length on these parameters is studied experimentally and modeled theoretically.

DOI: 10.1103/PhysRevA.71.033403 PACS number(s): 34.50.Rk, 32.80.Pj, 03.75.Nt, 34.20.Cf

I. INTRODUCTION

Feshbach resonances have become a central tool in the physics of ultracold quantum gases during the last years because they allow for a tuning of the interactions between atoms. Controlling interparticle interactions is a central key in many fields of modern physics and is especially relevant for future applications in quantum computation and exploring novel many-particle quantum effects. Beautiful experiments using magnetically tunable Feshbach resonances [1,2] have been performed, ranging from ultrahigh-resolution molecular spectroscopy [3] to the coherent coupling of atomic and molecular states [4] as well as the creation of bright matter wave solitons [5]. It also led to the production of new atomic [6] and molecular [7] Bose-Einstein condensates (BEC's) and allowed control of pairing in ultracold fermionic gases [8].

Recently we demonstrated how atom-atom interactions in a ^{87}Rb BEC can also be tuned with an optically induced Feshbach resonance [9] (see also [10]), a scheme which was originally proposed by Fedichev *et al.* [11,12]. Optically induced Feshbach resonances offer advantages over magnetically tuned Feshbach resonances since the intensity and detuning of optical fields can be rapidly changed. Furthermore, complex spatial intensity distributions can be easily produced and optical transitions are always available even when no magnetic Feshbach resonances exist. A disadvantage of optically induced Feshbach resonance is the inherent loss of atoms due to excitation and spontaneous decay of the molecular state [9]. Typical lifetimes for excited molecular states are on the order of 10 ns which corresponds to a linewidth of $2\pi\times 16$ MHz. Evidently, coupling to molecular states with longer lifetime should improve the situation. Ground-state molecules are stable against radiative decay, and narrow transition linewidths on the order of kHz have been observed in two-photon Raman photoassociation [13,14]. This raises the question whether it is possible to create optical Feshbach resonances using stimulated Raman transitions and whether this scheme might be advantageous compared to the one-photon optical Feshbach resonance.

In this paper we indeed demonstrate that optical Feshbach resonances can be induced using a coherent two-color Raman transition to a highly vibrationally excited molecular ground state in a ^{87}Rb BEC. In the experiment we show how the scattering length and loss rates can be tuned as a function of the intensity of the lasers and their detuning from molecular lines. We use Bragg spectroscopy [15] as a fast method to measure the scattering length in our sample [9]. To fit and analyze our data we use a model by Bohn and Julienne [16]. We find that using the Raman scheme for optically induced Feshbach resonances leads to similar results in tuning of the scattering length as for the single-photon Feshbach scheme. The Raman scheme does not lead to an improvement compared to the one-photon scheme because its atomic loss rate is not lower for a given change in scattering length. However, using a stimulated Raman transition does offer experimental advantages. To tune over the Feshbach resonance, the relative frequency of the two laser beams only has to be changed typically by several MHz which can be conveniently done using an acousto-optic modulator. This allows for very fast and precise control of the scattering length. On the other hand, working with a one-photon optical Feshbach resonance in the low-loss regime typically requires large detunings and scan ranges on the order of GHz. The Raman scheme relaxes the necessity for absolute frequency control of the lasers which can be tedious to maintain far away from atomic lines. Since off-resonant light fields in general lead to dipole forces acting on the atoms, a variation of the scattering length via optical tuning leads to a variation of the dipole forces on the atomic sample. This unwanted effect can be made negligible for the Raman scheme which tunes over resonance within a small frequency range.

The paper is organized as follows: We start in Sec. II by discussing the Raman scheme with a simple theoretical model. In Sec. III we describe in detail our experimental setup and the measurement method. In Sec. IV we discuss the experimental results which are compared with a theoretical model. The Appendix gives details of the model that is used to describe the data.

II. RAMAN SCHEME FOR OPTICAL FESHBACH TUNING

Before discussing optical Feshbach tuning based on a two-photon Raman transition, it is instructive to briefly recall

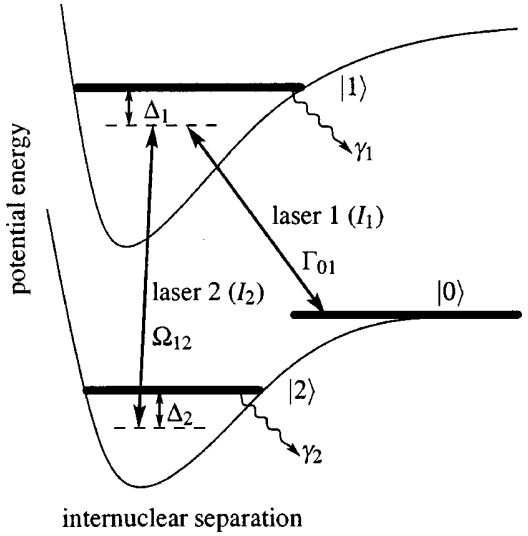

FIG. 1. Schematic diagram of the transitions used for optically coupling the collisional state $|0\rangle$ to molecular states $|1\rangle$ and $|2\rangle$. $|1\rangle$ is electronically excited whereas $|2\rangle$ is in the electronic ground state. Δ_1 and Δ_2 are defined to be positive for the shown configuration.

the one-photon scheme first [9,11,12]. This configuration uses a single laser beam tuned close to a transition from the scattering state of colliding atoms to a bound level in an excited molecular potential (states $|0\rangle$ and $|1\rangle$ in Fig. 1). Varying the detuning Δ_1 or the intensity I_1 modifies the coupling and hence the scattering length. Atomic loss can occur through population of the electronically excited molecular state which has a decay width of γ_1.

Introducing a second laser as shown in Fig. 1 will now couple the collisional state $|0\rangle$ to a bound level $|2\rangle$ in the ground-state potential. As we will show, this allows for a tuning of the scattering length similar to the one-photon scheme. We now have, however, four parameters which can be used to influence the scattering length: the intensities I_1 and I_2 of lasers 1 and 2 and the detunings Δ_1 and Δ_2 as shown in Fig. 1.[1]

From [16] [Eqs. (4.8)–(4.11)] one can extract approximate expressions for the inelastic collision rate coefficient K_{inel} and the scattering length a in a Bose-Einstein condensate:[2]

$$K_{\text{inel}} = \frac{2\pi\hbar}{m}\frac{1}{k_{\text{i}}}\frac{\Gamma_{01}\gamma_1}{(\Delta_1 - \Omega_{12}^2/\Delta_2)^2 + (\gamma_1/2)^2}, \tag{1}$$

[1]As we observe a significant light shift of level $|1\rangle$, depending on the intensity I_1 of laser 1 [9], we measure the detuning Δ_1 from the observed position of the one-photon line at a given intensity of laser 1. Note that Δ_1 is a one-photon detuning whereas Δ_2 is a two-photon detuning.

[2]K_{inel} is reduced by a factor of 2 as compared to the case of thermal atoms. This is because in a BEC all atoms share the same quantum state.

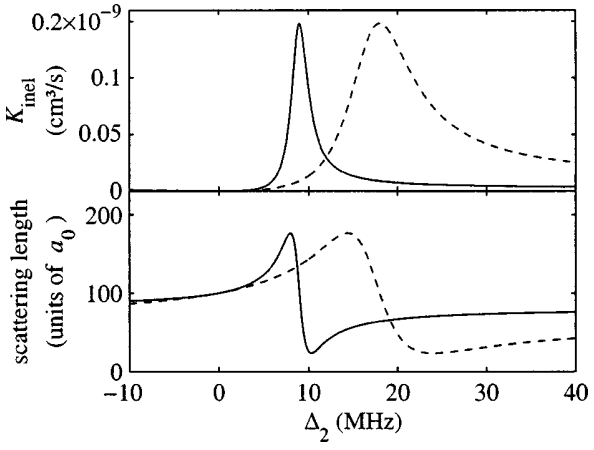

FIG. 2. K_{inel} and scattering length a according to Eqs. (1) and (2), plotted for two values of Δ_1. Solid line: $\Delta_1/2\pi = 100$ MHz. Dashed line: $\Delta_1/2\pi = 50$ MHz. The other parameters are $\Gamma_{01}/2\pi = 50$ kHz, $\Omega_{12}/2\pi = 30$ MHz, and $\gamma_1/2\pi = 25$ MHz. The wave number $k_{\text{i}} = 2.5\times10^5$ m^{-1} corresponds to the finite size of the condensate wave function. a_0 is the Bohr radius.

$$a = a_{\text{bg}} - \frac{1}{2k_{\text{i}}}\frac{\Gamma_{01}(\Delta_1 - \Omega_{12}^2/\Delta_2)}{(\Delta_1 - \Omega_{12}^2/\Delta_2)^2 + (\gamma_1/2)^2}. \tag{2}$$

Here Γ_{01} denotes the on-resonance stimulated transition rate from $|0\rangle$ to $|1\rangle$ which is proportional to I_1. Ω_{12} is the Rabi frequency for the coupling of the states $|1\rangle$ and $|2\rangle$ and is proportional to $\sqrt{I_2}$. $\hbar k_{\text{i}}$ is the relative momentum of the collision, where $\hbar$ is Planck's constant divided by 2π. a_{bg} is the background scattering length and m is the atomic mass.

Equations (1) and (2) neglect spontaneous decay from state $|2\rangle$ ($\gamma_2 = 0$) and assume $\Gamma_{01} \ll \gamma_1$. Setting $\Omega_{12} = 0$ yields the expressions for the one-photon Feshbach resonance as given in [9]. Equations (1) and (2) yield a Lorentzian and a corresponding dispersive line shape as a function of Δ_1. In our experiments, however, we hold Δ_1 constant and scan Δ_2. Figure 2 shows typical curves for K_{inel} and a for two detunings Δ_1. The curves for K_{inel} are slightly asymmetric, but for $\Delta_1 \gg \Omega_{12}$ they can be well approximated by Lorentzians. This can be seen by expanding the denominator of Eq. (1) in terms of Δ_2 at the resonance position. A light shift displaces the position of the resonance to ${\Omega_{12}}^2/\Delta_1$. It is also interesting to note that the resonance width decreases with increasing detuning Δ_1 as $\gamma_1(\Omega_{12}/\Delta_1)^2$.

In a sense the two-photon Raman-Feshbach resonance can be coined in terms of a one-photon Feshbach scheme. The detuning Δ_2 effectively replaces the detuning Δ_1 of the one-photon Feshbach scheme.[3]

Since Eqs. (1) and (2) have exactly the same form as for the one-photon Feshbach resonance, it follows that, given a

[3]There is even a more direct way to understand the two-photon Feshbach resonance in terms of a one-photon Feshbach resonance. Laser 1 couples the collision state $|0\rangle$ to a virtual level $|2'\rangle$, which is generated by laser 2 acting on level $|2\rangle$. The splitting between $|2'\rangle$ and $|1\rangle$ is given by $\Delta_{2'} = \Delta_1 - \Delta_2$. Its linewidth is $\gamma_1(\Omega_{12}/\Delta_{2'})^2$ and the transition rate $\Gamma_{02'} = \Gamma_{01}(\Omega_{12}/\Delta_{2'})^2$.

fixed free-bound transition rate Γ_{01}, the maximum tuning range of the scattering length for the two-photon case cannot be larger than in a one-photon scheme. Furthermore, given a fixed change in scattering length, the loss rate as determined by K_{inel} is not lower for the Raman scheme than for the one-photon scheme.

III. EXPERIMENTAL SETUP AND METHODS

A. Production of BEC's

For the experiments we produce ^{87}Rb BEC's of typically 1.2×10^6 atoms in the spin state $|F=1,m_F=-1\rangle$. Our setup comprises a magnetic transfer line [17] to transport atoms from a magneto-optic trap (MOT) chamber to a glass cell where the BEC is produced and all experiments are carried out. In a first step about 3×10^9 atoms are loaded within 4 s into a MOT directly from the background gas and are then cooled further to about 50 μK in a molasses cooling phase. After optically pumping into the $|F=1,m_F=-1\rangle$ state we load the atom cloud into a magnetic quadrupole trap with a gradient of 130 G/cm in the (strong) vertical direction. Within 1.4 s the atoms are then moved via a magnetic transfer line[4] over a distance of 48 cm including a 120° corner into a glass cell which is at a pressure below 10^{-11} mbar. In this cell we finally load the cloud into a QUIC trap (a type of magnetic trap that incorporates the quadrupole and Ioffe configuration) [18], ending up with typically 4×10^8 atoms at a temperature of about 250 μK. All three coils of the QUIC trap are operated at a current of 40 A, dissipating 350 W. This results in trap frequencies of $\omega_{\mathrm{radial}}/2\pi=150$ Hz and $\omega_{\mathrm{axial}}/2\pi=15$ Hz at a magnetic bias field of 2 G. To achieve Bose-Einstein condensation we use forced radio-frequency evaporation for a period of 20 s. The stop frequency is chosen so that we end up with condensates with a thermal background of about 25% of noncondensed atoms. At this value we concurrently get the highest number of atoms in the condensate and good reproducibility. For our measurements we consider only the condensed atoms.

B. Raman lasers

To realize the Raman scheme shown in Fig. 1 we use the electronically excited molecular state $|1\rangle=|0_g^-,\ \nu=1,\ J=2\rangle$ located 26.8 cm^{-1} below the $(S_{1/2}+P_{3/2})$ dissociation asymptote [9,19]. About 290 MHz below the $J=2$ line, there is another rotational level with $J=0$.[5] Although about 5 times weaker than the $J=2$ line, its effect cannot be totally neglected in our experiment. We choose level $|2\rangle$ to be the second to last bound state in the ground-state potential. It has a binding energy of 636 MHz$\times h$ [13] where h is Planck's constant.

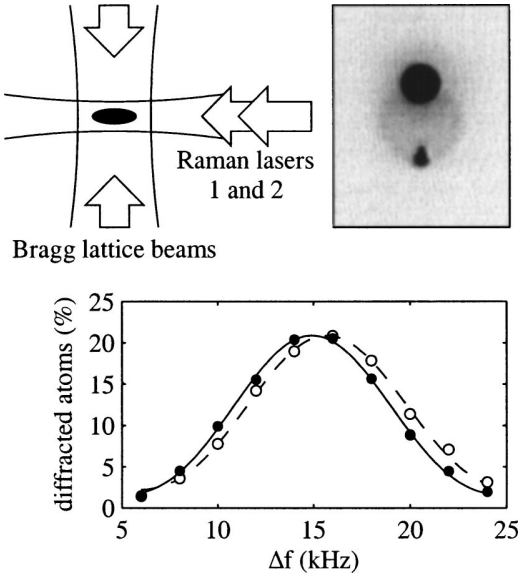

FIG. 3. Top left: experimental arrangement of the laser beams (top view). Top right: absorption image obtained after Bragg-diffracting a portion of the atoms to a state with a momentum of two photon recoils (lower atom cloud) and subsequent time of flight expansion. Bottom: Bragg resonance curves for two different relative detunings of the Raman lasers. The relative shift of 700 Hz is due to two different scattering lengths which are optically induced in the condensates. The atom numbers are the same for both curves. Shown is the percentage of diffracted atoms versus the frequency difference of the Bragg lattice beams. For better comparison we have scaled up the right curve by 10%.

The Raman laser beams are derived from a Ti:sapphire laser using an acousto-optical modulator at a center frequency of about 318 MHz in a double-pass configuration. This allows precise control of their relative frequency difference over several tens of MHz. Both Raman lasers propagate collinearly and are aligned along the weak axis of the magnetic trap (see Fig. 3). They have a $1/e^2$ waist of 76 μm, and their linear polarization is perpendicular to the magnetic bias field of the trap.

The Ti:sapphire laser is intensity stabilized and its frequency has a linewidth of about 3 MHz. In order to stabilize its frequency relative to the photoassociation lines, the laser is offset locked relative to the D_2 line of atomic rubidium with the help of a scanning optical cavity. This yields an absolute frequency accuracy of better than 10 MHz. In all our experiments the Raman laser intensities were set to $I_1=300$ W/cm^2 and $I_2=60$ W/cm^2 at the location of the condensate, if not stated otherwise.

C. Bragg spectroscopy

To measure optically induced changes in the scattering length a, we use Bragg spectroscopy [9,15]. This method allows for a fast measurement on time scales below 100 μs which is vital because of the rapid photoassociation losses

[4]For our magnetic transport (similar to that described in [17]) 13 pairs of quadrupole coils are used. These transfer coils each have an inner diameter of 23.6 mm, an outer diameter of 65 mm, and a height of 5.7 mm and consist of 34 windings. They are arranged in two layers above and below the vacuum chamber with a separation of 50 mm. Peak currents of 75 A are necessary to maintain a vertical gradient of 130 G/cm during transfer.

[5]Due to different light shifts [9] for the $J=0$ and $J=2$ lines, their splitting is intensity dependent. The value of 290 MHz is valid for an intensity of 300 W/cm^2.

we experience in our experiments. A moving lattice composed of two counter propagating beams with wave number k and a frequency difference Δf is used to diffract some of the condensate atoms to a state with nonzero momentum. When energy and momentum conservation are fulfilled, the Bragg lattice resonantly transfers a momentum of two photon recoils $2\hbar k$ in a first-order diffraction process. For the case of a homogeneous condensate of density n, the resonance energy for Bragg diffraction is given by the sum of transferred kinetic energy $h\Delta f_0=(2\hbar k)^2/2m$ and the change in mean-field energy $4\pi\hbar^2 na/m$.[6] This corresponds to a frequency difference of the Bragg lasers of

$$\Delta f_r = \Delta f_0 + \frac{2\hbar}{m} na. \tag{3}$$

If the condensate is initially not at rest, the kinetic energy contribution Δf_0 to the Bragg resonance frequency [Eq. (3)] contains an additional term $2\hbar kp/m$, where p is the initial atom momentum in the direction of the Bragg lattice. In our experiments we observe such a motional shift corresponding to condensate momentum of up to $p=0.1\ \hbar k$. This momentum can partly be attributed to optical dipole forces of Raman beams which are slightly noncentered on the condensate. Partly it can be attributed to a forced oscillation of the condensate in the magnetic trap at 150 Hz which coincides with the trapping frequency. Since this oscillation is driven by a higher harmonic of the line frequency (50 Hz), it is in phase with the line frequency and we are able to stabilize the initial condensate momentum by synchronizing the experiment to the line. A stable initial condensate momentum can then be determined and canceled out by measuring Δf_r alternately for Bragg diffraction to the $+2\hbar k$ and $-2\hbar k$ momentum components. After these measures we were left with a residual momentum noise level of up to $p=0.01\ \hbar k$.

In our setup the Bragg lattice beams are oriented along the horizontal direction perpendicular to the Raman laser beams (see Fig. 3) and have a width of $\approx$0.9 mm. We extract both beams from a single grating-stabilized diode laser and use two acousto-optical modulators to control the frequency difference. The laser is tuned 1.4 nm below the ^{87}Rb D_2 line which defines Δf_0 in Eq. (3) to be 15.14 kHz. This frequency is much larger than the typical mean-field contribution, $2\hbar na/m$, which in our experiments was below 3 kHz.

We illuminate the trapped condensate for 100 μs with the Bragg lattice light. After 12 ms of free expansion the diffracted atoms are spatially separated from the remaining atoms. Absorption imaging allows us to determine the diffraction efficiency. By adjusting the Bragg laser intensity (typically 1 mW) we keep the maximum diffraction efficiency between 15% and 20%. When we scan the frequency difference Δf and measure the fraction of Bragg-diffracted atoms we obtain curves as shown in Fig. 3 (bottom). These curves have a width of approximately 9 kHz as determined by the 100 μs length of our Bragg pulses. The shape of the curves is given by the Fourier transform of our square light pulses which we use to fit the data to obtain the resonance position Δf_r [9]. The shift between the two Bragg spectroscopy curves in Fig. 3 (bottom) is optically induced by shining in the Raman lasers at the same time as the Bragg lattice. For both curves the atom numbers are the same and $\Delta_1=60$ MHz. Only the Raman detuning Δ_2 differs by 26 MHz. According to Eq. (3) this observed shift in Bragg resonance frequency is then due to a change in scattering length, induced by tuning Δ_2. This demonstrates that we can tune the scattering length a with a Raman Feshbach resonance.

D. Determination of scattering length

We use Eq. (3) to determine the scattering length a from the measurements of the Bragg resonance frequency Δf_r. Equation (3), however, is derived for the case of a homogeneous condensate. Our trapped condensate, in contrast, which is subject to photoassociation losses, exhibits a time- and position-dependent density n. This can be taken into account by replacing the density n in Eq. (3) by an appropriate effective value $\bar{n}$.

A simple approach to estimate $\bar{n}$ is to calculate the spatial and time average of the condensate density n over the duration of the Raman pulse length T. For this we use the rate equation for the local density $\dot{n}=-2K_{\mathrm{inel}}n^2$ for two-atom losses. The inelastic collision rate coefficient K_{inel} governing this process is obtained from measuring the atom number at the beginning and end of the light pulse. This procedure already yields good results which differ less than 10% from an improved approach which we use for our data analysis and which is explained in the following.

The improved approach consists of a full numerical simulation which describes Bragg diffraction in a dynamically and spatially resolved way. We divide the condensate into density classes and treat their time dependence individually. The Bragg diffraction process is identified as a Rabi oscillation between a coherent two level system—i.e., the BEC component at rest and the Bragg-diffracted component. The changing density of the condensate due to loss is reflected in a time-dependent resonance frequency [see Eq. (3)]. As a result of these calculations we obtain for each density class a Bragg resonance curve similar to the experimental ones shown in Fig. 3. Averaging over these resonance curves and determining the center position yields the simulated value for the Bragg resonance Δf_r. Using $\Delta f_r=\Delta f_0+2\hbar\bar{n}a/m$ we can then determine the effective density $\bar{n}$.

IV. RESULTS

A. Raman scans

Figure 4 presents measurements where the detuning Δ_1 of laser 1 from the excited molecular state is set to $\Delta_1/2\pi=60$ MHz. The intensities of the Raman lasers 1 and 2 are 300 W/cm^2 and 60 W/cm^2, respectively. Figure 4(a) shows the atom number after illuminating a condensate of initially 1.4×10^6 atoms for 100 μs with the Raman lasers. Scanning the Raman detuning Δ_2 we find a strong loss of atoms on resonance. As already expected from Eq. (1) the line shape is slightly asymmetric. Figure 4(b) shows the resonance fre-

[6]This is valid in the limit that only a small fraction of the condensate is diffracted.

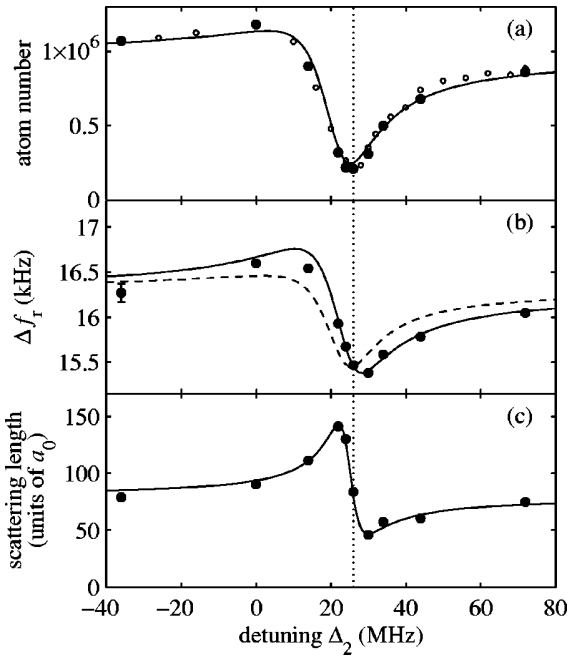

FIG. 4. Optical Feshbach resonance using a Raman scheme. (a) shows the measured atom number after the Raman pulse, (b) the measured Bragg resonance frequency, and (c) the scattering length, as determined from (a) and (b). In (a) the solid circles correspond to measurements where Bragg spectroscopy was used to determine the scattering length, while the small open circles stem from additional loss measurements without Bragg spectroscopy. From our measurements we estimate the uncertainty of the Bragg resonance frequency to be smaller then ±100 Hz, as indicated by the error bar in (b). The solid lines in (a), (b), and (c) are from a model calculation (see the Appendix and text). The dashed line in (b) shows the expected signal if there was only loss in atom number but no change in scattering length (see also discussion in text). The vertical line indicates the location of maximal loss in (a) and helps to compare the relative positions of the three curves.

quency Δf_r as measured by Bragg spectroscopy. When we analyze the data in Figs. 4(a) and 4(b) with the improved procedure described in Sec. III D we obtain values for the scattering length which are shown in Fig. 4(c). The scattering length a shows a dispersive variation between $50\,a_0$ and $140\,a_0$ as we scan over the resonance. The dispersive scattering length curve is offset by about $20\,a_0$ from the background scattering length $a_{bg}=100\,a_0$ for ^{87}Rb in the $|F=1, m_F=-1\rangle$ state [20–22]. This is due to the one-photon Feshbach tuning of laser 1, in agreement with our previous measurements [9].

We find that Eqs. (1) and (2) are not sufficient to describe these data properly, mainly because they neglect the decay rate γ_2. A more complete model (see the Appendix), also taking into account both the $J=0$ and $J=2$ rotational levels, was used for creating fit curves,[7] depicted as solid lines in Fig. 4. The fact that the data for atomic loss as well as for the scattering length a are both well described by the theoretical curves is an intrinsic consistency check for our model and our data analysis.

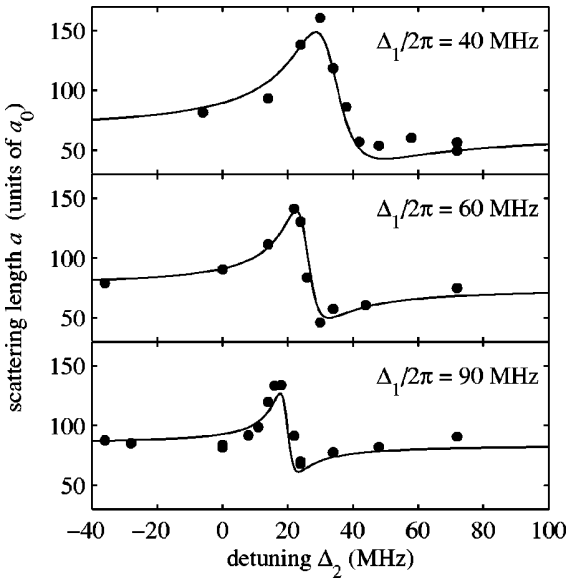

FIG. 5. Variation of the scattering length with Raman detuning for three various detunings Δ_1 from the excited molecular state. The solid line is a calculation (see the Appendix) which uses a single set of parameters for all curves.

The shape of the signal Δf_r in Fig. 4(b) is a combination of the effects of the varying scattering length a and the varying atom number [see Eq. (3)]. This is illustrated by the dashed and continuous lines in Fig. 4(b): The dashed line shows the expected signal if only the variations in atom number would occur and the scattering length stayed constant.[8] The solid line takes the variations in both atom number and scattering length into account. The deviation of the measured data points from the dashed line is due to an optical induced change of the scattering length.

B. Dependence on detuning

We now investigate how detuning Δ_1 affects the scattering length a. Figure 5 shows a set of three curves showing the scattering length for detunings $\Delta_1/2\pi=40$, 60, and 90 MHz.

The measurements clearly show that the position and width of the resonances depend on Δ_1. The change in position can be mainly explained as light shifts of levels $|1\rangle$ and $|2\rangle$ due to laser 2. The decrease of the resonance width with increasing detuning Δ_1 follows directly our discussion in Sec. II. The solid lines are model calculations as described in detail in the Appendix. They are derived from a simultaneous fit to the data shown in Fig. 5 and a large number of atom loss measurements with different detunings (not shown). The set of fit parameters is listed in the Appendix. We also use this same set of parameters for the theoretical curves in Figs. 6 and 7.

[7] The resulting fit parameters are similar to those given in the Appendix.

[8] To account for the one-photon Feshbach tuning of laser 1, a value for the background scattering length $a_{bg}=80\,a_0$ was used for the calculation.

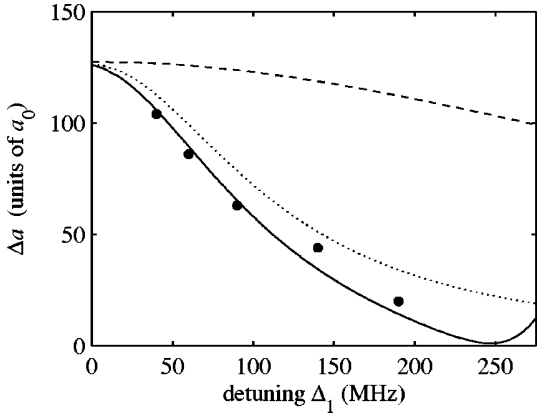

FIG. 6. Maximum variation in scattering length $\Delta a = a_{\max} - a_{\min}$ versus one-photon detuning Δ_1. Solid line: full model calculation (see the Appendix). Dotted line: three-level model (see Fig. 1), with $\gamma_2/2\pi = 2$ MHz. Dashed line: three-level model, with $\gamma_2/2\pi = 100$ kHz.

It is interesting to note from Fig. 5 that the amplitude of the dispersive scattering length signal decreases as Δ_1 becomes larger. This is not to be expected from the simple model Eqs. (1) and (2). To investigate this effect we have performed scans for atom loss and scattering length for several detunings Δ_1. Figure 6 shows the maximum variation in scattering length, $\Delta a = a_{\max} - a_{\min}$, obtained for detunings Δ_1 ranging from 40 MHz to 200 MHz. Here, $a_{\max}$ and $a_{\min}$ are the maximal and minimal scattering length values for corresponding scan curves. Typical scan curves are shown in Fig. 5. Each data point in Fig. 6 was derived from a complete scan and corresponds to one day of data collection.

An analysis of our data using our theoretical model indicates that the decrease of Δa as a function of Δ_1 is a consequence of two effects.

(i) To properly model these measurements we have to assign to the molecular state $|2\rangle$ in the ground-state potential a non-negligible decay width $\gamma_2/2\pi \approx 2$ MHz. For comparison, two calculations of a three-level model are plotted in Fig. 6. For small $\gamma_2/2\pi = 100$ kHz (dashed line) Δa decreases only weakly. For $\gamma_2/2\pi = 2$ MHz (dotted line) the theory fits the data much better. Such a large decay rate of a ground-state level is surprising. It seems too large to be explained purely by collisions. We find that the decay rate increases with the light intensity. At low light powers of a few W/cm^2 we have observed very narrow linewidths $\gamma_2/2\pi$ on the order of a few kHz, similar to the values reported by [13,14]. The broadening of the molecular ground level could be due to coupling to excited molecular levels. We can exclude, however, from our experimental data that these levels are located within our experimental scanning range between the states $|1\rangle$ and $|3\rangle$. This would lead to additional resonance features in the scattering length, absorption, and light shifts, which are inconsistent with our data. In contrast, our data indicate a relatively constant background loss rate of the ground level over the experimental scan range. This allows us to analyze the data successfully with our simple few-level model. Besides coupling to excited molecular states, we suspect that coupling to the *d*-wave shape resonance of the scattering channel also gives rise to a sizable contribution to the molecular decay rate. Because the *d*-wave shape resonance is located very close (a few MHz) to threshold, it is resonantly coupled to the molecular ground-state level via the Raman transition. To include the shape resonance is beyond the reach of our simple model and has to be investigated later.

(ii) The second reason for the decrease in Δa is a quantum interference effect involving both the $J=2$ and $J=0$ rotational levels as predicted by our model. At a detuning of $\Delta_1/2\pi \approx 250$ MHz the interference effect leads to a complete disappearance of the optical Feshbach resonance. We observe this in a corresponding disappearance of the atom loss feature in our measurements (not shown). The interference effect alone—i.e., without a 2 MHz linewidth—is not sufficient to explain the experimental data in Fig. 6.

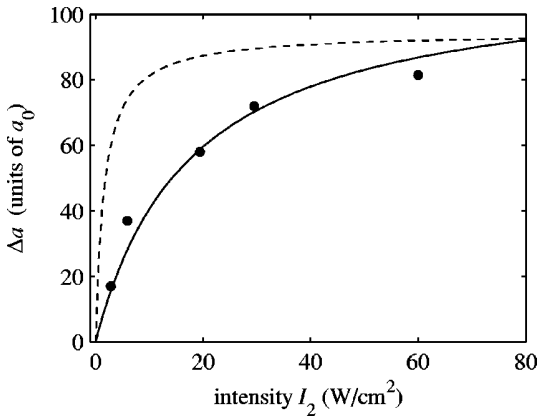

FIG. 7. Maximum variation in scattering length $\Delta a = a_{\max} - a_{\min}$ versus I_2. For this data set $I_1 = 300$ W/cm^2 and $\Delta_1 = 60$ MHz. The solid line is a full model calculation (see the Appendix). The dashed line stems from the same model, but with $\gamma_2/2\pi$ set to 100 kHz and is scaled by a factor of 0.84 for better comparison.

C. Dependence on intensity

From the simple model Eq. (2) it is clear that the maximum variation in scattering length Δa is proportional to Γ_{01} and consequently scales linearly with the intensity I_1 of laser 1. We have verified this dependence recently [9] for the case of a one-photon optical Feshbach resonance.

In contrast, the dependence of Δa on intensity I_2 of laser 2 is not so trivial. According to the simple model, Eqs. (1) and (2), which neglects the decay rate γ_2, the maximum change Δa is independent of I_2. It is also clear, that for $I_2 = 0$ we have $\Delta a = 0$ since there is no dependence of scattering length on Δ_2 at all. This unphysical discontinuous behavior can be resolved if we introduce a finite decay rate $\gamma_2 > 0$. We then find that for increasing intensity I_2, Δa rises monotonously from zero to a value where it saturates. We observe this general behavior in our measurements presented in Fig. 7. Our full model, as described in the Appendix, describes the measured data well if we set the decay rate to $\gamma_2/2\pi = 2$ MHz (solid line). In contrast, the dashed line in Fig. 7 shows the calculation for the same model where γ_2 is set to

$\gamma_2/2\pi=100$ kHz. Saturation then occurs at a much lower intensity I_2 than for $\gamma_2/2\pi=2$ MHz.

V. CONCLUSION

Our experiments demonstrate the use of an optical Feshbach resonance for tuning of the scattering length via stimulated Raman coupling to a bound molecular state. Our results show that there is no advantage over a one-photon scheme when comparing tuning range and loss rate. However, for certain applications a Raman scheme is experimentally more favorable since it demands a lower tuning range of the lasers. Our presented theoretical model is in good agreement with our data and might be helpful when tailoring experimental parameters for a specific application. Furthermore, it gives insight into the process of creating stable ultracold molecules via two-photon photoassociation.

ACKNOWLEDGMENTS

We appreciate the help of George Ruff and Michael Hellwig at an early stage of the experiment. We thank Paul Julienne, Eite Tiesinga, John Bohn, Olivier Dulieu, Peter Fedichev, Andrea Micheli, and Helmut Ritsch for valuable discussions. This work was supported by the Austrian Science Fund (FWF) within SFB 15 (project part 17) and the European Union in the frame of the Cold Molecules TMR Network under Contract No. HPRN-CT-2002-00290.

APPENDIX: THEORETICAL MODEL AND FIT PARAMETERS

We use a theoretical model by Bohn and Julienne [16] to fit the data in Figs. 4–7. In the following we give a short summary of this model and present the procedure to calculate the scattering matrix S, the loss coefficient K_{inel}, and the scattering length a. The model has the advantage that it is concise and intuitive and it allows treatment of multilevel systems with several couplings between the levels. The numerical calculations involve simple manipulations of small matrices.

In Fig. 8 the level scheme for our two models involving four and six levels are shown. We first restrict our description to the four-level model as shown in the right part of Fig. 8. In this way our description stays compact and matrices are kept small. The extension to six or more levels follows the same scheme.

Four-level model

Compared to Fig. 1 an additional excited level $|3\rangle$ is added. This level corresponds to the rotational level $J=0$ and lies 290 MHz below the $J=2$ rotational level $|1\rangle$ [9]. We work in the dressed atom picture and every level $|i\rangle$ is attributed a detuning Δ_i (see Fig. 8). Δ_0 is arbitrarily set to 0. The transition strengths from the continuum $|0\rangle$ to levels $|1\rangle$ and $|3\rangle$ are described by stimulated rates Γ_{01} and Γ_{03} which are proportional to the intensity I_1 of laser 1. The transitions between the bound levels $|2\rangle$ and $|1\rangle,|3\rangle$ are characterized by the Rabi frequencies Ω_{12} and Ω_{23}, respectively, which are

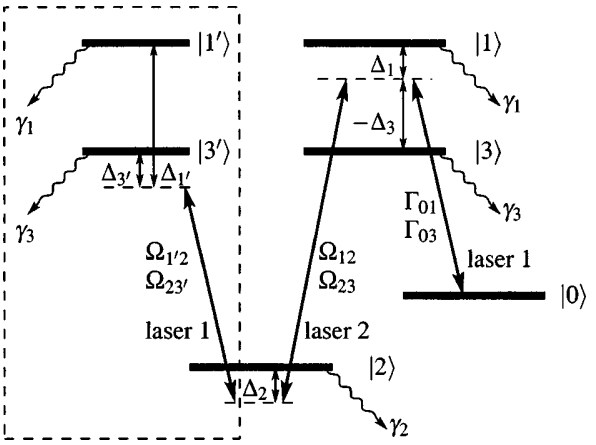

FIG. 8. Extended level scheme (compare to Fig. 1) for the four-level model (right-hand side) and its extension with six levels. State $|3\rangle$ corresponds to the $J=0$ level and lies 290 MHz below the $J=2$ level $|1\rangle$. The four-level model is based on levels $|0\rangle,|1\rangle,|2\rangle$, and $|3\rangle$. The auxiliary levels $|1'\rangle$ and $|3'\rangle$ are introduced in the extended model to describe the coupling between $|2\rangle$ and $|1\rangle,|3\rangle$, respectively, due to laser 1 (see text).

proportional to $\sqrt{I_2}$. Spontaneous decay from the bound levels leading to atomic losses is formally taken into account by introducing artificial levels $|\mathrm{a}_i\rangle$ for each level $|i\rangle$ to which a transition at rate γ_i takes place (not shown in Fig. 8). All these couplings between different levels are summarized in the symmetric reaction matrix K. We arrange the level names in the order $(0, \mathrm{a}_1, \mathrm{a}_2, \mathrm{a}_3, 1, 2, 3)$ and use them as row and column indices. The nonzero matrix elements of the K matrix then read $K_{01}=\sqrt{\Gamma_{01}/2}$, $K_{03}=\sqrt{\Gamma_{03}/2}$, $K_{i\mathrm{a}_i}=\sqrt{\gamma_i/2}$, $K_{12}=\Omega_{12}$, and $K_{23}=\Omega_{23}$. Levels 0, a_1, a_2, and a_3 are referred to as open channels, levels 1, 2, and 3 as closed channels. The reaction matrix K is partitioned into open and closed channel blocks,

$$K=\begin{pmatrix} \mathbf{0} & K^{\mathrm{oc}} \\ K^{\mathrm{co}} & K^{\mathrm{cc}} \end{pmatrix}.$$

K^{oc} reads in our case

$$K^{\mathrm{oc}}=\begin{pmatrix} \sqrt{\Gamma_{01}/2} & 0 & \sqrt{\Gamma_{03}/2} \\ \sqrt{\gamma_1/2} & 0 & 0 \\ 0 & \sqrt{\gamma_2/2} & 0 \\ 0 & 0 & \sqrt{\gamma_3/2} \end{pmatrix}.$$

K^{co} is the transposed matrix of K^{oc} and

$$K^{\mathrm{cc}}=\begin{pmatrix} 0 & \Omega_{12} & 0 \\ \Omega_{12} & 0 & \Omega_{23} \\ 0 & \Omega_{23} & 0 \end{pmatrix}.$$

From K the reduced K matrix

$$K^{\mathrm{red}}=K^{\mathrm{oc}}(D-K^{\mathrm{cc}})^{-1}K^{\mathrm{co}}$$

is calculated, eliminating the closed channels 1–3, where D denotes a diagonal matrix with diagonal elements

$(\Delta_1, \Delta_2, \Delta_3)$. This determines the unitary 4×4 scattering matrix S:

$$S = (\mathbf{1} + iK^{\mathrm{red}})(\mathbf{1} - iK^{\mathrm{red}})^{-1}.$$

From the matrix elements S_{ij} of S the trap loss coefficient K_{inel} is calculated by

$$K_{\mathrm{inel}} = \frac{\pi\hbar}{\mu k_{\mathrm{i}}} \sum_i |S_{0a_i}|^2 = \frac{\pi\hbar}{\mu k_{\mathrm{i}}}(1 - |S_{00}|^2),$$

where $\mu = m_{\mathrm{Rb}}/2$ is the reduced Rb mass and $\hbar k_{\mathrm{i}}$ the relative momentum of the colliding atoms. The scattering length is obtained from S_{00} via

$$a = a_{\mathrm{bg}} - \frac{1}{2k_{\mathrm{i}}} \frac{\mathrm{Im}(S_{00})}{\mathrm{Re}(S_{00})},$$

where $\mathrm{Re}(S_{00})$ and $\mathrm{Im}(S_{00})$ denote the real and imaginary parts of S_{00}, respectively.

In the limit of small relative momentum $\hbar k_{\mathrm{i}}$ and small coupling strengths $\Gamma_{0i} \ll \gamma_i$, K_{inel} and the light-induced change of the scattering length $a - a_{\mathrm{bg}}$ are independent of k_i because the Γ_{0i} are proportional to k_{i} (Wigner threshold regime) [16].

Extension of the four-level model

The four-level model neglects that laser 1 (of which the intensity is typically 5 times greater than that of laser 2) also couples the levels $|2\rangle$-$|1\rangle$ and $|2\rangle$-$|3\rangle$. However, this coupling should be taken into account since laser 1 is not far detuned from these transitions (see Fig. 8) due to the small binding energy of state $|3\rangle$ (636 MHz$\times h$) which is comparable to typical detunings Δ_1. It mainly leads to broadening and light shifting of level $|2\rangle$. The additional coupling can approximately be taken care of by adding another two auxiliary levels $|1'\rangle$ and $|3'\rangle$ with detunings $\Delta_{1'} = \Delta_1 + \Delta_2 + 2\pi \times 636$ MHz and $\Delta_{3'} = \Delta_3 + \Delta_2 + 2\pi \times 636$ MHz as shown in Fig. 8. The coupling strengths $\Omega_{1'2}$ and $\Omega_{23'}$ are fixed by $\Omega_{1'2} = \Omega_{12}\sqrt{I_1/I_2}$ and $\Omega_{23'} = \Omega_{23}\sqrt{I_1/I_2}$. Compared to the four-level model no new fit parameters are introduced. We can calculate K_{inel} and the scattering length a following the same recipe as for the four-level model, only with larger matrices. Fitting the data in Figs. 4–7 this extended model produced much better results than the four-level model. For completeness we give here the fit parameters which were used in the calculations in Figs. 5–7 ($I_1 = 300$ W/cm^2 and $I_2 = 60$ W/cm^2): $\Gamma_{01}/2\pi = 42$ kHz, $\Gamma_{03}/2\pi = 8$ kHz, $\Omega_{12}/2\pi = 32$ MHz, $\Omega_{23}/2\pi = 12$ MHz, $\gamma_1/2\pi = 25$ MHz, $\gamma_3/2\pi = 22$ MHz, and $\gamma_2/2\pi = 2$ MHz. We used $k_{\mathrm{i}} = 2.5\times10^{-5}$ m^{-1}. Due to the limitations of our model, these fit parameters should not be mistaken as the true values of the corresponding physical quantities.

[1] E. Tiesinga, B. J. Verhaar, and H. T. C. Stoof, Phys. Rev. A **47**, 4114 (1993).

[2] S. Inouye *et al.*, Nature (London) **392**, 151 (1998); Ph. Courteille, R. S. Freeland, D. J. Heinzen, F. A. van Abeelen, and B. J. Verhaar, Phys. Rev. Lett. **81**, 69 (1998); J. L. Roberts *et al.*, *ibid.* **81**, 5109 (1998).

[3] C. Chin, V. Vuletic, A. J. Kerman, and S. Chu, Phys. Rev. Lett. **85**, 2717 (2000); A. Marte *et al.*, *ibid.* **89**, 283202 (2002).

[4] E. A. Donley, N. R. Claussen, S. T. Thompson, and C. E. Wieman, Nature (London) **417**, 529 (2002).

[5] L. Khaykovich *et al.*, Science **296**, 1290 (2002); K. E. Strecker, G. B. Partridge, A. G. Truscott, and R. G. Hulet, Nature (London) **417**, 150 (2002).

[6] S. L. Cornish, N. R. Claussen, J. L. Roberts, E. A. Cornell, and C. E. Wieman, Phys. Rev. Lett. **85**, 1795 (2000); T. Weber, J. Herbig, M. Mark, H.-C. Nägerl, and R. Grimm, Science **299**, 232 (2003).

[7] S. Jochim *et al.*, Science **302**, 2101 (2003); M. Greiner, C. A. Regal, and D. S. Jin, Nature (London) **426**, 537 (2003); M. Zwierlein *et al.*, Phys. Rev. Lett. **91**, 250401 (2003); T. Bourdel *et al.*, *ibid.* **93**, 050401 (2004).

[8] C. A. Regal, M. Greiner, and D. S. Jin, Phys. Rev. Lett. **92**, 040403 (2004); M. W. Zwierlein *et al.*, *ibid.* **92**, 120403 (2004); C. Chin *et al.*, Science **305**, 1128 (2004).

[9] M. Theis *et al.*, Phys. Rev. Lett. **93**, 123001 (2004).

[10] F. K. Fatemi, K. M. Jones, and P. D. Lett, Phys. Rev. Lett. **85**, 4462 (2000).

[11] P. O. Fedichev, Y. Kagan, G. V. Shlyapnikov, and J. T. M. Walraven, Phys. Rev. Lett. **77**, 2913 (1996).

[12] J. L. Bohn and P. S. Julienne, Phys. Rev. A **56**, 1486 (1997).

[13] R. Wynar, R. S. Freeland, D. J. Han, C. Ryu, and D. J. Heinzen, Science **287**, 1016 (2000).

[14] T. Rom *et al.*, Phys. Rev. Lett. **93**, 073002 (2004); Ch. Lisdat, N. Vanhaecke, D. Comparet, and P. Pillet, Eur. Phys. J. D **21**, 299 (2002).

[15] J. Stenger *et al.*, Phys. Rev. Lett. **82**, 4569 (1999).

[16] J. L. Bohn and P. S. Julienne, Phys. Rev. A **60**, 414 (1999).

[17] M. Greiner, I. Bloch, T. W. Hänsch, and T. Esslinger, Phys. Rev. A **63**, 031401 (2001).

[18] T. Esslinger, I. Bloch, and T. W. Hänsch, Phys. Rev. A **58**, R2664 (1998).

[19] A. Fioretti *et al.*, Eur. Phys. J. D **15**, 189 (2001).

[20] E. Tiemann (private communication).

[21] P. Julienne and E. Tiesinga (private communication).

[22] P. S. Julienne, F. H. Mies, E. Tiesinga, and C. J. Williams, Phys. Rev. Lett. **78**, 1880 (1997).

Tuning the Scattering Length with an Optically Induced Feshbach Resonance

M. Theis,[1] G. Thalhammer,[1] K. Winkler,[1] M. Hellwig,[1] G. Ruff,[1,*] R. Grimm,[1,2] and J. Hecker Denschlag[1]
[1]*Institut für Experimentalphysik, Universität Innsbruck, Technikerstraße 25, 6020 Innsbruck, Austria*
[2]*Institut für Quantenoptik und Quanteninformation, Österreichische Akademie der Wissenschaften, 6020 Innsbruck, Austria*
(Received 21 April 2004; published 15 September 2004)

We demonstrate optical tuning of the scattering length in a Bose-Einstein condensate as predicted by Fedichev *et al.* [Phys. Rev. Lett. **77**, 2913 (1996)]. In our experiment, atoms in a ^{87}Rb condensate are exposed to laser light which is tuned close to the transition frequency to an excited molecular state. By controlling the power and detuning of the laser beam we can change the atomic scattering length over a wide range. In view of laser-driven atomic losses, we use Bragg spectroscopy as a fast method to measure the scattering length of the atoms.

DOI: 10.1103/PhysRevLett.93.123001 PACS numbers: 34.50.Rk, 03.75.Nt, 32.80.Pj, 34.20.Cf

The great progress in the field of ultracold quantum gases in recent years can be largely attributed to the existence of magnetically tunable Feshbach resonances [1]. Since their first experimental introduction into the field [2–4], they have been widely used to arbitrarily tune the interactions between atoms.

In general, a Feshbach resonance occurs when a colliding pair of atoms is resonantly coupled to a molecular bound state. A magnetically tunable Feshbach resonance is based on Zeeman shifting a bound molecular state into resonance with the scattering state. Alternative coupling schemes for inducing Feshbach resonances have been proposed but never experimentally applied to control atomic interactions. The use of radio frequency [5] and static electric fields [6] was suggested. Fedichev *et al.* [7] proposed optical coupling of the scattering state with the molecular state, which was theoretically analyzed further in [8,9]. This scheme, often referred to as "optical Feshbach resonance," can be controlled via laser detuning and laser power.

Inducing Feshbach resonances with optical fields offers experimental advantages compared to magnetic fields. The intensity and detuning of optical fields can be rapidly changed. Furthermore, complex spatial intensity distributions can be easily produced which result in corresponding scattering length patterns across the sample. Optical transitions are always available, even when no magnetic Feshbach resonances exist. Recently, Fatemi *et al.* [10] observed optical Feshbach resonances in photoassociation spectroscopy. They used photoionization to probe optically induced changes in the scattering wave function. However, the direct influence of the optical Feshbach resonance on the atomic scattering properties was not studied.

In this Letter, we report a direct measurement of the atomic scattering length a in a BEC of ^{87}Rb $|F = 1, m_F = -1\rangle$ as we cross an optical Feshbach resonance. With moderate laser intensities of about 500 W/cm^2, we can change the scattering length over 1 order of magnitude from 10 a_0 to 190 a_0 ($a_0 = 1$ Bohr radius).

To optically modify the scattering length, we use laser light tuned close to a photoassociation resonance which couples the continuum state of incoming free atoms to an excited molecular level (see inset in Fig. 1). This changes the wave function and consequently the scattering length of the scattering state. It also leads to atomic loss due to spontaneous decay via the molecular state. The resonant transition rate between the continuum state and the molecular state, which we denote Γ_{stim}, is proportional to the laser intensity. In our experiment, $\Gamma_{\mathrm{stim}}/2\pi$ is on the order of a few 10 kHz. This is 3 orders of magnitude less than the spontaneous decay rate Γ_{spon} from the excited molecular state. In [8], Bohn and Julienne give convenient expressions for the scattering length a and the inelastic collision rate coefficient K_{inel} which describes the photoassociation loss. For $\Gamma_{\mathrm{stim}} \ll \Gamma_{\mathrm{spon}}$, these expressions can

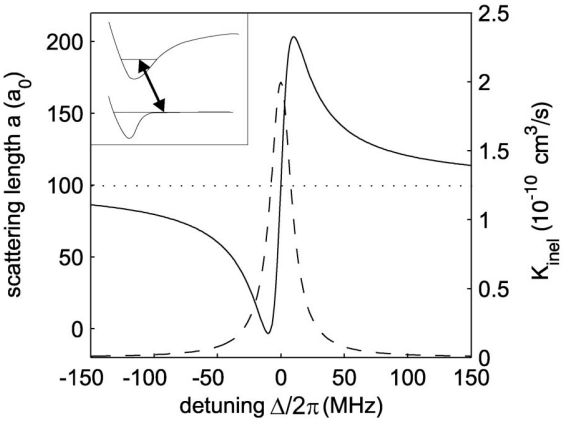

FIG. 1. Scattering length a (solid line) and inelastic collision rate coeffient K_{inel} (broken line) as a function of the laser detuning from the photoassociation resonance. The curves are based on Eqs. (1) and (2) for typical experimental parameters: $\Gamma_{\mathrm{stim}}/2\pi = 54$kHz, $\Gamma_{\mathrm{spon}}/2\pi = 20$MHz, $k_i = 2.47 \times 10^5 \mathrm{m}^{-1}$, $a_{\mathrm{bg}} = 100 a_0$ (dotted line). Inset: Scheme for optically coupling the scattering state with an excited molecular state.

be approximated and, for a condensate [11], read:

$$a = a_{\mathrm{bg}} + \frac{1}{2k_i}\frac{\Gamma_{\mathrm{stim}}\Delta}{\Delta^2 + (\Gamma_{\mathrm{spon}}/2)^2} \quad (1)$$

$$K_{\mathrm{inel}} = \frac{2\pi\hbar}{m}\frac{1}{k_i}\frac{\Gamma_{\mathrm{stim}}\Gamma_{\mathrm{spon}}}{\Delta^2 + (\Gamma_{\mathrm{spon}}/2)^2} \quad (2)$$

where a_{bg} is the scattering length in the absence of light, Δ is the detuning from the photoassociation line, m the atomic mass, and $\hbar k_i$ the relative momentum of the collision. Figure 1 shows a and K_{inel} as functions of the detuning Δ for typical experimental parameters. According to Eqs. (1) and (2), one should in general choose large detuning and strong coupling in order to maximize the change in scattering length while keeping the losses low.

Our experiments are carried out with an almost pure ^{87}Rb condensate in the $|F = 1, m_F = -1\rangle$ spin state with typically 1×10^6 atoms. The setup uses a magnetic transport scheme [12] to transfer atoms from a magneto-optical trap (MOT) chamber to a glass cell where the BEC is produced by rf-evaporation in a cigar shaped quadrupole and Ioffe configuration (QUIC) trap [13] with trap frequencies $\omega_{\mathrm{axial}}/2\pi = 15$Hz and $\omega_{\mathrm{radial}}/2\pi = 150$Hz. The intensity stabilized photoassociation laser beam (≈ 40 mW) is derived from a Ti:Sa laser. It is aligned along the axial direction of the cigar shaped BEC and has a waist radius of 76 μm. Its linear polarization is perpendicular to the trapping magnetic bias field of 2 Gauss. In our experiments, we limit the maximum laser intensities to about 500 W/cm^2 because we observe the appearance of a growing component of thermal atoms for higher intensities. This effect is negligible for laser powers below 500 W/cm^2.

In order to identify a suitable molecular level with strong coupling to the continuum state, we investigated molecular lines in the 1_g and 0_g^- potentials, which connect to the $(S_{1/2} + P_{3/2})$ and $(S_{1/2} + P_{1/2})$ asymptotes. We choose the excited state $|0_g^-(\sim S_{1/2} + P_{3/2}), \nu = 1, J = 2\rangle$ which is located 26.8 cm^{-1} below the $D2$ line [14]. Figure 2 shows the corresponding photoassociation line together with the line for $J = 0$. At a laser intensity of 460 W/cm^2, the measured atom losses yield a peak inelastic collision rate $K_{\mathrm{inel}} = (2 \pm 1) \times 10^{-10}$cm^3/s, which is a factor of 5 weaker than K_{inel} in the example of [8]. Losses due to excitation of the $D2$ line can be neglected. We observe a strong intensity dependent light shift of 215 MHz/(kW cm^{-2}) of the photoassociation line which might be mainly explained by coupling to a d-wave shape resonance [15].

Measuring the scattering length close to a photoassociation resonance requires a fast experimental method as atom losses restrict the observation time to below 100 μs in our experiments. Thus, the scattering length can neither be extracted from measurements of the collision rate

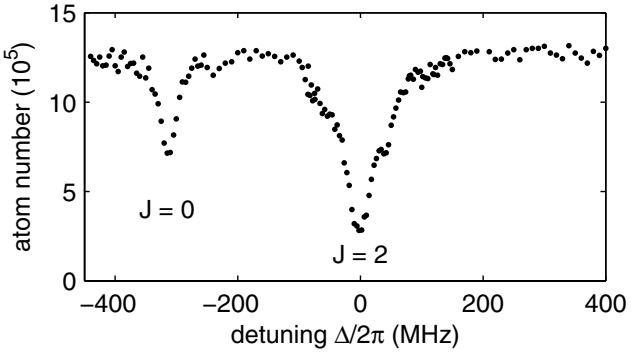

FIG. 2. Photoassociation spectrum of the excited molecular state used in the experiment. The two lines belong to the state $|0_g^-(\sim S_{1/2} + P_{3/2}), \nu = 1\rangle$ and have rotational quantum numbers $J = 0, 2$, respectively. Shown is the remaining atom number after exposing a BEC to a 70 μs light pulse of 460 W/cm^2 intensity. The detuning is given relative to the $J = 2$ line. Each data point is an average of three measurements.

[4] nor from the mean-field energy in a condensate expansion [2], both of which require a few ms. Instead, we use Bragg spectroscopy [16] to determine the mean-field energy by imposing on the atoms a moving optical lattice composed of two counter-propagating laser beams with wave number k and an adjustable frequency difference Δf. The Bragg lattice transfers a momentum of $2\hbar k$ to the atoms in a first order diffraction process. This is resonant when energy conservation is fulfilled, which for *noninteracting* atoms reads $h\Delta f_0 = (2\hbar k)^2/2m$. For a condensate, however, the resonance frequency Δf_r is shifted by the mean-field energy. In the Thomas-Fermi approximation, this yields a value of

$$\Delta f_r = \Delta f_0 + \frac{8\hbar}{7m} n_0 a \quad (3)$$

where n_0 denotes the atomic peak density [16]. Observing this shift of the Bragg resonance frequency therefore allows to measure the product of density and scattering length.

We derive the two Bragg beams from a laser which is 1.4 nm blue detuned relative to the ^{87}Rb $D2$ line. This determines Δf_0 to be 15.14 kHz. Two acousto-optical modulators are used to control the frequency difference Δf between the two counter-propagating beams. The beams have a diameter of ≈ 900 μm and are aligned along the radial trap axis in a horizontal direction. In our measurements, we apply a 70 μs square-pulse of Bragg light to the condensate. After 12 ms of time of flight, when the momentum components of the condensate have spatially separated, we use absorption imaging to measure the portion of condensate atoms that have been diffracted. We always choose the intensity of the lattice such that about 15%–20% of the atoms are diffracted at resonance. Scanning Δf and determining the percentage

of diffracted atoms yields curves as shown in Fig. 3 from which we extract the resonance positions. Shining in a photoassociation laser pulse (70 μs square-pulse) at the same time as the Bragg pulse shifts the resonance position. This shift depends on the detuning Δ from the molecular line (filled and open circles in Fig. 3).

For short illumination times T as in our experiment, the shape of the spectra fits well to the Fourier transform of the rectangular light pulse, $\sin^2[\pi(\Delta f - \Delta f_r)T]/(\Delta f - \Delta f_r)^2$, which we use to fit the data (see Fig. 3). Our measurements show that in spite of the Fourier-limited width of the Bragg resonance of 13 kHz (FWHM), we can resolve the peak position to better than ± 100 Hz.

When we invert the frequency difference of the Bragg laser beams and diffract atoms to a momentum state with $-2\hbar k$ instead of $+2\hbar k$, we notice that the absolute value of the resonance frequency $|\Delta f_r|$ changes. This can be explained by an initial condensate momentum of up to $0.05\ \hbar k$ which we find to slowly vary from day to day. This initial momentum is due to residual experimental imperfections like optical dipole forces of a slightly noncentered photoassociation beam. To eliminate this effect, we always measure Δf_r for $+2\hbar k$ as well as for $-2\hbar k$ and then take the difference.

Figure 4 shows the data we obtain from scanning the photoassociation laser over the optical resonance for a fixed laser intensity of 460 W/cm^2. The number of atoms in the condensate at the end of the laser pulse is plotted in Fig. 4(a) indicating the position of the molecular line. On resonance, about 90% of the atoms are lost after the 70 μs of interaction time. Figure 4(b) shows the resonance frequency Δf_r for Bragg diffraction as a function of laser detuning Δ. For large positive (and negative) detuning Δ, the value of Δf_r agrees with the 16.6 kHz expected from theory for the background scattering length $a_{bg} = 100\ a_0$ [17,18] and a BEC with $\approx 8.2 \times 10^5$ atoms. As we tune across the molecular resonance, the measured resonance frequencies exhibit a distorted dispersive shape. Following Eq. (3), this is the result of the combination of two effects: first, the scattering length a varies with Δ which alone should result in a dispersive line shape as in Fig. 1. Second, the atomic density n_0 decreases due to photoassociation losses which would, if the scattering length was constant, result in a symmetrical dip for Δf_r. On the right-hand side of the resonance, these two effects nearly compensate each other whereas on the left-hand side, the effects add up to produce a prominent dip in Δf_r.

In order to extract the scattering length a from the measured frequencies one can, in a first approach, replace the dynamically changing density n_0 in Eq. (3) by a time averaged value $\langle n_0 \rangle_t$. The average $\langle n_0 \rangle_t$ can be derived from the rate equation for the local density $\dot{n} = -2K_{inel}n^2$ [19] describing two-atom losses. This yields values for a which differ only marginally from the ones in Fig. 4(c). The data in Fig. 4(c) were obtained from a more

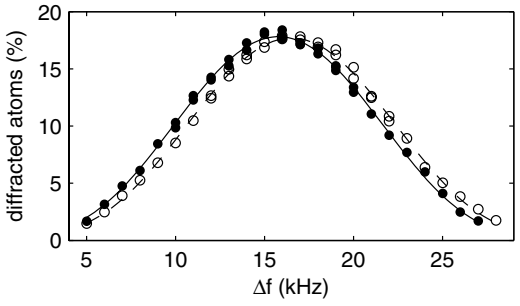

FIG. 3. Two Bragg resonance curves with an optically induced relative shift of 0.75 kHz. The percentage of the diffracted atoms is plotted against the frequency difference of the lattice beams. The two curves correspond to a detuning $\Delta/2\pi = -47$ MHz (filled circles) and $\Delta/2\pi = +47$ MHz (open circles) at a photoassociation laser intensity of 460 W/cm^2. The lines shown are fits to the data. For better comparison the right curve (open circles) has been scaled by a factor of 1.09 to the same height as the left one.

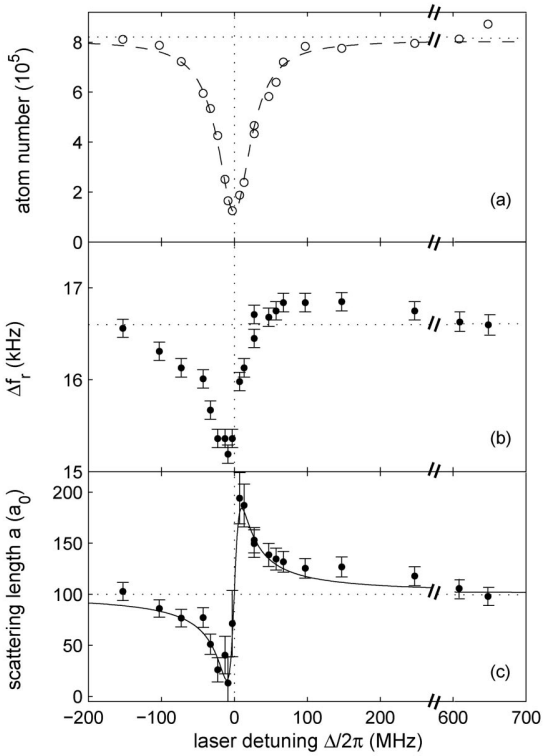

FIG. 4. Optical Feshbach resonance. In (a), the final atom number is plotted versus the detuning of the photoassociation laser (the dashed line is a Lorentz curve to guide the eye). The data in (b) display the measured Bragg resonance frequencies. In (c), the values for the scattering length obtained from the data in (a) and (b) are plotted. The continuous line is a fit of Eq. (1) to the data.

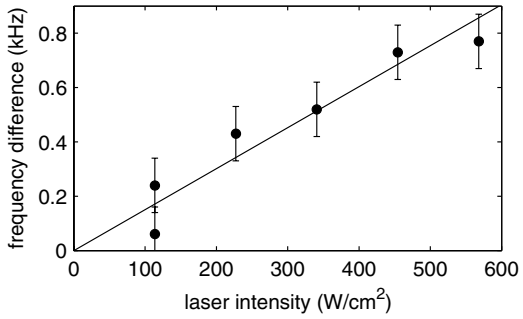

FIG. 5. Dependence of the optically induced mean-field shift on the laser intensity.

detailed examination which takes into account the full spatially resolved time evolution of the condensate density [20]. This includes the dynamical flattening of the condensate density profile caused by the rapid atom loss which is much faster than the trap frequencies [19]. Figure 4(c) shows that with a laser power of 460 W/cm^2, we can tune the scattering length over a range from 10 a_0 to 190 a_0. A fit of Eq. (1) to these data for a yields a spontaneous decay width $\Gamma_{\text{spon}}/2\pi$ of 20 MHz and a resonant inelastic collision rate coefficient $K_{\text{inel}} = 1.7 \times 10^{-10}\text{cm}^3/\text{s}$. These values agree with those we obtain from atom loss measurements. Thus, our data consistently confirm the intrinsic relation between a and K_{inel} as expressed in Eqs. (1) and (2).

The measured width $\Gamma_{\text{spon}}/2\pi$ of 20 MHz is larger than the expected molecular decay width of 12 MHz (corresponding to 2 times the atomic width). This might be explained by the line width of the Ti:Sa laser of about 4 MHz and a power broadening of the line due to different light shifts of unresolved molecular hyperfine states [18,19].

Figure 5 demonstrates the linear dependence of the scattering length a on the photoassociation laser intensity. For these measurements, we determine the Bragg resonance frequency for the detunings $\Delta/2\pi \approx \pm 50$ MHz at various photoassociation laser intensities. This is slightly complicated by the light shift and broadening of the photoassociation line which lead to an uncertainty in $\Delta/2\pi$ of ± 10 MHz. We keep the final atom number and density fixed by adjusting the pulse duration for each laser intensity. This ensures that only changes in a are reflected in the varying mean-field shift. In Fig. 5, we plot the frequency difference $\Delta f(+50\text{MHz}) - \Delta f(-50\text{MHz})$ which increases our signal.

In conclusion, our experiments demonstrate the tunability of the scattering length in ultracold samples by optically coupling free atoms to a bound molecular state. Because of the exquisite control one has over laser fields, we expect optical Feshbach resonances to be valuable when it comes to controlling atom-atom interactions in demanding applications. The inherent losses suggest the use of high laser intensities at large detuning and a good choice of the molecular state in order to optimize the ratio of change in scattering length and loss rate. Optical Feshbach tuning could be particularly useful to control atomic interactions in optical lattices which are discussed as potential future quantum information processors.

We thank Paul Julienne, Eite Tiesinga, John Bohn, Olivier Dulieu, Peter Fedichev, Andrea Micheli, and Helmut Ritsch for very helpful discussions. This work was supported by the Austrian Science Fund (FWF) within SFB 15 (project part 17) and by the European Union in the frame of the Cold Molecules TMR Network under Contract No. HPRN-CT-2002-00290.

*Permanent address: Department of Physics, Bates College, Lewiston, ME 04240.

[1] E. Tiesinga, B. J. Verhaar, and H. T. C. Stoof, Phys. Rev. A **47**, 4114 (1993).
[2] S. Inouye *et al.*, Nature (London) **392**, 151 (1998).
[3] Ph. Courteille *et al.*, Phys. Rev. Lett. **81**, 69 (1998).
[4] J. L. Roberts *et al.*, Phys. Rev. Lett. **81**, 5109 (1998).
[5] A. J. Moerdijk, B. J. Verhaar, and T. M. Nagtegaal, Phys. Rev. A **53**, 4343 (1996).
[6] M. Marinescu and L. You, Phys. Rev. Lett. **81**, 4596 (1998).
[7] P. Fedichev, Yu Kagan, G.V. Shlyapnikov, and J. T. M. Walraven, Phys. Rev. Lett. **77**, 2913 (1996).
[8] J. Bohn and P. S. Julienne, Phys. Rev. A **56**, 1486 (1997).
[9] V. Kokoouline, J. Vala, and R. Kosloff, J. Chem. Phys. **114**, 3046 (2001).
[10] F. K. Fatemi, K. M. Jones, and P. D. Lett, Phys. Rev. Lett. **85**, 4462 (2000).
[11] For condensed atoms, the collision rate coefficient is only half of the coefficient for thermal atoms as all atoms share the same quantum state.
[12] M. Greiner, I. Bloch, T.W. Hänsch, and T. Esslinger, Phys. Rev. A **63**, R031401 (2001).
[13] T. Esslinger, I. Bloch, and T.W. Hänsch, Phys. Rev. A **58**, R2664 (1998).
[14] A. Fioretti *et al.*, Eur. Phys. J. D **15**, 189 (2001).
[15] A. Simoni, P. S. Julienne, E. Tiesinga, and C. J. Williams, Phys. Rev. A **66**, 063406 (2002).
[16] J. Stenger *et al.*, Phys. Rev. Lett. **82**, 4569 (1999).
[17] Eberhard Tiemann (private communication).
[18] Paul Julienne and Eite Tiesinga (private communication).
[19] C. McKenzie *et al.*, Phys. Rev. Lett. **88**, 120403 (2002).
[20] This calculation is a simulation of the Rabi flopping between two levels corresponding to the condensate component at rest and the component with momentum $2\hbar k$. The changing density due to the loss is included by introducing a time dependent detuning.

B Acknowledgment

Danke...Donkschian...Grazie...Dankjewel...Gracias...Thank you!!!

Ich bedanke mich bei allen, die zum Gelingen dieser Arbeit beigetragen haben und die mich während meiner Doktorarbeit begleiteten: Rudi Grimm für die hervorragende Leitung der Arbeitsgruppe und seinen unermüdlichen Einsatz. Johannes Hecker Denschlag für die ausgezeichnete Betreuung meiner Dissertation und seine sehr gute Teamleitung. Ich danke auch Hanns-Christoph Nägerl: seine interessanten Praktika und sein lockerer Umgang mit den Studenten haben in mir erst die Begeisterung für dieses Forschungsgebiet geweckt.
Besonders danke ich meinen alten Mitstreitern aus erster Stunde, Matthias und Gregor, mit denen ich die Ehre hatte ein neues "ultracooles" Experiment aufbauen zu dürfen. Von beiden habe ich viel gelernt. Außerdem möchte ich allen ehemaligen und aktuellen Rubidium Team-Mitglieder danken die dabei geholfen haben aus dem Experiment einen vollen Erfolg zu machen: Florian, Stefan, Sascha, Ina, Michael, Christian und Birgit. Der ganzen restlichen Arbeitsg(t)ruppe für das super Umfeld und den freundschaftlichen Umgang.
Ich möchte mich ebenfalls bei den Gastprofessoren George Ruff, Herman Batelaan und Peter van der Straten für ihre Hilfe und die anregenden Diskussionen bedanken. Zusätzlich danke ich den fleißigen Korrekturlesern dieser Arbeit, Francesca, Steven und Gregor. Ein großer Dank gebührt den Mitarbeitern im Sekretariat sowie in der Elektronik- und Mechanikwerkstätte, die uns immer mit Rat und Tat beistanden.
Ich möchte mich auch bei allen bedanken die mich mehr oder weniger freiwillig ertragen haben und mir das Leben außerhalb des "Elfenbeinturms" versüßten: Francesca, Stefan, Jörg, Astrid, Salva, Daniel, Chris, Heidi, Diego, Manuel, Michi, Katrin, Tobias, Hans, Christof, Moni, Alex, Veri, Burbel und Valen. Danke für die netten Stunden in steilen Felswänden und tiefen Schluchten, beim Biken und Snowboarden, beim Feiern und Rocken.
Ein großes Dankeschön an meine Familie für ihre Unterstützung.

Bibliography

Anderson, M. H., J. R. Ensher, M. R. Matthews, C. E. Wieman, and E. A. Cornell.
Observation of Bose-Einstein condensation in a dilute atomic vapor.
Science 269: 198–201 (1995).

Anglin, J. R. and W. Ketterle.
Bose-Einstein condensation of atomic gases.
Nature 416: 211–218 (2002).

Arimondo, E. and G. Orriols.
Nonabsorbing atomic coherences by coherent two-photon transitions in a three-level optical pumping.
Lettere al Nuovo Cimento della Societa Italiana di Fisica 17: 333–338 (1976).

Ben Dahan, M., E. Peik, J. Reichel, Y. Castin and C. Salomon.
Bloch oscillations of atoms in an optical potential.
Physical Review Letters 76: 4508–4511 (1996).

Bergmann, K., H. Theuer and B. W. Shore.
Coherent population transfer among quantum states of atoms and molecules.
Reviews of Modern Physics 70: 1003–1025 (1998).

Boller, K.-J., A. Imamolu and S. E. Harris.
Observation of electromagnetically induced transparency.
Physical Review Letters 66: 2593–2596 (1991).

Bradley, C. C., C. A. Sackett, J. J. Tollett and R. G. Hulet.
Evidence of Bose-Einstein condensation in an atomic gas with attractive interactions.
Physical Review Letters 75: 1687–1690 (1995).

Chin, C., M. Bartenstein, A. Altmeyer, S. Riedl, S. Jochim, J. H. Denschlag and R. Grimm.
Observation of the pairing gap in a strongly interacting Fermi gas.
Science 305: 1128–1130 (2004).

Chin, C., T. Kraemer, M. Mark, J. Herbig, P. Waldburger, H.-C. Nagerl and R. Grimm.
Observation of Feshbach-like resonances in collisions between ultracold molecules.
Physical Review Letters 94: 123201 (2005).

Chin, J. K., D. E. Miller, Y. Liu, C. Stan, W. Setiawan, C. Sanner, K. Xu and W. Ketterle.
Evidence for superfluidity of ultracold fermions in an optical lattice.
Nature 443 (7114): 961–964 (2006).

Cohen Tannoudji, C., B. Diu and F. Laloe.
Quantenmechanik.
de Gruyter, 2. Auflage (1999).

Cserti, J.
Application of the lattice Green's function for calculating the resistance of an infinite network of resistors.
American Journal of Physics 68: 896–906 (2000).

Dalfovo, F., S. Giorgini, L. P. Pitaevski and S. Stringari.
Theory of Bose-Einstein condensation in trapped gases.
Reviews of Modern Physics 71: 463–512 (1999).

Davidson, N., H. J. Lee, M. Kasevich and S. Chu.
Raman cooling of atoms in two and three dimensions.
Physical Review Letters 72: 3158–3161 (1994).

Davis, K. B., M. O. Mewes, M. R. Andrews, N. J. van Druten, D. S. Durfee, D. M. Kurn and W. Ketterle.
Bose-Einstein condensation in a gas of Sodium atoms.
Physical Review Letters 75: 3969–3973 (1995).

DeMille, D.
Quantum computation with trapped polar molecules.
Physical Review Letters 88: 067901 (2002).

Donley, E. A., N. R. Claussen, S. T. Thompson and C. E. Wieman.
Atom-molecule coherence in a Bose-Einstein condensate.
Nature 417: 529–533 (2002).

Doyle, J., B. Friedrich, R. Krems and F. Masnou-Seeuws.
Quo vadis, cold molecules?
Eur. Phys. J. D 31: 149–164 (2004).

Dürr, S., T. Volz, A. Marte and G. Rempe.
Observation of molecules produced from a Bose-Einstein condensate.
Physical Review Letters 92: 020406 (2004a).

Dürr, S., T. Volz and G. Rempe.
Dissociation of ultracold molecules with Feshbach resonances.
Phys. Rev. A 70: 031601(R) (2004b).

Esslinger, T., I. Bloch and T. W. Hänsch.
Bose-Einstein condensation in a quadrupole-Ioffe configuration trap.
Physical Review A 58: R2664 (1998).

Fioretti, A., C. Amiot, C. M. Dion, O. Dulieu, M. Mazzoni, G. Smirne and C. Gabbanini.
Cold rubidium molecule formation through photoassociation: A spectroscopic study of the 0_g^- long-range state of $^{87}Rb_2$.
European Physical Journal D 15: 189–198 (2001).

Fisher, M. P. A., P. B. Weichmann, G. Grinstein and D. S. Fisher.
Boson localization and the superfluid-insulator transition.
Physical Review B 40: 546–570 (1989).

Gaubatz, U., P. Rudecki, M. Becker, S. Schiemann, M. Külz and K. Bergmann.
Population switching between vibrational levels in molecular beams.
Chemical physics letters 149: 463–468 (1988).

Günter, K., T. Stöferle, H. Moritz, M. Köhl and T. Esslinger.
Bose-fermi mixtures in a three-dimensional optical lattice.
Physical Review Letters 96 (18): 180402 (2006).

Góral, K., T. Köhler, S. A. Gardine, E. Tiesinga and P. S. Julienne.
Adiabatic association of ultracold molecules via magnetic-field tunable interactions.
J. Phys. B: At. Mol. Opt. Phys. 37: 3457–3500 (2004).

Greiner, M.
Ultracold quantum gases in three-dimensional optical lattice potentials.
Dissertation, Ludwig-Maximilians-Universität München (2003).

Greiner, M., I. Bloch, T. W. Hänsch and T. Esslinger.
Magnetic transport of trapped cold atoms over a large distance.
Physical Review A 63: 031401 (2001).

Greiner, M., O. Mandel, T. Esslinger, T. W. Hänsch and I. Bloch.
Quantum phase transition from a superfluid to a Mott insulator in gas of ultracold atoms.
Nature 415: 39–44 (2002).

Greiner, M., C. A. Regal and D. S. Jin.
Emergence of a molecular Bose-Einstein condensate from a Fermi gas.
Nature 426: 537–540 (2003).

Grimm, R., M. Weidemüller and Y. B. Ovchinnikov.
Optical dipole traps for neutral atoms.
Adv. At. Mol. Opt. Phys. 42: 95–170 (2000).

Hau, L. V., S. E. Harris, Z. Dutton and C. H. Behroozi.
Light speed reduction to 17 metres per second in an ultracold atomic.
Nature 397: 594–598 (1999).

Hecker Denschlag, J. and A. J. Daley.
Exotic atom pairs: Repulsively bound states in an optical lattice.
Proceedings of the International School of Physics "Enrico Fermi", Course CLXIV on Ultra-Cold Fermi Gases. cond-mat/0610393 (2006).

Hecker Denschlag, J., J. E. Simsarian, H. Häffner, C. McKenzie, A. Browaeys, D. Cho, K. Helmerson, S. L. Rolston and W. D. Phillips.
A Bose-Einstein condensate in an optical lattice.
J. Phys. B: At. Mol. Opt. Phys. 35: 3095–3110 (2002).

Hellwig, M.
Stabilisierung von Laser-Systemen für Experimente mit ultrakalten Atomen.
Master thesis, University of Innsbruck (2005).

Herbig, J., T. Krämer, M. Mark, T. Weber, C. Chin, H.-C. Nägerl and R. Grimm.
Preparation of a pure molecular quantum gas.
Science 301: 1510–1513 (2003).

Hofstetter, W., J. I. Cirac, P. Zoller, E. Demler and M. D. Lukin.
High-temperature superfluidity of fermionic atoms in optical lattices.
Physical Review Letters 89: 220407 (2002).

Inouye, S., M. R. Andrews, J. Stenger, H.-J. Miesner, D. M. Stamper-Kurn and W. Ketterle.
Observation of Feshbach resonances in a Bose-Einstein condensate.
Nature 392: 151–154 (1998).

Jaksch, D., C. Bruder, J. I. Cirac, C. W. Gardiner and P. Zoller.
Cold bosonic atoms in optical lattices.
Physical Review Letters 81: 3108 (1998).

Jaksch, D., V. Venturi, J. I. Cirac, C. J. Williams and P. Zoller.
Creation of a molecular condensate by dynamically melting a Mott insulator.
Physical Review Letters 89: 040402 (2002).

Jaksch, D. and P. Zoller.
The cold atom Hubbard toolbox.
Annals of Physics 315: 52–79 (2005).

Jochim, S., M. Bartenstein, A. Altmeyer, G. Hendl, C. Chin, J. H. Denschlag and R. Grimm.
Pure gas of optically trapped molecules created from fermionic atoms.
Physical Review Letters 91: 240402 (2003).

Jones, K. M., E. Tiesinga, P. D. Lett and P. S. Julienne.
Ultracold photoassociation spectroscopy: Long-range molecules and atomic scattering.
Reviews of Modern Physics 78: 483 (2006).

Ketterle, W., D. S. Durfee and D. M. Stamper-Kurn.
Making, probing and understanding Bose-Einstein condensates.
In M. Inguscio, S. Stringari and C. E. Wieman, Herausgeber, *Bose-Einstein Condensation in Atomic Gases*, Band CXL von *Proceedings of the International School of Physics »Enrico Fermi«*. IOS Press (1999).

Köhler, T., K. Goral and P. S. Julienne.
Production of cold molecules via magnetically tunable feshbach resonances.
Reviews of Modern Physics 78: 1311 (2006).

Kuklinski, J. R., U. Gaubatz, F. T. Hioe and K. Bergmann.
Adiabatic population transfer in a three-level system driven by delayed laser pulses.
Phys. Rev. A 40: 6741–6744 (1989).

Lewenstein, M., L. Santos, M. A. Baranov and H. Fehrmann.
Atomic bose-fermi mixtures in an optical lattice.
Physical Review Letters 92: 050401 (2004).

Marte, A., T. Volz, J. Schuster, S. Dürr, G. Rempe, E. G. M. v. Kempen and B. J. Verhaar.
Feshbach resonances in Rubidium 87: Precision measurement and analysis.
Physical Review Letters 89: 283202 (2002).

Messiah, A.
Quantenmechanik 2, Band 2.
de Gruyter, 3. Auflage (1990).

Metcalf, H. and P. van der Straten.
Laser Cooling and Trapping.
Springer (2002).

Moritz, H., T. Stöferle, K. Günter, M. Köhl and T. Esslinger.
Confinement induced molecules in a 1D Fermi gas.
Physical Review Letters 94: 210401 (2005).

Oreg, J., F. T. Hioe and J. H. Eberly.
Adiabatic following in multilevel systems.
Phys. Rev. A 29: 690–697 (1984).

Ospelkaus, C., S. Ospelkaus, L. Humbert, P. Ernst, K. Sengstock and K. Bongs.
Ultracold heteronuclear molecules in a 3d optical lattice.
Physical Review Letters 97 (12): 120402 (2006).

Ott, H., E. de Mirandes, F. Ferlaino, G. Roati, G. Modugno and M. Inguscio.
Collisionally induced transport in periodic potentials.
Physical Review Letters 92 (16): 160601 (2004).

Regal, C. A., M. Greiner and D. S. Jin.
Observation of resonance condensation of fermionic atom pairs.
Physical Review Letters 92: 040403 (2004).

Rom, T., T. Best, O. Mandel, A. Widera, M. Greiner, T. W. Hansch and I. Bloch.
State selective production of molecules in optical lattices.
Physical Review Letters 93: 073002 (2004).

Schollwöck, U.
The density-matrix renormalization group.
Reviews of Modern Physics 77: 259 (2005).

Scully, M. O., S.-Y. Zhu and A. Gavrielides.
Degenerate quantum-beat laser: Lasing without inversion and inversion without lasing.
Physical Review Letters 62: 2813–2816 (1989).

Shore, B. W.
Theory of Coherent Atomic Excitation.
Wiley (1990).

Staanum, P., S. D. Kraft, J. Lange, R. Wester and M. Weidemüller.
Experimental investigation of ultracold atom-molecule collisions.
Physical Review Letters 96: 023201 (2006).

Stöferle, T., H. Moritz, K. Günter, M. Köhl and T. Esslinger.
Molecules of fermionic atoms in optical lattices.
Physical Review Letters 96: 030401 (2006).

Stähler, M., R. Wynands, S. Knappe, J. Kitching, L. Hollberg, A. Taichenachev and V. Yudin.
Coherent population trapping resonances in thermal 85Rb vapor: D1 versus D2 line excitation.
Opt. Lett. 27: 1472–1474 (2002).

Thalhammer, G.
Ultrakalte gepaarte Atome in kohärenten Lichtfeldern.
Phd thesis, University of Innsbruck (2007).

Thalhammer, G., M. Theis, K. Winkler, R. Grimm and J. Hecker Denschlag.
Inducing an optical Feshbach resonance via stimulated Raman coupling.
Physical Review A 71: 033403 (2005).

Thalhammer, G., K. Winkler, F. Lang, S. Schmid, R. Grimm and J. H. Denschlag.
Long-lived Feshbach molecules in a three-dimensional optical lattice.
Physical Review Letters 96: 050402 (2006).

Theis, M.
Optical Feshbach resonances in a Bose-Einstein condensate.
Phd thesis, University of Innsbruck (2005).

Vitanov, N. V. and S. Stenholm.
Population transfer via a decaying state.
Phys. Rev. A 56: 1463–1471 (1997).

Volz, T., S. Dürr, S. Ernst, A. Marte and G. Rempe.
Charakterization of elastic scattering near a Feshbach resonance in ^{87}Rb.
Physical Review A 68: 010702(R) (2003).

Volz, T., N. Syassen, D. M. Bauer, E. Hansis, S. Dürr and G. Rempe.
Preparation of a quantum state with one molecule at each site of an optical lattice.
Nature Physics 2: 692–695 (2006).
ArXiv:cond-mat/0605184.

Weitz, M., B. C. Young and S. Chu.
Atomic interferometer based on adiabatic population transfer.
Physical Review Letters 73: 2563–2566 (1994).

Winkler, K.
Aufbau einer magnetischen Transportapparatur für ultrakalte Atome.
Diploma thesis, University of Innsbruck (2002).

Winkler, K., F. Lang, G. Thalhammer, P. v. d. Straten, R. Grimm and J. H. Denschlag.
Coherent optical transfer of feshbach molecules to a lower vibrational state.
Physical Review Letters 98: 043201 (2007).

Winkler, K., G. Thalhammer, F. Lang, R. Grimm, J. H. Denschlag, A. J. Daley, A. Kantian, H. P. Büchler and P. Zoller.
Repulsively bound atom pairs in an optical lattice.
Nature 441: 853–856 (2006).

Winkler, K., G. Thalhammer, M. Theis, H. Ritsch, R. Grimm and J. Hecker Denschlag.
Atom-molecule dark states in a Bose-Einstein condensate.
Physical Review Letters 95: 063202 (2005).

Wynar, R., R. S. Freeland, D. J. Han, C. Ryu and D. J. Heinzen.
Molecules in a Bose-Einstein Condensate.
Science 287: 1016–1019 (2000).

Wynar, R. H.
Ultra-cold molecules in an atomic Bose-Eeinstein condensate.
Dissertation, University of Texas at Austin (2000).

Xu, K., T. Mukaiyama, J. R. Abo-Shaeer, J. K. Chin, D. E. Miller and W. Ketterle.
Formation of quantum-degenerate Sodium molecules.
Physical Review Letters 91: 210402 (2003).

Zahzam, N., T. Vogt, M. Mudrich, D. Comparat and P. Pillet.
Atom-molecule collisions in an optically trapped gas.
Physical Review Letters 96: 023202 (2006).

Zwierlein, M. W., C. A. Stan, C. H. Schunck, S. M. F. Raupach, S. Gupta, Z. Hadzibabic and W. Ketterle.
Observation of Bose-Einstein condensation of molecules.
Physical Review Letters 91: 250401 (2003).

Zwierlein, M. W., C. A. Stan, C. H. Schunck, S. M. F. Raupach, A. J. Kerman and W. Ketterle.
Condensation of pairs of fermionic atoms near a Feshbach resonance.
Physical Review Letters 92: 120403 (2004).